# INTENTIONAL NONLINEARITY IN THE SMALL SCALE WITH APPLICATIONS TO ATOMIC FORCE MICROSCOPY (AFM) AND MASS SENSING

BY

RANDI POTEKIN

DISSERTATION

Submitted in partial fulfillment of the requirements
for the degree of Doctor of Philosophy in Theoretical and Applied Mechanics
in the Graduate College of the
University of Illinois at Urbana-Champaign, 2018

Urbana, Illinois

Doctoral Committee:

Professor Alexander F. Vakakis, Chair and Director of Research
Professor Lawrence A. Bergman, Co-Director of Research
Assistant Professor Seok Kim
Assistant Professor Sameh Tawfick
Adjunct Research Professor Michael McFarland
Assistant Professor Hanna Cho, The Ohio State University

# Abstract

Over the past several decades, the development of ultra-sensitive nano/micromechanical sensor technology has had a transformative effect on the field of nanoscience. These devices are currently used in many different applications including biological, chemical and inertial sensing; atomic force microscopy and infrared spectroscopy; and precise time keeping and synchronization. Traditionally, these systems were studied within the framework of linear dynamics, and incidental nonlinearity was suppressed by design. More recently, researchers have intentionally incorporated nonlinearity in the design of such devices in order to exploit the rich nonlinear behavior. Some of the nonlinear phenomena that researchers aim to utilize include internal resonance, resonant bandwidth expansion, ultra-sensitive bifurcation frequencies associated with sudden jumps in the response, coexistence of multiple solution branches and higher harmonic generation. In this dissertation, I investigate further ways in which intentional nonlinearity can be leveraged to enhance micromechanical resonant sensing techniques. In particular, I focus on applications to AFM and mass sensing.

Within the area of AFM, the performance of a new cantilever design during multi-frequency tapping mode AFM is studied. The system consists of a base cantilever with an inner paddle which, under harmonic excitation, vibrates like a system of linearly coupled oscillators engaging simultaneously a lower, in-phase and a higher, out-of-phase resonant mode. The cantilever is designed so that the $2^{nd}$ mode frequency (i.e., the out-of-phase eigenfrequency) coincides with an integer multiple of the fundamental mode frequency, providing the necessary conditions for realization of internal resonance. During tapping mode, the nonlinear tip-sample force activates the internal resonance and thereby amplifies the out-of-phase resonant mode. In contrast to other multi-frequency AFM techniques, the advantage of this approach is that multiple harmonics with strong signal-to-noise ratios (SNR) are excited while maintaining the simplicity of a single excitation frequency. The ability of this inner-paddled cantilever to measure compositional properties of polymers and bacteria was studied, and it was found that the internal resonance-based design results in enhanced sensitivity to Young's modulus.

In another study, a new micromechanical resonant mass sensor design is introduced consisting of a doubly clamped beam having a concentrated mass at its center, subjected to harmonic base excitation. The resonator is specifically designed to exhibit geometric nonlinearity due to midplane stretching. The reduced order model of the system's fundamental bending mode is that of a Duffing oscillator (i.e., an oscillator having cubic stiffness in addition to linear stiffness) under harmonic base excitation. For positive cubic stiffness, it is well known that the Duffing oscillator exhibits hardening in the frequency response curve resulting in a broadband resonance. The bandwidth of the resonator is determined by the linear resonant frequency (lower bound) and the jump-down bifurcation frequency (upper bound). Under harmonic excitation at a fixed forcing level, the jump down bifurcation frequency is proportional to the forcing level, and at each forcing level there indeed exists a jump down bifurcation. In the proposed system, the forcing level is not fixed; rather, it is proportional to the square of the driving frequency of the base excitation. Interestingly, analytical and computational analyses predict the existence of a critical excitation amplitude above which there is no theoretically predicted jump down bifurcation. It is shown that the effect of the concentrated mass is to lower the threshold of the critical excitation amplitude to a realizable level.

In practice, there must inevitably be a jump down bifurcation and this bifurcation may be triggered by the excitation of internal resonances, shrinking domain of attraction of the upper solution branch, variations in the initial state due to noise and/or the presence of nonlinear damping. However, the critical excitation amplitude appears to correspond to sudden and significant bandwidth expansion. Experimental results from a Duffing-like oscillator provide some verification of the powerful theoretical predictions. Ultimately, by operating at an excitation amplitude above the critical level, the ultra-wide resonant bandwidth can be exploited in a mass detection scheme based on amplitude tracking. In comparison to other micromechanical mass sensors, this technique and design offers a wide range of operational frequencies and amplitudes with strong SNR, eliminates the need for frequency sweeping and sophisticated feedback control, and requires relatively simple actuation and microfabrication methods.

*I dedicate this to my mother for teaching me the value of education and lifelong learning.*

# Acknowledgements

I am grateful for the tremendous support I received from advisors, colleagues and committee members during my Ph.D. studies. First and foremost I would like to acknowledge my co-advisors, Professor Alexander F. Vakakis and Professor Lawrence A. Bergman, for their insight and guidance over the years. Throughout my graduate studies, I always felt lucky to have such kind and talented advisors. Their technical expertise and creativity have been a constant source of inspiration. From taking Introduction to Dynamics and Vibrations with Professor Vakakis, to publishing my first paper as an undergraduate student, to working on a variety of different research topics as a graduate student, I have always had great respect and appreciation for Professors Vakakis and Bergman as teachers and mentors. Our weekly research meetings were always filled with interesting discussion, enthusiasm and laughter.

I would also like to acknowledge Dr. Hanna Cho for her invaluable help and advice. Dr. Cho has provided me with keen insight throughout my studies, especially with regard to experimental analysis. I will always cherish the exciting and productive trips I took to visit Dr. Cho's lab at the Ohio State University. I was lucky enough to attend a conference with her during which she helped me pursue a post-doctoral position that I ultimately accepted.

Dr. Michael McFarland also had an instrumental role in my pursuit of a Ph.D., for which I am very thankful. I can recall countless times when I came across a hurdle in my research endeavors and he was able to help me move past it. He was very generous about offering help whether it involved meeting with me for further discussions in his office, going over the details of a code, or coming down to the lab to help resolve an issue.

I am also grateful to have had the opportunity to work with Professor Seok Kim and his student, Zining Yang. If it weren't for Professor Kim's impressive capabilities in the area of microfabrication, the experimental analysis in my Ph.D. studies would not have been possible. I would like to thank Sajith Dharmasena for a constructive collaboration and for his valuable experimental expertise in AFM. I gratefully acknowledge Professor Sameh Tawfick for serving on my committee. I am likewise grateful for having such supportive and motivating lab mates at the Linear and Nonlinear Dynamics and Vibrations Laboratory.

Finally, I would like to express my gratitude to my family, close friends and boyfriend for all of their love and support.

## Table of Contents

# Chapter 1: Introduction

In recent decades, micro and nanomechanical resonators have drawn considerable attention due to their high sensitivity, portability and relatively low-cost. They are currently used for a wide variety of applications including precise frequency generation and timekeeping, nanoscale imaging and sensor technology (Antonio et al., 2012; Arlett et al., 2011; Brand et al., 1998; Garcia, 2010; Garcia and Perez, 2012; Johnson and Mutharasan, 2012; Schmidt and Howe, 1987; Stemme, 1991). In general, nano/micromechanical resonators have relatively low damping with Q-factors in the range of $10^2$ to $10^5$ and high resonant frequencies ranging from $10^4$ to $10^9$ Hz. These amazing properties result in sharp resonance peaks at high frequencies, which are extremely sensitive to physical properties like force and mass. For example, such sensors are capable of detecting forces present in intramolecular covalent bonds (de Oteyza et al., 2013) and even quantifying the mass of a single proton (Chaste et al., 2012).

Broadly speaking, most micromechanical resonant sensing techniques utilize a micro beam structure under harmonic excitation, undergoing either torsional or flexural vibrations. Qualitative or quantitative changes in the dynamic response at resonance are monitored and serve as the detection mechanism. The harmonic excitation may be applied at the base or directly to the structure from a variety of different actuation forces including piezoelectric, electrostatic and magnetic. Until recently, these resonators were designed and studied within the framework of linear dynamics. Nevertheless, nonlinearity is not entirely avoidable and may arise from a variety of different sources. Nonlinearity may be generated by large deformations of the resonator (i.e., geometric nonlinearity), nonlinear interactions with external structures, nonlinear potential forces associated with the actuation mechanism, nonlinear constitutive relations of the structure's material and/or nonlinear damping. Traditionally, nonlinearity was undesirable in the dynamics of micro/nano resonators and researchers focused on mitigating sources of incidental nonlinearity (Ekinci et al., 2004; Ekinci and Roukes, 2005; Kacem et al., 2010). Over the past couple of decades, a new approach to nonlinearity in micro/nanoresonantors has emerged and is now an expanding, active research area. In this approach, nonlinearity is intentionally incorporated into the device design in order to leverage the rich nonlinear behavior for practical purposes. Some of the unique nonlinear phenomena that designers aim to exploit include resonance bandwidth expansion, internal resonance, parametric resonance, bifurcation frequencies associated with sudden jumps in the response amplitude, coexistence of multiple solutions and higher harmonic generation.

Antonio et al. (2012) utilized an internal resonance between the first flexural mode and the first torsional mode of an electrostatically actuated microresonator to achieve frequency stabilization of the jump-down bifurcation frequency. In practice, the frequency stabilization can be used in time-keeping and synchronization schemes with enhanced signal-to-noise-ratios (SNR) as compared to the SNR achievable in the linear dynamic regime. In a more recent study, it was further shown that the mode coupling in this device results in coherent energy transfer between vibrational modes that can precisely counterbalance energy dissipation in the absence of an external energy supply (Chen et al., 2017). In several studies, it was shown that the jump bifurcations associated with nonlinear resonances are considerably more sensitive to the addition of mass than the linearized resonant frequency due to extremely low effective Q-factors. This novel feature has given rise to a burgeoning research area known as bifurcation-based mass sensing, in which a variety of different resonator designs and actuation methods have been considered. In some cases, parametric resonance is used to generate the jump bifurcation, which is achieved by harmonically varying the resonators effective linear stiffness and driving the system at twice the unperturbed natural frequency (Miller et al., 2010; Burgner et al., 2010; Li et al., 2014b; Prakash et al., 2012; Turner et al., 1998; Zhang et al., 2002; Zhang and Turner, 2005; Yie et al., 2011). In other approaches, nonlinear resonances exhibiting either strong hardening behavior or strong softening behavior give rise to the ultra-sensitive jump bifurcation, where the hardening behavior is typically the result of geometric nonlinearity and the softening behavior is often caused by electrostatic actuation (Cho et al., 2010; Bajaj et al., 2016; Bouchaala et al., 2016; Kumar et al., 2011; Kumar et al., 2012; Younis and Alsaleem, 2009). Alternatively, resonance bandwidth expansion resulting from parametric resonance can be used in mass detection schemes based on amplitude tracking (Hiller et al., 2015; Li et al., 2014a) or in electromechanical pass-band filtering (Rhoads et al., 2005).

In atomic force microscopy (AFM) applications, the microresonator (i.e., probe) itself is a linear system but interaction with the sample introduces nonlinearity into the dynamics. The nonlinear interaction between the probe tip and sample may result in the co-existence of two stable solution branches at resonance and higher harmonics in the cantilever's response. Usually, it is undesirable for the cantilever's dynamics to transition from one solution branch to the other while collecting an AFM image because it may generate artifacts. To address this issue, Cho et al. (2012) theoretically introduced a new probe design that intentionally incorporates geometric nonlinearity in order to eliminate one of the solution branches. In contrast, under certain conditions, branch jumping throughout an AFM scan can be beneficial since the branch selection provides qualitative compositional information (Garcia, 2010). Recently, quantitative compositional mapping has become a popular research area in AFM and, in what is termed *multi-harmonic AFM*, the higher harmonics are utilized to compute quantitative material property measurements (Cartagena et al., 2013; Cartagena-Rivera, 2015; Raman et al., 2011).

The focus of this dissertation is to further contribute to the research area discussed above and consider new ways in which nonlinearity can be exploited to improve micromechanical resonant sensing techniques. Specifically, we consider applications in AFM and mass sensing. This dissertation is composed of six Chapters, each of which contains its own references and numbering system. In Chapter 2, we discuss some fundamental concepts and common applications of microresonant sensing. An outline of the theoretical modeling and analysis of linear microresonant sensors is presented in Section 2.1, with a focus on mass and force sensors. In Section 2.2, motivations for intentional nonlinearity in the design of microresonant sensors, common sources of nonlinearity and relevant nonlinear phenomena are discussed.

In Chapter 3, we present work in the area of AFM in which a new design of the AFM probe is proposed. The new cantilever design utilizes intentional internal resonance to passively amplify higher harmonics for use in multi-harmonic, tapping mode AFM. The necessary conditions for internal resonance are achieved by specifically designing the cantilever so that a higher vibrational mode coincides exactly with a higher harmonic and the internal resonance is then activated by the nonlinear tip-sample interaction. The proposed cantilever design consists of a base micro-cantilever with an inner paddle where the base cantilever is a structurally modified commercial AFM cantilever and the inner paddle is a 300nm thick *Si* membrane (Keum et al., 2012; Keum et al., 2016). Under harmonic excitation, this system behaves like two linearly coupled damped harmonic oscillators involving a lower, in-phase vibrational mode and a higher, out-of-phase vibrational mode. The length of the inner paddle is specifically chosen so that the higher eigenfrequency is an integer multiple of the lower eigenfrequency. If the ratio of the higher eigenfrequency to the lower eigenfrequency is *n,* then the nonlinear tip-sample interaction will trigger a 1:*n* internal resonance in the inner-paddled cantilever resulting in strong amplification of the $n^{\text{th}}$ harmonic. The efficacy of this new probe design was theoretically and experimentally shown in a previous study (Jeong et al., 2016). In contrast to other multi-frequency AFM techniques, this approach provides multiple channels with strong signal to noise ratios while maintaining the simplicity of a single excitation frequency. I experimentally and computationally studied the capability of this cantilever to characterize material properties of polymers, bacteria and viruses and found that the internal resonance-based design results in enhanced sensitivity to Young's modulus. In some cases, the enhanced material sensitivity is due to differences in branch selection among coexisting solution branches, which are not detected by the first harmonic amplitude. In other cases, I found that, in contrast to commercial AFM cantilevers, the internal resonance based design introduces sensitivity to Young's modulus among the first harmonic phase for a purely elastic sample. The chapter concludes with a detailed outline for material property inversion analysis that could be used to convert the observables of this inner-paddled cantilever into quantitative compositional information.

In Chapter 4, a new micromechanical resonant sensor deign is introduced consisting of a clamped-clamped beam having a concentrated mass at its center. A reduced order model of the beam system is constructed in the form of a discrete spring-mass system that contains cubic stiffness due to axial stretching of the beam in addition to linear flexural stiffness. The beam is intentionally designed to enhance the cubic nonlinearity in order to cause nonlinear axial tension and thereby generate a broadband resonance of the fundamental flexural mode in the frequency response curve. For a fixed forcing level of the beam, the range of frequencies that constitutes the broadband resonance is determined by the linearized frequency (lower bound) and the drop bifurcation frequency (upper bound). However, harmonic base excitation at the two clamped ends of the beam is used in this study and therefore the forcing level is not fixed, but rather is proportional to the square of the excitation frequency. Interestingly, we see that for sufficiently large base excitation amplitudes, there is theoretically no drop frequency. Computational results confirm this theoretical prediction and we find that the presence of the concentrated mass significantly lowers the threshold amplitude required to achieve the *no drop phenomenon*. In practice, of course, it is not feasible to truly have no drop down bifurcation in the frequency response curve; the drop bifurcation may occur due to the excitation of internal resonances (Antonio et al., 2012; Chen et al., 2017), shrinking of the upper solution branch's domain of attraction, variations in the initial state due to noise and the presence of nonlinear damping. Each of these practical limitations will be discussed in Section 4.5. However, it's likely that the threshold amplitude corresponds to a critical excitation amplitude above which the bandwidth suddenly expands considerably.

Since the *no drop phenomenon* is valid for a general class of systems whose reduced order model is that of a Duffing oscillator excited by harmonic base excitation, I experimentally study a different Duffing system in an effort to verify this phenomenon. The system consists of a *Si* microcantilever restricted at its free end by a polymer bridge and is excited at the base via piezoelectric actuation. It has previously been shown that the flexural motion of this system is also governed by the Duffing equation, with an additional nonlinear damping term (Asadi et al., 2017). Indeed we experimentally observe a sudden and significant increase in the resonant bandwidth above a critical excitation voltage, which provides some experimental verification of the theoretical predictions outlined in Sections 4.1 - 4.4. Further, we see that the nonlinear damping term has the effect of limiting the maximum drop frequency when operating above the threshold excitation amplitude.

Chapter 5 theoretically outlines a mass sensing technique involving the doubly-clamped microbeam sensor design introduced in Chapter 4. By operating at an excitation amplitude above the critical threshold, the ultra-wide resonant bandwidth can be leveraged in a mess sensing method based on amplitude tracking. A secondary effect of the cubic nonlinearity in the system is strong amplification of the third harmonic and, hence, both the first and third harmonics are monitored as mass is added to the device. In a computational study, I track changes in the steady-state amplitudes of the first and third harmonics as mass is added to the device, at a fixed excitation frequency within the broadband. In practice, the base excitation could be provided via piezoelectric actuation and the purely mechanical device could be fabricated using conventional microfabrication techniques. This scheme would require an initial forward sweep of the drive frequency in order to attract the high-amplitude solution, and changes in the steady-state amplitude would serve as the mass detection mechanism thereafter. This eliminates the need for time-consuming frequency sweeps each time mass is added and/or sophisticated feedback control loops. The advantage of this approach is that the ultra-wide bandwidth allows for a considerably larger range of operational frequencies and amplitudes with strong SNR, as compared to other mass sensors that rely on amplitude tracking (both linear and nonlinear designs). Additionally, the device design and actuation mechanism are relatively simple.

## 1.1 References

Antonio D., Zanette D.H., López D. (2012). Frequency stabilization in nonlinear micromechanical oscillators. *Nat. Commun.,. 3*, 806.

Arlett J.L, Myers E.B., RoukesM.L. (2011). Comparative advantages of mechanical biosensors. *Nature Nanotech*. 6: 203-215. Feedback. *Journal of Microelectromechanical Systems*, *25*(1), 2–10.

Asadi, K., Li, J., Peshin, S., Yeom, J., and Cho, H. (2017). Mechanism of geometric nonlinearity in a nonprismatic and heterogeneous microbeam resonator. *Physical Review B*, *96*(11).

Bajaj, N., Sabater, A.B., Hickey, J.N., Chiu, G.T. C., Rhoads, J.F.J. (2016). Design and Implementation of a Tunable, Duffing-Like Electronic Resonator via Nonlinear Feedback. *Journal of Microelectromechanical systems*, *25*(1), 2-10.

Bouchaala, A., Jaber, N., Yassine, O., Shekhah, O., Chernikova, V., Eddaoudi, M., Younis, M.I. (2016). Nonlinear-based MEMS sensors and active switches for gas detection. *Sensors*, *16*(6), 758.

Brand, O. and Baltes, H. (1998). Micromachined Resonant Sensors: An Overview. *Sens. Update, 4(1),* 3–51.

Burgner C.B., Miller N., Shaw S., and Turner K. (2010). Parameter sweep strategies for sensing using bifurcations in MEMS. *Proc. Solid-State Sens., Actuators, Microsyst. Workshop, Hilton Head Workshop*, 130–133.

Burgner C., Turner K., Miller N., and Shaw S. (2011). Noise squeezing control for bifurcation sensing in MEMS. *Proc. ASME Int. Design Eng. Tech. Conf. Comput. Inf. Eng. Conf.*, 117–123.

Cartagena-Rivera, A.X., Wang, W.-H., Geahlen, R.L., and Raman, A. (2015). Fast, multi-frequency, and quantitative nanomechanical mapping of live cells using the atomic force microscope. *Scientific Reports*, *5*(June), 11692.

Cartagena, A., Hernando-Pérez, M., Carrascosa, J.L., de Pablo, P.J., and Raman, A. (2013). Mapping in vitro local material properties of intact and disrupted virions at high resolution using multi-harmonic atomic force microscopy. *Nanoscale*, *5*, 4729–36.

Chaste J., Eichler A., Moser J., Ceballos G., Rurali R., Bachtold A. (2012) A nanomechanical mass sensor with yoctogram resolution. *Nature Nanotech*. *7*(5), 301-304.

Chen C., Zanette D.H., Czaplewski D.A., Shaw S. and Lopez, D. (2017). Direct observation of coherent energy transfer in nonlinear micromechanical oscillators. *Nature Communications, 8,* 15523.

Cho H., Yu M.-F., Vakakis A., Bergman L., McFarland D.M. (2010). Tunable, broadband nonlinear nanomechanical resonator. *Nano Lett*., *10*(5), 1793-1798.

Cho H., Jeong B., Yu M.F., Vakakis A.F., McFarland D.M., Bergman L.A. (2012). Nonlinear hardening and softening resonances in micromechanical cantilever-nanotube systems originated from nanoscale geometric nonlinearities. *Int. J. Solids Str*., *49*, 2059-2065.

Ekinci, K.L., Yang, Y.T., Roukes, M.L. (2004). Ultimate limits to inertial mass sensing based upon nanoelectromechanical systems. *J. Appl. Phys*., *95*, 2682–2689.

Ekinci, K.L., Roukes, M.L. (2005). Nanoelectromechanical systems. *Rev. Sci. Instr., 76*, 061101.

Garcia R. (2010). *Amplitude Modulation Atomic Force Microscopy*. Wiley-VCH Verlag GmbH & Co. KGaA, Weinheim, Germany.

Garcia R., Perez R. (2002). Dynamic atomic force microscopy methods. *Surf. Sci., 47*, 197-301.

Hiller, T., Li, L.L., Holthoff, E.L., Bamieh, B., Turner, K.L. (2015). System Identification, Design, and Implementation of Amplitude Feedback Control on a Nonlinear Parametric MEM Resonator for Trace Nerve Agent Sensing. *Journal of Microelectromechanical Systems*, *24*(5), 1275–1284.

Jeong B., Pettit C., Dharmasena S., Keum H., Lee J., Kim J., Kim S., McFarland D.M., Bergman L.A., Vakakis A.F. (2016). Utilizing internal resonance to achieve multi-harmonic atomic force microscopy. *Nanotechnology*, *27*, 125501.

Johnson B.N. and Mutharasan R. (2012). Biosensing using dynamic-mode cantilever sensors: A review. *Biosens. Bioelectr.*, *32*, 1-18.

Kacem, N., Arcamone, J., Perez-Murano, F., Hentz, S. (2010). Dynamic range enhancement of nonlinear nanomechanical resonant cantilevers for highly sensitive NEMS gas/mass sensor applications. *Journal of Micromechanics and Microengineering*, *20*(4), 45023.

Keum, H., Carlson, A., Ning, H., Mihi, A., Eisenhaure, J. D., Braun, P.V, Rogers J.A., Kim, S. (2012). Silicon micro-masonry using elastomeric stamps for three-dimensional microfabrication. *Journal of Micromechanics and Microengineering*, *22*, 055018.

Keum, H., Yang, Z., Han, K., Handler, D.E., Nguyen, T.N., Schutt-Aine, J., Bahl G., Kim, S. (2016). Microassembly of Heterogeneous Materials using Transfer Printing and Thermal Processing. *Scientific Reports*, *6*, 29925.

Kumar V., Boley J.W., Yang Y., Ekowaluyo H., Miller J.K., Chiu T.-C., Rhoads J.F. (2011). Bifurcation-based mass sensing using piezoelectrically-actuated microcantilevers. *Appl. Phys. Lett., 98*, 153510.

Kumar, V., Yang, Y., Boley, J.W., Chiu, T.-C, Rhoads, J.F. (2012). Modeling , Analysis , and Experimental Validation of a Bifurcation-Based Microsensor. *J Microelectromech Syst.*, *21*(3), 549–558.

Li, L., Hiller, T., Bamieh, B., and Turner, K. (2014). Amplitude control of parametric resonances for mass sensing. *Proceedings of IEEE Sensors*, (December): 198–201.

Li L.L., Holthoff E.L., Shaw L.A., Burgner C.B., and Turner K.L. (2014). Noise squeezing controlled parametric bifurcation tracking of MIP-coated microbeam MEMS sensor for TNT explosive gas sensing, *J. Microelectromech. Syst., 23*, 1228–1236.

Miller N., Burgner C., Dykman M., Shaw S., and Turner K. (2012). Fast estimation of bifurcation conditions using noisy response data. Proc. SPIE, *Sensors Smart Struct. Technol. Civil, Mech., Aerosp. Syst.*, *7647*, 76470O.

de Oteyza D.G., Gorman P., Chen Y.-C., Wickenburg S., Riss A., Mowbray D.J., Etkin G., Pedramrazi Z., Tsai H.-Z., Rubio A., Crommie M.F., and Fischer F.R. (2013). Direct imaging of covalent bond structure in single-molecule chemical reactions. *Science, 340*, 1434-1437.

Prakash G., Raman A., Rhoads J., and Reifenberger R.G. (2012). Parametric noise squeezing and parametric resonance of microcantilevers in air and liquid environments. *Rev. Sci. Instrum., 83*, 065109.

Raman, A., Trigueros, S., Cartagena, A., Stevenson, A. P., Susilo, M., Nauman, E., Contera, S. A. (2011). Mapping nanomechanical properties of live cells using multi-harmonic atomic force microscopy. *Nat Nanotechnol*, *6*, 809–814.

Rhoads, J., Shaw, S., Turner, K., Baskaran, R. (2005). Tunable microelectromechanical filters that exploit parametric resonance. *J. Vib. Acoust., 127*, 423-430.

Schmidt, M A. and Howe, R.T. (1987). Silicon Resonant Microsensors. *Ceram. Eng. Sci. Proc.*, *8(9–10)*, 1019–1034.

Stemme, G. (1991). Resonant Silicon Sensors. *J. Micromech. Microeng.*, *1(2),* 113–125.

Turner, K., Miller, S., Hartwell, P., MacDonald, N., Strogatz, S. (1998). Five parametric resonances in a microelectromechanical system. *Nature, 396*(6707), 149-152.

Yie Z., Zielke M.A., Burgner C.B., and Turner K.L. (2011). Comparison of parametric and linear mass detection in the presence of detection noise. *J. Micromech. Microeng.*, *21*, 025027.

Younis M.I., Alsaleem F. (2009). Electrostatically-actuated structures based on nonlinear phenomena. *J. Comp. Nonl. Dyn.*, *4*, 021010.

Zhang, W., Baskaran, R., Turner, K.L. (2002). Effect of cubic nonlinearity on auto-parametrically amplified resonant MEMS mass sensor. *Sensors and Actuators, A: Physical*, *102*(1–2), 139–150.

Zhang W., Turner K.L. (2005). Application of parametric resonance amplification in a single-crystal silicon micro-oscillator based mass sensor. *Sensors and Actuators A,* 122, 23-30.

# Chapter 2: Dynamics of micro/nanomechanical resonators

In this Chapter, I discuss linear and nonlinear dynamics of micro/nanomechanical resonators. Traditionally, micro/nanomechanical resonators have been designed to operate in the linear dynamic regime, which simplifies the theoretical modeling considerably. In Section 2.1, I outline a general approach to reduced order modeling of linear micro/nanomechanical resonators and summarize the fundamental operating principles of micro/nanomechanical mass and force sensing within the linear dynamic regime. More recently, researchers have explored the advantages of intentionally incorporating nonlinearity in the design of micro/nanoresonators (Cho et al., 2016; Lifshits and Cross, 2008; Rhoads et al., 2010; Younis, 2011). In Section 2.2, I summarize the motivation for nonlinearity in micro/nanomechanical resonant sensing and discuss several of the prominent sources of nonlinearity.

## 2.1 Linear dynamic regime

### 2.1.1 Beam mechanics

Most micro/nanomechanical resonators are beam structures that undergo either flexural or torsional motion. The dynamics of such structures remain in the linear regime when the beam deflection is small enough that axial elongation of the neutral axis is negligible. Further, for beams with sufficiently large length to thickness ratios (i.e. relatively thin beams), the shear deformation is negligibly small and it can be assumed that plane sections remain plane after deformation. The boundary conditions vary depending on the specific application, with clamped-clamped and clamped-free boundary conditions being the most common types encountered in micro/nanomechanical resonators. In this sub-section, I introduce the equations governing transverse motion of Euler-Bernoulli beam structures and focus on clamped-clamped and clamped-free boundary conditions in particular.

### 2.1.1.1 Governing equations

Consider the transverse motion $v(x,t)$ of a thin beam with a distributed mass $\bar{m}(x)$ and bending stiffness $EI(x)$ as shown in Fig. 2.1a, and a differential element of the beam, as shown in Fig. 2.1b. Bending moment $M$, shear force $Q$, and infinitesimal variations of these quantities act on the differential element, along with a distributed force $f(x,t)$. In this analysis, the following assumptions are made:

1) There is no shear deformation in the beam; cross-sections initially perpendicular to the neutral axis of the beam remain plane and perpendicular to the neutral axis during bending.
2) The Y axis is an axis of symmetry of the cross-section; thus, motion is in-plane, and there are no out-of-plane effects.
3) There are neither axial deformations nor axial forces present in the neutral axis.
4) There are no rotational inertia effects.
5) The slopes, angles and deflections of the beam are small.

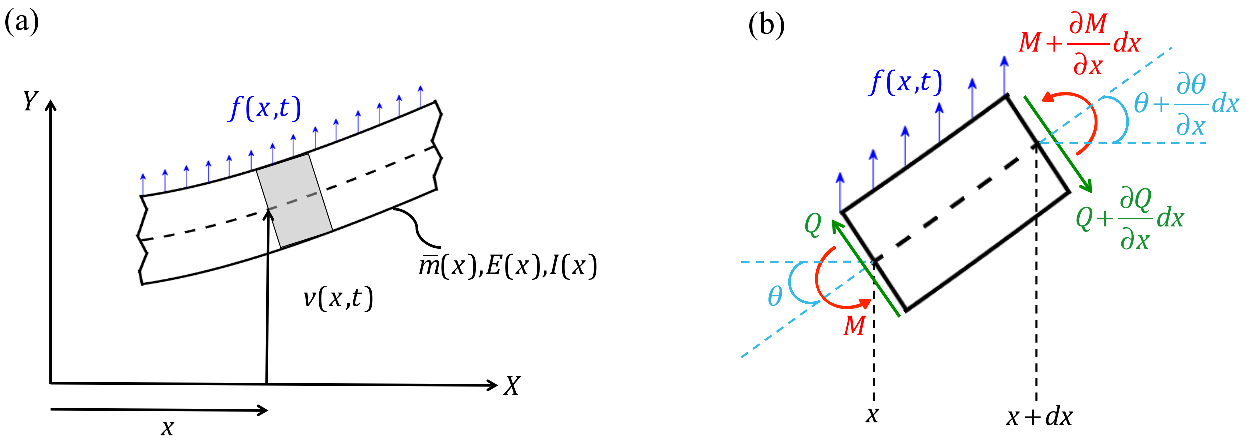

*Figure 2.1: (a) Element of a beam in the X-Y plane and (b) a corresponding differential element.*

By balancing the forces acting on the differential element shown in Fig.2.1b, the equilibrium relation is given by

$$\left(Q+\frac{\partial Q}{\partial x}dx\right)\cos\left(\theta+\frac{\partial \theta}{\partial x}dx\right)-Q\cos\theta+f\left(x,t\right)dx=\bar{m}\left(x\right)\frac{\partial^2 v}{\partial t^2}dx \tag{2.1}$$

where $Q=Q(x,t)$, $\theta=\theta(x,t)$ and $v=v(x,t)$. Equation (2.1) can be asymptotically expanded with respect to the small parameter *dx*,

$$\frac{\partial}{\partial x}\left(Q\cos\theta\right)dx+f\left(x,t\right)dx+O\left(dx^2\right)=\bar{m}\left(x\right)\frac{\partial^2 v}{\partial t^2}dx \tag{2.2}$$

In light of the small angle assumption, approximate $\cos\theta\approx 1$ giving, to leading order,

$$\frac{\partial Q}{\partial x}+f\left(x,t\right)=\bar{m}\left(x\right)\frac{\partial^2 v}{\partial t^2} \tag{2.3}$$

The balance of moments at x gives

$$0=M-\left(M+\frac{\partial M}{\partial x}dx\right)-\frac{1}{2}f\left(x,t\right)dx^2-\left(Q+\frac{\partial Q}{\partial x}dx\right)dx \tag{2.4}$$

which, to leading order, reduces to

$$Q=-\frac{\partial M}{\partial x} \tag{2.5}$$

where $M=M(x,t)$. The assumption stated in (1) implies that the longitudinal strains vary linearly with respect to the depth of the beam and that the neutral axis of the beam coincides with the centroid of the cross-section. This results in the following relation between the curvature, $\kappa(x,t)$, and the bending stiffness, $EI(x)=E(x)I(x)$,

$$\kappa(x,t)=\frac{M(x,t)}{EI(x)} \tag{2.6}$$

from the geometry,

$$\kappa(x,t)=\frac{\partial^2 v(x,t)}{\partial x^2}/\left\{1+\frac{\partial^2 v(x,t)}{\partial x^2}\right\}^{1/2} \tag{2.7}$$

Taking into account the assumption of small slopes in the beam, (2.6) and (2.7) give the relation

$$\frac{M(x,t)}{EI(x)}\approx\frac{\partial^2 v(x,t)}{\partial x^2} \tag{2.8}$$

Finally, substitution of (2.8) and (2.5) into (2.3) gives

$$\bar{m}(x)\frac{\partial^2 v}{\partial t^2}+\frac{\partial^2}{\partial x^2}\left[EI(x)\frac{\partial^2 v}{\partial x^2}\right]=f(x,t) \tag{2.9}$$

as the governing equation for transverse motion of a thin beam.

#### 2.1.1.2 Modal analysis of a prismatic beam

Consider an unforced, undamped, thin beam having uniform density and flexural rigidity,

$$\bar{m}\frac{\partial^2 v}{\partial t^2}+EI\frac{\partial^4 v}{\partial x^4}=0 \tag{2.10}$$

Two types of simple boundary conditions are considered in particular. In the resonator chosen for a mass sensing application (Chapter 5), I focus on clamped-clamped boundary conditions,

$$v(0,t) = \frac{\partial v}{\partial x}(0,t) = v(l,t) = \frac{\partial v}{\partial x}(l,t) = 0 \tag{2.11}$$

and in the AFM application (Chapter 3), clamped-free boundary conditions are considered,

$$v(0,t) = \frac{\partial v}{\partial x}(0,t) = 0 \tag{2.12a}$$

$$M(l,t) = 0 \quad \Rightarrow \quad \frac{\partial^2 v}{\partial x^2}(l,t) = 0 \tag{2.12b}$$

$$Q(l,t) = 0 \quad \Rightarrow \quad \frac{\partial^3 v}{\partial x^3}(l,t) = 0 \tag{2.12c}$$

Introduce the method of separation of variables, i.e., $v(x,t) = \varphi(x)\eta(t)$, and separate (2.10) into a set of time- and space-dependent equations,

$$\ddot{\eta} + \omega^2 \eta = 0, \quad \phi'''' - \frac{\omega^2}{c^4}\phi = 0, \quad c^4 = \frac{EI}{\bar{m}} \tag{2.13}$$

where overdot denotes differentiation with respect to *t* and prime denotes differentiation with respect to *x*. The general solution to the space-dependent equation is given by

$$\phi(x) = C_1 \sin\lambda x + C_2 \cos\lambda x + C_3 \sinh\lambda x + C_4 \cosh\lambda x, \quad \lambda^4 = \omega^2 / c^4 \tag{2.14}$$

The constants $C_1$, $C_2$, $C_3$ and $C_4$ and eigenvalue $\lambda$ are determined from the boundary conditions of the beam. In the following analysis the specific boundary value problem is solved for the case of a clamped-clamped beam and a cantilever.

**Clamed-clamped beam**

For a clamped-clamped beam, the boundary conditions are

$$\phi(0)=\phi^{'}(0)=\phi(l)=\phi^{'}(l)=0 \tag{2.15}$$

The conditions $\phi(0)=\phi^{'}(0)$ imply $C_2=-C_1$ and $C_4=-C_3$ so that

$$\begin{bmatrix} \sin\lambda l-\sinh\lambda l & \cos\lambda l-\cosh\lambda l \\ \cos\lambda l-\cosh\lambda l & -\sin\lambda l-\sinh\lambda l \end{bmatrix}\begin{Bmatrix} C_1 \\ C_2 \end{Bmatrix}=A\begin{Bmatrix} C_1 \\ C_2 \end{Bmatrix}=0 \tag{2.16}$$

For nontrivial solutions of $C_1$ and $C_2$, the determinant of matrix $A$ must be nonzero. In other words, the following condition must be true

$$\cos\lambda l\cosh\lambda l=1 \tag{2.17}$$

The infinity of $\lambda$ that satisfy the transcendental equation in (2.17) are the eigenvalues, and the corresponding eigenfrequencies are given by,

$$\omega_i=\lambda_i^2\sqrt{\frac{EI}{\bar{m}}} \tag{2.18}$$

The ratios $\left(C_1/C_2\right)_i$ are obtained by substituting $\lambda$ into (2.16)

$$\left(C_1/C_2\right)_i=\frac{\sin\lambda_i l+\sinh\lambda_i l}{\cos\lambda_i l-\cosh\lambda_i l} \tag{2.19}$$

Hence, the eigenfunction that characterizes the $i^{\text{th}}$ normal mode of vibration is given by

$$\phi_i(x) = C_i \left\{ \left( \frac{\sin\lambda_i l + \sinh\lambda_i l}{\cos\lambda_i l - \cosh\lambda_i l} \right) \left( \sin\lambda_i x - \sinh\lambda_i x \right) + \cos\lambda_i x - \cosh\lambda_i x \right\} \tag{2.20}$$

where $C_i$ is an arbitrary multiplicative constant. Introduce the *normalized* eigenfunctions, $\Phi_i(x)$, defined as

$$\Phi_i(x) = \alpha_i \psi_i(x), \quad \psi_i(x) = \left( \frac{\sin\lambda_i l + \sinh\lambda_i l}{\cos\lambda_i l - \cosh\lambda_i l} \right) \left( \sin\lambda_i x - \sinh\lambda_i x \right) + \cos\lambda_i x - \cosh\lambda_i x,$$

$$\alpha_i = \left( \bar{m} \int_0^l \psi_i^2(x)\,dx \right) \tag{2.21}$$

Note that normalization is not a unique process and other normalization definitions can be used. The specific normalization in (2.21) is chosen so that,

$$\int_0^l \bar{m}\Phi_i^2(x)\,dx = 1 \tag{2.22}$$

**Clamped-free beam (Cantilever)**

For a clamped-free beam, the boundary conditions are

$$\phi(0) = \phi'(0) = \phi''(l) = \phi'''(l) = 0 \tag{2.23}$$

By following the same steps as for the clamped-clamped beam, the infinity of eigenvalues, $\lambda_i$, are found to satisfy

$$\cos\lambda l \cosh\lambda l = -1 \tag{2.24}$$

and the associated $\left(C_1/C_2\right)_i$ are given by

$$\left(C_1/C_2\right)_i = \frac{\sin\lambda_i l - \sinh\lambda_i l}{\cos\lambda_i l - \cosh\lambda_i l} \tag{2.25}$$

Hence, the eigenfunction that characterizes the *i*th normal mode of vibration is given by

$$\phi_i(x) = C_i\left\{\left(\frac{\sin\lambda_i l - \sinh\lambda_i l}{\cos\lambda_i l - \cosh\lambda_i l}\right)\left(\sin\lambda_i x - \sinh\lambda_i x\right) + \cos\lambda_i x - \cosh\lambda_i x\right\} \tag{2.26}$$

where $C_i$ is an arbitrary multiplicative constant. The *normalized* eigenfunctions, $\Phi_i(x)$, are defined as

$$\Phi_i(x) = \alpha_i\psi_i(x), \quad \psi_i(x) = \left(\frac{\sin\lambda_i l - \sinh\lambda_i l}{\cos\lambda_i l - \cosh\lambda_i l}\right)\left(\sin\lambda_i x - \sinh\lambda_i x\right) + \cos\lambda_i x - \cosh\lambda_i x,$$

$$\alpha_i = \left(\bar{m}\int_0^l \psi_i^2(x)dx\right)^{-1/2} \tag{2.27}$$

Again, the specific normalization is selected so that

$$\int_0^l \bar{m}\Phi_i^2(x)dx = 1 \tag{2.28}$$

Finally, the solution to (2.10) can be written as the linear superposition of the infinite normal modes of vibration,

$$v(x,t) = \sum_{i=1}^{\infty}\Phi_i(x)\mathrm{N}_i(t) \tag{2.29}$$

where $\mathrm{N}_i(t)$ are the generalized coordinates, or, equivalently, the principle coordinates of the normalized mode shapes, $\Phi_i(x)$. That is, $\mathrm{N}_i(t)$ is the contribution of the $i^{\text{th}}$ vibration mode in the beam response, where the vibration modes are associated with an infinite, discrete spectrum of distinct eigenfrequencies and corresponding eigenfunctions.

#### 2.1.1.3 Forced vibration of a damped prismatic beam

Consider a forced, damped, thin beam having uniform density and flexural rigidity,

$$\bar{m}\frac{\partial^2 v}{\partial t^2}+\bar{c}\frac{\partial v}{\partial t}+EI\frac{\partial^4 v}{\partial x^4}=f(x,t) \tag{2.30}$$

Assume that the motion of the beam can be written as a linear superposition of the countably infinite set of normalized eigenfunctions characterizing the vibration modes of the underlying undamped, unforced beam. To this end, a solution to (2.30) of the form

$$v(x,t)=\sum_{i=1}^{\infty}\Phi_i(x)\mathrm{N}_i(t) \tag{2.31}$$

is assumed where $\Phi_i(x)$ are the normalized eigenfunctions and $\mathrm{N}_i(x)$ are the corresponding generalized coordinates. Substituting (2.31) into (2.30) gives

$$\bar{m}\sum_{i=1}^{\infty}\Phi_i(x)\ddot{\mathrm{N}}_i(t)+\bar{c}\sum_{i=1}^{\infty}\Phi_i(x)\dot{\mathrm{N}}_i(t)+EI\sum_{i=1}^{\infty}\Phi_i(x)\mathrm{N}_i(t)=f(x,t) \tag{2.32}$$

Now, each eigenfrequency and eigenfunction pair, $\left\{\omega_i,\phi_i(x)\right\}$, must satisfy the relation

$$EI\phi_i''''(x)-\bar{m}\omega_i^2\phi_i(x)=0 \tag{2.33}$$

It can be shown that, the eigenfunctions obey the following orthogonality condition (Meirovitch, 1975),

$$\int_0^l \bar{m}\phi_i(x)\phi_j(x)dx = 0, \quad i \neq j \tag{2.34}$$

That is, the eigenfunctions are orthogonal with respect to the mass distribution. It follows that

$$\int_0^l EI\phi_i''''(x)\phi_j(x)dx = 0, \quad i \neq j \tag{2.35}$$

In accordance with the specific normalizations considered here, the *normalized* eigenfunctions satisfy the following mass-orthonormality condition

$$\int_0^l \bar{m}\Phi_i(x)\Phi_j(x)dx = \delta_{ij} \tag{2.36}$$

from which the stiffness-orthonormality condition follows,

$$\int_0^l EI\Phi_i''''(x)\Phi_j(x)dx = \omega_i^2\delta_{ij} \tag{2.37}$$

where $\delta_{ij}$ is the Kronecker delta. Finally, multiplying (2.14) by $\Phi_j(x)$, integrating from $x=0$ to $x=l$ and using the orthonormality conditions stated in (2.36) and (2.37), results in

$$\ddot{\mathrm{N}}_j(t)+2\zeta_j\omega_j\dot{\mathrm{N}}_j(t)+\omega_j^2\mathrm{N}_j(t)=F_j(x,t), \quad 2\zeta_j\omega_j=\frac{\bar{c}}{\bar{m}}, \quad F_j(x,t)=\int_0^l f(x,t)\Phi_j(x)dx \tag{2.38}$$

where $\mathrm{N}_j(t)$ is the *projection* of the solution, $v(x,t)$, onto the normalized $j^{\text{th}}$ eigenmode shape, multiplied by the mass distribution,

$$\mathrm{N}_j(t)=\int_0^l \bar{m}v(x,t)\Phi_j(x)dx \tag{2.39}$$

Hence, the original partial differential equation has been reduced to a countably infinite set of uncoupled, ordinary differential equations. In other words, each vibration mode can be reduced to a single-degree-of-freedom modal oscillator. Each modal oscillator has an effective stiffness, effective mass and effective damping coefficient. In (2.21), for the general $j^{\text{th}}$ mode, $\omega_j^2$ represents the ratio of the effective stiffness to the effective mass, $2\zeta_j\omega_j$ is the ratio of the effective damping coefficient to the effective mass and $F_j\left(x,t\right)$ is the ratio of the force imparted to the $j^{\text{th}}$ modal oscillator to the effective mass. In the following section, I will outline a technique that is commonly used to compute the effective mass and stiffness for a given vibration mode of various beam systems. Once the effective mass and stiffness are known, the so-called lumped-parameter model can be constructed.

### 2.1.1.4 Effective mass and stiffness

When analyzing the dynamics of micro/nanoresonators, it is convenient to develop a lumped-parameter model corresponding to a particular vibration mode of interest. The lumped parameter model consists of a point mass connected to a linear spring and damper as shown in Fig. 2.2c. The point mass is characterized by the effective mass, $m_{\text{ef}}$, the spring is characterized by an effective stiffness, $k_{\text{ef}}$, and the damper is characterized by an effective damping coefficient, $c_{\text{ef}}$. In general, the displacement of the point mass, $z$, corresponds to the displacement at a particular point along the beam. It is common for $z$ to denote the displacement of the anti-node (i.e., the maximum displacement) for the vibrational mode of interest, as shown in Figs. 2.2b and 2.2c for the fundamental bending modes of a doubly clamped beam and cantilever, respectively.

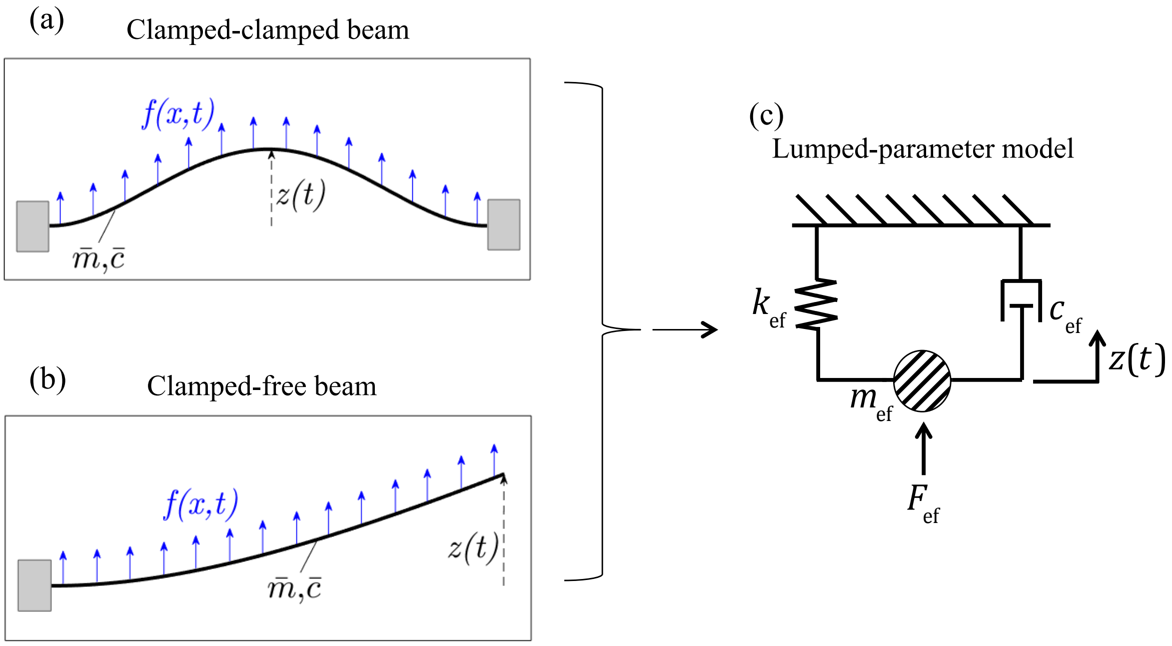

*Figure 2.2: A prismatic beam having distributed mass* $\bar{m}$ *and distributed damping* $\bar{c}$*, under the distributed load* $f(x,t)$ *with (a) clamped-clamped boundary conditions and (b) clamped-free boundary conditions. Both beams are depicted in their fundamental bending modes. For a clamped-clamped beam, the anti-node (location of maximum displacement) of the fundamental bending mode is at the center of the beam and for a clamped-free beam, the anti-node of the fundamental bending mode is at the free end of the beam. (c) The reduced order lumped-parameter model with effective mass,* $m_{\text{ef}}$*, effective stiffness,* $k_{\text{ef}}$*, effective damping coefficient,* $c_{\text{ef}}$*, and effective loading* $F_{\text{ef}}$*. Typically, the displacement of the point mass in the lumped-parameter model corresponds to the displacement at the anti-node as indicated here.*

The effective force, $F_{\text{ef}}$, denotes the projection of the distributed force, $f(x,t)$, onto the vibrational mode of interest scaled by the effective mass. The parameters are "lumped" in the sense that a point mass is used to isolate the inertial effects and a massless spring is used to isolate the stiffness effects. In reality, of course, the mass and stiffness are distributed continuously throughout the beam structure. However, as shown in the previous section, by projecting the governing equation onto a particular vibration mode, a discrete modal oscillator can be recovered. Here a widely used method to determine the effective stiffness and effective mass is outlined. Note, that by determining either the effective mass or effective stiffness, the other lumped parameters immediately follow from (2.38).

We will take $z$ to be the displacement at an arbitrary point along the beam, $x = a$, provided that the point does not coincide with a node. To compute the effective stiffness, we want to write the total potential energy, PE, in the form

$$\mathrm{PE} = \frac{1}{2} k_{\mathrm{ef}} z^2 \tag{2.40}$$

To begin, we compute the total potential energy in the system:

$$\mathrm{PE} = \frac{1}{2} \int_0^l EI (v_{xx})^2 dx \tag{2.41}$$

where $(\ )_x$ denotes partial differentiation with respect to $x$ so that $v_{xx} = \dfrac{\partial^2 v(x,t)}{\partial x^2}$. For the general $j^{\mathrm{th}}$ mode, the displacement can be written as

$$v(x,t) = \mathrm{N}_j(t) \Phi_j(x) \tag{2.42}$$

The displacement at $x = a$ is given by

$$z(t) = v(a,t) = \mathrm{N}_j(t) \Phi_j(a) \tag{2.43}$$

Hence, the displacement along the beam can be written as

$$v(x,t) = z(t) \frac{\Phi_j(x)}{\Phi_j(a)} \tag{2.44}$$

By substituting (2.44) into (2.41), we get

$$\mathrm{PE}=\frac{1}{2}\left[\frac{EI}{\Phi_j^2(a)}\int_0^l\left(\Phi_j''\right)^2 dx\right]z^2 \tag{2.45}$$

Using integration by parts and assuming simple boundary conditions, we have

$$\int_0^l\left(\Phi_j''\right)^2 dx=\int_0^l \Phi_j''''\Phi_j\,dx \tag{2.46}$$

Substituting (2.46) into (2.45) and using the stiffness-orthonormality condition in (2.37) gives

$$\mathrm{PE}=\frac{1}{2}\left(\frac{\omega_j^2}{\Phi_j^2(a)}\right)z^2 \tag{2.47}$$

Hence, the effective stiffness is

$$k_{\mathrm{ef}}=\frac{\omega_j^2}{\Phi_j^2(a)} \tag{2.48}$$

It follows (2.38) that the effective mass, effective damping coefficient and effective force are given by

$$m_{\mathrm{ef}}=\frac{k_{\mathrm{ef}}}{\omega_j^2}=\frac{1}{\Phi_j^2(a)} \tag{2.49}$$

$$c_{\mathrm{ef}}=m_{\mathrm{ef}}\frac{\bar{c}}{\bar{m}}=\frac{1}{\Phi_j^2(a)}\frac{\bar{c}}{\bar{m}} \tag{2.50}$$

$$F_{\mathrm{ef}} = m_{\mathrm{ef}} \int_0^l f(x,t)\Phi_j(x)dx = \frac{1}{\Phi_j^2(a)} \int_0^l f(x,t)\Phi_j(x)dx \tag{2.51}$$

Now, for the modal oscillator corresponding to the $j^{\mathrm{th}}$ vibration mode, equation (2.38) can equivalently be written in the form

$$m_{\mathrm{ef}}\ddot{z} + c_{\mathrm{ef}}\dot{z} + k_{\mathrm{ef}}z = F_{\mathrm{ef}} \tag{2.52}$$

Alternatively, one can first compute the effective mass by writing the total kinetic energy, KE, in the form

$$\mathrm{KE} = \frac{1}{2} m_{\mathrm{ef}} \dot{z}^2 \tag{2.53}$$

The total kinetic energy in the beam is

$$\mathrm{KE} = \frac{1}{2} \int_0^l \bar{m}(v_t)^2 dx \tag{2.54}$$

By differentiating (2.44) with respect to time and substituting the relation into (2.54) we have,

$$\mathrm{KE} = \frac{1}{2} \left[ \frac{\bar{m}}{\Phi_j^2(a)} \int_0^l \left(\Phi_j\right)^2 dx \right] \dot{z}^2 \tag{2.55}$$

Employing the mass-orthonormality condition in (2.36) gives

$$\mathrm{KE} = \frac{1}{2} \left( \frac{1}{\Phi_j^2(a)} \right) \dot{z}^2 \tag{2.56}$$

and, hence, the effective mass $m_{\mathrm{ef}} = \dfrac{1}{\Phi_j^2(a)}$ is recovered.

### 2.1.2 Basic principles of resonant micro/nanomechanical sensing

#### 2.1.2.1 Harmonic excitation of a micro/nanomechanical resonator

Generally micro/nanomechnical resonators are excited harmonically and the transient and/or steady state response of the resonator is used to detect physical properties like force and mass. Specifically, changes in the transient resonant frequency or steady-state amplitude often serve as the detection mechanism for sensing. Hence, the effective force often has the form $F_{\mathrm{ef}} = F\cos\omega t$ so that the initial value problem governing the motion of the resonator is given by,

$$m_{\mathrm{ef}}\ddot{z} + c_{\mathrm{ef}}\dot{z} + k_{\mathrm{ef}}z = F\cos\omega t, \quad z(0) = z_0, \quad \dot{z}(0) = \dot{z}_0 \tag{2.57}$$

The solution $z(t)$ is the sum of a transient response, $z_{\mathrm{t}}(t)$, resulting from the initial conditions and the steady-state response, $z_{\mathrm{ss}}(t)$, caused by the harmonic excitation. The steady-state response is

$$z_{\mathrm{ss}}(t) = Z_{\mathrm{ss}}\cos\left(\omega t - \varphi_{\mathrm{ss}}\right), \quad Z_{\mathrm{ss}} = \frac{P}{\sqrt{(\omega_n^2 - \omega^2)^2 + 4\zeta^2\omega_n^2\omega^2}}, \quad \varphi_{\mathrm{ss}} = \tan^{-1}\left(\frac{2\zeta\omega_n\omega}{\omega_n^2 - \omega^2}\right) \tag{2.58}$$

and the transient response is

$$z_t(t) = Z_t e^{-\zeta\omega_n t}\cos\left(\omega_d t - \varphi_t\right), \quad \varphi_t = \tan^{-1}\left(\frac{z_0 - Z_{\mathrm{ss}}\cos\varphi_{\mathrm{ss}}}{\dot{z}_0/\omega_d - Z_{\mathrm{ss}}\sin\varphi_{\mathrm{ss}}}\right)$$

$$Z_{\mathrm{t}} = \left(z_0 - Z_{\mathrm{ss}}\cos\varphi_{\mathrm{ss}}\right)\cos\varphi_{\mathrm{t}} + \left(\dot{z}_0/\omega_d - Z_{\mathrm{ss}}\sin\varphi_{\mathrm{ss}}\right)\sin\varphi_{\mathrm{t}} \tag{2.59}$$

where

$$\omega_n^2 = \frac{k_{\text{ef}}}{m_{\text{ef}}}, \quad 2\zeta\omega_n = \frac{c_{\text{ef}}}{m_{\text{ef}}}, \quad P = \frac{F}{m_{\text{ef}}}, \quad \omega_d = \omega_n\sqrt{1-\zeta^2} \tag{2.60}$$

Here we assume that the resonator is underdamped so that $\zeta < 1$ which is indeed the case for micro/nanomechanical resonators. In applications involving micro/nanoresonators it is common to characterize the damping in terms of the quality factor or *Q*-factor. The *Q*-factor is defined as the ratio of the resonant frequency to the bandwidth of the resonance curve at half of the peak amplitude, $\Delta\omega$,

$$Q = \frac{\omega_n}{\Delta\omega} \tag{2.61}$$

and is inversely related to the effective damping coefficient:

$$Q = \frac{\omega_n m_{\text{ef}}}{c_{\text{ef}}} = \frac{1}{2\zeta} \tag{2.62}$$

A schematic of the steady-state response of the resonator for various damping levels is shown in Fig. 2.3. We can see that the response near resonance is in the form of a Lorentz curve where the location of the peak is determined by the resonant frequency and the damping level determines the width of the curve. Note that the peak of the resonance curve does not occur exactly at the natural frequency $\omega_n$, rather the peak occurs at $\omega_{\text{peak}} = \omega_n\sqrt{1-2\zeta^2}$. However, in applications involving micro/nanomechanical resonators, the damping is relatively low with *Q*-factors in the range of 100 to 10,000 and, hence, $\omega_{\text{peak}} \approx \omega_d \approx \omega_n$.

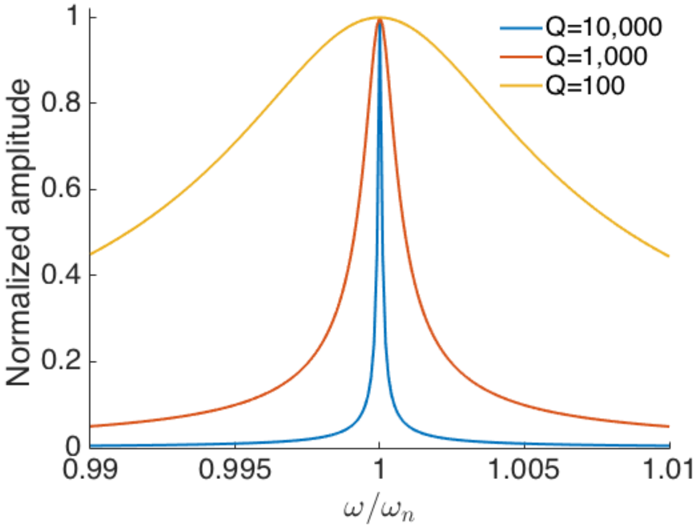

*Figure 2.3: Resonance curves for various damping levels; normalized steady-state amplitude,* $\frac{Z_{\text{ss}}\omega_n^2}{P\tilde{Z}_{\text{pk}}}$*, versus the normalized drive frequency for Q=100, Q=1,000 and Q=10,000, where* $\tilde{Z}_{\text{pk}} = \max\left(\frac{Z_{\text{ss}}\omega_n^2}{P}\right)$.

In sensing applications involving micro/nanomechanical resonators, variations in the frequency of the transient response, i.e. the damped natural frequency $\omega_d$, or variations in the steady-state amplitude, $Z_{\text{ss}}$, often serve as the sensing mechanism. The relations in (2.58) and (2.59) clearly indicate that $\omega_d$ and $Z_{\text{ss}}$ depend on the undamped natural frequency, $\omega_n$, of the vibrational mode of interest. Further, $\omega_n^2$ is proportional to the ratio of the effective stiffness, $k_{\text{ef}}$, to the effective mass, $m_{\text{ef}}$, which indicates that external contributions to the effective mass or the effective stiffness of the modal oscillator may be observed by monitoring the frequency of the transient response or the amplitude and phase of the steady-state response. In mass sensing applications, typically mass is deposited onto the resonator thereby modifying the effective mass of the oscillator and, in turn, causing variations in the transient and steady-state observables. If for example the resonator is pre-functionalized to attract a specific chemical or bio-molecule, the mass sensor further becomes a chemical- or bio-sensor. In contrast, in force sensing applications such as AFM, the interaction forces between the resonator and a sample influence the effective stiffness of the oscillator, resulting in variations in the transient and steady-state observables.

#### 2.1.2.2 Mass and force sensors

In this section, we present a summary of the mathematical analysis required to quantitatively relate the transient and steady-state observables to the amount of added mass (in the case of a mass sensor) or the gradient of the external force (in the case of a force sensor). Additionally, quantitative measurements of the sensitivities and resolutions are shown. It is important to note that these analyses are all within the context of linear micro/nanomechanical sensors and are not appropriate in the nonlinear dynamical regime. For mass sensing, the only external force present is the harmonic excitation and hence, the resonator behaves linearly for sufficiently small deformations, as will be discussed in more detail in Section 2.2. The most prominent force sensor that utilizes a micromechanical resonator is the atomic force microscope (AFM), which senses the interaction force between a sharp tip at the end of a cantilever and a sample to achieve high-resolution imaging. For AFM, in addition to harmonic excitation, the interaction force between the sharp tip and the sample is present and, in general, this interaction force is nonlinear. However, for small perturbations in the vicinity of an equilibrium point, the interaction force is approximately linear. Specifically, the equilibrium points correspond to positions of the cantilever where the mechanical restoring force exactly counter-balances the tip-sample interaction force. If the motion of the cantilever is such that the interaction force is smooth and in the vicinity of an equilibrium point, then the interaction force may be approximated as linear and the following analysis is valid.

**Mass sensors**

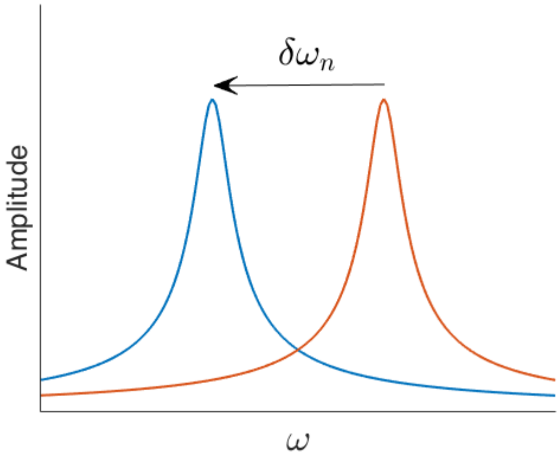

*Figure 2.4: Qualitative depiction of the downward shift in the resonance curve that occurs when the effective mass of a resonator increases.*

When mass is added to a micro/nanomechanical resonator, the primary resonance curves shifts downward toward lower frequencies (see Fig. 2.4) and by tracking the shifts in the linear resonant frequency, $\delta\omega_n$, one can deduced the amount of added mass. The added mass is typically small enough that contributions to the effective stiffness of the beam are negligible and we will assume here that there is no change in the effective stiffness due to the presence of added mass. For an added mass, $m$, the effective mass becomes

$$m_{\text{ef}} = m_{\text{ef0}} + m \tag{2.63}$$

where $m_{\text{ef0}}$ is the initial effective mass of the resonator before the mass $m$ is added. The resonant frequency can be written as

$$\omega_n = \omega_{n0} + \delta\omega_n \tag{2.64}$$

where $\omega_{n0}=\sqrt{k_{\text{ef}}/m_{\text{ef0}}}$ is the initial resonant frequency. Substitution of (2.64) and (2.63) into the relation $\omega_n^2=k_{\text{ef}}/m_{\text{ef}}$ gives

$$\omega_{n0}+\delta\omega_n=\sqrt{\frac{k_{\text{ef}}}{m_{\text{ef0}}+m}}=\omega_{n0}\left(1+\frac{m}{m_{\text{ef0}}}\right)^{-1/2} \tag{2.65}$$

Assuming that $m/m_{\text{ef0}}<<1$, we can asymptotically expand (2.65) with respect to $m/m_{\text{ef0}}$

$$\omega_{n0}+\delta\omega_n\approx\omega_{n0}\left(1-\frac{m}{2m_{\text{ef0}}}\right) \tag{2.66}$$

which can be rearranged to give the relation

$$m=-\frac{2m_{\text{ef0}}}{\omega_{n0}}\delta\omega_n \tag{2.67}$$

Equation (2.67) gives a quantitative measurement for the amount of added mass, $m$, based on a measured change in the resonant frequency, $\delta\omega_n$. The quantity $-2m_{\text{ef0}}/\omega_{n0}$ is the inverse of the mass responsivity of the resonator, $R_m$, defined as the ratio of the shift in the resonant frequency for a given change in the effective mass

$$R_m=\frac{\partial\omega_n}{\partial m_{\text{ef}}} \tag{2.68}$$

where, for $m/m_{\text{ef0}}<<1$, $R_m=-\frac{\omega_{n0}}{2m_{\text{ef0}}}$. The minimum detectable added mass, $m_{\min}$, is then dictated by the minimum detectable shift in the resonant frequency, $\delta\omega_{n,\min}$,

$$m_{\min} = -\frac{2m_{\text{ef0}}}{\omega_{n0}}\delta\omega_{n,\min} \tag{2.69}$$

The minimum detectable shift in resonant frequency is limited by the presence of noise in the system. Any source of damping in the system can in turn serve as a source of noise due to thermal fluctuations, according to the dissipation-fluctuation theorem (Heer, 1972). Such thermal fluctuations account for Nyquist-Johnson noise in the readout circuitry and thermomechanical noise in the resonator. Regarding thermomechanical noise, the damping-mechanisms present in the resonator's dynamics cause random vibrations along the beam such that the mean square amplitude of the resulting motion is nonzero. As will be discussed in Chapter 5, there are often additional sources of noise that are not necessarily associated with thermal losses, including adsorption and desorption of molecules in the surrounding medium, temperature fluctuations that induce thermal stresses, and defect motion within the resonator (Cleland and Roukes, 2002). For linear resonators, a rigorous analysis of such noise sources and the resulting minimum detectable frequency shift has been considered in previous studies (Albrecht et al., 1991; Butt and Jaschke, 1995; Cleland, 2005; Cleland and Roukes, 2002; Ekinci et al., 2004). Considering only the presence of thermomechanical noise, the minimum detectable frequency shift is given by

$$\delta\omega_{n,\min} = \sqrt{\frac{\omega_{n0} k_B T \Delta\omega}{E_c Q}} \tag{2.70}$$

where $k_B$ is the Boltzmann constant, $T$ is the temperature and $E_c$ is the maximum mechanical energy stored in the resonator. By substituting (2.70) into (2.69) the ultimate mass resolution can be computed

$$m_{\min} = 2m_{\text{ef0}}\sqrt{\frac{k_B T \Delta\omega}{E_c Q \omega_{n0}}} \tag{2.71}$$

## Force sensors

There are many different operational modes of AFM, which will be discussed in detail in Chapter 3. In this section we focus on dynamic modes of AFM wherein harmonic excitation is applied to a cantilever as it scans the surface of a sample and the cantilever's dynamics remain within the linear regime. The cantilever has a sharp tip at one end and the interaction force between the tip and sample, $F_{ts}$, is used to measure the topography. Specifically, the force gradient $\frac{\partial F_{ts}}{\partial z}$ is used as an indicator for measuring the sample height. As the tip approaches the sample, it initially feels the attractive van der Waals forces between the tip and sample, and once the tip makes contact with the sample, it feels repulsive Hertz forces along with the attractive van der Waals forces. There are many additional types of forces that may be present in the tip-sample interaction, such as electrostatic forces, adhesive forces and viscous forces; but a commonly used tip sample force model is the Derjaguin-Muller-Toporov (DMT) contact model which accounts for only the attractive van der Waals and repulsive Hertz forces, as shown in Fig. 2.5. In addition to the tip-sample interaction force $F_{ts}$, the tip is under the action of the mechanical restoring force from the resonator, $k_{\mathrm{ef}}z$. Positions where the mechanical restoring force exactly counter-balances the tip-sample force correspond to equilibrium positions, $z_{\mathrm{eq}}$. This is illustrated in Fig. 2.5 where the parameter $z_0$ denotes the un-deflected tip-sample separation. When $z > -z_0$, the tip is not in contact with the sample, and only the attractive van der Waals force is present. When $z < -z_0$, the tip is in contact with the sample and both attractive and repulsive Hertz-like forces act on the cantilever tip. There may exist two equilibrium positions, one position corresponding to a point above the sample where $z > -z_0$, and one corresponding to a point on the surface of the sample where $z < -z_0$, as shown in Fig. 2.5. For small perturbations in the displacement with respect to an equilibrium position, the tip sample interaction force may be approximated as

$$F_{ts}(z) = F_{ts}(z_{\text{eq}}) + \left(\frac{\partial F_{ts}}{\partial z}\right)_{z_{\text{eq}}} (z - z_{\text{eq}}) \tag{2.72}$$

Hence, the effective stiffness of the resonator becomes

$$k_{\text{ef}} = k_{\text{ef0}} + k, \quad k = -\left(\frac{\partial F_{ts}}{\partial z}\right)_{z_{\text{eq}}} \tag{2.73}$$

If the equilibrium position corresponds to a point above the sample (i.e., the tip is not in contact with the sample), then the force gradient is positive, and the presence of the tip-sample interaction force decreases the effective stiffness. In contrast, if the equilibrium position is in the sample (i.e., the tip and sample are in contact), the force gradient is negative, and the tip-sample interaction increases the effective stiffness.

In a method known as frequency-modulation AFM (FM-AFM), the resonant frequency of the transient cantilever response is used to track variations in the force gradient. The force gradient is thus determined from a measureable shift in the resonant frequency, $\partial\omega_n$. Substituting (2.64) and (2.73) into the relation $\omega_n^2 = k_{\text{ef}} / m_{\text{ef}}$ gives

$$\omega_{n0} + \partial\omega_n = \sqrt{\frac{k_{\text{ef}0} + k}{m_{\text{ef}0}}} = \omega_{n0}\sqrt{1 + \frac{k}{k_{\text{ef}0}}} \tag{2.74}$$

For $k / k_{\text{ef0}} << 1$ we can asymptotically expand (2.74) with respect to $k / k_{\text{ef0}}$,

$$\omega_{n0} + \partial\omega_n \approx \omega_{n0}\left(1 + \frac{k}{2k_{\text{ef}0}}\right) \tag{2.75}$$

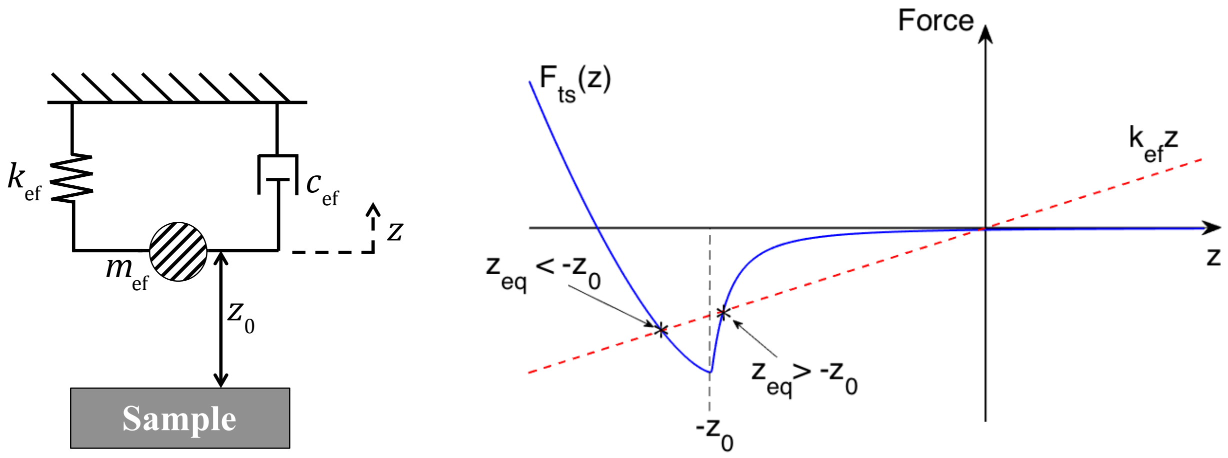

(a) (b)

*Figure 2.5: (a) A schematic of the lumped-parameter-model of a conventional AFM cantilever interacting with a sample and (b) a qualitative plot of the tip-sample interaction force,* $F_{ts}(z)$, *and the mechanical restoring force* $k_{ef}z$ *versus z. When the tip is not in contact with the sample, it holds that* $z > -z_0$, *and when the tip is in contact with the sample, it holds that* $z < -z_0$. *Positions for which* $k_{ef}z$ *is equal to* $F_{ts}(z)$ *correspond to equilibrium positions. In (b), two equilibrium points are shown: one corresponding to a point on the surface of the sample for which* $z_{eq} < -z_0$, *and the other corresponding to a point just above the sample for which* $z_{eq} > -z_0$.

By rearranging (2.75), we can relate the force gradient to the measured change in the resonant frequency,

$$\left(\frac{\partial F_{ts}}{\partial z}\right)_{z_{eq}} = -k = -\frac{2k_{ef0}}{\omega_{n0}}\delta\omega_n \tag{2.76}$$

The quantity $2k_{ef0}/\omega_{n0}$ is the inverse of the stiffness responsivity of the resonator, $R_k$, defined as the ratio of the shift in the resonant frequency for a given change in the effective stiffness,

$$R_k = \frac{\partial \omega_n}{\partial k_{\text{ef}}} \tag{2.77}$$

which, for $k/k_{\text{ef0}} << 1$, gives $R_k = \frac{\omega_{n0}}{2k_{\text{ef0}}}$.

As with the ultimate mass resolution, the ultimate stiffness resolution is governed by the minimum detectable shift in the resonant frequency (see equation (2.70)). Assuming that all noise sources other than thermomechanical are negligible, the minimum detectable force gradient is

$$\left| \left( \frac{\partial F_{ts}}{\partial z} \right)_{z_{\text{eq}}} \right|_{\min} = |k|_{\min} = 2k_{\text{ef0}} \sqrt{\frac{k_B T \Delta\omega}{E_c Q \omega_{n0}}} \tag{2.78}$$

In a different AFM technique known as amplitude-modulation AFM (AM-AFM), the amplitude of the steady-state cantilever response is used to detect variations in the force gradient while the excitation frequency is held fixed at a set-point value, $\omega_{\text{sp}}$. In an AM-AFM scan (in which the dynamics of the cantilever remain in the linear regime), variations in the sample height cause changes in the force gradient, which, in turn, modify the steady-state amplitude. In order to avoid artifacts in the image, it is important that the set-point excitation frequency either 1) remains larger than the instantaneous resonant frequency throughout the scan so that the condition $\omega_{\text{sp}} > \omega_{n0} + \delta\omega_n$ holds, or 2) remains smaller than the resonant frequency throughout the scan so that the condition $\omega_{\text{sp}} \leq \omega_{n0} + \delta\omega_n$ holds.

To explain in more detail how the force gradient is used to measure topography and the problems associated with driving the cantilever exactly at the natural frequency, consider AM-AFM measurements taken at three different locations in a sample corresponding to different sample heights, as shown in Fig. 2.6a. At location 1, the undeflected tip-sample separation is $z_{01}$ ; at location 2, the undeflected tip-sample separation is $z_{02}$ and at location 3, the undeflected tip-sample separation is $z_{03}$, where $z_{03} < z_{02} < z_{01}$. Note that, at each location, the absolute height of the cantilever base (with respect to a fixed reference frame) is the same so that the sample height is smallest at location 1 and largest at location 3. Here we will assume that the motion of the cantilever is restricted to small displacements about the equilibrium point in the repulsive force regime so that the tip is always in contact with the sample and the force gradient is always negative.

The corresponding force-displacement curves and equilibrium points for the three locations are depicted in Fig. 2.6b. We see that, as the sample height increases, the force-displacement curve shifts and the equilibrium position increases from $z_{\mathrm{eq1}}$ at location 1, to $z_{\mathrm{eq2}}$ at location 2, to $z_{\mathrm{eq3}}$ at location 3. Further, the magnitude of the gradient at the equilibrium position increases from $k_1 = -\left(\frac{\partial F_{\mathrm{ts}}}{\partial z}\right)_{z_{\mathrm{eq1}}}$, to $k_2 = -\left(\frac{\partial F_{\mathrm{ts}}}{\partial z}\right)_{z_{\mathrm{eq2}}}$, to $k_3 = -\left(\frac{\partial F_{\mathrm{ts}}}{\partial z}\right)_{z_{\mathrm{eq3}}}$, and as a result the effective stiffness of the oscillator increases from $k_{\mathrm{ef1}} = k_{\mathrm{ef0}} + k_1$, to $k_{\mathrm{ef2}} = k_{\mathrm{ef0}} + k_2$, to $k_{\mathrm{ef3}} = k_{\mathrm{ef0}} + k_3$.

Let us consider separately two different scenarios: an AM-AFM scan from location 2 to location 1, and an AM-AFM scan from location 2 to location 3. In Figs. 2.7 and 2.8, we show the resulting shifts in the resonance curves that occur before the feedback control acts. When the tip moves from location 2 to location 3, the sample height increases, and the effective stiffness increases causing the entire resonance curve to shift upward. Alternatively, when the tip moves from location 2 to 1, the sample height decreases, the effective stiffness decreases and the resonance curve shifts downward. We can see in Fig. 2.7 that if the set-point excitation frequency is exactly equal to the initial resonant frequency, i.e. if $\omega_{\mathrm{sp}} = \omega_{n2} = \sqrt{k_{\mathrm{ef2}} / m_{\mathrm{ef}}}$, the resulting change in the steady-state amplitude due to an increase in sample height and due to a decrease in sample height may be indecipherable.

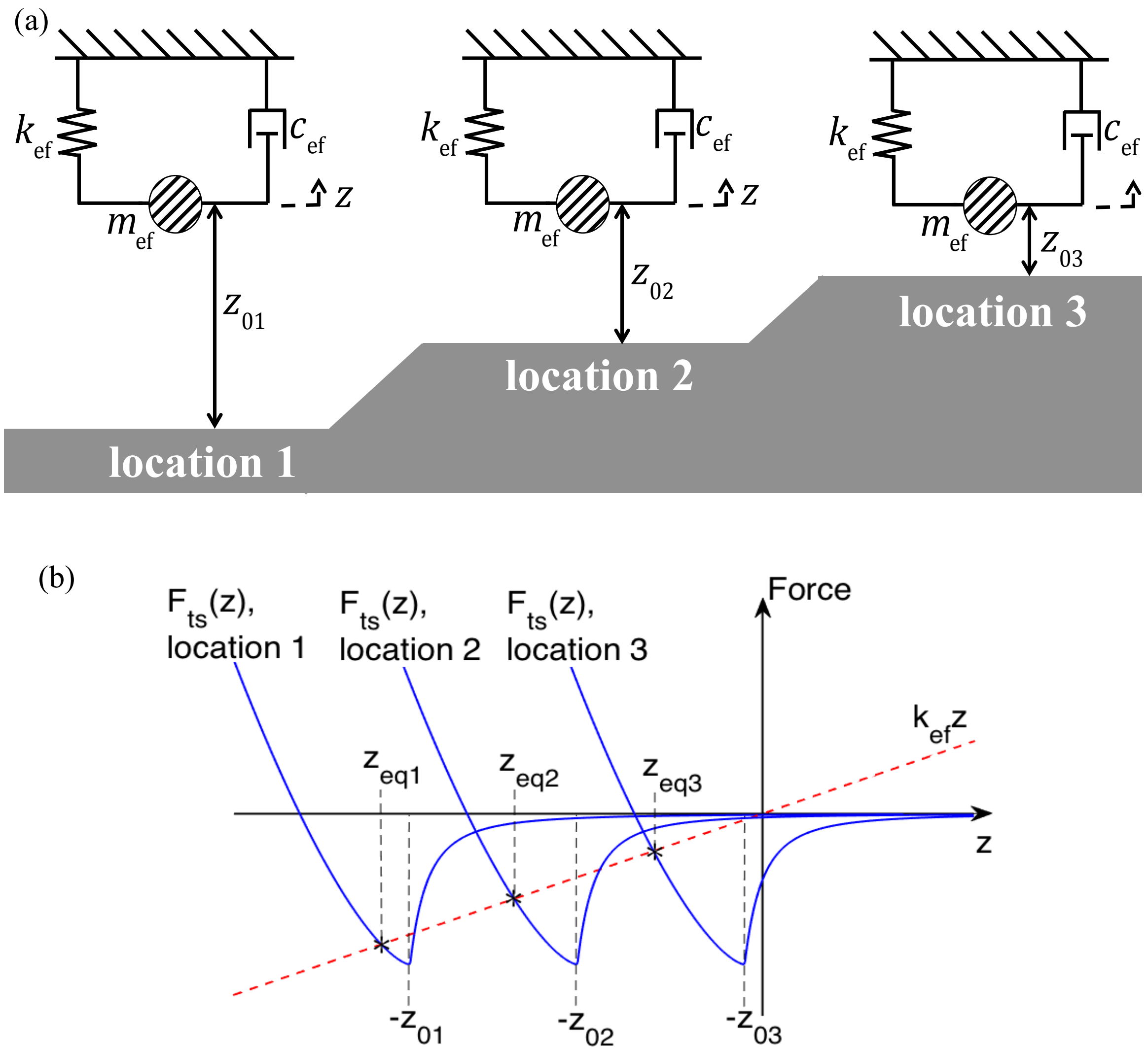

*Figure 2.6: (a) A schematic of the lumped-parameter-model for an AFM cantilever interacting with a sample at three different locations corresponding to different sample heights: location 1, location 2 and location 3. At location 1, the sample height is lowest and at location 3, the sample height is highest. (b) A qualitative plot of the tip-sample interaction force versus z at the three different locations depicted in (a). Notice that as the sample height increases, the force gradient at the equilibrium point on the surface of the sample (i.e. the equilibrium point for which* $z_{eq} < -z_0$*) increases in magnitude.*

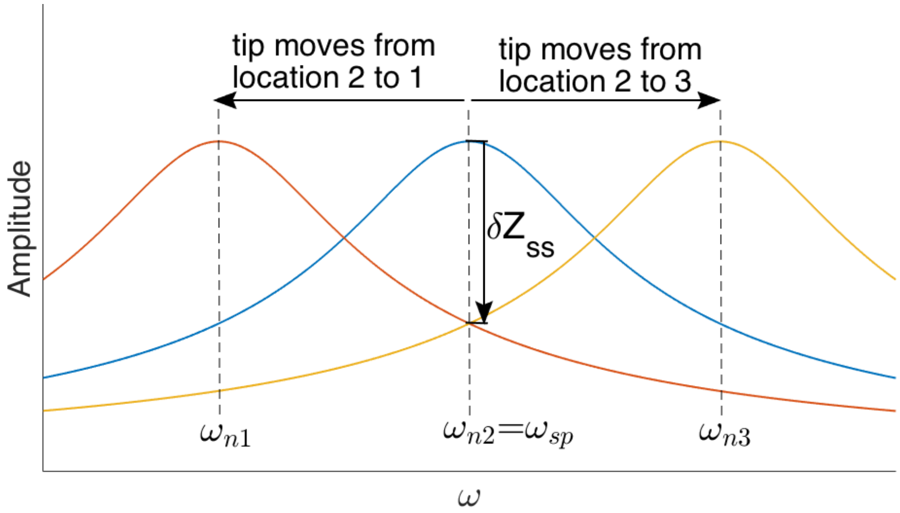

*Figure 2.7: Resonance curves at locations 1, 2 and 3 shown in Fig. 2.6a. When the tip moves from location 2 to 1, the effective stiffness decreases and the resonance curve shifts downward toward lower frequencies and when the tip moves from location 2 to 3, the effective stiffness increases and the resonance curve shifts upward. This figure illustrates that if the set-point frequency is set equal to the initial resonant frequency at location 2, the steady-state amplitude will decrease if the sample height increases and if the sample height decreases.*

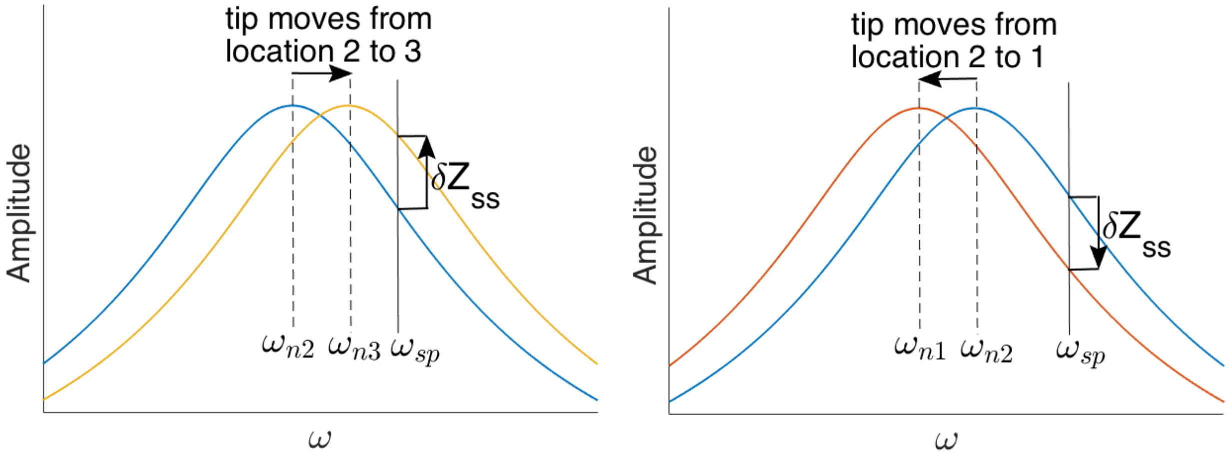

*Figure 2.8: Resonance curves at locations 1, 2 and 3 shown in Fig. 2.6a. Here we see that if the set-point frequency is larger than the initial resonant frequency at location 2, the steady-state amplitude will decrease if the sample height decreases and increase if the sample height increases.*

In Fig. 2.8 we see that if the set-point excitation frequency is instead chosen to be larger than the initial resonant frequency, i.e. $\omega_{\mathrm{sp}} > \omega_{n2}$, then an upward shift in the steady-state amplitude may clearly be interpreted as an increase in the sample height, and a downward shift in the steady-state amplitude may be interpreted as a decrease in the sample height. Feedback control would then be used to adjust the distance between the cantilever base and the sample in order to recover the initial, set-point amplitude of the steady-state response. Equivalently, the set-point excitation frequency could be selected to be smaller than the initial resonant frequency. What is important is that, as the sample height increases or decreases, the steady-state amplitude varies monotonically in order to avoid artifacts in the image.

Assuming that, indeed, the set-point excitation frequency remains either larger or smaller than the instantaneous resonant frequency, we can approximately compute the change in the effective stiffness associated with a measurable change in the steady-state amplitude. The instantaneous steady-state amplitude is

$$Z_{\mathrm{ss}} = Z_{\mathrm{ss}0} + \delta Z_{\mathrm{ss}} \tag{2.79}$$

The change in the steady-state amplitude is implicitly related to the change in effective stiffness via the shift in the resonant frequency. By substituting (2.58) and (2.64) into (2.79), gives

$$\begin{aligned} Z_{\mathrm{ss}0} + \delta Z_{\mathrm{ss}} &= \frac{P}{\sqrt{\left[\left(\omega_{n0} + \delta\omega_{n}\right)^{2} - \omega^{2}\right]^{2} + 4\zeta^{2}\omega^{2}\left(\omega_{n0} + \delta\omega_{n}\right)^{2}}} \\ &= \frac{P}{\sqrt{\left[\omega_{n0}^{2}\left(1 + \frac{\delta\omega_{n}}{\omega_{n0}}\right)^{2} - \omega^{2}\right]^{2} + 4\zeta^{2}\omega^{2}\omega_{n0}^{2}\left(1 + \frac{\delta\omega_{n}}{\omega_{n0}}\right)^{2}}} \end{aligned} \tag{2.80}$$

Substituting $\frac{\delta\omega_n}{\omega_{n0}} = \frac{k}{2k_{\text{ef}0}}$ into (2.80) and asymptotically expanding the right-hand-side with respect to $\frac{k}{k_{\text{ef}0}}$, under the assumption that $\frac{k}{k_{\text{ef}0}} << 1$, we have

$$k \approx \begin{cases} \dfrac{2k_{\text{ef}0}}{Z_{\text{ss}0}\omega_{n0}^2 \left|(1-2\zeta^2)\omega_{\text{sp}} - \omega_{n0}^2\right|}\delta Z_{\text{ss}}, & \omega_{\text{sp}} > \omega_n \\ \dfrac{-2k_{\text{ef}0}}{Z_{\text{ss}0}\omega_{n0}^2 \left|(1-2\zeta^2)\omega_{\text{sp}} - \omega_{n0}^2\right|}\delta Z_{\text{ss}}, & \omega_{\text{sp}} < \omega_n \end{cases} \tag{2.81}$$

So that if the set-point excitation frequency remains greater than the instantaneous resonant frequency, a downward (upward) shift in the steady-state amplitude indicates a decrease (increase) in the effective stiffness and sample height. In contrast, if the set-point excitation frequency remains less than the instantaneous resonant frequency, an downward (upward) shift in the steady-state amplitude indicates an increase (decrease) in the effective stiffness and sample height. This of course is only valid for dynamic AFM modes in which the tip remains in contact with the sample and the dynamics can be approximated as linear. In other words, when the tip undergoes small displacements with respect to an equilibrium position on the surface of the sample for which the force gradient is negative. Opposite trends would be observed in the case of small displacements with respect to an equilibrium position above the sample for which the force gradient is positive.

## 2.2 Nonlinear dynamic regime

### 2.2.1 Motivation for intentional nonlinearity in micro/nanomechanical resonators

It is clear from (2.69) and (2.78) that the mass and force sensitivity of micro/nanomechanical resonators can be improved by decreasing the effective mass and stiffness, increasing the resonant frequency, increasing the *Q*-factor and decreasing the ratio of the thermal energy, $k_B T$, to the maximum mechanical energy. Decreasing the overall size of the resonator simultaneously results in a decrease in effective mass and effective stiffness and an increase in the resonant frequency and the *Q*-factor. To illustrate this effect, consider the dependence of the effective stiffness, effective mass and the resonant frequency on system parameters (deduced from (2.18), (2.36), (2.48) and (2.49))

$$k_{\mathrm{ef}} \sim Ew\left(\frac{t}{l}\right)^3, \quad m_{\mathrm{ef}} \sim \rho wtl, \quad \omega_n^2 \sim \frac{E}{\rho}\left(\frac{t}{l^2}\right)^2 \tag{2.82}$$

where $w$ is the beam width, $t$ is the thickness, $l$ is the length, $E$ is Young's modulus and $\rho$ is the density. If the length, width and thickness are uniformly scaled down by a factor of $n$, then the effective stiffness decreases by a factor of $n$, the effective mass decreases by a factor of $n^3$ and the resonant frequency increases by a factor of $n^2$. Decreasing the size of the resonator also reduces internal damping by minimizing or eliminating grain boundaries and defects within the beam (e.g. single crystal *Si*). The external damping due to interfacial friction with the surrounding medium can be reduced by decreasing the pressure, as is often done in micro/nanoresonant sensing applications. In the case of nanoscale resonators operating in ultra-high-vacuum (UHV) conditions, further reductions in device scale may additionally reduce the thermoelastic damping within the structure due to the increase in the resonant frequency itself. Thermoelastic damping plays a large role when other sources of dissipation have been substantially mitigated and it constitutes the losses associated with transverse heat flow from the warmed material in compression to the cooled material in tension. If the resonant frequency is sufficiently large, the oscillation period is small compared to the characteristic time associated with the thermoelastic heat flow (i.e. the time it takes for the material to equilibrate) and the losses are therefore reduced (Roszhart, 1990; Sosale, 2011).

In the ongoing push for enhanced sensitivity, the size of state-of-the-art (with regard to sensitivity) resonant sensors are becoming increasingly small. Recall that, in the derivation of the linear beam equation, we assumed relatively small displacements and slopes. If in contrast, the relative response amplitude compared to the characteristic size of the device becomes large, axial strain along the beam induces a nonlinear term in the equation governing transverse motion of the beam. In this sense, all beam structures have a threshold amplitude above which they behave nonlinearly and the aforementioned linear analysis is not applicable. As the characteristic size of the resonator decreases, this threshold amplitude decreases as well and in extreme cases, the linear dynamic regime may occur entirely below the noise floor. In any event, by operating at larger amplitudes that are further within the nonlinear regime, the signal-to-noise-ratio (SNR) may be enhanced, which is one source of motivation for intentional nonlinearity in micro/nanoresonators. Further, in some cases, nonlinear phenomena may be exploited to achieve paradigm-shifting improvements in the area of micro/nanoresonant sensing (Cho et al., 2016; Lifshitz and Cross, 2008; Rhoads et al., 2010; Younis, 2011).

Nonlinearity due to mid-plane stretching of the beam is known as geometric nonlinearity and is often observed in clamped-clamped structures. Geometric nonlinearity is the most common type of nonlinearity encountered in micro/nanoresonators, especially in mass-sensing applications. Other sources of nonlinearity include nonlinear interactions, like the interaction between the tip and sample in AFM, nonlinear damping, material nonlinearity and nonlinear external potentials associated with the actuation or sensing mechanism. In the following section, various sources of nonlinearity will be discussed in more detail.

### 2.2.2 Sources of nonlinearity

#### 2.2.2.1 Geometric nonlinearity

When a mechanical structure undergoes transverse motion and is restricted at its boundaries, elongation of the material generates axial tension, which in turn, introduces geometric nonlinearity with respect to the transvers deflection. Nayfeh and Mook (1985) present a detailed derivation of the equations governing the transverse motion of a beam undergoing geometric mid-plane stretching. In this exposition, it is assumed that plane sections remain plane, rotary inertia effects are negligible and the stress is linearly related to strain. Depending on the boundary conditions, they distinguish between two important cases: 1) when the axial displacement along the beam is of the same order as the transverse displacement and 2) when the axial displacement is of the same order as the square of the transverse displacement and out-of-plane motion can be neglected. The second case is far more common in the analysis of geometrically nonlinear beam structures but the first case has been shown to be appropriate for hinged-hinged boundary conditions. Since in micro/nanoresonant sensing, clamped-clamped boundary conditions are more common, we will focus on the second case. Following the notation of Section 2.1, the governing equation is given by

$$\bar{m}v_{tt} + EIv_{xxxx} - \frac{EA}{2l}v_{xx}\int_0^l v_x^2\,dx = 0 \tag{2.81}$$

where $A$ is the cross-sectional area of the beam. If we incorporate linear damping, assume the beam vibrates in its fundamental mode shape of the underlying linear system and project (2.81) onto the fundamental mode shape (stated in (2.21) for $i$=1), the resulting reduced order model is

$$m_{\text{ef}}\ddot{z} + c_{\text{ef}}\dot{z} + k_{\text{ef}}z + k_3 z^3 = 0 \tag{2.82}$$

where $k_{\text{ef}}$, $m_{\text{ef}}$ and $c_{\text{ef}}$ are the effective linear stiffness, mass and damping coefficient defined in (2.48), (2.49) and (2.50) for $a=l/2$ and $i$=1, $z$ is the displacement of the center of the beam ($z=v(l/2,t)$) and $k_3$ is the effective cubic stiffness given by

$$k_3 = \frac{EA}{\phi_1^4(l/2)}\left(-\int_0^l \phi_1''\phi_1\,dx\int_0^l \left(\phi_1'\right)^2 dx\right) \tag{2.83}$$

The reduced order model (2.82) has the form of the well-known Duffing equation (in the absence of external forcing). Under harmonic excitation, the steady-state amplitude as a function of drive frequency is not a Lorentz curve as it is for the linear case; rather the frequency-amplitude curve bends so that the resonant frequency is amplitude dependent. The nonlinear bending of the resonance curve causes hysteresis, bifurcation points and a multi-valued region for which there coexists two stable solutions and one unstable solution.

To discuss these nonlinear phenomena in more detail, the method of multiple-scales will be employed to analyze a Duffing oscillator under harmonic excitation. To this end, we incorporate harmonic excitation into (2.82)

$$m_{\mathrm{ef}}\ddot{z}+c_{\mathrm{ef}}\dot{z}+k_{\mathrm{ef}}z+k_3z^3=F_0\cos\omega t \tag{2.84}$$

and for convenience, we introduce the parameters,

$$2\mu=\frac{c_{\mathrm{ef}}}{m_{\mathrm{ef}}},\quad \alpha=\frac{k_3}{m_{\mathrm{ef}}},\quad q_0=\frac{F_0}{m_{\mathrm{ef}}} \tag{2.85}$$

and write (2.84) in the form

$$\ddot{z}+2\mu\dot{z}+\omega_n^2z+\alpha z^3=q_0\cos\omega t \tag{2.86}$$

The method of multiple scales is an analytical technique that is part of a larger family of perturbation techniques used to analyze weakly nonlinear systems. In this method, we isolate the dynamics occurring at different time scales by considering expansions in terms of multiple independent time variables instead of a single independent time variable. We introduce the small parameter $\varepsilon$ and the new independent time scales,

$$T_n=\varepsilon^n t,\quad n=0,1,2,\ldots\ . \tag{2.87}$$

Further, we rescale the displacement, damping coefficient and forcing level $z\to\varepsilon z$, $\mu\to\varepsilon\mu$, $q_0\to\varepsilon q_0$, and express the solution as an asymptotic series with respect to $\varepsilon$,

$$z(t;\varepsilon)=z_0(T_0,T_1,\ldots)+\varepsilon z_1(T_0,T_1,\ldots)+\ldots\ . \tag{2.88}$$

We are interested in studying the response of the system near fundamental resonance and hence, we introduce the frequency detuning parameter $\sigma$ of $O(1)$, and consider small perturbations in the excitation frequency with respect to the linearized resonant frequency

$$\omega = \omega_n + \varepsilon\sigma \tag{2.89}$$

By substituting (2.87) through (2.89) into (2.86), one recovers a series of coupled linear ordinary differential equations (ODEs) governing the response at different orders of $\varepsilon$. As shown by Nayfeh and Mook (1985), by solving the ODEs corresponding to $O(1)$ and $O(\varepsilon)$, the response to leading order can be computed and is given by,

$$z(t) = a\cos(\omega t - \gamma) + O(\varepsilon) \tag{2.90}$$

where $a$ and $\gamma$ vary slowly as compared to *z* and satisfy the set of autonomous, coupled ODEs,

$$\begin{aligned} a' &= -\mu a + \frac{1}{2}\frac{q_0}{\omega_n}\sin(\gamma) \\ a\gamma' &= \sigma a - \frac{3}{8}\frac{\alpha}{\omega_n}a^3 + \frac{1}{2}\frac{q_0}{\omega_n}\cos(\gamma) \end{aligned} \tag{2.91}$$

The steady-state values of $a$ and $\gamma$ correspond to fixed points of (2.91). By substituting $a' = \gamma' = 0$ into (2.91) and rearranging, we obtain the steady-state frequency-amplitude relation

$$\left[\mu^2 + \left(\sigma - \frac{3\alpha}{8\omega_n}a^2\right)^2\right]a^2 = \frac{q_0^2}{4\omega_n^2} \tag{2.92}$$

When $\mu = q_0 = 0$, (2.92) defines the frequency-amplitude relation of the transient response of an unforced, undamped oscillator. This curve is the so-called backbone curve and is given by,

$$a=\left(\frac{8\sigma\omega_n}{3\alpha}\right)^{1/2} \tag{2.93}$$

In Fig. 2.9, we plot the amplitude versus frequency for two different cases: $\alpha > 0$ and $\alpha < 0$. If $\alpha = 0$, the system is linear and the resonance curve is a Lorentz curves as discussed in Chapter 2.1. For $\alpha > 0$, the frequency-amplitude curve bends forward towards larger frequencies, known as a hardening effect in the resonance curve. This is the case for geometric nonlinearity in doubly-clamped beams. Alternatively, for $\alpha < 0$ the frequency-amplitude curve bends backward towards lower frequencies, which is known as a softening effect. As shown in Fig. 2.10, for $\alpha \neq 0$ there exist frequency ranges for which only one solution exists and frequency ranges for which three solutions exist. The multivalued response leads to the *jump phenomenon* where small changes in the frequency lead to abrupt changes in the steady-state amplitude. The frequencies, at which an abrupt change or jump in the response occurs, correspond to bifurcation points, and these bifurcation points cause hysteresis loops in the frequency response. For $\alpha > 0$ ( $\alpha < 0$), if the drive frequency is incrementally swept forward (backward), the response will track the upper solution branch in the multivalued region and then abruptly decrease at the jump-down bifurcation point. On the other hand, for $\alpha > 0$ ($\alpha < 0$), if the drive frequency is incrementally swept backward (forward), the response will track the lower solution branch in the multivalued region and then abruptly increase at the jump-up bifurcation point.

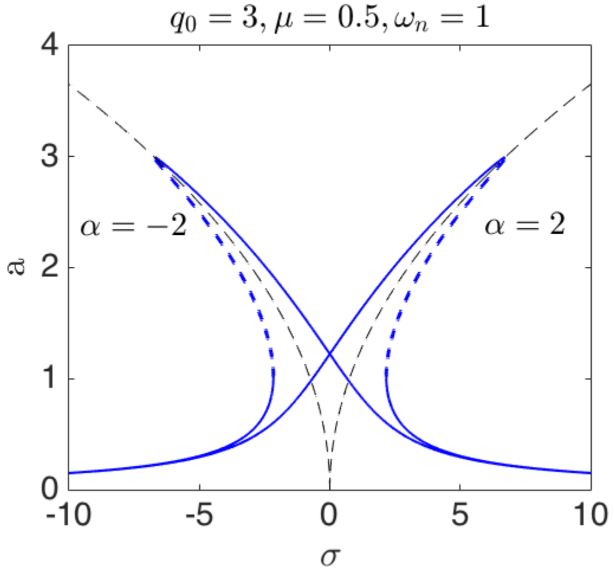

*Figure 2.9: The frequency amplitude curves at steady state for a Duffing oscillator. When the nonlinear stiffness coefficient, $\alpha$, is negative, we observe softening behavior in the resonance curve, and when $\alpha$ is positive, we see hardening in the resonance curve. The black dashed lines denote the backbone curves corresponding to zero damping and zero forcing.*

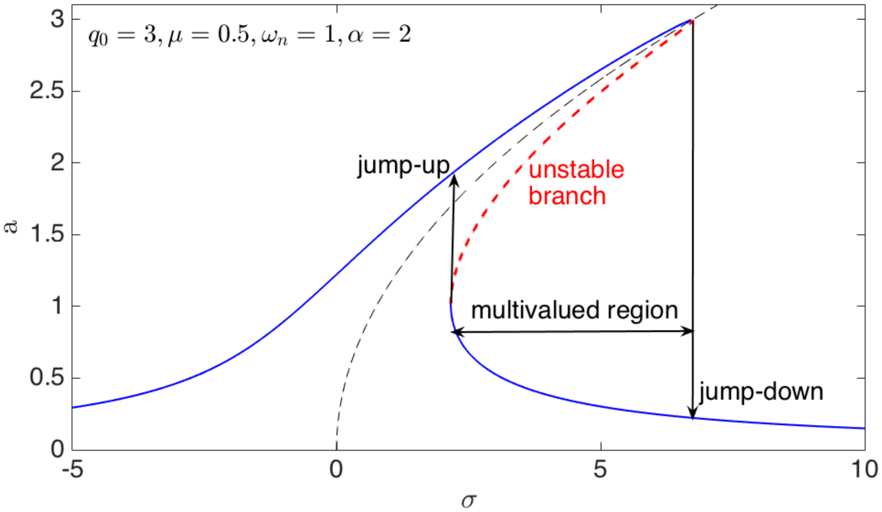

*Figure 2.10: Primary resonance curve of Duffing oscillator having positive cubic stiffness. The nonlinear bending in the frequency-amplitude curve leads to the jump phenomenon, hysteresis loops and a multivalued region in which there coexists two stable solution branches (solid blue curves) and one unstable solution branch (dashed red curve).*

To determine which solutions are physically realizable, a stability analysis must be performed. If a solution is unstable, it is not physically realizable. To this end, we investigate the nature of the equilibrium points of the autonomous set of equations (2.91). Let $a = a_0 + \xi$ and $\gamma = \gamma_0 + \psi$ where $|\xi| << 1$, $|\psi| << 1$ and $(a_0, \gamma_0)$ corresponds to an equilibrium point of (2.91). By substituting these relations into (2.85) and Taylor expanding about $(a_0, \gamma_0)$, we obtain the set of linear first order differential equations governing the perturbations $\xi$ and $\psi$

$$\begin{Bmatrix} \xi' \\ \psi' \end{Bmatrix} = \begin{bmatrix} -\mu & \frac{q_0}{2\omega_n}\cos(\gamma_0) \\ -\left(\frac{3\alpha a_0}{4\omega_n} + \frac{q_0}{2\omega_n a_0^2}\right)\cos(\gamma_0) & -\frac{q_0}{2\omega_n a_0}\sin(\gamma_0) \end{bmatrix} \begin{Bmatrix} \xi \\ \psi \end{Bmatrix} \tag{2.94}$$

This linear set of homogenous first order differential equations has a solution of the form

$$\xi = \Xi e^{\lambda t}, \quad \psi = \Psi e^{\lambda t} \tag{2.95}$$

Substituting (2.95) into (2.94) we obtain the expression satisfied by $\lambda$,

$$\begin{vmatrix} -\mu - \lambda & \frac{q_0}{2\omega_n}\cos(\gamma_0) \\ -\left(\frac{3\alpha a_0}{4\omega_n} + \frac{q_0}{2\omega_n a_0^2}\right)\cos(\gamma_0) & -\frac{q_0}{2\omega_n a_0}\sin(\gamma_0) - \lambda \end{vmatrix} = 0$$

$$\Rightarrow \quad \lambda^2 + 2\mu\lambda + \mu^2 + \left(\sigma - \frac{3\alpha a_0^2}{8\omega_n}\right)\left(\sigma - \frac{9\alpha a_0^2}{8\omega_n}\right) = 0 \tag{2.96}$$

For stability, both eigenvalues must have non-positive real parts and, hence, the steady-state response is unstable when

$$\Lambda = \mu^2 + \left( \sigma - \frac{3\alpha a_0^2}{8\omega_n} \right)\left( \sigma - \frac{9\alpha a_0^2}{8\omega_n} \right) < 0 \tag{2.97}$$

It can be shown that the region of instability encompasses the middle solution branch within the multivalued region, as indicated in Fig. 2.10. When multiple stable solutions exist, the initial conditions determine which solution is physically realized. The set of all initial conditions that give rise to a particular steady solution constitute the domain of attraction for that solution.

To summarize some important points regarding geometric nonlinearity in beams, this type of nonlineaity is due to mid-plane stretching and is a common type of nonlineaity encountered in micro/nanoreosnators. The reduced order model of the fundamental bending mode is that of a Duffing oscillator which has cubic stiffness. For sufficiently small response amplitudes, the Duffing oscillator behaves nearly linearly and the frequency-response curve approaches a Lorentz curve. As the amplitude increases, nonlinear bending of the frequency-amplitude curve occurs leading to the *jump phenomenon*, hysteresis loops, and frequency ranges for which two stable solutions exist.

#### 2.2.2.2 Nonlinear interactions

Geometric nonlinearity does not play a significant role in the dynamics of an AFM cantilever interacting with a sample due to the free boundary condition at the cantilever tip. The free boundary condition substantially lowers the axial tension in the beam and thereby reduces mid-plane stretching. That is to say, the AFM cantilever itself is a linear system but the interaction of the tip and the sample introduces nonlinearity in the dynamics of the cantilever (Eaton and West, 2010; Garcia, 2010; Garcia and Perez, 2002; Raman et al., 2008).

As discussed in Section 2.1, depending on the sample and operating conditions, the tip-sample interaction may contain van der Waals forces, Hertzian forces, capillary forces, electrostatic forces, magnetic forces and viscous forces; but for simplicity, we consider the DMT contact model, which includes only the van der Waals and Hertzian forces. When the tip is not in contact with the sample, the attractive van der Waals force governs the interaction and when the tip is in contact with the sample, both the repulsive Hertzian force and attractive van der Waals force govern the interaction. For relatively large indentations of the tip into the sample, the Hertz force dominates the interaction (Binning et al., 1986; Derjaguin et al., 1980). In Section 2.1, we considered the case when the tip oscillates with small amplitude in the immediate vicinity of an equilibrium point. In this scenario, it is appropriate to Taylor expand the DMT contact law, allowing for a complete linearization of the dynamics. However, in most AFM applications, the displacement of the tip is not confined to small perturbations near an equilibrium point, and the dynamics are therefore non-linearizeable (Lee et al., 2003; Rutzel at al., 2003; Stark et al., 2010).

In the most common type of dynamic AFM mode known as *tapping mode AFM*, the tip taps against the surface so that, for most of the oscillation period, the tip is not in contact with the sample. The non-smooth vibro-impacts between the tip and sample are strongly nonlinear and result in nonlinear bending of the resonance curves of the cantilever. For example, a resonance curve of a commercial AFM cantilever interacting with a sample is shown in Fig. 2.11. The solid curves denote the response of the cantilever when it is interacting with a sample and the blue dashed curve is the linear response of the cantilever in absence of interaction with a sample. The red crosses denote the unstable solution branch. In this case, the tip is about 150nm above sample and, hence, the onset of the nonlinear bending in the frequency response curve occurs at an amplitude of ~150nm. In other words, the cantilever responds linearly for amplitudes small enough that the tip does not feel the sample, but for amplitudes large enough, the tip sample interaction causes bending of the resonance curve. As the response amplitude increases into the nonlinear regime, initially the attractive van der Waals forces are felt resulting in a softening effect in the resonance curve; and as the amplitude further increases, the repulsive Hertz forces dominate resulting in a stiffening effect. We see that the nonlinear bending of the resonance curve results in a multivalued region where there coexist two stable branches and one unstable branch. The significance of the coexisting solution branches will be discussed in detail in Chapter 3. The nonlinear interaction between the tip and sample also generates higher harmonics in the cantilever's response and, in general, these higher harmonics have poor SNR. Special techniques can be used to amplify these higher harmonic signals for use in compositional AFM imaging, and one such approach is presented in Chapter 3.

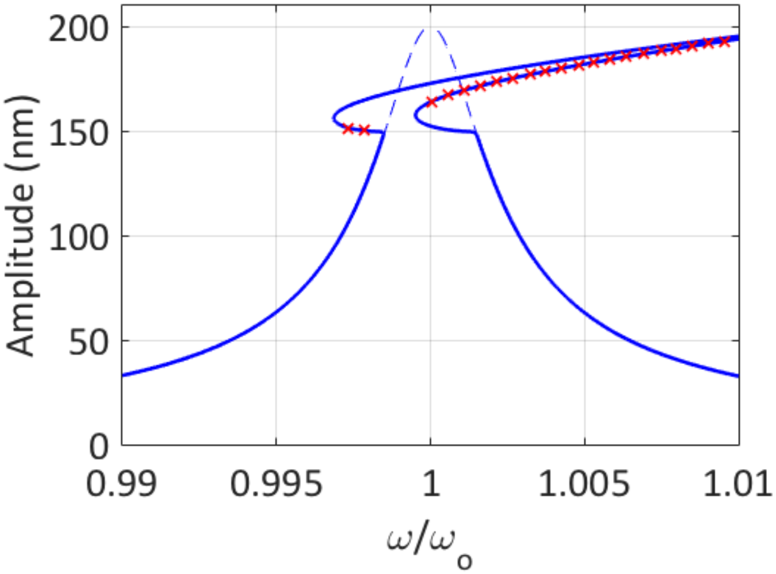

*Figure 2.11: The solid blue curve corresponds to the resonance curve of a commercial AFM cantilever interacting with a sample having a Young's modulus of 0.1 GPa, at a static tip-sample distance of 150 nm. The dashed blue curve denotes the linear response of the cantilever in absence of interaction with the sample. The red crosses denote the unstable solution branches.*

### 2.2.2.3 Nonlinear damping

Typically, the damping mechanisms present in micro/nanomechanical systems are approximated as a linear viscous element in the reduced order model but, in some cases, this simple linear model is not sufficient. More recently, researchers have explored nonlinear damping models to approximate the dynamics of microresonators (Eichler 2011, Zaitsev 2012, Jeong 2013, Asadi 2017, Anderson 2012). In particular, it has been shown that a nonlinear damping model proportional to the product of the square of the displacement and the velocity captures the amplitude-dependent damping effect observed in some microresonant systems. In Chapter 4 we analyze a *Si* cantilever that is attached at its free end to a fixed base via a polymer bridge. Asadi et al. (2017) previously showed that the reduced order model governing flexural motion of this system is that of a Duffing equation with an additional nonlinear damping term. Whereas, previously, Asadi et al. considered harmonic excitation at a fixed forcing level, we consider a forcing level proportional to the square of the excitation frequency (owing to the presence of base excitation) and study how the nonlinear damping term affects the resonant bandwidth of the system.

#### 2.2.2.4 Nonlinear external potentials

A common technique used for the excitation and sensing of vibration in micro/nanoresonators is parallel-plate electrostatic actuation and/or detection. In the simplest variation of electrostatic actuation, the resonator is excited with an electrostatic force applied directly to the beam structure (rather than at the base) and acting in the transverse direction. The microbeam constitutes a non-stationary upper electrode, which forms a parallel-plate-capacitor with a stationary lower electrode mounted below the microbeam. A constant DC load is superimposed on a harmonic AC load causing the resonator to vibrate about a deflected position. The electrostatic force is an essentially nonlinear function of the distance between the upper and lower electrodes, and to leading order, this force is quadratic in nature (Batra et al., 2007; Younis, 2011). The quadratic term in the reduced order model of the resonator has a softening effect on the primary resonance curve. Typically, geometric nonlinearity due to midplane stretching also plays a role in the dynamics of these systems. Depending on the relative strength of the cubic term (resulting from geometric nonlinearity) and quadratic term (resulting from electrostatic nonlinearity), the system may exhibit strong Duffing-like hardening behavior, strong softening behavior or mixed behavior. In some mass sensing applications, the drop down bifurcation resulting from either strong softening or strong hardening behavior is utilized as an ultrasensitive switch detecting a threshold amount of mass (Bajaj et al., 2016; Bouchaala et al., 2016; Younis et al., 2009). In other studies, researchers have leveraged the hardening and softening effects against each other in order to expand the linear dynamic regime (Kacem et al., 2010). In the work presented in this thesis, I have only considered piezoelectric excitation at the base of microbeam structures and, hence, this type of nonlinearity does not play a role in the systems we consider.

## 2.3 References

Anderson D., Starosvetsky Y., Vakakis A., and Bergman L. (2012). *Nonlinear Dyn., 67,* 807-827.

Asadi, K., Li, J., Peshin, S., Yeom, J., and Cho, H. (2017). Mechanism of geometric nonlinearity in a nonprismatic and heterogeneous microbeam resonator. *Physical Review B*, *96*(11).

Batra R.C., Porfiri M., and Spinello D. (2007). Review of modeling electrostatically actuated microelectromechanical systems. *Smart Mater. Struct., 16,* R23-R31.

Binnig, G., Quate, C.F., and Gerber, Ch. (1986). Atomic Force Microscope. *Physical Review Letters*, 56, 930–933.

Cho, H., Yu, M.-F., Vakakis, A. F., and Bergman, L. A., (2016). Intentional Nonlinearity for Design of Micro/Nanomechanical Resonators, *Nanocantilever Beams: Modeling, Fabrication and Applications*, Pan Stanford Publishing/CRC Press, Boca Raton, FL.

Derjaguin, B., Muller, V., and Toporov, Y. (1980). On different approaches to the contact mechanics. *Journal of Colloid and Interface Science*, *73*, 293–294.

Eaton P., West P. (2010). *Atomic Force Microscopy*. Oxford University Press, Oxford, UK.

Eichler A., Moser J., Chaste J., Zdrojek M., Wilson-Rae I., and Bachtold A. (2011). *Nature Nanotechnology, 6,* 339-342.

Garcia R., Perez R. (2002). Dynamic atomic force microscopy methods. *Surf. Sci., 47*, 197-301.

Garcia R. (2010). *Amplitude Modulation Atomic Force Microscopy*. Wiley-VCH Verlag GmbH & Co. KGaA, Weinheim, Germany.

Jeong, B., Cho, H., Yu, M.-F., Vakakis, A., McFarland, D. M., and Bergman, L.A. (2013) Modeling and measurement of geometrically nonlinear damping in a microcantilever nanotube system, *ACS Nano, 10*, 8547-8553.

Kacem, N., Arcamone, J., Perez-Murano, F., Hentz, S. (2010). Dynamic range enhancement of nonlinear nanomechanical resonant cantilevers for highly sensitive NEMS gas/mass sensor applications. *Journal of Micromechanics and Microengineering*, *20*(4), 45023.

Lee S.I., Howell S.W., Raman A., Reifenberger R. (2003). Nonlinear dynamic perspectives on dynamic force microscopy. *Ultramicroscopy, 97*, 185-198.

Lifshitz, R., and Cross, M. C., (2008). Nonlinear Dynamics of Nanomechanical and Micromechanical Resonators, *Reviews of Nonlinear Dynamics and Complexity*, Vol. 1, H. G. Schuster, ed., Wiley, Hoboken, NJ, pp. 1–52.

Meirovitch, L. (1975). *Elements of Vibration Analysis*. McGraw-Hill, New York, N.Y.

Nayfeh, A.H., Mook D. (1995). *Nonlinear Oscillations*. Wiley Interscience.

Raman, A., Melcher, J., Tung, R. (2008). Cantilever dynamics in atomic force microscopy. *Nano Today*, *3*, 20–27.

Rhoads, J.F., Shaw, S.W., Turner, K.L. (2010), Nonlinear dynamics and its applications in micro- and nanoresonators. *J. Dyn. Sys., Meas., Control.*, *132*(3), 034001, 1-14.

Roszhart T.V. (1990). The effect of thermoelastic internal friction on the q of micromachined silicon resonators. *Solid-State Sensor and Actuator Workshop, 4th Technical Digest., IEEE.*

Rutzel, B.S., Lee S.I., and Raman A. (2003). Nonlinear dynamics of atomic-force-microscope probes driven in Lennard-Jones potentials. *Proc. R. Soc. Lond. A, 459,* 1925-1948.

Sosale G., Das K., Frechette L., and Vengallatore S. (2011). *J. Micromech. Microeng., 21,* 105010.

Stark W.R. (2010). Bistability, higher harmonics and chaos in AFM. *Materials Today, 13,* 24-32.

Younis, M. I., (2011). *MEMS Linear and Nonlinear Static and Dynamics (Microsystems)*, Springer, Berlin.

Zaitsev S., Shtempluck O., and Buks E. (2012) Nonlinear damping in a micromechanical oscillator. *Nonlinear Dyn., 67,* 859-883.

# Chapter 3

## Performance of an inner-paddled AFM cantilever designed to promote internal resonance

### 3.1 Introduction

As applications of nanotechnology multiply, increasingly small samples and devices emerge calling for nano-scale morphological and compositional measurements. Assessing the mechanical properties of bio-samples is particularly important, because it can help us understand the relationships between mechanical properties and biological processes and enhance our fundamental understanding of the bio-sample. For example, the mechanical stiffness of cells has been related to malignancy (Suresh et al., 2015), and the loss tangent of cancer cells has been linked to metastatic potential (Rother et al., 2014). A cornerstone of nanoscience is the dependence of material properties on the physical dimensions of the material and, hence, the quantification of material properties such as Young's (or elastic) modulus in the nano-scale can be challenging. In fact, the nano-scale quantitative measurement of material properties is a research area of immense interest and, while considerable headway has been made, there is still much to understand and develop in this field. A measurement technique that has made great strides in nano-scale compositional mapping is Atomic Force Microscopy (AFM), which was invented in 1986 by Binning, Quate, and Gerber (Binning, Quate, and Gerber, 1986) .

AFM is an imaging technique that uses a mechanical cantilever with a sharp tip to scan the surface of a sample while the deflection of the cantilever is detected with a laser system. In the original format known as *contact mode AFM*, the tip remains in constant contact as it scans the sample, and the static deflection of the cantilever is used to provide a topographical measurement of the surface. Soon after the invention of AFM, *dynamic mode AFM* (Martin, Williams, and Wickramasinghe, 1987) was introduced and has since become a mainstay for the many different variations of AFM. In dynamic mode AFM, a resonant harmonic excitation is applied to either the base of the cantilever, the base of the sample or directly to the tip, and a feedback mechanism is employed to capture the sample's morphology (García, 2002). While the cantilever responds harmonically to the excitation as it scans the sample, it may remain in contact with the sample in a variation known as contact resonance AFM (Cartagena-Rivera et al., 2015; Gannepalli et al., 2011; Mahaffy et al., 2000; Mahaffy et al., 2004; Yablon et al., 2012; Yuya, Hurley, and Turner, 2008), or it may be in contact with the sample for only part or none of the oscillation cycle in formats known as *tapping mode AFM* (or *intermittent-contact mode AFM)* and *non-contact mode AFM* (Eaton, 2010; García, 2010). The primary advantage of using either intermittent-contact mode or non-contact mode AFM is that the reduced tip-sample interaction results in minimal damage to the tip and sample while achieving high sensitivity due to the high quality factor of the micro-cantilever employed in the AFM operation.

The most common technique used in AFM operation is known as *amplitude modulation AFM (AM-AFM)* wherein the steady-state response amplitude of the cantilever serves as the feedback parameter, and the relative tip-sample separation is adjusted in order to maintain a predetermined "set-point" amplitude. The resulting relative tip-sample separation conveys topographical information while the phase of the steady-state cantilever response with respect to the excitation provides a qualitative compositional map (García, 2010). Nanomechanical imaging based on the phase in an AM-AFM configuration is known as *phase imaging* or *loss tangent imaging* (Paulo and García, 2001; Proksch et al., 2016; Proksch and Yablon, 2012; Tamayo and Garcia, 1997). While phase imaging and loss-tangent imaging provide useful qualitative compositional maps, their main drawback is that, for an inelastic tip-sample interaction, the information delivered by the phase couples the contributions of the conservative and non-conservative constituents of the tip-sample force. Specifically, the AFM loss tangent has been analytically related to the *ratio* of the loss modulus to the storage modulus (Hurley et al., 2015; Proksch et al., 2016). Moreover, for a completely elastic tip-sample interaction, the phase shows no variation with respect to changes in the Young's modulus (Garcia and Proksch, 2013; Tamayo and Garcia, 1997). This implies that in the absence of dissipative forces in the tip-sample interaction, the phase provides no compositional information regarding stiffness.

In order to gather more information about the sample, researchers began measuring the response at more than one frequency in what is generally known as *multi-frequency AFM* (Dufrêne et al. 2017; Garcia and Herruzo 2012; Rodríguez and García 2004). While multi-frequency AFM is not limited to intermittent-contact and non-contact mode AFM and, in fact, significant effort has been devoted to contact resonant mode AFM (Cartagena-Rivera et al., 2015; Gannepalli et al., 2011; Yablon et al., 2012) where the tip-sample interaction is approximately linear, in this work we restrict our attention to tapping mode AFM. A common approach, called *bimodal AFM*, relies on the excitation and detection of two resonant frequencies. Some studies have investigated the use of the first flexural and first torsional modes in bimodal AFM (Kawai et al., 2010), but most have focused on the first two flexural modes (Garcia and Proksch, 2013; Herruzo et al., 2013; Herruzo, Perrino, & Garcia, 2014; Hurley et al., 2015; Kocun et al., 2017; Labuda et al., 2016; Martinez-Martin et al., 2011; Rodríguez and García, 2004). Typically, the fundamental resonant mode is operated in either *amplitude modulation (AM)* or *frequency modulation (FM)* mode to track topographical variations while the higher mode is used to deliver compositional information. Martinez-Martin et al. used a bimodal configuration wherein the fundamental mode was controlled via FM and the higher mode operated in open loop to quantitatively measure the Young's modulus of a single immunoglobin M (IgM) anti-body (Martinez-Martin et al., 2011). Herruzo et al. extended the approximate analytical model used by Martin-Martniez et al. (Kawai et al., 2009; Sader and Jarvis, 2004) to compute the damping coefficient, storage modulus and maximum sample deflection of various polymer blends in a technique that involved a total of five feedback loops (Herruzo et al., 2014). Kokun et al. used bimodal AM-FM to generate quantitative compositional maps of samples encompassing a wide stiffness range, including a compliant gel, DNA and stiff metals (Kocun et al., 2017; Labuda et al., 2016). Solares and his colleagues extended the bimodal concept to *trimodal AFM* where the excitation of three eigenmodes adds subsurface imaging capabilities for soft samples (Ebeling, Eslami, and Solares, 2013; Solares and Chawla, 2010a, 2010b). Furthermore, the excitation of four eigenmodes – *tetramodal AFM* – and five eigenmodes – *pentamodal AFM* – has been explored, and the benefits of such techniques are still under investigation (Solares, An, and Long, 2014).

Another approach to multi-frequency AFM is *multi-harmonic AFM*, in which the cantilever is excited with a single frequency while the response is measured at several frequencies corresponding to integer multiples of the excitation frequency (i.e., harmonics) (Cartagena et al., 2013; Raman et al., 2011; Sahin et al., 2007). Raman et al. have developed analytical models relating the 0th harmonic amplitude (DC offset), 1st harmonic phase, 2nd harmonic amplitude and 2nd harmonic phase of the cantilever's response to four quantitative compositional measurements: Maximum adhesive tip-sample force, maximum sample indentation, effective sample stiffness and intrinsic viscosity (Cartagena et al., 2013). In this method, the only feedback parameter is the 1st harmonic amplitude, which is used to track topography with the typical AM-AFM scheme. The analytical relations were recovered by assuming that the response and tip-sample force contain only the 0th, 1st and 2nd harmonics (other harmonics were assumed to be trivially small), balancing the harmonics and, finally, relating the quantitative force harmonics to material properties via the appropriate Fourier integrals. The model was then used to image and map *Bacillus subtillis* bacteriophage $\phi$29 in liquid. Sahin et al. considered a new cantilever design having a tip that is offset from the long axis so that, during tapping mode AFM, the tip-sample interaction generates a torque about the long axis and thereby excites torsional vibrations. This cantilever is driven only at the fundamental flexural eigenfrequency yet, due to the relatively large gain and bandwidth of the torsional mode's transfer function, the torsional response contains multiple harmonics with strong signal-to-noise ratios (SNR). The higher harmonics in the torsional response are then used to quantify the adhesive forces and effective Young's moduli of polymer samples with the assumption of an elastic tip-sample interaction and known (or measurable) transfer functions for the fundamental flexural and torsional modes (Sahin et al., 2007).

While the achievements of multi-frequency AFM in quantitative compositional mapping are significant, the governing theoretical models are still under development and require further verification. The measurement techniques and feedback control schemes involved in bimodal AFM are sophisticated and may not be available to many AFM users. Moreover, the multi-harmonic AFM technique relies on harmonics with sufficient SNR that can be challenging to recover in the absence of liquid (Cartagena et al., 2013; Raman et al., 2011). To this end, the potential of a new approach to compositional mapping that relies on a unique variation of multi-frequency AFM is investigated. By designing the cantilever system so that one of the harmonics coincides with a higher resonant mode, the higher harmonic is amplified via *intentional internal resonance*. In that context the technique developed in this work may be regarded as a combination of multi-harmonic AFM and bimodal AFM. The key distinction is that, unlike other bimodal approaches, the input signal contains only a single frequency, yet the cantilever response contains two frequencies with large SNR. The efficacy of this new inner-paddled cantilever design was theoretically and experimentally demonstrated in some recent work of our group (Jeong et al., 2016). Quantification of the SNR and a detailed analysis of the effect of noise is outside the scope of this study, but readers are referred to the work of Santos et al. (2014) for such a discussion.

The proposed AFM cantilever consists of a base micro-cantilever with an inner *Si* paddle as shown Fig. 3.1a. When base harmonic excitation is applied to it, the cantilever system behaves like a system of two linearly coupled harmonic oscillators exhibiting dominant in-phase and out-of-phase resonant modes. That is, the two-degree-of-freedom reduced order model of the cantilever system has two resonant modes corresponding to synchronous motions of the two effective masses of the system. In the absence of damping, there is no phase lag between the motions of the two effective masses during the in-phase mode, while there is a 180-degree phase lag between the motions of the two effective masses during the out-of-phase mode. In the presence of weak damping, the in-phase and out-of-phase modes are preserved, but the phase differences between the oscillations of the two effective masses are (only slightly) perturbed from the aforementioned values. The inner-paddled cantilever is specifically designed so that the higher eigenfrequency corresponding to the out-of-phase mode is an integer multiple, say $n$, of the lower, in-phase eigenfrequency as described in a previous work (Jeong et al., 2016; Potekin et al., 2017; Potekin et al., 2018).

To this end, computational and experimental studies are performed aiming toward an understanding of the underlying dynamics of this new internal resonance–based high-frequency AFM operation. Accordingly, the embedded information in the measured $n^{\text{th}}$ harmonic signal is considered in detail, and its implementation to more efficient AFM operation is explored. To begin, a description of the design and theoretical model of the inner-paddle cantilever is presented in Section 3.2. In Section 3.3, the performance of an inner-paddled cantilever designed to support 1:3 internal resonance is studied. In particular, the ability of this cantilever to distinguish the material properties of a blended polystyrene-low density polyethylene (PS – LDPE) specimen is investigated. Additionally, an approximate empirical model that relates the 3rd harmonic amplitude to the average tip-sample interaction force is developed, further enabling the predictive design of the proposed new microcantilever system. The focus of Section 3.4 is on optimizing the cantilever design by studying the efficacy of a 1:3 internal resonance as compared with a 1:2 internal resonance. In Section 3.5, the cantilever designed with an intentional 1:2 internal resonance is used to generate topographical and compositional maps of cyanobacteria. Then, in Section 3.6, the amplitude-modulation feedback control of the fundamental mode is computationally modeled to study variations in the phase of the first mode, amplitude of the higher mode and phase of the higher mode with respect to changes in the Young's modulus. Finally, an outline of an approximate analytical method that could be used to convert the AM-AFM observables of the inner-paddled cantilever into quantitative compositional maps is presented in Section 3.7.

### 3.2 Inner-paddled cantilever design and reduced-order model

**S**canning electron microscope (SEM) images of the inner-paddled cantilevers designed to support 1:3 internal resonance and 1:2 internal resonance are shown in Figs. 3.1a and 3.1b, respectively. The cantilever system consists of a base microcantilever having a middle cavity in which a 300 nm thick silicon (*Si*) nanomembrane oscillates. The base cantilever was constructed from a commercially available AFM cantilever that was structurally modified to accommodate an inner paddle added via transfer printing-based microassembly (Keum et al., 2012; Keum et al., 2016). Details of the inner-paddled cantilever design and fabrication process used can be found in a previous paper (Jeong at al., 2016). The length of the inner paddle was carefully chosen to achieve a 1:*n* ratio, where *n* is an integer, between the eigenfrequencies of the two leading in-phase and out-of-phase bending modes of the combined system. This provides the conditions required for the realization of a 1:*n* internal resonance in this system, which can only be activated in the presence of nonlinearity.

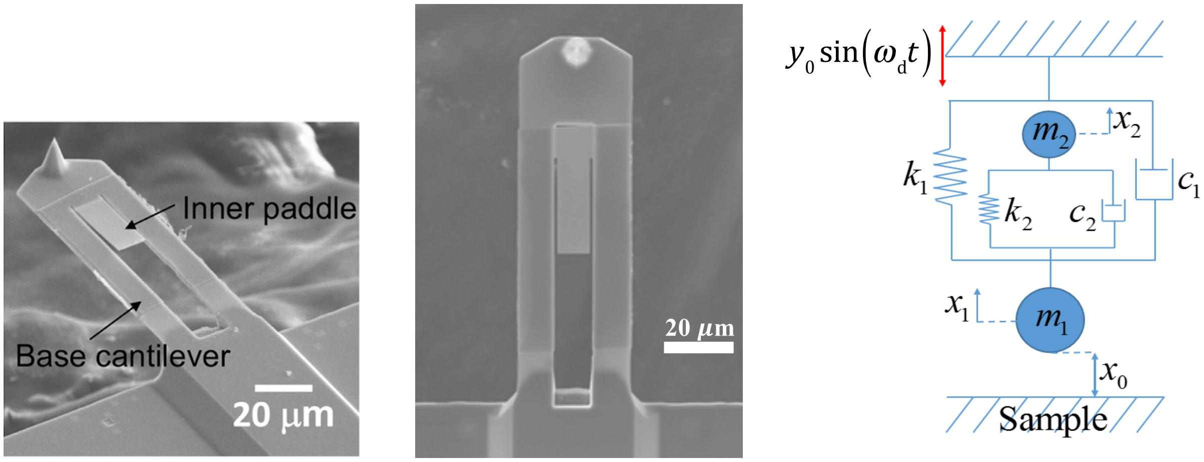

(a) (b) (c)

*Figure 3.1: SEM images of the inner-paddled cantilevers designed with a (a) 1:3 IR and (b) 1:2 IR*, and *(b) a shcematic of the inner-paddled cantilever's lumped-parmater reduced-order model.*

The source of nonlinearity that eventually triggers the 1:*n* internal resonance is the realization of non-smooth, vibro-impacts between the tip and sample during tapping mode AFM operation. When the AFM system is harmonically excited at a frequency equal to its first, in-phase natural frequency in the presence of the nonlinear tip-sample interactions, the result is energy transfer from low-to-high frequencies resulting in the generation of strong higher harmonics in the cantilever's response. By design, the $n^{\text{th}}$ harmonic coincides with the second, out-of-phase natural frequency, and this provides the nonlinear dynamical mechanism whereby the 1:*n* internal resonance amplifies the response of the $n^{\text{th}}$ harmonic in the measured responses.

By contrast, in the absence of the nonlinear non-smooth tip-sample interactions, the cantilever system is designed to operate in a linear dynamic regime. Assuming that both the base cantilever and inner paddle oscillate in their corresponding fundamental bending modes, the integrated system can be approximated by a set of linearly coupled damped harmonic oscillators as depicted in Fig. 3.1c. This represents the lumped reduced-order model of the dynamics of this system. The corresponding equations of motion for the coupled oscillators are stated in equation (3.1), where $m_1$ ($m_2$) is the effective mass, $k_1$ ($k_2$) the effective stiffness, and $c_1$ ($c_2$) the effective damping coefficient of the base cantilever (inner paddle):

$$m_1\ddot{x}_1 + c_1\dot{x}_1 + k_1x_1 + k_2(x_1 - x_2) + c_2(\dot{x}_1 - \dot{x}_2) = k_1y_0\sin\omega_d t + c_1\omega_d y_0\cos\omega_d t + F_{ts}(x_1) \tag{3.1a}$$

$$m_2\ddot{x}_2 + k_2(x_2 - x_1) + c_2(\dot{x}_2 - \dot{x}_1) = 0 \tag{3.1b}$$

To model the force applied to the cantilever system through a piezoelectric shaker during dynamic AFM operation, we incorporate harmonic base excitation in the reduced order model with amplitude $y_0$ and drive frequency $\omega_\mathrm{d}$. Finally, $x_1$ and $x_2$ are the displacements of $m_1$ and $m_2$, respectively; $x_0$ is the static separation between the cantilever tip and the sample; and $F_\mathrm{ts}$ is the tip-sample interaction force. The DMT contact model (Derjaguin, Muller, and Toporov, 1980) was used to approximate the nonlinear vibro-impacts between the tip and sample and is given in equation (3.2):

$$F_\mathrm{ts}(x_1) = \begin{cases} -\dfrac{2HR^3}{3\left[2R+(x_0+x_1)\right]^2(x_0+x_1)^2}, & x_1 > a_0 - x_0 \\ -\dfrac{HR}{6a_0^2}+\dfrac{4}{3}E^*\sqrt{R}\left[a_0-(x_0+x_1)\right]^{3/2}, & x_1 < a_0 - x_0 \end{cases} \tag{3.2}$$

In (3.2), $H$ is the Hamakar's constant, $R$ is the radius of curvature of the tip, $E^*$ is the effective tip-sample Young's modulus and $a_0$ is the intermolecular distance. The DMT tip-sample force is piecewise continuous with respect to $x_1$; when the tip *is not* in contact with the sample, it holds that $x_1 > a_0 - x_0$ and $F_\mathrm{ts}$ is equal to the attractive van der Waals force whereas, when the tip *is* in contact with the sample, it holds that $x_1 < a_0 - x_0$ and $F_\mathrm{ts}$ is equal to the sum of a repulsive Herztian component and a (constant) attractive van der Waals term.

To avoid lengthy descriptions and redundancies, we will now establish a nomenclature for the aforementioned inner-paddled cantilever design. As described above, a cantilever with a single inner paddle can be approximated by a two-degree-of-freedom reduced order model consisting of two coupled harmonic oscillators. This system of two coupled oscillators gives rise to two vibration modes associated with two distinct eigenfrequencies, $\omega_1$ and $\omega_2$. Assuming the eigenfrequencies are ordered so that $\omega_1 < \omega_2$, the ratio of these two eigenfrequencies, $n = \omega_2 / \omega_1$, will be used to distinguish between different inner-paddled cantilever designs. An inner-paddled cantilever designed so that the ratio of the two eigenfrequencies of its reduced order model is equal to 1:*n*, will be referred to as a "1:*n* cantilever". There is a significant distinction between the inner-paddled cantilever designs for which *n* is an integer and those for which *n* is not an integer. If *n* is an integer, the inner-paddled cantilever can support an internal resonance activated by the nonlinear tip-sample interaction; otherwise, internal resonance is not possible. Similarly, an inner-paddled cantilever having two inner paddles (as shown in Fig.5a) can be modeled as a system of three linearly coupled harmonic oscillators with three vibration modes and corresponding eigenfrequencies, $\omega_1$, $\omega_2$ and $\omega_3$, where it is assumed that $\omega_1 < \omega_2 < \omega_3$. Accordingly, a cantilever with two inner paddles designed so that the ratio of its three eigenfreqencies is denoted by 1:*n:m,* where $n = \omega_2 / \omega_1$ and $m = \omega_3 / \omega_1$, will be referred to as a "1:*n:m* cantilever".

### 3.3 Computational and experimental results for the 1:3 cantilever

In order to test the efficacy of this new AFM system for enhanced measurement of material properties, a two-component polymeric sample mounted on a glass slide (see Figure 3.2) was tested. The circular island contains relatively "compliant" low-density Polyolefin Elastomer (LDPE) with an elastic modulus of ~ 0.1 GPa on the macro-scale, whereas the surrounding matrix is relatively "stiff" Polystyrene (PS) with an elastic modulus of ~ 2 GPa on the macro-scale. In Table 3.1, the parameters of the reduced-order model and the materials are listed. The measurements were performed under base excitation of the base cantilever at the fixed forcing frequency of $\omega_d = 0.9995\,\omega_{m1}$ (where $\omega_{m1}$ is the natural frequency of the lower in-phase mode of the beam-paddle system), and at fixed excitation amplitude $y_0$. Then the amplitude and phase of the measured 1st and 3rd harmonic signals (corresponding to the lower and higher modes of the system incorporating 1:3 internal resonance) were obtained while varying the static tip-sample separation $x_0$ at a fixed location on the LDPE island or the PS surrounding matrix.

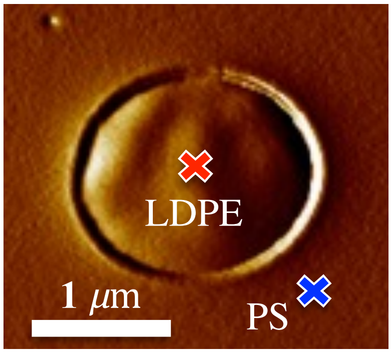

*Figure 3.2: AFM image of a PS sample containing an inner LDPE island.*

This experiment was numerically simulated by integrating the model (3.1) in Python for several hundreds of cycles to steady-state and performing a fast Fourier transform (FFT) of the response to compute the amplitudes and phases of the first and third harmonics. To simulate the tip approaching the sample, I began at an $x_0$ value sufficiently large so that the tip was not in contact with the sample and incrementally decreased $x_0$ for a fixed excitation amplitude, $y_0$. For each new simulation, the initial conditions were set equal to the final conditions of the simulation corresponding to the previous $x_0$ value. Additionally, the total simulation time was set equal to an integer multiple of the drive period to achieve consistency in the base motion, and the steady state segmentation used in the FFT was chosen to be an integer multiple of the drive period to mitigate edge effects.

Comparisons of experimental and computational results for both the stiff PS region and the compliant LDPE region of the sample are depicted in Fig. 3.3. For both materials, there was strong qualitative agreement between the experimental and computational results, which demonstrates the predictive capability of the theoretical model for this new cantilever design. This suggests that the DMT contact model is capable of predicting the response of the microcantilever tip interacting with both tested materials, over most of the initial separation distances $x_0$.

| Parameter description | Value |
|---|---|
| Effective masses, 1:2 cantilever | $m_1 = 6.27\text{ng}, \quad m_2 = 0.0756\text{ng}$ |
| Effective stiffnesses, 1:2 cantilever | $k_1 = 5.22\text{N/m}, \quad k_2 = 0.244\text{N/m}$ |
| Lower eigenfrequency, 1:2 cantilever | $\omega_1 = 9.051 \times 10^5 \text{rad/s}$ |
| Effective masses, 1:3 cantilever | $m_1 = 6.27\text{ng}, \quad m_2 = 0.0615\text{ng}$ |
| Effective stiffnesses, 1:3 cantilever | $k_1 = 5.22\text{N/m}, \quad k_2 = 0.453\text{N/m}$ |
| Lower eigenfrequency, 1:3 cantilever | $\omega_1 = 9.074 \times 10^5 \text{rad/s}$ |
| Effective masses, 1:3.5 cantilever | $m_1 = 6.27\text{ng}, \quad m_2 = 0.057\text{ng}$ |
| Effective stiffnesses, 1:3.5 cantilever | $k_1 = 5.22\text{N/m}, \quad k_2 = 0.569\text{N/m}$ |
| Lower eigenfrequency, 1:3.5 cantilever | $\omega_1 = 9.079 \times 10^5 \text{rad/s}$ |
| Damping coefficients, all cantilevers | $c_1 = c_2 = 2.85 \times 10^{-8} \text{Ns/m},$ |
| Tip radius, all cantilevers | $R = 30\text{nm}$ |
| Tip elastic modulus, all cantilevers | $E_{\text{tip}} = 169\text{GPa}$ |
| Elastic modulus of LDPE | $E_{\text{LDPE}} = 0.1\text{GPa}$ |
| Hamakar's constant of LDPE | $H_{\text{LDPE}} = 3 \times 10^{-19} \text{J}$ |
| Elastic modulus of PS | $E_{\text{PS}} = 2\text{GPa}$ |
| Hamakar's constant of PS | $H_{\text{PS}} = 2 \times 10^{-19} \text{J}$ |

*Table 3.1: System parameters of the 1:2 cantilever, the 1:3 cantilever, the 1:3.5 cantilever, the LDPE material and the PS material.*

Considering first the stiffer PS sample, the trend of the amplitude of both harmonics in the numerical results coincides with that of the experimental results in most of the considered range of $x_0$. As the tip approaches the sample (i.e., in the limit of small values of $x_0$), we note that the decreasing trend of the phase is also captured by the numerical model for most values of $x_0$. At very small initial displacements $x_0$, however, there is a discrepancy in the trend of the phases between the experimental and numerical results, e.g., see the results in Figures 3b and 3d; we attribute this discrepancy to limitations of the DMT model at small separation distances, as well as to complex sample-tip interactions due to the dynamics of the sample itself (i.e., due to the flexibility of the sample) which cannot be captured by the vibro-impact model (3.1) used herein. Similarly, for the compliant LDPE sample, the trends in all experimental signals are reflected in the numerical results at most initial tip-sample separations $x_0$, but again we see some discrepancies at very small values of $x_0$. Specifically, the amplitude and phase of the 3rd harmonic become unsteady for small $x_0$, whereas the corresponding amplitude of the 1st harmonic decreases abruptly. These unsteady dynamics could also be due to a dynamic transition into a regime where the tip is sticking to the sample (i.e., transition to a state of motion in which the tip oscillates about an equilibrium point on the sample while maintaining continuous contact with the sample), but this trend is not observed in the experimental results (Lee et al., 2003).

Considering the results of Fig. 3.3 in detail, we note that for both materials the amplitudes of the 1st harmonics (i.e., the components of the responses at the excitation frequency) linearly decrease as the tip approaches the surface, and the slopes measured on both materials are almost identical. In contrast, there is a clear discrepancy between the slopes of the 3rd harmonic amplitudes (which are intensified by the intentional 1:3 internal resonance introduced by the design) of the responses in the co-polymer and PS regions. Additionally, we see a clear difference in the reversed trend of the phases (both of the 1st harmonics and the 3rd harmonics) corresponding to the two stiff and compliant materials. The phases of the 1st and 3rd harmonics increase as the tip approaches the more compliant LDPE region, but decrease as the tip approaches the stiffer PS region. Note that, since the amplitudes of the 1st and 3rd harmonics are the root mean square values of oscillation amplitude, meaningful phase lags occur over a range of 180 degrees. However, we plot the phase over a larger range so as to eliminate possibly misleading jumps in the phase.

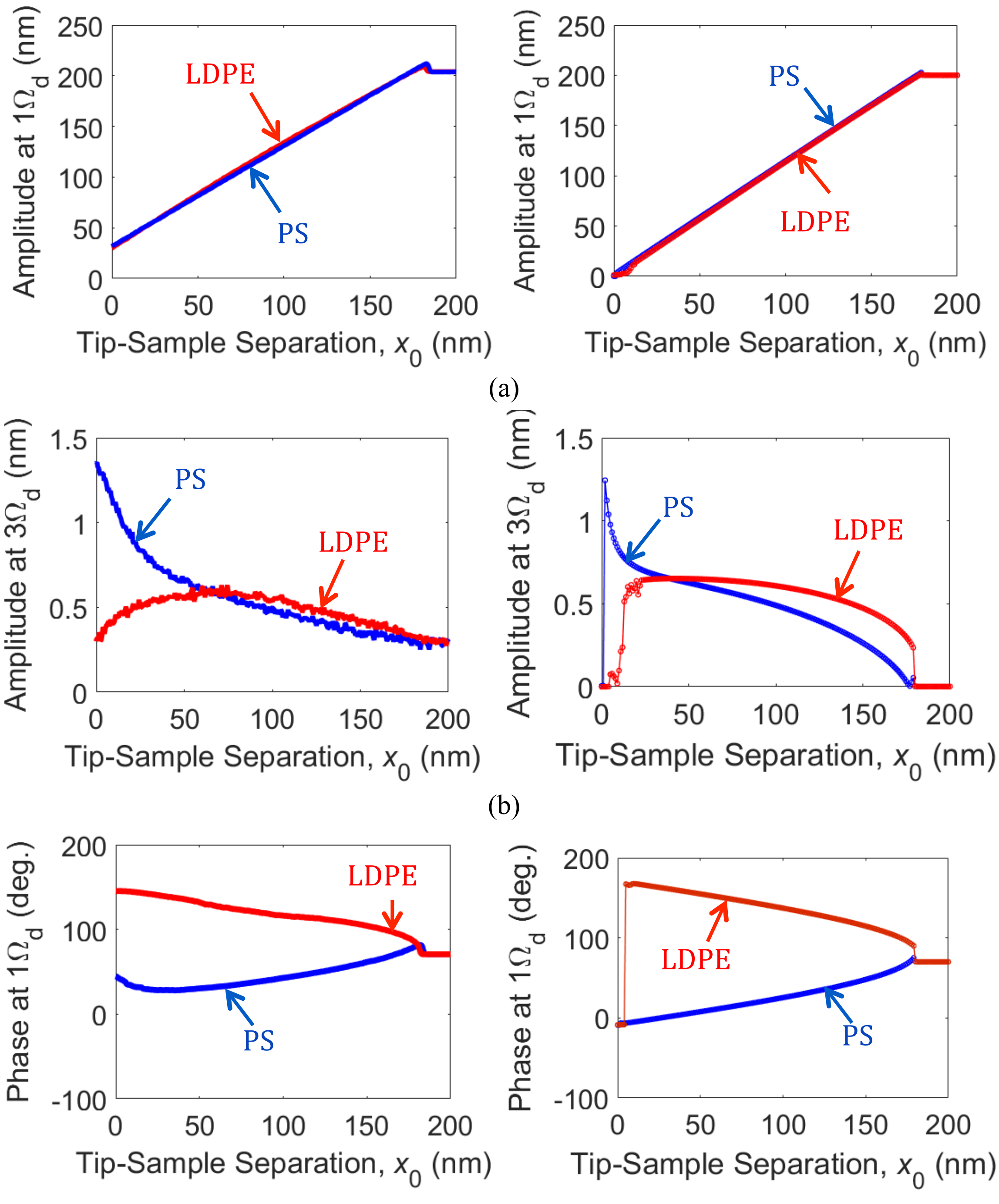

(a)

(b)

(c)

*Figure 3.3. Experimental (left column) and numerical (right column) sensitivity curves of the inner paddle response for the PS sample (blue) and the LDPE sample (red), for excitation amplitude* $y_0 = 0.91\,\text{nm}$*: (a,b) Amplitudes of 1*$^{st}$ *and 3*$^{rd}$ *harmonics versus static tip-sample distance, (c,d) phases of first and third harmonics versus static tip-sample distance (note that the phase of the 3*$^{rd}$ *harmonic has no meaning when the amplitude is zero).*

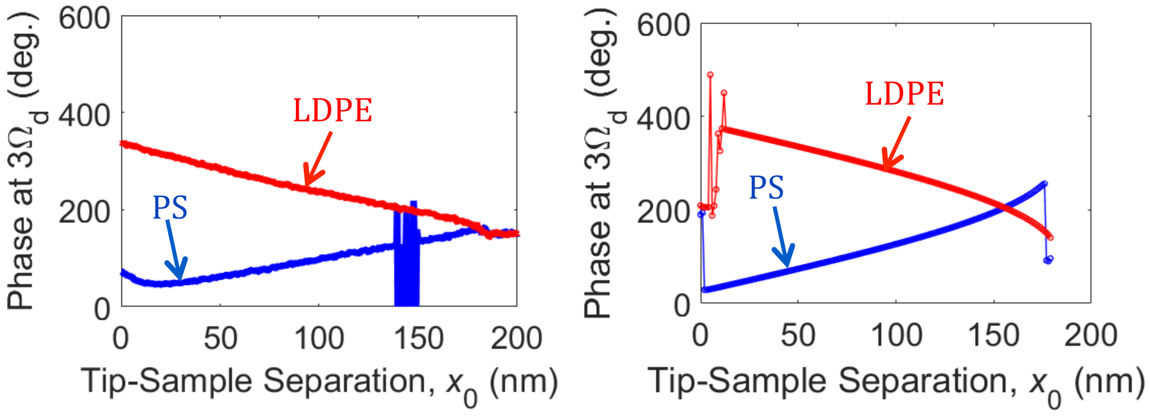

(d)

*Figure 3.3 (cont.)*

These results can be placed in proper context when noting that, for a conventional AFM cantilever (without a paddle), it is well known that the cantilever dynamics during dynamic mode operation is highly nonlinear, leading to the coexistence of two stable steady-state solutions, namely a low-amplitude solution (designated as the "lower solution branch"), and a high-amplitude solution (namely the "upper solution branch"). The low-amplitude solution corresponds to attraction-dominant regimes between the tip and the sample, whereas the high-amplitude solutions typically correspond to repulsion-dominant regimes. On the lower branch, the phase (of the first harmonic) is known to increase as the tip approaches the sample, whereas on the upper branch, typically the phase decreases as the tip approaches the sample (Lee et al., 2003; Stark, 2010; Garcia, 2010).

Based on the above, it follows that the trends in the phases of the 1st and 3rd harmonics as well as the amplitude of the third harmonic in the numerical and experimental results appear to differentiate between two nonlinear dynamical regimes occurring separately in the two dissimilar materials. Indeed, for the case of the stiffer PS material, the steady state nonlinear dynamics appear to be attracted to and stably track the upper solution (repulsive) branch, whereas for the case of the LDPE material the dynamics appear to be attracted by the lower solution (attractive) branch. To confirm this, after fixing the tip-sample separation to $x_0 = 100\ \text{nm}$, additional computations of the tip-sample interaction forces as functions of the distances $\delta = a_0 - (x_0 + x_1)$ for both materials during dynamic AFM mode operation were performed. The results are depicted in Figure 3.4, from which it is clear that for the compliant LDPE sample, the interaction force is in the attractive dynamic regime dominated by the van der Waals forces; whereas for the stiff PS sample, the interaction force is predominantly in the repulsive dynamic regime dominated by the repulsive Hertzian forces which confirm our previous assertions.

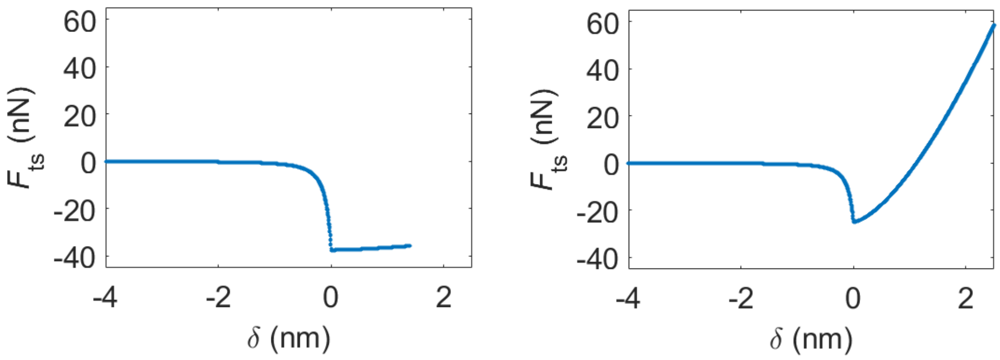

(a) (b)

*Figure 3.4. Nonlinear tip-sample interaction force,* $F_{ts}$*, versus distance* $\delta = a_0 - (x_0 + x_1)$ *during dynamic AFM mode operation for a tip-sample separation of* $x_0 = 100\, nm$ *and base excitation amplitude of* $y_0 = 0.91\, nm$*: (a) Purely attractive dynamic regime for the case of the LDPE (compliant) sample, and (b) Predominantly repulsive dynamic regime for the case of the PS (stiff) sample.*

It follows that the difference in branch selection among the two materials results from a difference in material properties (namely, elastic modulus) since the PS material is significantly stiffer than the LDPE. Furthermore, the phase of a typical AFM cantilever is well known to depend on material properties, which is the reason why the phase is currently used to construct qualitative compositional maps. Hence, regarding the new cantilever design, the fact that the amplitude and phase of the third harmonic also exhibit different trends among the two materials indicates that these may be utilized as additional channels with which material properties can be measured qualitatively. This is the motivation for this work, which aims to characterize the relationship between material properties and information delivered by the third harmonic.

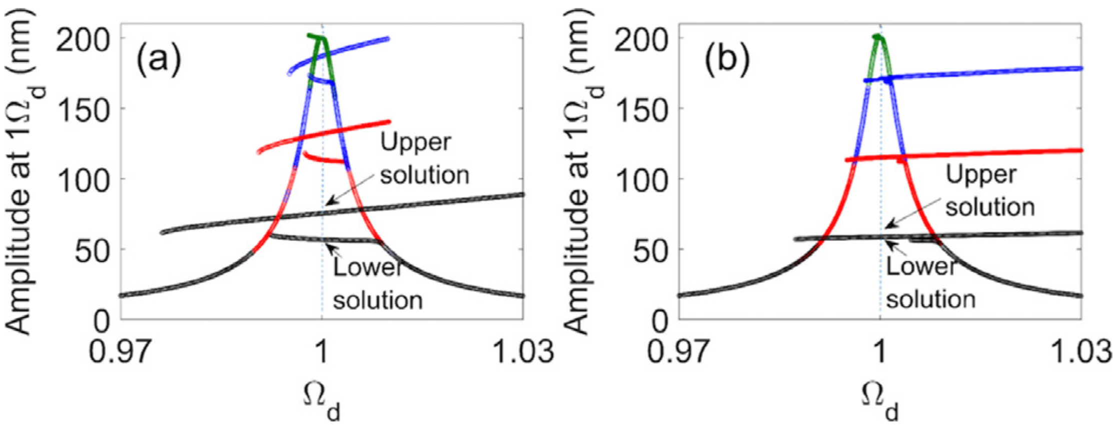

*Figure 3.5. Amplitude of the 1st harmonic versus normalized drive frequency* $\Omega_d$ *for a base excitation amplitude of* $y_0 = 0.91\,nm$ *and for four different normalized static tip-sample distances (*$x_s = x_0/180\,nm$*), namely,* $x_s = 0.99$ *(green),* $x_s = 0.83$ *(blue),* $x_s = 0.56$ *(red) and* $x_s = 0.28$ *(black): (a) Compliant LDPE sample (note two co-existing upper and lower solution branches at the driving frequency* $\Omega_d = 0.9995$ *– denoted by the dashed vertical line); (b) stiff PS sample (note the existence of only the upper solution branch at the driving frequency). These results explain theoretically the experimental AFM measurements reported in Figures 3.3 and 3.4.*

To gain further insight into why the two tested materials seem to be attracted to and eventually track different solution branches, a detailed computational study of the steady state dynamics of the reduced order model (3.1) under conditions of dynamic AFM operation was performed. In Fig. 3.5, the resonance curves of this system for several different normalized static tip-sample distances $x_s$ are presented. In the plots the static tip sample distance is normalized by the free amplitude of the base cantilever according to $x_s = x_0/180$ nm. The drive frequency used in these simulations is indicated with a vertical dashed line in each of the plots of Fig. 3.5. From the results shown in Fig. 3.5b, I deduce that as the tip approaches the stiff PS sample, there exists only the upper solution branch at a normalized drive frequency of $\Omega_d = \omega_d / \omega_{m1} = 0.9995$ (this was the frequency used for producing the results of Figs. 3.3 and 3.4). It follows that the upper solution represents the only possible stable attractor for the steady state dynamics of the system at $\Omega_d = 0.9995$, which explains why in the AFM measurements of the PS sample, the nonlinear dynamics is attracted by the upper solution branch and not by the lower one. On the contrary, in

Fig. 3.5a, I deduce that as the tip approaches the compliant LDPE sample, both the upper and lower solution branches co-exist in the steady state dynamics, so both high and low amplitude solutions can act as attractors at $\Omega_d = 0.9995$. This holds for all static tip-sample distances $x_s$, except for $x_s = 0.99$. Interestingly, at $x_s = 0.99$ it appears that only the lower branch exists for the co-polymer sample, which explains the selection of the lower branch upon approach to the sample. Hence, as the tip continues to approach the LDPE sample, the dynamics stably track the lower branch. Note that when two or more co-existing stable attractors exist in the dynamics, the actual path of the steady state solution depends solely on the choice of initial conditions.

Finally, the change in the amplitude of the 3rd harmonic and the average interaction force as functions of the normalized drive frequency, $\Omega_d$, were computed for both samples, as seen in Fig. 3.6. Interestingly, these results indicate that the amplitude of the third harmonic is directly proportional to the absolute value of the average force per cycle. Also, even greater amplification of the third harmonic is achieved on the upper branch at larger driving frequencies.

Fig. 3.6 indicates that the magnitude of the average tip-sample interaction force is linearly related to the amplitude of the third harmonic. Accordingly, as a means to develop an empirical model relating the two quantities, it is assumed that

$$\left|\bar{F}_{ts}\right| \approx C A_3 \tag{3.3}$$

where $\left|\bar{F}_{ts}\right|$ is the magnitude of the average tip-sample interaction force per cycle during steady state, $A_3$ is the amplitude of the measured third harmonic, and $C$ is a real constant. We then find $C$ such that the average error among twelve different computational data sets is minimized. The twelve data sets include the force curves for the PS at two base excitation levels, namely, $y_0 = 0.91$ nm and 1.02 nm (presented in Fig. 3.3 and Fig. 3.7, respectively); the force curves for the LDPE at the same two base excitation levels (again presented in Fig. 3.3 and Fig. 3.7, respectively); and the resonance curves at four different normalized tip-sample separations, $x_s = 0.28, 0.56, 0.83$ and $0.99$, for the LDPE and PS samples (shown in Figs. 3.5a and 3.5b, respectively). At each value of $C$, the root mean square error (RMSE) for each data set is computed, and the unweighted average of the twelve different RMSE values is calculated. Note that data points corresponding to the linear response are not included in this numerical computation. The corresponding constant that minimizes this average RMSE value is found to be $C_{\min} = 3.57$.

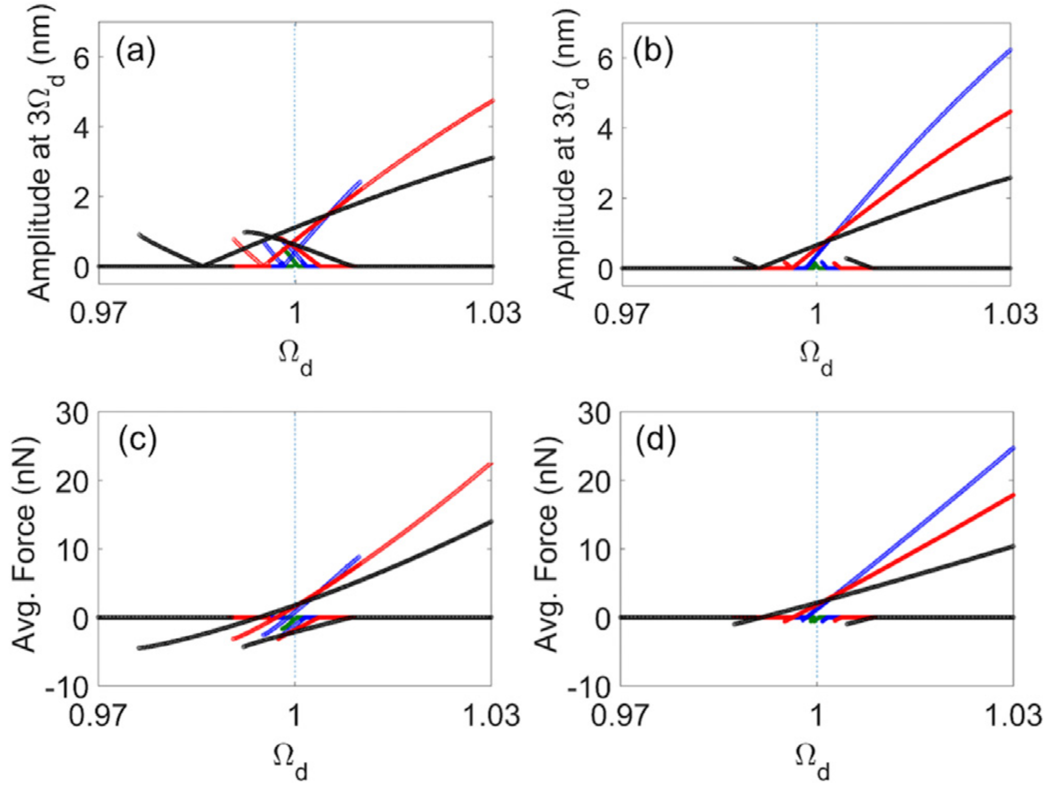

*Figure 3.6. Amplitude of the 3rd harmonic versus normalized drive frequency for, (a) the LDPE sample, and (b) the PS sample; and average tip-sample interaction force per cycle during steady state versus normalized drive frequency for, (c) the LDPE sample, and (d) the PS sample. The same base excitation amplitude of* $y_0 = 0.91\ nm$ *and normalized static tip-sample distances are considered as in Fig. 3.5, namely,* $x_s = 0.99$ *(green),* $x_s = 0.83$ *(blue),* $x_s = 0.56$ *(red) and* $x_s = 0.28$ *(black), and the vertical dashed line corresponds to the driving frequency at* $\Omega_d = 0.9995$ *as for the results in Figs. 3.3-3.5.*

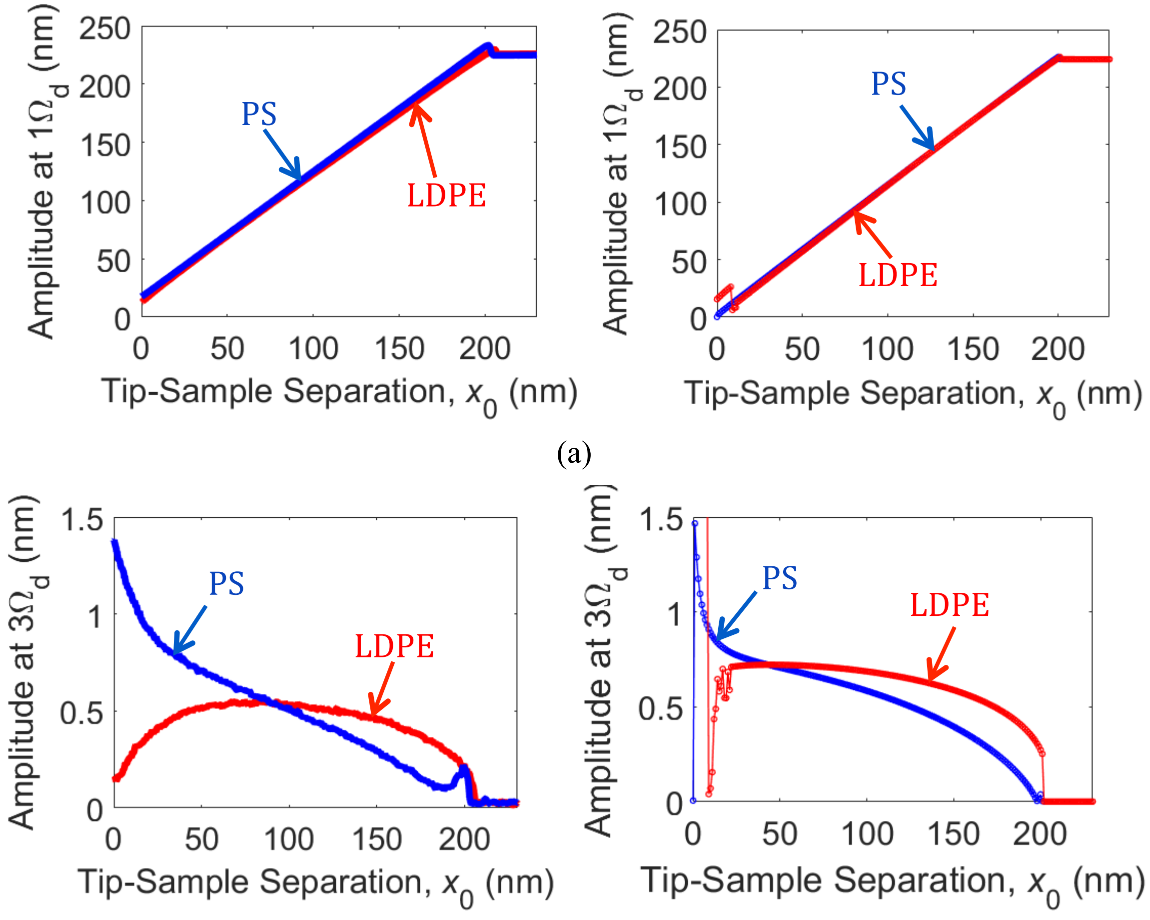

(a)

(b)

*Figure 3.7. Experimental (left column) and numerical (right column) sensitivity curves of the inner paddle for the PS sample (blue) and the LDPE sample (red) with excitation amplitude* $y_0 = 1.02$ nm*: (a,b) Amplitudes of 1st and 3rd harmonics versus static tip-sample distance, (c,d) phases of first and third harmonics versus static tip-sample distance (note the phase of the third harmonic has no meaning when the amplitude is zero). Similar to the results shown in Fig. 3.3, strong correspondence between the computational and experimental results is observed for most* $x_0$*, but a discrepancy is seen at small* $x_0$*. In this case, the computational results show evidence of branch jumping at low* $x_0$*, which did not occur in the experiment.*

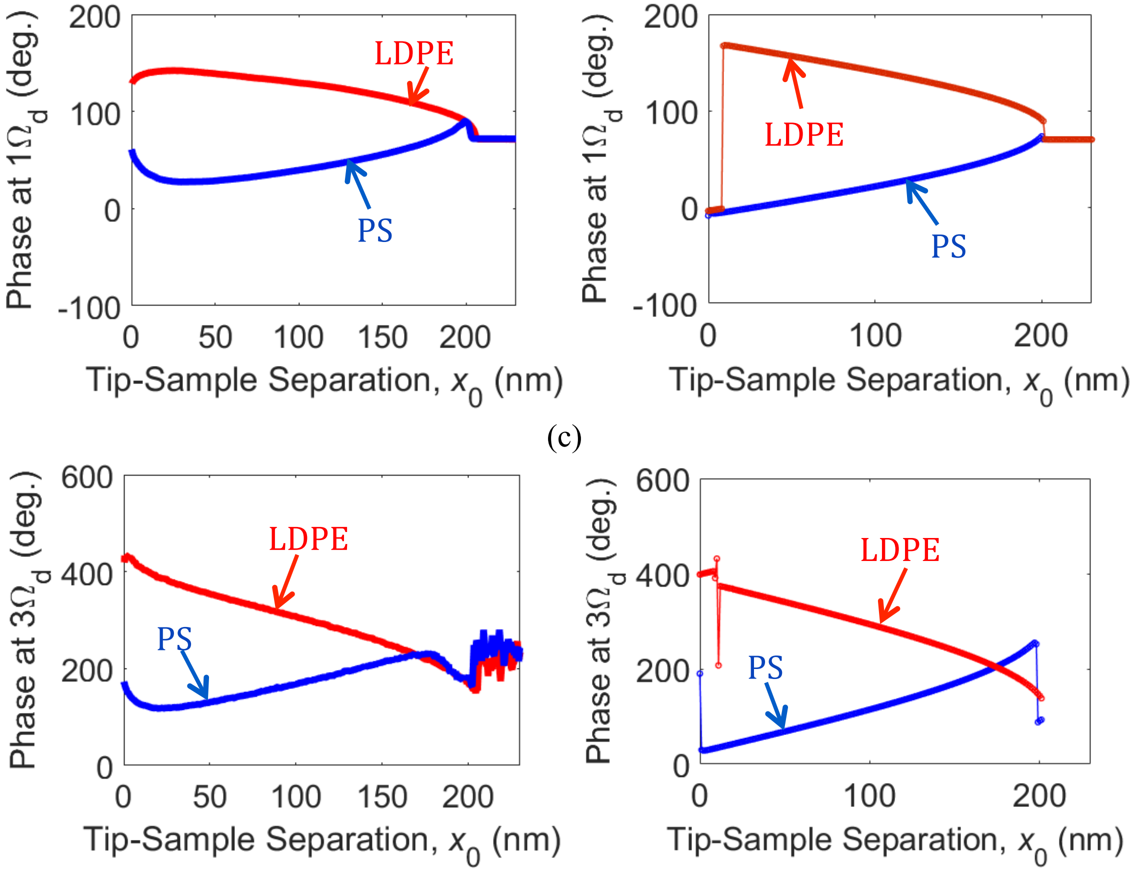

(c)

(d)

*Figure 3.7 (cont.)*

A comparison of $\left|\bar{F}_{ts}\right|$ and $C_{\min}A_3$ for twelve data sets are shown in Figs. 3.8 and 3.9. Overall, strong correspondence between $\left|\bar{F}_{ts}\right|$ and $C_{\min}A_3$ is observed for most of the data, which suggests that indeed the average force is nearly proportional to the amplitude of the third harmonic. This is significant since it demonstrates the potential of the amplified (due to 1:3 internal resonance) third harmonic to measure the average tip-sample interaction force. Further, since the tip-sample interaction force is directly related to material properties of the sample and the average tip-sample force is linearly related to the amplitude of the third harmonic, it follows that the amplitude of the third harmonic serves as an effective parameter to use in the construction of compositional maps. It is reasonable to expect that compositional maps based on the amplitude of the third harmonic using this new cantilever design may more accurately indicate qualitative measurements of elastic modulus as compared to the phase of a typical cantilever. Currently, compositional maps measured with typical cantilevers are based on the phase (of the 1st harmonic) and the phase has been related analytically to the average power dissipated by the tip-sample interaction (Anczykowski et al., 1999). This makes the phase a good candidate for qualitative measurements of viscoelastic material properties associated with dissipation. However, the amplitude of the third harmonic in our new cantilever design is found to be proportional to the average tip-sample force of an elastic tip-sample interaction, which suggests that it may be a better indicator of elastic material properties like Young's modulus.

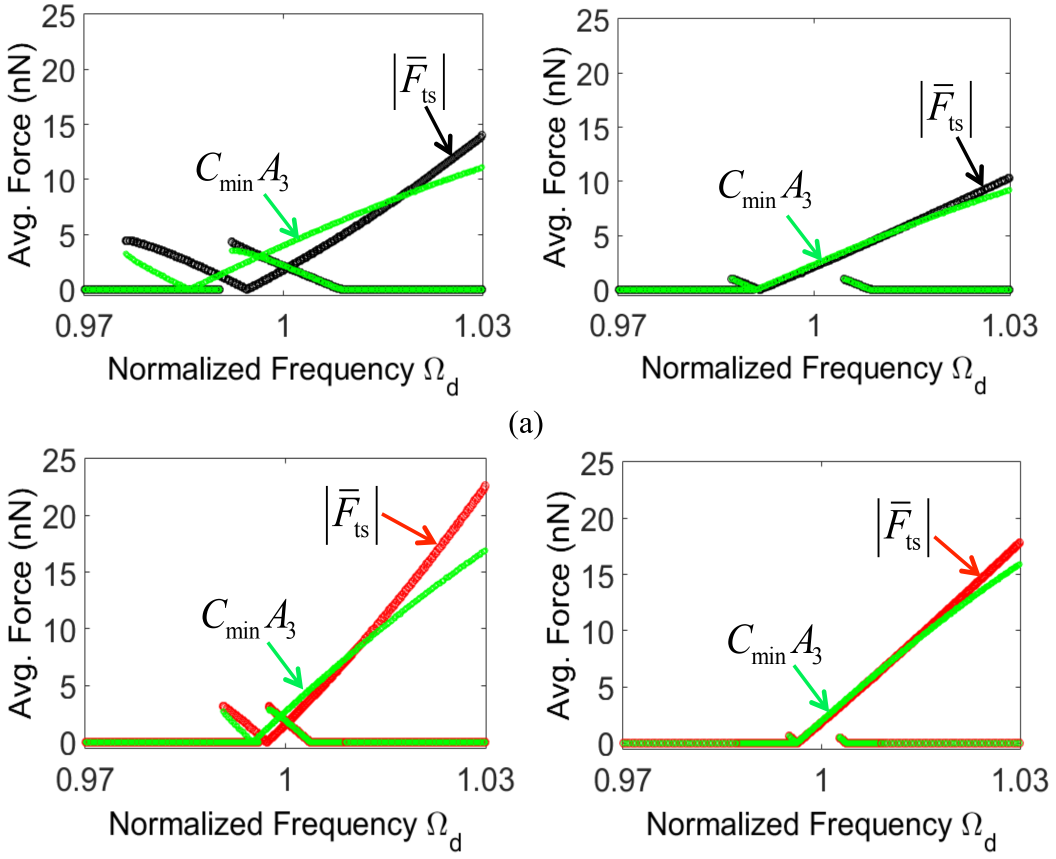

(a)

(b)

*Figure 3.8. Comparison of the average tip-sample interaction force,* $\left|\bar{F}_{\text{ts}}\right|$*, and* $C_{\min}A_3$ *as functions of the normalized drive frequency. Results are shown for the LDPE sample (left column) and the PS sample (right column) for a normalized static tip-sample distance of (a)* $x_s = 0.28$*, (b)* $x_s = 0.56$*, (c)* $x_s = 0.88$*, and (d)* $x_s = 0.99$*. The base excitation amplitude is* $y_0 = 0.91$ nm.

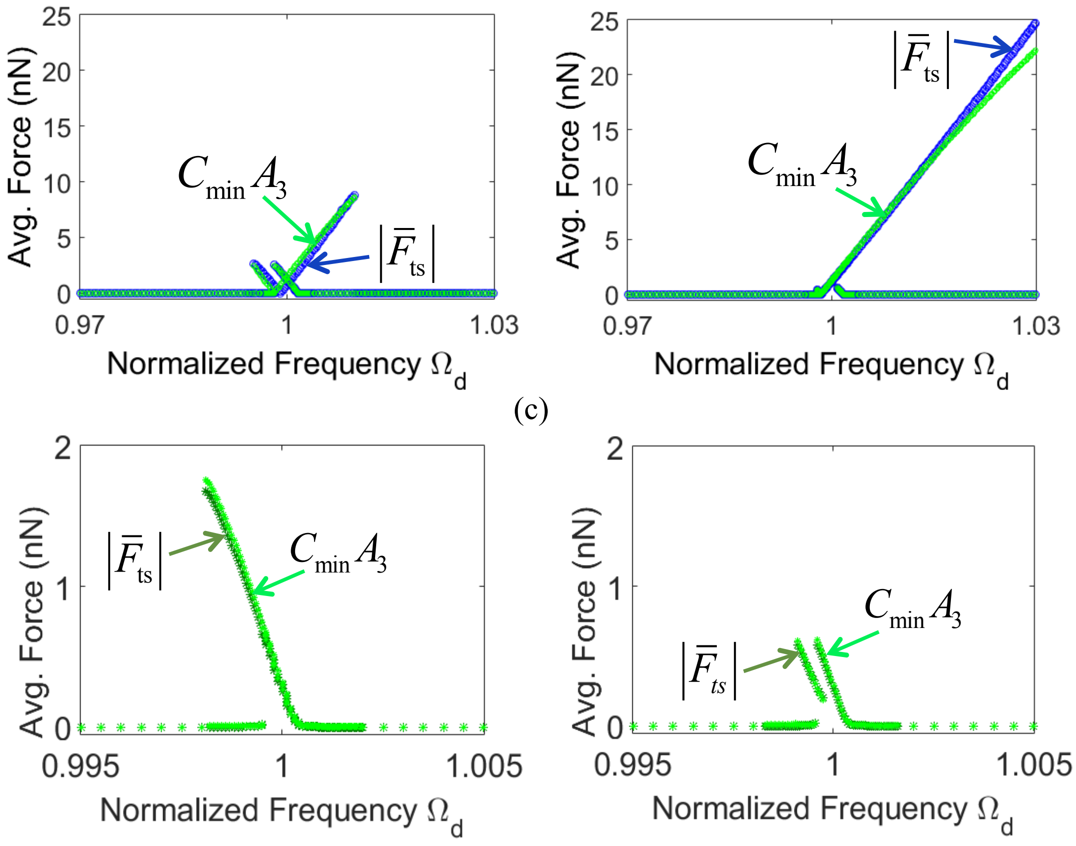

(c)

(d)

*Figure 3.8 (cont.)*

Note again that discrepancies appear in the limit of small tip-sample distances in the force curves of both materials (see Fig. 3.9), as well as in the resonance curves for the LDPE region (see Fig. 3.8). These are attributable to limitations of the DMT contact model and to complicated sample-tip dynamic interactions due to adhesion and viscoelasticity of the sample (which is not taken into account in the current model), as discussed previously. In addition, it is clear that there is stronger agreement of the correlation (3.3) for the lower solution branch compared to the upper solution branch.

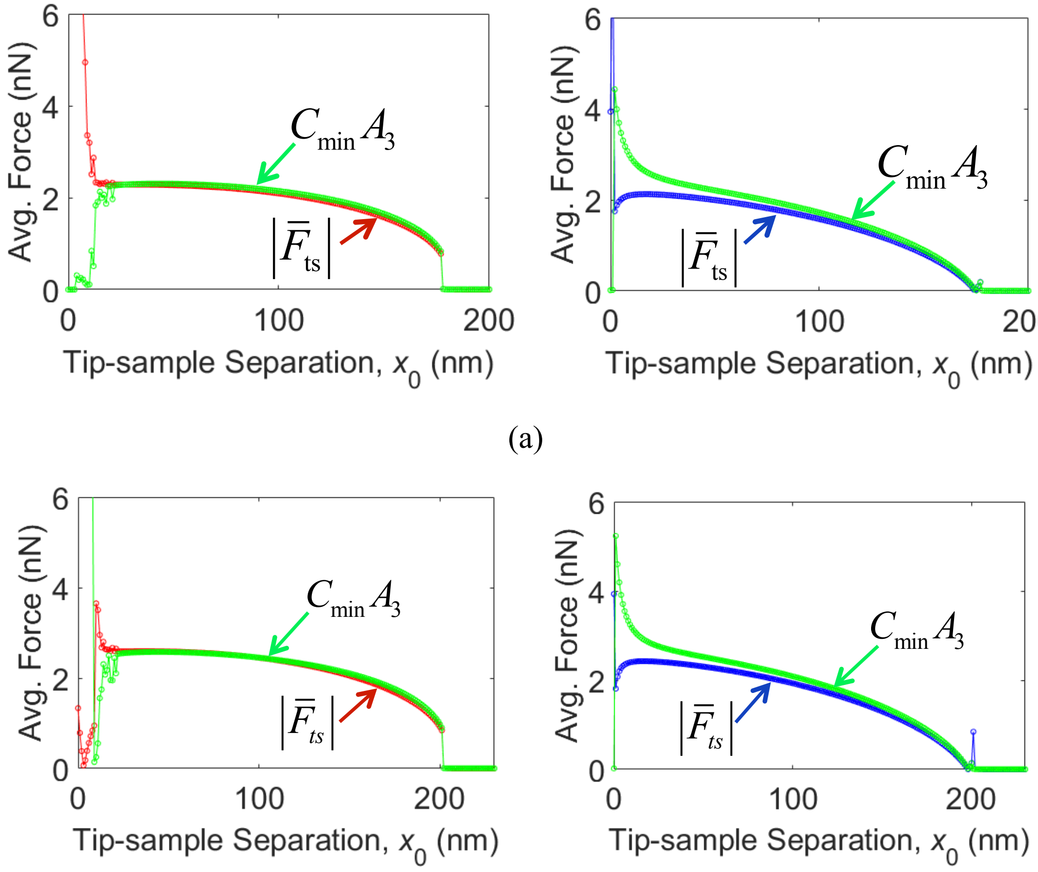

(a)

(b)

*Figure 3.9. Comparison of the average tip-sample interaction force,* $\left|\bar{F}_{\mathrm{ts}}\right|$*, and* $C_{\min} A_3$ *as functions of the static tip-sample distance. Results are shown for the LDPE sample (left column) and the PS sample (right column) at a base excitation amplitude of (a)* $y_0 = 0.91\, nm$*, and (b)* $y_0 = 1.02\, nm$*. The normalized drive frequency is* $\Omega_d = 0.9995$.

### 3.4 Computational study of a 1:2 cantilever, 1:3 cantilever and 1:3.5 cantilever

In this section, I computationally study the performance of three different multi-paddle cantilever designs; namely, a 1:2 cantilever, a 1:3 cantilever and a 1:3.5 cantilever. The 1:2 and 1:3 cantilevers are designed to support a 1:2 and 1:3 internal resonance, respectively, whereas the 1:3.5 cantilever represents the off-resonance case. To compare the efficacy of the 1:2 and 1:3 internal resonances for high frequency enhancement, energy transfer from the directly excited fundamental harmonic to higher harmonics will be studied. Indeed, for each of the cantilever designs, higher harmonics will be present in the inner paddle response due to the nonlinear tip-sample interaction force. Further, for a general 1:*n* cantilever design where *n* is an integer, the $n^{\text{th}}$ harmonic will coincide with the second (or out-of-phase) eigenfrequency and thereby provide excitation to the second vibrational mode. By indirectly exciting the second mode, in addition to directly driving the fundamental mode, a steady-state resonant response at the second eigenfrequency is induced, as well as another at the first eigenfrequency (i.e., the excitation frequency). This is precisely the mechanism of intentional internal resonance, and I will measure the effectiveness of a 1:*n* internal resonance by the energy transferred to the $n^{\text{th}}$ harmonic in the inner paddle response.

To this end, the energy partition among different harmonics is computed in both the base cantilever and the inner paddle. The total energy in the system is the sum of its kinetic energy, $T(t)$, and its potential energy, $V(t)$, and is given by

$$T(t)+V(t)=\frac{1}{2}m_1\dot{x}_1^2+\frac{1}{2}m_2\dot{x}_2^2+\frac{1}{2}k_1(x_1-x_d)^2+\frac{1}{2}k_2(x_1-x_2)^2 \tag{3.4}$$

or, equivalently,

$$T(t)+V(t)=E_1(t)+E_2(t) \tag{3.5}$$

where $E_1$(t) is the total energy in the base cantilever and $E_2$(t) the total energy in the inner paddle:

$$E_1(t)=\frac{1}{2}m_1\dot{x}_1^2+\frac{1}{2}k_1(x_1-x_d)^2+\frac{1}{4}k_2(x_1-x_2)^2 \tag{3.6}$$

$$E_2(t)=\frac{1}{2}m_2\dot{x}_2^2+\frac{1}{4}k_2(x_1-x_2)^2 \tag{3.7}$$

Furthermore, the displacements of the base cantilever and inner paddle can be decomposed into their 1st, 2nd and 3rd harmonic components and the higher frequency remainders as

$$x_1(t)=\eta_1(t)+\eta_2(t)+\eta_3(t)+r_1(t), \quad x_2(t)=\xi_1(t)+\xi_2(t)+\xi_3(t)+r_2(t) \tag{3.8}$$

where $\eta_i$ ($\xi_i$), $i$ = 1,2,3 are the three leading harmonics of the base cantilever (inner paddle) response and $r_1$ ($r_2$) is the higher frequency remainder of the displacement of the base cantilever (inner paddle) response. The 1st, 2nd, and 3rd harmonic components are given by

$$\eta_1(t)=B_1\sin(\omega_{\mathrm{d}}t+\psi_1), \quad \eta_2(t)=B_2\sin(2\omega_{\mathrm{d}}t+\psi_2), \quad \eta_3(t)=B_3\sin(3\omega_{\mathrm{d}}t+\psi_3) \tag{3.9}$$

$$\xi_1(t)=A_1\sin(\omega_{\mathrm{d}}t+\phi_1), \quad \xi_2(t)=A_2\sin(2\omega_{\mathrm{d}}t+\phi_2), \quad \xi_3(t)=A_3\sin(3\omega_{\mathrm{d}}t+\phi_3) \tag{3.10}$$

where $B_i$ ($A_i$), $i$ = 1,2,3 are the amplitudes of the first three harmonics of the base cantilever (inner paddle) response and $\psi_i$ ($\phi_i$) are the phases of the first three harmonics with respect to the excitation in the base cantilever (inner paddle). By substituting (3.8) into (3.6), the energy of the base cantilever can be decomposed into energy in the 1st harmonic, $E_1^1$; energy in the 2nd harmonic, $E_1^2$; energy in the 3rd harmonic, $E_1^3$; and the higher frequency energy remainder, $E_1^r$, as

$$E_1(t)=E_1^1(t)+E_1^2(t)+E_1^3(t)+E_1^r(t) \tag{3.11}$$

$$E_1^1(t)=\frac{1}{2}m_1\dot{\eta}_1^2+\frac{1}{2}k_1(\eta_1-x_{\mathrm{d}})^2+\frac{1}{4}k_2(\eta_1-\xi_1)^2 \tag{3.12}$$

$$E_1^i(t)=\frac{1}{2}m_1\dot{\eta}_i^2+\frac{1}{4}k_2(\eta_i-\xi_i)^2, \quad i=2,3 \tag{3.13}$$

$$E_1^r(t)=E_1(t)-E_1^1(t)-E_1^2(t)-E_1^3(t) \tag{3.14}$$

Similarly, by substituting (3.8) into (3.7), the energy in the inner paddle can be decomposed into energy in the 1st, 2nd, and 3rd harmonics and the remaining energy, given by

$$E_2(t)=E_2^1(t)+E_2^2(t)+E_2^3(t)+E_2^r(t) \tag{3.15}$$

$$E_2^1(t)=\frac{1}{2}m_2\dot{\xi}_1^2+\frac{1}{4}k_2(\eta_1-\xi_1)^2 \tag{3.16}$$

$$E_2^i(t)=\frac{1}{2}m_2\dot{\xi}_i^2+\frac{1}{4}k_2(\eta_i-\xi_i)^2, \quad i=2,3 \tag{3.17}$$

$$E_2^r(t)=E_2(t)-E_2^1(t)-E_2^2(t)-E_2^3(t) \tag{3.18}$$

The base cantilever and inner paddle participate in both the fundamental (in-phase) mode and the second (out-of-phase) mode, which means energy transfer to the *n*th harmonic resulting from a 1:*n* internal resonance will occur in the base cantilever as well as the inner paddle. However, the focus is on energy partition in the inner paddle because the inner paddle plays a significantly larger role in the second mode than the base cantilever due to the inner paddle’s relatively small mass. Specifically, regarding the eigenvector associated with the second mode, the component corresponding to the inner paddle’s participation is nearly an order of magnitude larger than the component corresponding to the base cantilever’s participation. As a result, the amplitude of the *n*th harmonic in the inner paddle is much larger than the amplitude of the *n*th harmonic in the base cantilever, making the response of the inner paddle a better candidate for measurement. For this reason, attention is restricted to the response of the inner paddle.

The energy in the 1st, 2nd, and 3rd harmonics and the remaining energy versus the static tip-sample separation, $x_0$, are shown in Fig. 3.10 for the 1:2, 1:3 and 1:3.5 cantilevers. In this study, I numerically simulated the steady-state responses of the three different cantilevers as they approached a LDPE sample while being harmonically excited at their fundamental frequencies. This was achieved using the same procedure that was used to generate the dynamic force curves shown in Figs. 3.3 and 3.7, a description of which is provided in Section 3.3. Then, equations (3.15) through (3.18) were used to compute the energy decomposition among the different harmonics. The system parameters used for the simulations are listed in Table 3.1. The excitation amplitude was fixed at $y_0 = 0.35$ nm for the 1:2 cantilever and $y_0 = 0.39$ nm for the 1:3 cantilever and 1:3.5 cantilever. The excitation amplitudes were chosen so that the total energy in the system during steady state was the same for all three cantilevers.

As expected, energy transfer to higher harmonics is present in all three cantilevers due to the nonlinear tip-sample interaction, but the realization of internal resonance in the 1:2 cantilever and 1:3 cantilever amplifies energy transfer to the 2nd and 3rd harmonics, respectively. Indeed, the energy in the 2nd harmonic is largest for the 1:2 cantilever (Fig. 3.10b) whereas the energy in the 3rd harmonic is largest for the 1:3 cantilever (Fig. 3.10c). Furthermore, the remaining energy is largest for the 1:3.5 cantilever (Fig. 3.10d), which is the result of this cantilever's inability to transfer energy from the remaining higher harmonics to the harmonic coinciding with the second eigenfrequency. While both the 1:2 cantilever and 1:3 cantilever notably outperform the 1:3.5 cantilever due to internal resonance, the 1:2 cantilever appears to transfer energy to the 2nd harmonic more efficiently than the 1:3 cantilever transfers energy to the 3rd harmonic. This is evident by the fact that the remaining energy is lowest for the 1:2 cantilever, and by also noting that the energy in the 3rd harmonic for the 1:3 cantilever is lower than the energy in the 2nd harmonic for the 1:2 cantilever.

The enhanced performance of the 1:2 cantilever as compared with the 1:3 cantilever can be attributed to the lack of anti-symmetry in the force-displacement curve of the tip-sample interaction (see Fig. 3.4). Regarding higher harmonic generation in nonlinear dynamical systems under harmonic excitation, it is well known that, typically, harmonics corresponding to higher frequencies have smaller amplitudes. A notable exception is when the force-displacement curve of the nonlinearity exhibits anti-symmetry. In this case, the nonlinear forcing contains no even Fourier components in the frequency domain and, therefore, there is no presence of even harmonics in the response. For such systems, e.g., in systems with cubic nonlinearity, the third harmonic will generally be the harmonic with the largest amplitude. However, if the external forcing exhibits asymmetry, the second harmonic is generally expected to be the dominant higher harmonic in the response. Referring back to Fig. 3.4, it is clear that the force-displacement curve of the sole source of nonlinearity is asymmetric indicating that, in general, the second harmonic should have the largest amplitude of all the higher harmonics. This means that the 2nd harmonic is more capable of transferring energy via an internal resonance than any other harmonic, hence the 1:2 cantilever's superior performance shown in Fig. 3.10.

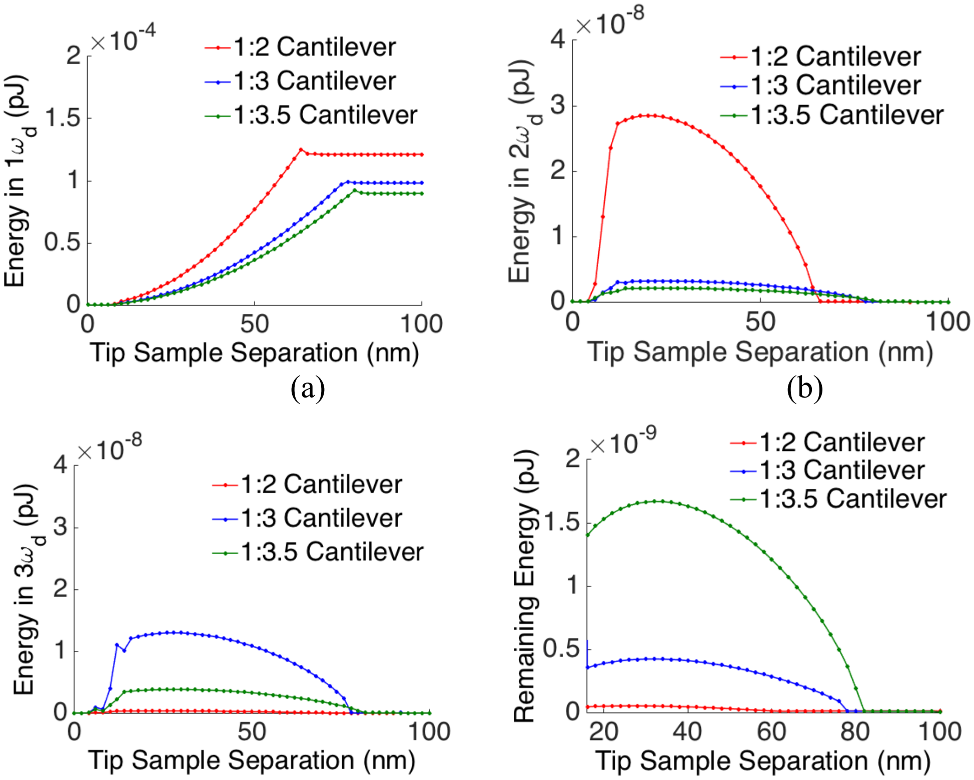

(a) (b)

(c) (d)

*Figure 3.10: Computational energy partition within the inner paddle among the first three harmonics.*

As a next step, quantities that are directly measured during dynamic AFM operation are compared for the 1:2 cantilever, 1:3 cantilever and 1:3.5 cantilever. In Fig.3.11, the amplitudes at the 1st harmonic (Fig. 3.11a), 2nd harmonic (Fig. 3.11b) and 3rd harmonic (Fig. 3.11c) are plotted versus static tip-sample separation for all three cantilevers. Similarly, the phases with respect to the base excitation at the 1st harmonic (Fig. 3.11d), 2nd harmonic (Fig. 3.11e) and 3rd harmonic (Fig. 3.11f) are plotted versus static tip-sample separation, for each cantilever. Due to the enhanced efficacy of the 1:2 internal resonance as compared with the 1:3 internal resonance, the amplitude of the 2nd harmonic for the 1:2 cantilever is significantly larger than the amplitude of the 3rd harmonic for the 1:3 cantilever. This means that the SNR for the higher harmonic will be greater for the 1:2 cantilever than the 1:3 cantilever. The significance of the improved SNR is that it results in enhanced sensitivity to compositional information.

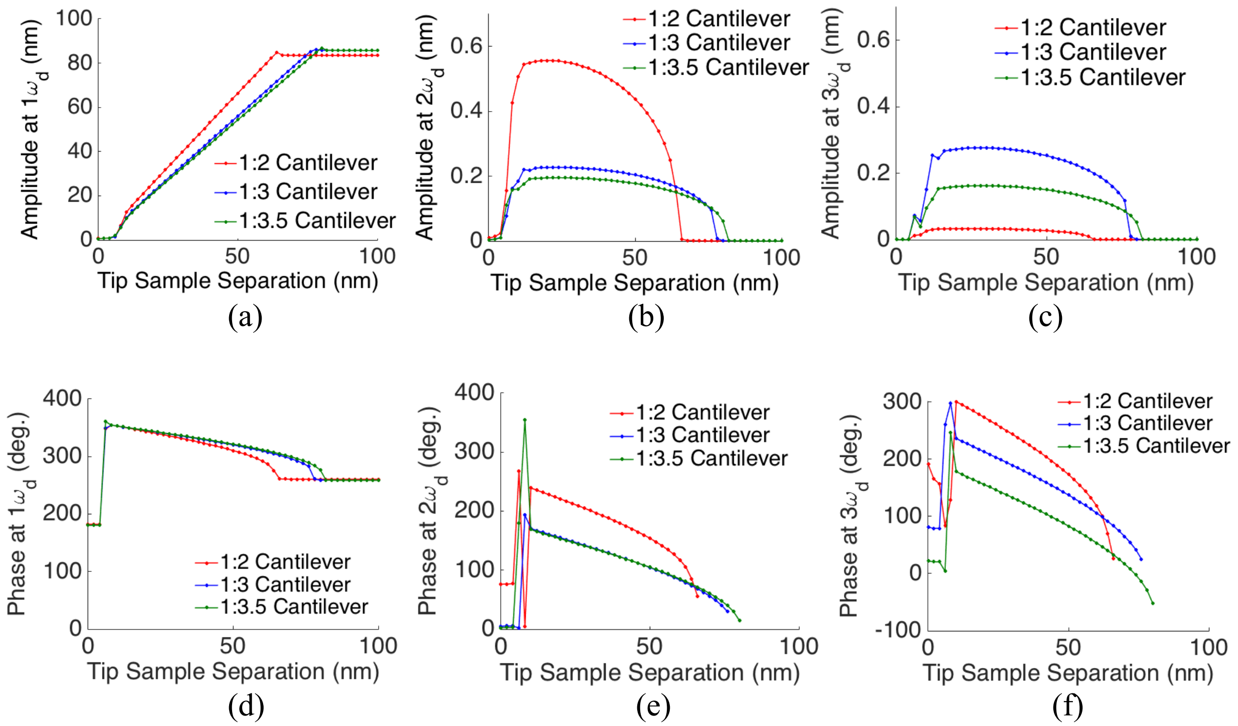

(a) (b) (c)

(d) (e) (f)

*Figure 3.11: Computational force curves of the inner paddle.*

As discussed in detail in Section 3.3, it is well known that the nonlinear tip-sample interaction in AFM may result in the co-existence of two solutions: An “upper branch” solution associated with a large response amplitude and repulsive averaged tip-sample interaction, and a “lower branch” solution associated with a relatively small response amplitude and attractive averaged tip-sample interaction. Along with the phase of the first harmonic, the higher harmonic amplitude and phase can distinguish between the upper and lower branch selection due to a difference in the slopes of the corresponding force curves. In other words, as $x_0$ varies, the trends in the higher harmonic phase, higher harmonic amplitude and first harmonic phase are different for the lower branch solution than for the upper branch solution. In contrast, the slopes of the first harmonic amplitude versus $x_0$ are nearly identical for the two coexisting solution branches. Accordingly, the slopes of the curves shown in Figs. 3.11b – 3.11f indicate a lower branch selection due to the sample’s low stiffness (0.1GPa).

### 3.5 Experimental study of the 1:2 cantilever and the 1:3:4 cantilever

Motivated by the computational results presented in Section 3.4, the performance of a 1:2 cantilever (shown in Fig. 3.1b) and a 1:3:4 cantilever (shown in Fig. 3.12) were experimentally investigated. Specifically, the sensitivity force curves were experimentally obtained for each cantilever interacting with a LDPE specimen. The LDPE specimen is part of the two-component polymeric sample mounted on a glass slide as shown in Fig. 3.2. Again, the circular island contains relatively compliant LDPE with elastic modulus of ~0.1GPa whereas the surrounding material is relatively stiff polystyrene (PS) with elastic modulus of ~2GPa. Using a MFP-3D Infinity AFM system from Asylum, the response was measured at two frequencies simultaneously: the excitation frequency, $\omega_{\mathrm{d}}$, and the amplified (via internal resonance) higher harmonic. Each cantilever was driven at its fundamental eigenfrequency with a fixed base excitation amplitude ($y_0 = 0.35$ nm for the 1:2 cantilever and $y_0 = 0.39$ nm for the 1:3:4 cantilever).

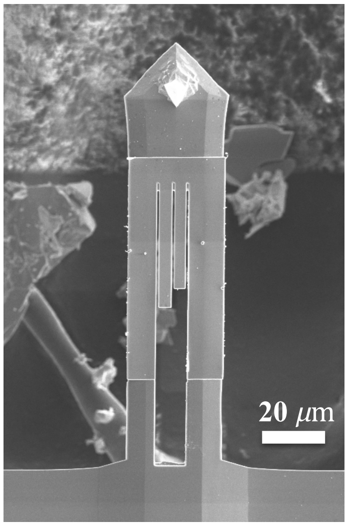

*Figure 3.12: (a) SEM image of a 1:3:4 IR cantilever and (b) an AFM image of a PS sample containing an inner LDPE island.*

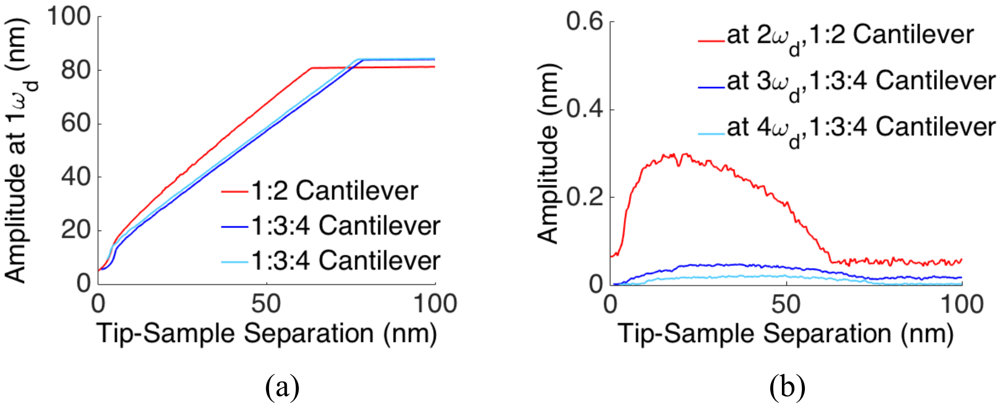

*Figure 3.13: Experimental force curves of the (a) 1st harmonic and (b) nth harmonic for a 1:n IR.*

Fig. 3.13 shows the variation in the experimental amplitude of the first harmonic and higher harmonic with respect to the tip-sample separation. For the 1:2 cantilever, the response was measured at $\omega_d$ and $2\omega_d$ (red curve in Fig. 3.13); and for the 1:3:4 cantilever, the response was measured at $\omega_d$, $3\omega_d$, and $4\omega_d$. Since the "bi-modal function" using the MFP-3D Infinity allows for the measurement of only two harmonics at once, the 1:3:4 cantilever was characterized with two separate experimental force curves: one in which the response was measured at $\omega_d$ and $3\omega_d$ (dark blue curve in Fig. 3.13) and one in which the response was measured at $\omega_d$ and $4\omega_d$ (light blue curve in Fig. 3.13). The measurement of the 1:3:4 cantilever at $3\omega_d$ illustrates the efficacy of a 1:3 internal resonance, whereas the measurement at $4\omega_d$ demonstrates the efficacy of a 1:4 internal resonance. In Fig. 3.13, it is clear that the 1:2 cantilever's second harmonic response is significantly larger than the 1:3:4 cantilever's 3rd and 4th harmonic responses while the first harmonic responses of both cantilevers are nearly identical. These results coincide well with the computational force curves shown in Fig. 3.11, providing some experimental verification of the computational study presented in Section 3.4. In particular, this result experimentally validates the prediction that, for a cantilever system designed with a 1:$n$ internal resonance, energy transfer to the $n^{\text{th}}$ harmonic is larger for $n = 2$ than for $n = 3, 4$. It should be noted that the higher harmonic energy transfer in the 1:3:4 cantilever is partitioned among two harmonics via internal resonance rather than one harmonic as it is for the 1:2 cantilever. However, since the 2nd harmonic amplitude for the 1:2 cantilever is nearly an order of magnitude larger than the 3rd and 4th harmonic amplitudes of the 1:3:4 cantilever, the aforementioned conclusions are still valid. As discussed in detail in Section 3.4, the enhanced efficacy of the 1:2 IR as compared to the 1:3 IR can be attributed to asymmetry in the tip-sample interaction force.

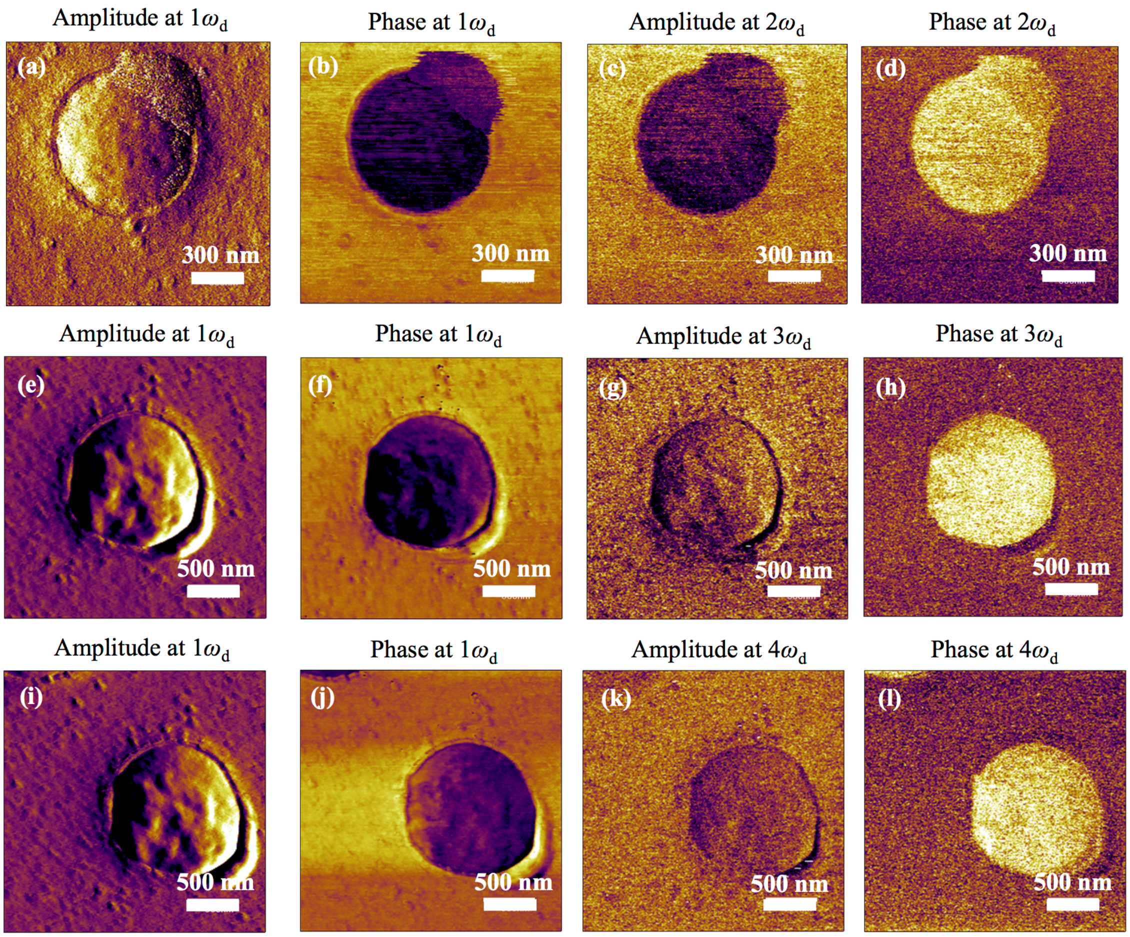

*Figure 3.14: AFM images of a blended PS-LDPE sample using the (a-d) 1:2 IR of the 1:2 cantilever, (e-h) 1:3 IR of the 1:3:4 cantilever and the 1:4 IR of the 1:3:4 cantilever. Beginning at the left, the first column is the amplitude of the 1st harmonic, the second column is the amplitude of nth harmonic for a 1:n IR, the third column is the phase of the 1st harmonic and the fourth column is the phase of the nth harmonic for 1:n IR. Note that the color scale for each image is different.*

To evaluate the cantilever systems in actual dynamic mode AM-AFM, three different AFM measurements were taken on a polystyrene (PS) sample with an inner low-density polyolefin elastomer island (LDPE) as shown in Fig. 3.14. In Figs. 3.14a-3.14d are the results from one

AFM scan in which the amplitudes and phases at $\omega_\mathrm{d}$ and $2\omega_\mathrm{d}$ were measured using the 1:2 cantilever; in Figs. 3.14e-3.14h are the results from a second scan in which the amplitudes and phases at $\omega_\mathrm{d}$ and $3\omega_\mathrm{d}$ were measured using the 1:3:4 cantilever; and in Figs. 3.14i-3.14l are the results from a third scan in which the amplitudes and phases at $\omega_\mathrm{d}$ and $4\omega_\mathrm{d}$ were measured using the 1:3:4 cantilever. Since the focus is on qualitative comparisons, the color scales for each image are omitted.

Considering first the amplitudes and phases measured at $\omega_\mathrm{d}$, the quality of the images from all three scans look similar. This is to be expected since $\omega_\mathrm{d}$ is the directly excited frequency which coincides with the resonant frequency of the fundamental eigenmode. As a result, a large resonant response is elicited from the fundamental mode, at $\omega_\mathrm{d}$, leading to clear images for all three scans. In contrast, the higher harmonic (that coincides with the out-of-phase mode) is not *directly* excited; rather, it is *indirectly* excited via internal resonance. The effectiveness of a 1:*n* internal resonance is what determines the strength of the implicit excitation at $n\omega_\mathrm{d}$ and the resulting response at $n\omega_\mathrm{d}$. Due to the enhanced efficacy of the 1:2 internal resonance as compared with the 1:3 internal resonance and 1:4 internal resonance, the amplitude and phase images measured at $2\omega_\mathrm{d}$ with the 1:2 cantilever show a distinct color change between two dissimilar materials with higher SNR. Contrary to the 1:2 resonance, a smaller energy transfer to $3\omega_\mathrm{d}$ and $4\omega_\mathrm{d}$ in the 1:3 and 1:4 internal resonances results in loss of material sensitivity in the higher harmonic amplitude images.

### 3.6. Performance of the 1:2 cantilever in AFM scans of bacteria cells

The phase of a conventional AFM cantilever has been used to construct qualitative compositional maps. In section 3.3 the behavior of a 1:3 cantilever was investigated and the third harmonic amplitude and phase were found to be sensitive to sample properties as well. It was shown there that branch selection is detected by the 1st harmonic phase and higher harmonic observables, which is the basis for compositional sensitivity. The branch selection reveals compositional information because, interestingly, the domains of attraction for the coexisting solutions are influenced by the material properties of the sample (Potekin et al., 2017; Cho et al., 2012; García and San Paulo, 2000; Raman et al., 2008; Stark, 2010).

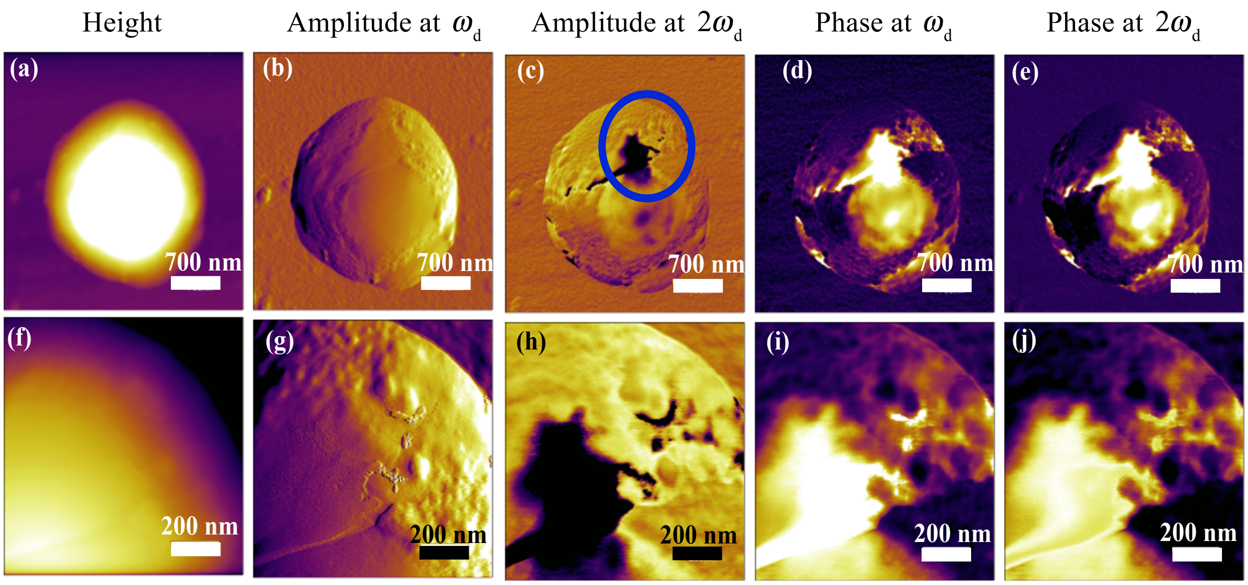

*Figure 3.15: AFM Images of a cyanobacteria cell that has not been exposed to cyanophage (control sample) using the 1:2 cantilever; (a-e) show a full scale image of a cell and (f-j) show a zoomed in image near the outer edge of the cell. Beginning at the left, the first column is the height data, the second column is the amplitude of 1st harmonic, the third column is the amplitude of the 2nd harmonic, the fourth column is the phase of the 1st harmonic and the fifth column is the phase of the 2nd harmonic. Notice that compositional differences are detected with the amplitude of the 2nd harmonic and the phases of the 1st and 2nd harmonics that are not detected with the height measurement nor the amplitude of the 1st harmonic.*

Motivated by these results, a 1:2 cantilever was used to image *Microcutis aeruginosa* cyanobacteria taken from Lake Erie, and the results are shown in Fig. 3.15. Water samples were originally collected from western Lake Erie to isolate M. aeruginosa and (named as Ma-LEP). After isolation, cyanophage were concentrated by Centriprep® Centrifugal Filters YM-50. The propagated cyanophage (1 ml) or autoclaved cyanophage (control) was inoculated into 300 ml of M. aeruginosa culture and incubated at room temperature under light/dark conditions for 2 weeks, and samples were collected at designated time intervals. Several drops of the culture were immobilized onto gelatin-coated mica, and after 10 minutes they were washed and air-dried and subjected to AFM imaging. Figs. 3.15a – 3.15e correspond to a single measurement of the cyanobacteria cell (control sample) constructed with (a) the height data obtained from the feedback controller error of $\omega_\mathrm{d}$, (b) the amplitude at $\omega_\mathrm{d}$, (c) the amplitude at $2\omega_\mathrm{d}$, (d) the phase at $\omega_\mathrm{d}$, and (e) the phase at $2\omega_\mathrm{d}$. Below this row of images, Figs. 3.15f – 3.15j show a zoomed-in view of the bacteria cell indicated by the blue circle in Fig. 3.15c. The images in Figs. 3.15f – 3.15j were each constructed with the same metric as the image directly above them.

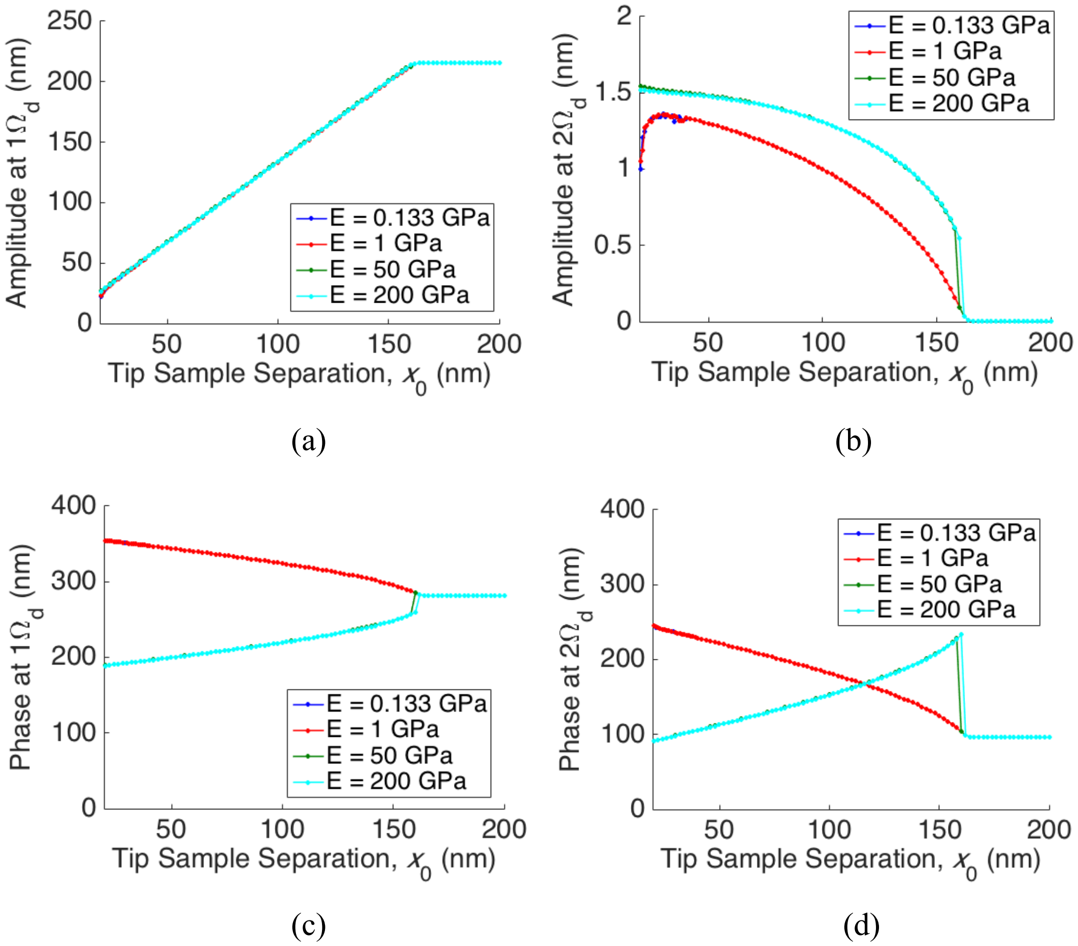

(a) (b)

(c) (d)

*Figure 3.16: Computational force curves corresponding to the tip approaching the sample; (a) amplitude of the 1st harmonic versus the static tip-sample separation, (b) amplitude of the 2nd harmonic versus the static tip-sample separation, (c) phase of the 1st harmonic versus the static tip-sample separation and (d) phase of the 2nd harmonic versus the static tip-sample separation. Note that the curves corresponding to E=1GPa nearly cover up the curves corresponding to E=0.133GPa and similarly, the curves corresponding to E=200GPa nearly cover up the curves correspond E=50GPa.*

Interestingly, the 2nd harmonic amplitude, 2nd harmonic phase and 1st harmonic phase reveal stark contrast in parts of the bacteria that are neither detected by the 1st harmonic amplitude nor the height data. Since the higher harmonic amplitude and phase are known to deliver compositional information, whereas the height and first harmonic amplitude provide topographical information, these regions of stark contrast likely indicate a change in material properties of the bacteria cell. To verify this interpretation, compositional force curves of the 1:2 cantilever approaching samples of varying stiffness were constructed and are shown in Fig. 3.16. Specifically, the variation of the 1st harmonic amplitude with respect to tip-sample separation (Fig. 3.16a), 2nd harmonic amplitude with respect to tip-sample separation (Fig. 3.16b), 1st harmonic phase with respect to tip-sample separation (Fig. 3.16c) and 2nd harmonic phase with respect to tip-sample separation (Fig. 3.16d) are shown for four different Young's modulus values, namely 0.133GPa, 1GPa, 50GPa, and 200GPa, while the attractive force is the same for all cases. The excitation amplitude was held fixed at 0.9nm for all simulations.

The force curves corresponding to the 1st harmonic amplitude appear to be nearly identical for the four different stiffness values considered. In contrast, the force curves corresponding to the 2nd harmonic amplitude, 1st harmonic phase and 2nd harmonic phase display different trends for $E = 0.133\text{GPa}$ and $E = 1\text{GPa}$ than for $E = 50\text{GPa}$ and $E = 200\text{GPa}$. Following the discussion in Section 3.3, the trends in the force curves of the 2nd harmonic amplitude, 1st harmonic phase and 2nd harmonic phase for $E = 0.133\text{GPa}$ and $E = 1\text{GPa}$ indicate a lower branch selection, whereas the trends for $E = 50\text{GPa}$ and $E = 200\text{GPa}$ indicate an upper branch selection. The difference in branch selection for relatively compliant samples versus stiff samples is due to the influence that the Young's modulus of the sample has on the domains of attraction for each solution (Cho et al., 2012; García and San Paulo, 2000; Raman et al., 2008; Stark, 2010). For samples with low Young's moduli, the domain of attraction giving rise to the lower solution branch dominates the phase space. As the Young's modulus of the sample increases, the lower branch's domain of attraction shrinks while the upper branch's domain of attraction expands until, for large Young's moduli, the upper branch becomes the dominant attractor. It is interesting that the two force curves belonging to the lower branch corresponding to different stiffness values $E = 0.133\text{GPa}$ and $E = 1\text{GPa}$, look almost identical. This is because, on the lower branch, the tip does not actually contact the sample (in the repulsive regime); rather, it interacts with the sample via attractive forces. Hence, the sample's stiffness does not have a large effect on the resulting dynamics. In contrast, on the upper branch, the tip-sample interaction is dominated by the Hertzian contact force, which indeed depends on the sample's stiffness. However, as the Young's modulus increases, the cantilever's response converges and, for this reason, the two force curves belonging to the upper branch corresponding to $E = 50\text{GPa}$ and $E = 200\text{GPa}$ are also very similar. Further, the converged 1st harmonic response amplitude on the upper branch is similar to the 1st harmonic response amplitude on the lower branch and, for this reason, no difference is observed in the force curves corresponding to the 1st harmonic amplitude for all four stiffness values considered. Variations in upper branch force curves due to changes in Young's modulus are explored in Section 3.7.

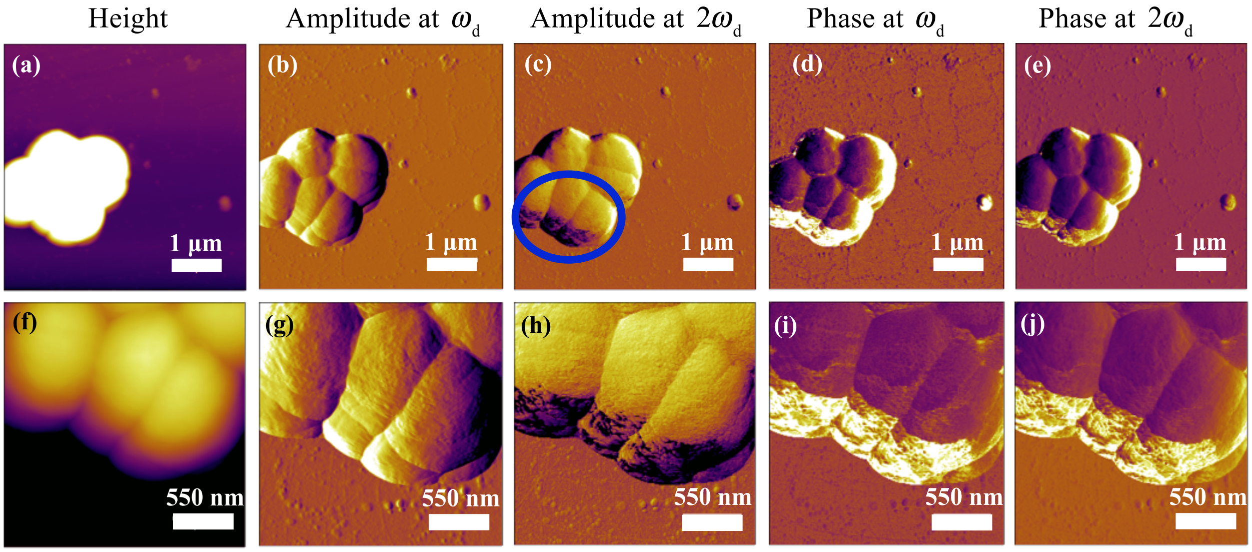

*Figure 3.17: AFM Images of another cyanobacteria cell that has not been exposed to cyanophage (control sample) using the 1:2 cantilever; (a-e) show a full-scale image of a cell and (f-j) show a zoomed in image near the outer edge of the cell. Beginning at the left, the first column is the height data, the second column is the amplitude of 1st harmonic, the third column is the amplitude of the 2nd harmonic, the fourth column is the phase of the 1st harmonic and the fifth column is the phase of the 2nd harmonic. Notice that compositional differences are detected with the amplitude of the 2nd harmonic and the phases of the 1st and 2nd harmonics that are not detected with the height measurement nor the amplitude of the 1st harmonic.*

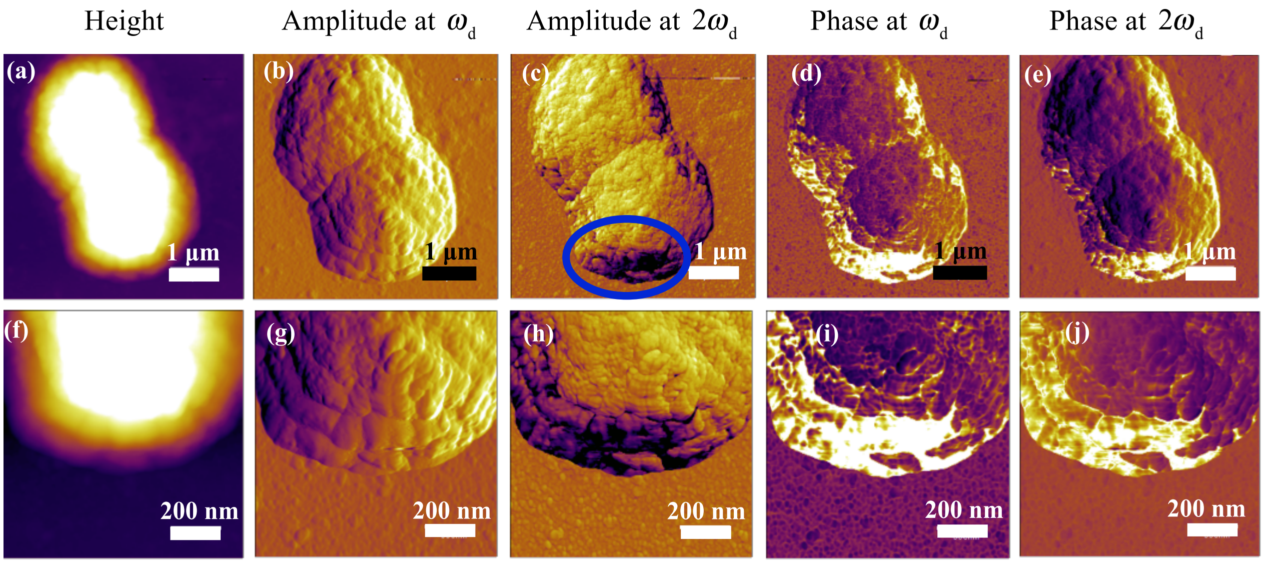

*Figure 3.18: AFM Images of a cyanobacteria cell that has been exposed to cyanophage for 6 hours using the 1:2 cantilever; (a-e) show a full scale image of the cell and (f-j) show a zoomed in image near the outer edge of the cell. Beginning at the left, the first column is the height data, the second column is the amplitude of 1st harmonic, the third column is the amplitude of the 2nd harmonic, the fourth column is the phase of the 1st harmonic and the fifth column is the phase of the 2nd harmonic. Notice that compositional differences are detected with the amplitude of the 2nd harmonic and the phases of the 1st and 2nd harmonics that are not detected with the height measurement nor the amplitude of the 1st harmonic.*

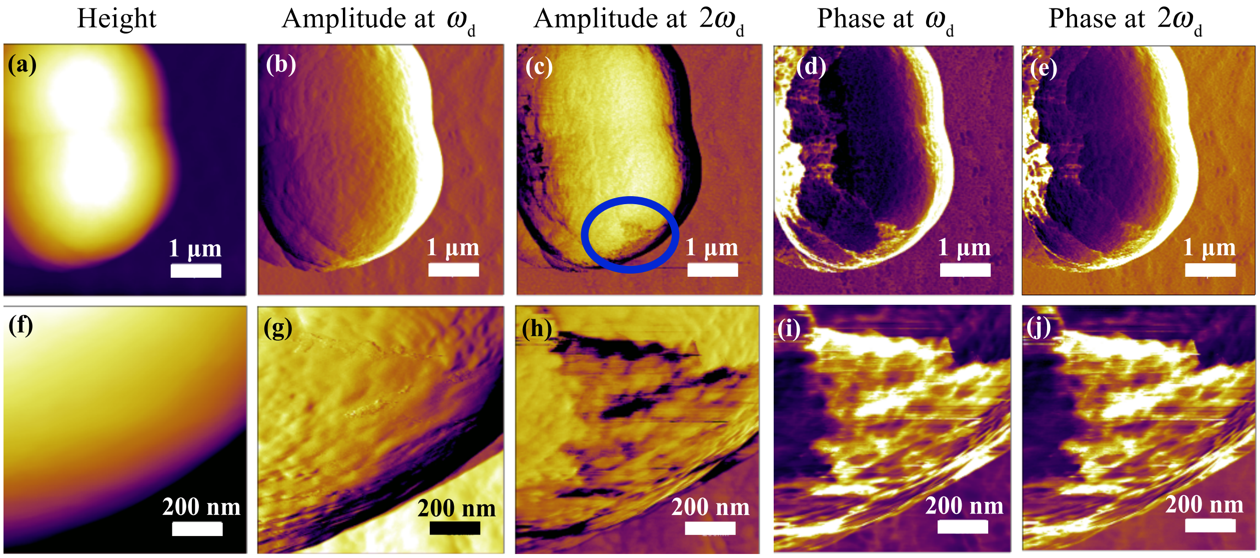

*Figure 3.19: AFM Images of another cyanobacteria cell that has been exposed to cyanophage for 6 hours using the 1:2 cantilever; (a-e) show a full scale image of the cell and (f-j) show a zoomed in image near the outer edge of the cell. Beginning at the left, the first column is the height data, the second column is the amplitude of 1*$^{st}$ *harmonic, the third column is the amplitude of the 2*$^{nd}$ *harmonic, the fourth column is the phase of the 1*$^{st}$ *harmonic and the fifth column is the phase of the 2*$^{nd}$ *harmonic. Notice that compositional differences are detected with the amplitude of the 2*$^{nd}$ *harmonic and the phases of the 1*$^{st}$ *and 2*$^{nd}$ *harmonics that are not detected with the height measurement nor the amplitude of the 1*$^{st}$ *harmonic.*

The computational force curves shown in Fig. 3.16 suggest that the sharp contrast in the cyanobacteria AFM scans that appear in the images constructed with the amplitude at $\omega_d$, phase at $2\omega_d$ and phase at $\omega_d$ but *not* in the images constructed with the amplitude at $\omega_d$ and height data, is due to variation in the cell's material properties. This pattern was observed in several other measurements of the bacteria, both before and after exposure to the cyanophage virus, that are shown in Figs. 3.17 - 3.19. To experimentally verify the interpretation that the regions of contrast correspond to distinct compositional regions in which the lower branch was selected due to relatively low Young's modulus, experimental force curves at two different points on the bacteria cell depicted in Fig. 3.15h were obtained. The points selected are indicated in Fig. 3.20d, and the corresponding force curves are shown in Figs. 3.20a – 3.20d; the blue force curves were taken at a point *inside* the region of contrast, and the red force curves were taken *outside* this region.

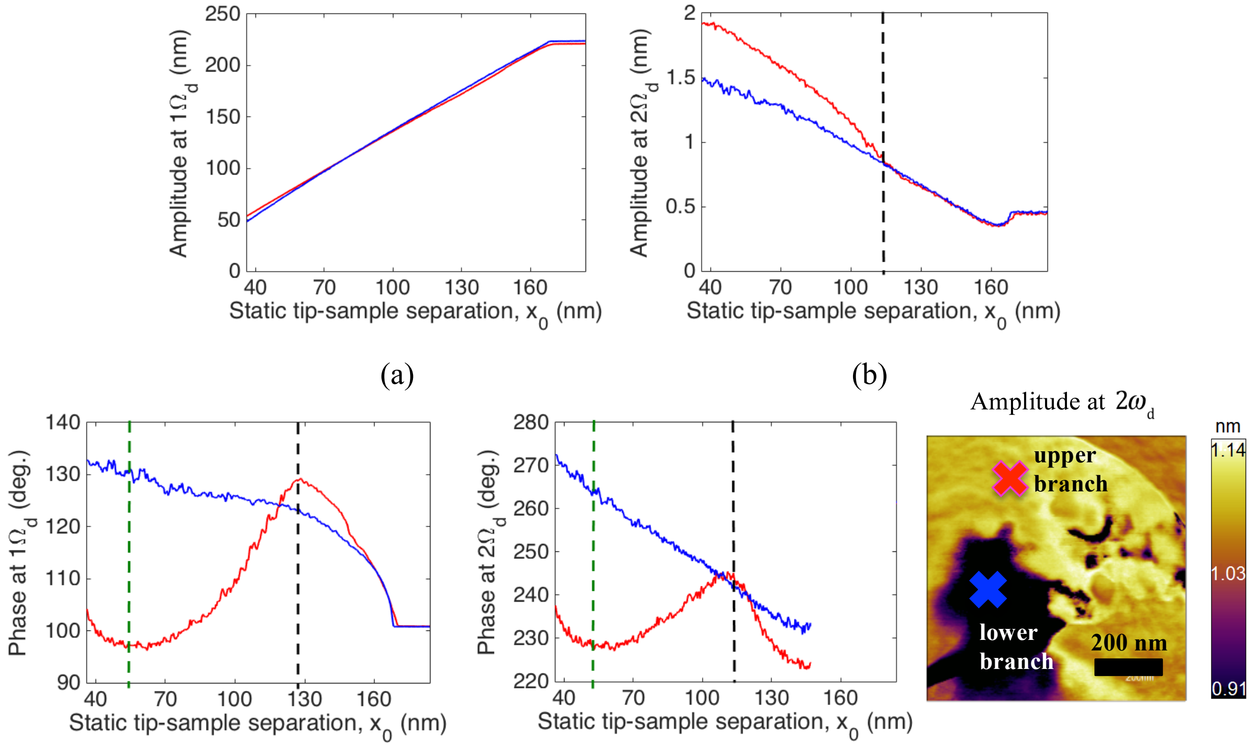

(a) (b)

(c) (d) (e)

*Figure 3.20: (a-d) Dynamic force curves taken at the locations indicated by crosses in (e). The image shown in (e) corresponds to the cyanobacteria image shown in Fig. 3.15h.*

Indeed the experimental force curves in Fig. 3.20 show a difference in branch selection among the two distinct regions shown in Fig. 15, for a set-point amplitude of 100 nm. In the force curves corresponding to a point outside the region (red curves), upon approaching the sample the lower branch is initially selected by the cantilever's dynamics, and around $x_0 = 115\text{nm}$ the response jumps to the upper branch. As with the computational force curves, the jump from the lower to upper branch is not visible in the force curves of the 1st harmonic amplitude, but it is indicated by changes in the trends of the 1st harmonic phase, 2nd harmonic phase and 2nd harmonic amplitude. A vertical black line denotes the point at which the red force curves show a switch in branch selection. The set-point amplitude used to construct the images of the cyanobacteria was 100 nm and, hence, the branch selection among the two distinct regions shown in Fig. 3.15 is different. In the region containing the point marked by a blue cross, the lower branch is selected, and in the region containing the point marked by a red cross, the upper branch is selected. Note that the 2nd harmonic phase is only plotted when the 2nd harmonic amplitude is above the noise floor because, otherwise, the phase has no meaning. Also, notice that the phases of the red force curves show another change in their trend for small $x_0$ , which is indicated by a vertical green line. In previous studies, this behavior was shown to be attributed to adhesion hysteresis, which was not accounted for in the numerical model (Tamayo & Garcia, 1997).

To summarize, in the AFM images shown in Figs. 3.15 and 3.17-3.19, the relatively dark (light) regions in the 2nd harmonic amplitude images (1st and 2nd harmonics phase images) that are neither delineated in the height nor 1st harmonic amplitude images denote relatively compliant regions of the cells for which the lower branch is selected, and the surrounding material corresponds to a relatively stiff region for which the upper branch is selected. The robustness of this experimental observation together with the computational and experimental force curves provide verification that the regions of sharp contrast correspond to a distinct compositional landscape that is only detectable by the higher harmonic and the 1st harmonic phase.

### 3.7 Sensitivity of the amplified higher harmonic to sample stiffness

In addition to influencing the domains of attraction for the upper and lower solution branches, the material properties affect the response of the cantilever on a given solution branch. In particular, the higher harmonic amplitude in the inner-paddled cantilever was shown to be directly proportional to the average force of a conservative tip-sample interaction (Section 3.3), suggesting that the higher harmonic amplitude is closely related to elastic properties such as Young's modulus.

To better understand the relationship between the compositional observables in the inner-paddled cantilever system and material properties, compositional force curves for various Young's moduli ranging from 0.1GPa to 200GPa were constructed. In Fig. 3.21, variations in the amplitudes of the first three harmonics with respect to tip-sample separation are shown for a 1:2 cantilever (Figs. 3.21a, 3.21d and 3.21g), a 1:3 cantilever (Figs. 3.21b, 3.21e and 3.21h), and a commercial cantilever for comparison (Figs. 3.21c, 3.21f and 3.21i). The corresponding variations in the phases of the first three harmonics with respect to tip-sample separation for each cantilever are shown in Fig. 3.22. The parameters of the 1:2 and 1:3 cantilevers are stated in Table 3.1, which differ only in the length of their inner paddles. The commercial cantilever considered has no inner paddle and, hence, it can be modeled as a (single) damped harmonic oscillator with an effective mass of 6.27ng, effective stiffness of 5.22N/m and damping coefficient of $2.85\times10^{-8}\mathrm{Ns/m}$. The excitation amplitude was held fixed at $y_0 = 0.35\mathrm{nm}$, and the Hamakar's constant set equal to $6\times10^{-19}\mathrm{J}$ for all simulations. For each cantilever, the amplitudes at $\omega_\mathrm{d}$ (Fig.9a-9c) are given in nm whereas the amplitudes at $2\omega_\mathrm{d}$ (Fig.10d-10f) and $3\omega_\mathrm{d}$ (Fig.10g-10i) are normalized by the free amplitude at $\omega_\mathrm{d}$ (i.e., the amplitude in the absence of the interaction with the sample), to facilitate comparison among the different cantilevers.

To construct the force curves in Figs. 3.21 and 3.22, I began with $x_0 = 10\mathrm{nm}$ and initial conditions that lie within the domain of attraction for the upper branch. After integrating the system in (3.1) well into steady state, I increased $x_0$ by 1nm, set the initial conditions for the new simulation equal to the final conditions of the previous simulation and repeated this procedure until $x_0 = 80\mathrm{nm}$. For all simulations it appears that initially, as $x_0$ increases from 10nm, the upper branch is stably tracked. The initial upper branch selection is indicated by the trends in the higher harmonic amplitudes as well as the 1st harmonic phases and higher harmonic phases. Depending on the sample stiffness and the cantilever, the solution transitions from the upper branch to the lower branch somewhere between $x_0 = 36\mathrm{nm}$ and $x_0 = 60\mathrm{nm}$. This dynamic transition is denoted by a sudden jump in each of the force curves and a change in the slopes of the higher harmonic amplitudes, 1st harmonic phases and higher harmonic phases thereafter.

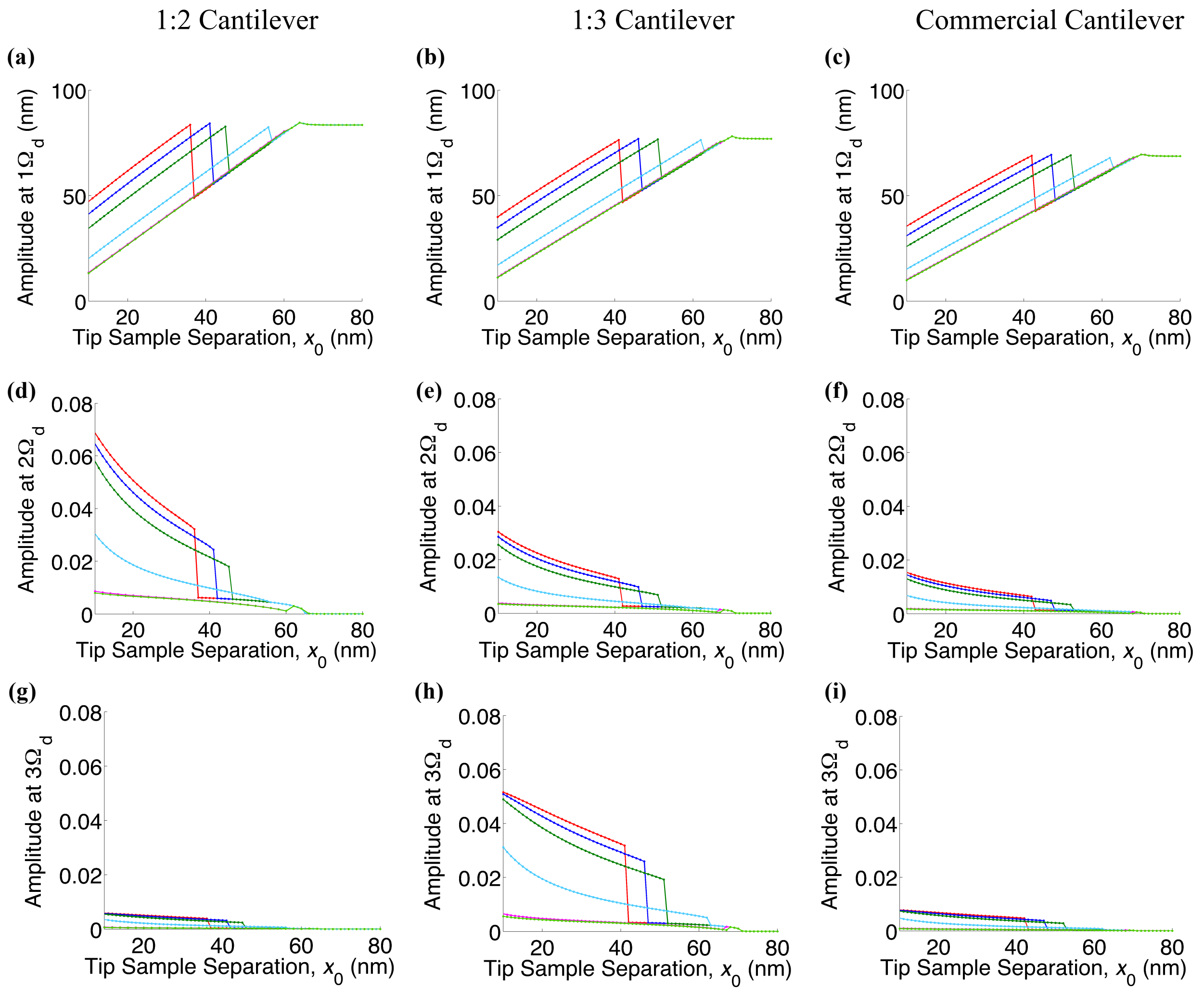

*Figure 3.21: Steady-state amplitudes versus static tip-sample separation for six different sample stiffnesses:* — *E = 0.1GPa,* — *E = 0.133GPa,* — *E = 0.2GPa,* — *E = 1GPa,* — *E = 50GPa and* — *E = 200GPa. The left column corresponds to the 1:2 cantilever, the center column to the 1:3 cantilever and the right column to a commercial cantilever. The amplitudes at $2\omega_d$ and $3\omega_d$ are normalized by the amplitude at $\omega_d$ in the absence of interaction with the sample.*

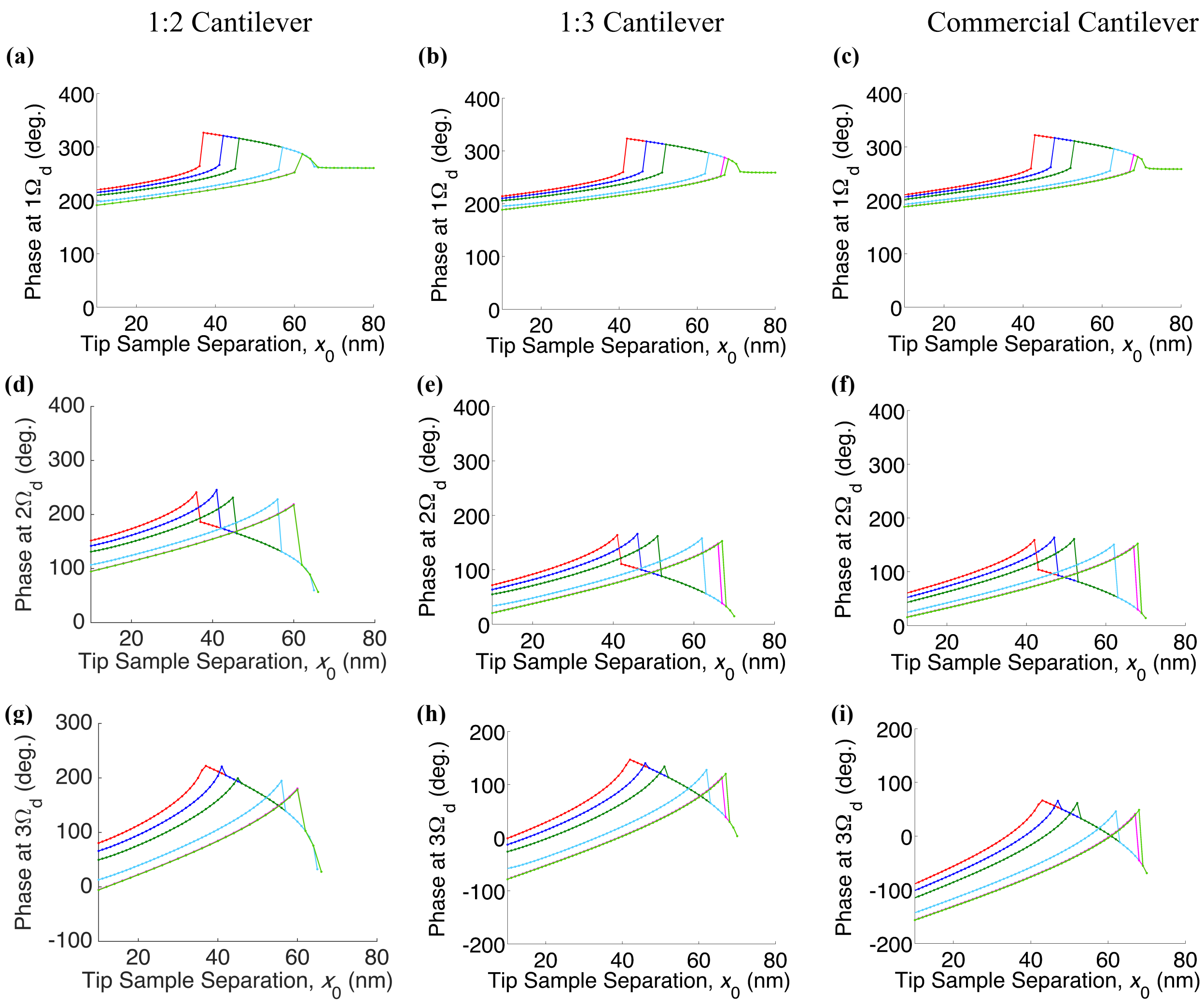

*Figure 3.22: Steady-state phases versus static tip-sample separation for six different sample stiffnesses: — E = 0.1GPa, — E = 0.133GPa, — E = 0.2GPa, — E = 1GPa, — E = 50GPa and — E = 200GPa. The left column corresponds to the 1:2 cantilever, the center column to the 1:3 cantilever and the right column to a commercial cantilever.*

The jump from the upper to lower branch occurs because, for each stiffness value, the domain of attraction of the upper branch shrinks and, eventually, disappears as $x_0$ increases. Additionally, since the domain of attraction for the upper branch expands as the stiffness increases, the value of $x_0$ at which this transition happens increases as $E$ increases. Finally, the tip loses contact with the sample around $x_0 = 64\text{nm}$ for the 1:2 cantilever and $x_0 = 70\text{nm}$ for the 1:3 cantilever and the commercial cantilever. The $x_0$ value for which the tip ceases to interact with the sample corresponds to the point at which the amplitude of the base cantilever is approximately equal to the tip-sample separation. Finally, by comparing Fig. 3.21d with Fig. 3.21h, it is clear that, for all values of $E$, the 1:2 cantilever is more effective at transferring energy to the 2nd harmonic than the 1:3 cantilever is at transferring energy to the 3rd harmonic. This further emphasizes the superiority of a 1:2 IR over a 1:3 IR in our multi-paddle cantilever design.

Notice that, in the $x_0$ region for which the lower branch is attracted, there is practically no variation in the force curves corresponding to different Young's moduli for a given cantilever. In contrast, in the region of $x_0$ corresponding to the upper branch, the response depends quite strongly on the sample's stiffness. This makes sense since, on the lower branch, the tip-sample interaction is characterized by attractive van der Waals forces whereas, on the upper branch, the repulsive Hertzian force dominates the interaction. In order to further understand the dependence of the cantilever's response on the sample's stiffness (on the upper solution branch) during AM-AFM imaging, the computational study was modified to incorporate feedback control of the first harmonic amplitude. A set point amplitude, $A_{sp}$, was selected for the first harmonic and, as $E$ increased from 0.1GPa to 200GPa, the tip-sample separation was varied until the amplitude at $\omega_d$ matched the set-point amplitude, as depicted in Fig. 3.23. This computation simulates an AM-AFM scan across a flat sample with stratified stiffness.

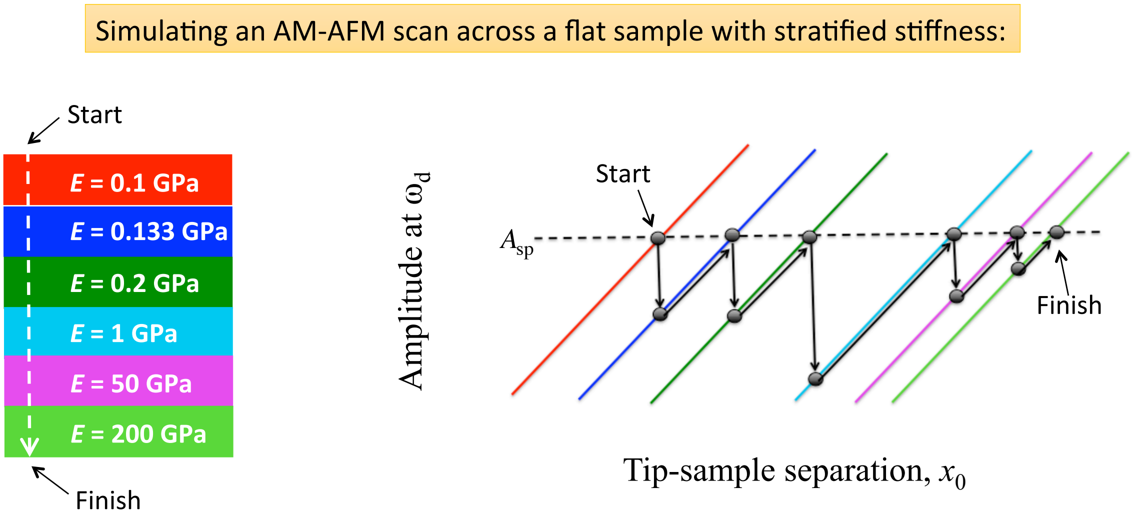

*Figure 3.23: Schematic of the feedback control simulation used to generate the results presented in Fig. 3.24. The simulation begins in the most compliant region of the sample and ends in the stiffest region.*

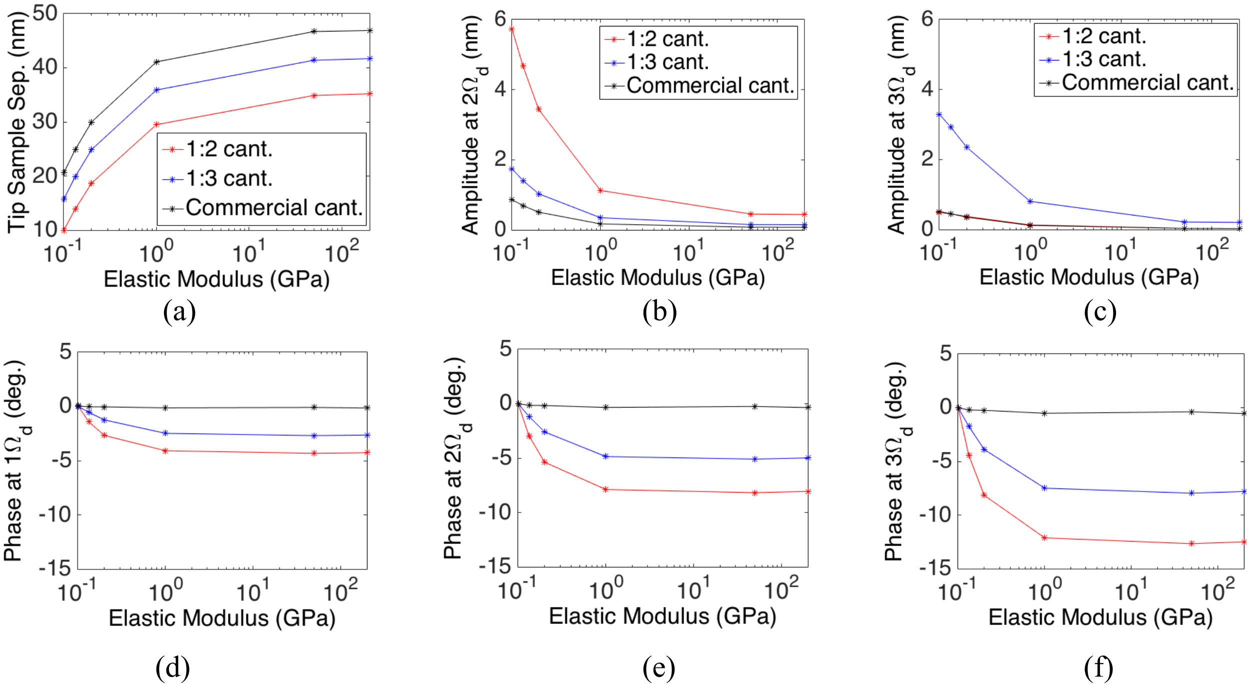

(a) (b) (c)

(d) (e) (f)

*Figure 3.24: Results from a numerical simulation of an AFM scan across a sample with varying stiffness and uniform height. Plots of the (a) tip-sample separation versus sample stiffness, (b) amplitude of the 2nd harmonic versus sample stiffness, (c) amplitude of the 3rd harmonic versus sample stiffness, (d) phase of the 1st harmonic versus sample stiffness, (e) phase of the 2nd harmonic versus sample stiffness and (f) phase of the 3rd harmonic versus sample stiffness are shown for the 1:2 cantilever, 1:3 cantilever and commercial cantilever. The phases are shifted so that the phases of all three cantilevers coincide at E = 0.1GPa, to facilitate comparison.*

In Fig. 3.24, we show the results of the 1:2 cantilever, 1:3 cantilever and commercial cantilever for a set-point amplitude of 47nm. Specifically, the $x_0$ values required to maintain 47nm at $\omega_\mathrm{d}$ (Fig.3.24a), and the corresponding amplitude at $2\omega_\mathrm{d}$ (Fig.3.24b), amplitude at $3\omega_\mathrm{d}$ (Fig.3.24c), phase at $\omega_\mathrm{d}$ (Fig.3.24d), phase at $2\omega_\mathrm{d}$ (Fig.3.24e), and phase at $3\omega_\mathrm{d}$ (Fig.3.24f) are plotted versus $E$. To facilitate comparison among the different curves in Fig.3.24, the phases have been shifted so that at $E$=0.1GPa they are equal to 0. Again, note the superior performance of the 1:2 IR as compared with the 1:3 IR in the inner-paddled cantilevers. This is evident in the fact that the amplitude at $2\omega_\mathrm{d}$ for the 1:2 cantilever is larger than the amplitude at $3\omega_\mathrm{d}$ for the 1:3 cantilever.

Furthermore, unlike the commercial cantilever, the phases (of all three harmonics) of the inner-paddled cantilevers show variation with respect to the Young's modulus even though the tip-sample interaction is conservative. For commercial cantilevers (with or without the use of multi-frequency AFM), the phase of the 1st harmonic shows no sensitivity to the Young's modulus for a conservative tip-sample interaction. This means that, for samples that have negligible dissipative forces, no compositional information is delivered by the 1st harmonic phase while using a commercial cantilever (Garcia & Proksch, 2013; Tamayo & Garcia, 1997). However, the 1st harmonic phases of the proposed multi-paddle cantilevers (both the 1:2 cantilever and 1:3 cantilever) clearly show sensitivity to Young's modulus in the absence of dissipative tip-sample forces. The sensitivity of the multi-paddle cantilever's 1st harmonic phase to stiffness (for an elastic tip-sample interaction) marks a unique advantage of the new cantilever design as compared to commercial cantilevers.

| | Percent decrease from E = 0.1GPa to E = 200GPa (%) | | |
|---|---|---|---|
| | Amplitude at $2\omega_d$ | Phase at $\omega_d$ | Phase at $2\omega_d$ |
| $H = 3\times10^{-19}$ J | 77.9 | 0.28 | 0.69 |
| $H = 6\times10^{-19}$ J | 92.3 | 2.00 | 5.33 |

*Table 3.2: Percent increase in the 2nd harmonic amplitude, 1st harmonic phase and 2nd harmonic phase during the numerical simulation of an AM-AFM scan across a flat sample with stratified stiffness (see Figure 3.23) with the 1:2 cantilever. Two different values of the Hamakar's constant are considered.*

As a final step, the sensitivity of the 1st harmonic phase, 2nd harmonic phase and 2nd harmonic amplitude to stiffness are compared for the 1:2 cantilever. Until now, sensitivity to material properties has been observed in both the 1st harmonic phase and the higher harmonic observables. Material characterization based upon branch selection discussed in previous sections was evident in the 1st harmonic phase as well as the higher harmonic amplitude and phase. The goal in this step is to see whether using the higher harmonic observables provides an advantage over the 1st harmonic phase in material characterization. To this end, the percent changes in the amplitude at $2\omega_d$, phase at $\omega_d$ and phase at $2\omega_d$ during the AM-AFM simulation (depicted in Fig.3.24) were computed for two different values of the Hamakar's constant, and the results are summarized in Table 3.2. Indeed we see that the higher harmonic amplitude provides a distinct advantage over the 1st harmonic phase for sensitivity to sample stiffness; from *E* = 0.1GPa to *E* = 200GPa, the amplitude at $2\omega_d$ decreases by 92.3% (77.9%) while the phase at $\omega_d$ decreases by only 0.28% (2%) for $H=6\times10^{-19}\mathrm{J}$ ($H=3\times10^{-19}\mathrm{J}$). The enhanced sensitivity of the higher harmonic amplitude compared with that of the 1st harmonic phase suggests that the higher harmonic amplitude, amplified by internal resonance, may be a better candidate for compositional maps of Young's modulus.

### 3.8 Material property inversion analysis

In order to convert our 1st and 2nd harmonic AM-AFM observables into quantitative compositional measurements, the theoretical models developed by Prof. A. Raman's group at Purdue University (Raman et al., 2011; Cartagena et al., 2013) can be adapted for the proposed inner-paddled cantilever. Since the 1:2 cantilever was shown to be superior to the 1:3 cantilever earlier in the manuscript, attention will be restricted to the 1:2 cantilever. Recall that the laser directly measures the response of the inner paddle rather than the response of the base cantilever, but it is the base cantilever that actually interacts with the sample. The first step towards quantitative compositional mapping is converting the observables $A_1$,$A_2$, $\phi_1$, and $\phi_2$, which correspond to the amplitudes and phases of the 1st and 2nd harmonics of the inner paddle's motion, into the corresponding measurements for the base cantilever. The displacement of the inner paddle, $x_2$, is assumed to have the form

$$\begin{aligned} x_2 &\approx A_1\sin\left(\omega t+\phi_1\right)+A_2\sin\left(2\omega t+\phi_2\right) \\ &= A_1\sin\left(\theta\right)+A_2\sin\left(2\theta+\Phi\right) \end{aligned} \tag{3.19}$$

where $\theta=\omega t+\phi_1$, $\Phi=\phi_2-2\phi_1$ and $A_1$, $A_2$, $\phi_1$, and $\phi_2$ are directly measured by the laser during AM-AFM. The displacement of the base cantilever, $x_1$, is assumed to have the form

$$\begin{aligned} x_1 &\approx B_1 \sin\left(\omega t + \psi_1\right) + B_2 \sin\left(2\omega t + \psi_2\right) \\ &= B_1 \sin\left(\theta + \Theta\right) + B_2 \sin\left(2\theta + \Psi\right) \end{aligned} \tag{3.20}$$

where $\Theta = \psi_1 - \phi_1$ and $\Psi = \psi_2 - 2\psi_1$. By substituting (3.19) and (3.20) into (3.1b), neglecting damping ($c_1 = c_2 = 0$), and balancing the 1st and 2nd harmonics, the following relations are recovered

$$\psi_1 = \phi_1, \quad B_1 = \left(k_2 - m_2\omega^2\right) A_1 / k_2 \tag{3.21}$$

$$\psi_2 = \phi_2 - \pi, \quad B_2 = \left(k_2 - 4m_2\omega^2\right) A_2 / k_2 \tag{3.22}$$

The equations in (3.21) relate the amplitudes and phases of the inner paddle's motion to that of the base cantilever's motion at $1\omega$. Similarly, the equations in (3.22) relate the amplitudes and phases of the inner paddle's motion to that of the base cantilever's motion at $2\omega$. Given that $\omega \approx \omega_1$ and $2\omega \approx \omega_2$ where $\omega_1$ ($\omega_2$) is the resonant frequency of the in-phase (out-of-phase) vibrational mode, the relations in (3.21) correspond to the lower, in-phase mode shape and the relations in (3.22) correspond to the higher, out-of-phase eigenmode shape. This result is expected in light of the assumption that $c_1 = c_2 = 0$.

In order to perform harmonic balance analysis of equation (3.1a), following the work of Cartagena et al. (2013), the tip-sample interaction force must be decomposed into its harmonic components; i.e., $F_{ts}$ must be written as a Fourier series

$$F_{ts} = F_{ts}^0 + \sum_{n=1}^{\infty} F_{ts}^n \sin\left(n\theta\right) \tag{3.23}$$

The frequency response (or transfer function) of the inner-paddled cantilever serves as a filter that passes the frequencies corresponding to the in-phase and out-of-phase vibration modes and filters out the other harmonic components in (3.23). Since the in-phase modal frequency corresponds to the 1st harmonic and the out-of-phase modal frequency corresponds to the 2nd harmonic, all other harmonics of $F_{\text{ts}}$ can be neglected in the harmonic balance analysis of (1.a). Substituting (3.19) and (3.20) into (1.a) and retaining only the 1st and 2nd harmonic components of $F_{\text{ts}}$ gives

$$\begin{aligned}&\left\{B_1\left(k_1-m_1\omega^2+k_2\right)-A_1k_2\right\}\sin\theta+\left\{k_1\left(B_1+B_2\right)-k_1B_2-4m_1\omega^2B_2\right\}\cos\psi\sin(2\theta)\\&+\left\{k_1\left(B_1+B_2\right)-k_1B_2-4m_1\omega^2B_2\right\}\sin\psi\cos(2\theta)=\left(F_{ex}\cos\psi_1+F_{ts}^1\right)\sin\theta-F_{ex}\sin\psi_1\cos\theta+F_{ts}^2\sin 2\theta\end{aligned} \tag{3.24}$$

Note that, for consistency with the assumptions made previously, damping has been neglected in this step ($c_1=c_2=0$). Since it is assumed that the tip-sample interaction is purely elastic, the 1st and 2nd Fourier components of $F_{\text{ts}}$ are conservative (i.e., they contain only a $\sin\theta$ term). The coefficients of the 1st and 2nd Fourier components of $F_{\text{ts}}$ are given by

$$F_{ts}^1=\frac{1}{\pi}\int_0^{2\pi}\sin\theta F_{\text{ts}}\,d\theta \tag{3.25}$$

$$F_{ts}^2=\frac{1}{\pi}\int_0^{2\pi}\sin 2\theta F_{\text{ts}}\,d\theta \tag{3.26}$$

For $0<\theta<\pi$, the displacement of the base cantilever, $x_1$, is positive indicating that the base cantilever is deflected upward (w.r.t to its static position), away from the sample and is therefore not in contact with the sample. For $\pi<\theta<2\pi$, $x_1$ is negative indicating that the cantilever is deflected downward (with respect to its static position), towards the sample. To simplify the following analysis, a modified version of the DMT contact model (3.2) will be considered. Here, the tip-sample interaction force will be approximated as

$$F_{\mathrm{ts}}\left(x_1\right)=\begin{cases} 0, & x_1>-x_0 \\ F_{\mathrm{vW}}+\frac{4}{3}E^*\sqrt{R}\left[-\left(x_0+x_1\right)\right]^{3/2}, & x_1<-x_0 \end{cases} \tag{3.27}$$

where $F_{\mathrm{vW}}$ is the maximum attractive van der Waals force between the tip and sample. When $x_1>-x_0$, the tip is not in contact with the sample, and there is no tip-sample interaction force. When $x_1<-x_0$, the tip is in contact with the sample, and the tip-sample interaction force contains an attractive van der Waals component, $F_{\mathrm{vW}}$ and a repulsive Hertz component. Regarding the expressions in (3.25) and (3.26), contributions to the integral occur only when the tip is in contact with the sample. At the moment the tip makes contact with the sample, it holds that

$$B_1\sin\left(\theta_0\right)+B_2\sin\left(2\theta_0+\psi\right)=-x_0,\quad \pi<\theta_0<3\pi/2 \tag{3.28}$$

where $\theta=\theta_0$ corresponds to the time the tip contacts the sample. Further, $\sin\theta$ is symmetric with respect to $\theta=3\pi/2$ and, hence, the coefficients of the 1st and 2nd Fourier components can be written in the form

$$F_{ts}^1=\frac{2}{\pi}\int_{\theta_0}^{3\pi/2}\sin\theta F_{\mathrm{ts}}\,d\theta \tag{3.29}$$

$$F_{ts}^2=\frac{2}{\pi}\int_{\theta_0}^{3\pi/2}\sin 2\theta F_{\mathrm{ts}}\,d\theta \tag{3.30}$$

Returning now to (S6) and balancing the $\cos\theta$ and $\cos 2\theta$ terms, we have

$$\sin\psi_1=0\quad\Rightarrow\psi_1=0,\pi \tag{3.31}$$

$$\sin\Psi = 0 \quad \Rightarrow \Psi = 0,\pi \tag{3.32}$$

where $\psi_1 = \Psi = 0$ if $\omega < \omega_1$ and $\psi_1 = \Psi = \pi$ if $\omega > \omega_1$. This too is an expected result since damping has been neglected in the dynamics of the inner-paddled cantilever. Balancing the $\sin\theta$ terms in (3.24) gives

$$B_1\left(k_1 - m_1\omega^2 + k_2\right) - A_1 k_2 = \pm F_{ex} + F_{ts}^1 \tag{3.33}$$

and balancing the $\sin 2\theta$ terms gives

$$\pm\left[B_2\left(k_1 + k_2\right) + k_2 A_2 - 4m_1\omega^2 B_2\right] = F_{ts}^2 \tag{3.34}$$

for $\psi_1 = \Psi = 0,\pi$ (i.e. the coefficients of $F_{ex}$ and $F_{ts}^2$ are +1 for $\psi_1 = \Psi = 0$ and -1 for $\psi_1 = \Psi = \pi$ ). By evaluating the integrals in (3.29) and (3.30), the 1st and 2nd Fourier components of $F_{\mathrm{ts}}$ can be related to the van der Waals force, $F_{vW}$, and the effective Young's modulus, $E^*$, such that

$$\begin{aligned}
F_{ts}^1 &= \frac{2}{\pi}\int_{\theta_0}^{3\pi/2} \sin\theta\left[F_{\mathrm{vW}} + \frac{4}{3}E_{eff}\sqrt{R}\left[-\left(x_1 + x_0\right)\right]^{3/2}\right]d\theta \\
&= \frac{2}{\pi}\int_{\theta_0}^{3\pi/2} \sin\theta F_{\mathrm{vW}}\, d\theta + \frac{8E_{eff}\sqrt{R}}{3\pi}\int_{\theta_0}^{3\pi/2} \sin\theta\left[-\left(B_1\sin\left(\theta\right) + B_2\sin\left(2\theta + \psi\right) + x_0\right)\right]^{3/2} d\theta \\
&= \frac{2}{\pi}F_{\mathrm{vW}}\cos\theta_0 + \frac{8E_{eff}\sqrt{R}}{3\pi}\mathrm{Int}_1\left(B_1, B_2, \psi, x_0\right)
\end{aligned} \tag{3.35}$$

$$\begin{aligned} F_{ts}^{2} &= \frac{2}{\pi}\int_{\theta_0}^{3\pi/2} \sin 2\theta \left[ F_{\mathrm{vW}} + \frac{4}{3}E_{eff}\sqrt{R}\left[-\left(x_1 + x_0\right)\right]^{3/2} \right] d\theta \\ &= \frac{2}{\pi}\int_{\theta_0}^{3\pi/2} \sin 2\theta F_{\mathrm{vW}}\, d\theta + \frac{8E_{eff}\sqrt{R}}{3\pi}\int_{\theta_0}^{3\pi/2} \sin 2\theta \left[-\left(B_1\sin\left(\theta\right) + B_2\sin\left(2\theta + \psi\right) + x_0\right)\right]^{3/2} d\theta \\ &= \frac{2}{\pi}F_{\mathrm{vW}}\cos^2\theta_0 + \frac{8E_{eff}\sqrt{R}}{3\pi}\mathrm{Int}_2\left(B_1, B_2, \psi, x_0\right) \end{aligned} \tag{3.36}$$

where

$$\mathrm{Int}_1\left(B_1, B_2, x_0\right) = \int_{\theta_0}^{3\pi/2} \sin\theta\left[-\left(B_1\sin\theta \pm B_2\sin 2\theta + x_0\right)\right]^{3/2} d\theta \tag{3.37}$$

$$\mathrm{Int}_2\left(B_1, B_2, x_0\right) = \int_{\theta_0}^{3\pi/2} \sin 2\theta\left[-\left(B_1\sin\theta \pm B_2\sin 2\theta + x_0\right)\right]^{3/2} d\theta \tag{3.38}$$

Substituting (3.35) and (3.36) into (3.33) and (3.34) results in

$$B_1\left(k_1 - m_1\omega^2 + k_2\right) - A_1k_2 = \pm F_{ex} + \frac{1}{\pi}F_{vW}\cos\theta_0 + \frac{4E_{eff}\sqrt{R}}{3\pi}\mathrm{Int}_1\left(B_1, B_2, \psi, x_0\right) \tag{3.39}$$

$$\pm\left[B_2\left(k_1 + k_2\right) + k_2A_2 - 4m_1\omega^2B_2\right] = \frac{1}{\pi}F_{vW}\cos^2\theta_0 + \frac{4E_{eff}\sqrt{R}}{3\pi}\mathrm{Int}_2\left(B_1, B_2, \psi, x_0\right) \tag{3.40}$$

for $\psi_1 = \Psi = 0, \pi$. Here $k_1$, $k_2$, $m_1$, $m_2$ and $R$ are known parameters of the inner-paddled cantilever, $A_1$ and $A_2$ are directly measured by the laser, $B_1$ and $B_2$ are determined from $A_1$ and $A_2$ using (3.21) and (3.22) and $x_0$ can be determined from the calibrated Z-piezo data (where Z-piezo is the vertical displacement of cantilever's base).

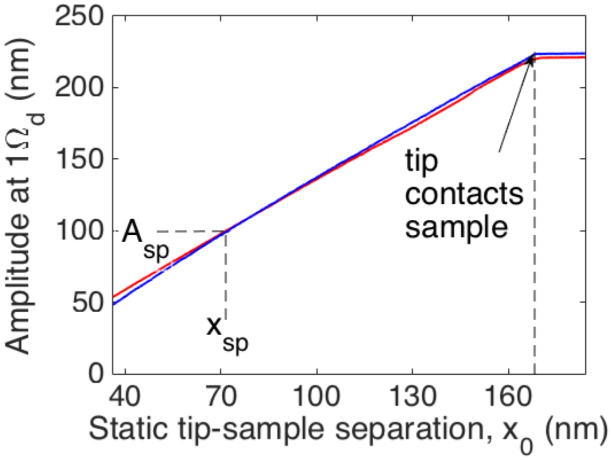

*Figure 3.25: Dynamic force curves from Fig. 3.20 (a), annotated to illustrate the $x_0$ at which the tip contacts the sample, the set-point amplitude, $A_{sp}$,* and the set-point tip-sample separation, $x_{sp}$.

Determination of $x_0$ requires an initial dynamic force curve to be taken just before the AFM scan in order to calibrate the Z-piezo data. For example the experimental dynamic force curve shown in Fig. 3.25 has been calibrated in the sense that the Z-piezo distance that is directly measured by the AFM has been converted into an equivalent static tip-sample separation, $x_0$. This was done by assuming that the $x_0$ at which the tip makes contact with the sample (see Fig. 3.25) is equal to the 1st harmonic amplitude of the base cantilever, $B_1$, and that, at $x_0=0$, the response of the base cantilever is approximately 0. These assumptions are most appropriate when the cantilever's dynamics track the lower branch, or when the sample is relatively stiff (and the cantilever's dynamics track either branch). Of course, the laser directly measures $A_1$ rather than $B_1$, but by neglecting damping $B_1$ can be computed from $A_1$ via (3.21). By making these assumptions in order to calibrate the Z-piezo data, it follows that the slope of the dynamic force curve of the 1st harmonic amplitude ($A_1$ vs $x_0$) is assumed to have a slope equal to the ratio $A_1/B_1 = k_2/\left(k_2 - m_2\omega^2\right)$. In other words, the slope of the dynamic force curve (of the 1st harmonic amplitude) is approximated as

$$\frac{dA_1}{dx_0} = \frac{k_2}{\left(k_2 - m_2\omega^2\right)} \tag{3.41}$$

Finally, associated with a particular set-point value for $A_1$, $A_{\mathrm{sp}}$, is a set-point value for $x_0$, $x_{\mathrm{sp}}$, as illustrated in Fig. 3.25. Based on $A_{\mathrm{sp}}$, $x_{\mathrm{sp}}$ and the slope of the force curve, the instantaneous $x_0$ can be computed:

$$x_0 = x_{\mathrm{sp}} + \left(\frac{dA_1}{dx_0}\right)^{-1}\left(A_1 - A_{\mathrm{sp}}\right) \tag{3.42}$$

For the parameters listed in Table 1 for the 1:2 cantilever, $k_2 / \left(k_2 - m_2\omega_1^{\,2}\right) = 1.34$ and therefore,

$$x_0 = x_{\mathrm{sp}} + \frac{\left(A_1 - A_{\mathrm{sp}}\right)}{1.34} \tag{3.43}$$

Note that, in theory, the feedback control maintains $A_1 = A_{\mathrm{sp}}$ throughout the AM-AFM scan but, in practice, $A_1$ varies slightly throughout the scan. Hence, it would be reasonable to assume $A_1 = A_{\mathrm{sp}}$ and $x_0 = x_{\mathrm{sp}}$ but more accurate to use the instantaneous $A_1$ and $x_0$. Finally, with $x_0$ determined, (3.28), (3.39) and (3.40) can be used to compute $F_{vW}$ and $E^*$ numerically.

### 3.9 Conclusions

In this work we studied the compositional mapping performance of a newly introduced AFM cantilever consisting of a base cantilever and inner paddle during tapping mode AFM. Under harmonic base excitation, the cantilever system behaves like a system of two coupled harmonic oscillators involving a lower, in-phase eigenmode and a higher, out-of-phase eigenmode. The cantilever is specifically designed to support a 1:*n* internal resonance between the two eigenmodes so that the *n*th harmonic coincides with the out-of-phase resonant frequency. By directly exciting the in-phase frequency, the nonlinear tip-sample interaction activates the internal resonance and thereby amplifies the *n*th harmonic.

An experimental and computational study of a cantilever designed to support 1:3 internal resonance is presented in Section 3.3. Sensitivity curves were constructed in which the amplitudes and phases of the first and third harmonics were plotted versus the static tip-sample separation for two distinct materials in a blended PS-LDPE specimen. Strong correspondence between the experimental and numerical results was observed, providing verification of the reduced order lumped-parameter model for the new cantilever design. Additionally, a large variation in the trend of the amplitude of the third harmonic and phases of the first and third harmonics depending on the measured materials was observed, whereas the corresponding trend of the first harmonic amplitude appeared to be nearly unchanged for both materials. The stark contrast in the trends of the amplitude of the third harmonic and phases of the first and third harmonics as functions of tip-sample approach distance was attributed to a difference in branch selection among the two materials; namely, the "stiff" PS region leads to steady dynamics that are attracted by a stable upper branch (corresponding to a high-amplitude solution) which is associated with a Hertzian- dominated repulsive interaction regime, whereas the "compliant" co-polymer region leads to dynamics attracted by a lower branch (low amplitude solution) which is associated with a van der Waals- dominated attractive interaction regime. Moreover, in the computational study, a strong correspondence between the magnitude of the average tip-sample interaction force per cycle and the magnitude of the third harmonic was observed. These two quantities appeared to be linearly related by a constant of proportionality $C_{\mathrm{min}}$. While $C_{\mathrm{min}}$ was computed numerically in this study, in practice this value may be determined with the use of a calibration sample with known material properties. The linear relation between average tip-sample force and the amplitude of the third harmonic may then me used to obtain quantitative measurements of the average tip-sample interaction force for a given material.

In Section 3.4, we presented results from a computational study of energy transfer to the $n^{\mathrm{th}}$ harmonic for different 1:$n$ internal resonance designs and found the case of $n = 2$ to be optimal due to asymmetry in the tip-sample force-deflection curve. Experimental force curves and AFM scans of the blended PS-LDPE sample shown in Section 3.5 confirmed the enhanced performance of the 1:2 internal resonance as compared with a 1:3 internal resonance and a 1:4 internal resonance. The 1:2 cantilever was then used to construct compositional maps of cyanobacteria in Section 3.6. The compositional maps constructed with the 2nd harmonic amplitude, 2nd harmonic phase and 1st harmonic phase revealed stark contrast that was not observed in the topographical image. Computational and experimental force curves showed that the contrast was due to a difference in branch selection owing to variations in the sample's Young's modulus, which is consistent with the findings presented in Section 3.3.

Finally, we numerically simulated the feedback control in AM-AFM and studied the variations of the first three harmonics (amplitude and phase) with respect to changes in Young's modulus in Section 3.7. The amplitude of the $n^{\mathrm{th}}$ harmonic for a 1:$n$ internal resonance showed significantly enhanced sensitivity to stiffness as compared to the phases, underscoring the utility of the higher harmonic in compositional mapping. Furthermore, unlike for a commercial cantilever, the phase of the first harmonic showed sensitivity to stiffness for a conservative tip-sample force, which is attributed to the large presence of the $n^{\mathrm{th}}$ harmonic in the response. Overall, the amplification of the 2nd harmonic in the 1:2 cantilever due to internal resonance provides a unique advantage over other multi-harmonic techniques. The presence of the higher harmonic with a relatively strong SNR could be exploited in a material property inversion scheme based on the adaptation of existing models (Sahin et al., 2007; Cartagena et al., 2013). An outline of the theoretical analysis that would be required to convert the AM-AFM observables of the 1:2 cantilever into quantitative material properties is presented in Section 3.8.

## 3.10 References

Anczykowski B., Gotsmann B., Fuchs H., Cleveland J.P., Elings V.B. (1999). How to measure energy dissipation in dynamic mode atomic force microscopy. *Appl. Surf. Sci,, 140*, 376-382.

Baumann M., Stark R.W. (2010), Dual frequency atomic force microscopy on charged surfaces. *Ultramicroscopy, 110*, 578-581.

Binnig, G., Quate, C.F., and Gerber, Ch. (1986). Atomic Force Microscope. *Physical Review Letters*, 56, 930–933.

Cartagena-Rivera, A.X., Wang, W.-H., Geahlen, R.L., and Raman, A. (2015). Fast, multi-frequency, and quantitative nanomechanical mapping of live cells using the atomic force microscope. *Scientific Reports*, *5*(June), 11692.

Cartagena, A., Hernando-Pérez, M., Carrascosa, J.L., de Pablo, P.J., and Raman, A. (2013). Mapping in vitro local material properties of intact and disrupted virions at high resolution using multi-harmonic atomic force microscopy. *Nanoscale*, *5*, 4729–36.

Cho H., Jeong B., Yu M.F., Vakakis A.F., McFarland D.M., Bergman L.A. (2012). Nonlinear hardening softening resonances in micromechanical cantilever-nanotube systems originated from nanoscale geometric nonlinearities. *Int. J. Solids Str.*, *49*, 2059-2065.

Cho H., Yu M.F., Vakakis A.F., Bergman L.A., McFarland D.M. (2010). Tunable and broadband nonlinear nanomechanical resonator. *Nano Letters* , *10*, 1793-1798.

Cho, H., Yu, M.F., Vakakis, A.F., Bergman, L.A., and McFarland, D.M. (2012). Dynamics of microcantilever integrated with geometric nonlinearity for stable and broadband nonlinear atomic force microscopy. *Surface Science*, *606*, L74–L78.

Cleveland J.P., Anczykowski B., Schmid A.E., Elings V.B. (1998). Energy dissipation in tapping-mode atomic force microscopy. *Appl. Phys. Lett.*, *72*, 2613-2615.

Derjaguin, B., Muller, V., and Toporov, Y. (1980). On different approaches to the contact mechanics. *Journal of Colloid and Interface Science*, *73*, 293–294.

Dufrêne, Y.F., Ando, T., Garcia, R., Alsteens, D., Martinez-Martin, D., Engel, A., Gerber, C., Müller, D.J. (2017). Imaging modes of atomic force microscopy for application in molecular and cell biology. *Nature Nanotechnology*, *12*, 295–307.

Eaton P., West P. (2010). *Atomic Force Microscopy*. Oxford University Press, Oxford, UK.

Ebeling, D., Eslami, B., and Solares, S.D.J. (2013). Visualizing the subsurface of soft matter: Simultaneous topographical imaging, depth modulation, and compositional mapping with triple frequency atomic force microscopy. *ACS Nano*, *7*(11), 10387–10396.

Gannepalli, A., Yablon, D.G., Tsou, A.H., and Proksch, R. (2011). Mapping nanoscale elasticity and dissipation using dual frequency contact resonance AFM. *Nanotechnology*, *22*(35), 355705.

Garcia R., Perez R. (2002). Dynamic atomic force microscopy methods. *Surf. Sci., 47*, 197-301.

Garcia R. (2010). *Amplitude Modulation Atomic Force Microscopy*. Wiley-VCH Verlag GmbH & Co. KGaA, Weinheim, Germany.

Garcia, R., Herruzo, E.T. (2012). The emergence of multifrequency force microscopy. *Nature Nanotechnology*, *7*, 217–226.

Garcia R., Magerle R., Perez R. (2007). Nanoscale compositional mapping with gentle forces. *Nature, 6*, 405-411.

Garcia, R., Proksch, R. (2013). Nanomechanical mapping of soft matter by bimodal force microscopy. *European Polymer Journal*, *49*, 1897–1906.

García, R., San Paulo, A. (2000). Dynamics of a vibrating tip near or in intermittent contact with a surface. *Physical Review B*, *61*(20), R13381–R13384.

Herruzo, E.T., Asakawa, H., Fukuma, T., and Garcia, R. (2013). Three-dimensional quantitative force maps in liquid with 10 piconewton, angstrom and sub-minute resolutions. *Nanoscale*, *5*, 2678–2685.

Herruzo, E.T., Perrino, A.P., and Garcia, R. (2014). Fast nanomechanical spectroscopy of soft matter. *Nature Communications*, *5*, 3126.

Hurley, D., Kocun, M., Revenko, I., Ohler, B., and Proksch, R. (2015). Fast, quantitative AFM nanomechanical measurements using AM-FM Viscoelastic Mapping Mode. *Microscopy and Analysis*, SPM Supplement, March/April, 9-13.

Jeong B., Pettit C., Dharmasena S., Keum H., Lee J., Kim J., Kim S., McFarland D.M., Bergman L.A., Vakakis A.F. (2016). Utilizing internal resonance to achieve multi-harmonic atomic force microscopy. *Nanotechnology*, *27*, 125501.

Kawai, S., Glatzel, T., Koch, S., Such, B., Baratoff, A., Meyer, E. (2009). Systematic achievement of improved atomic-Scale contrast via bimodal dynamic force microscopy. *Physical Review Letters*, *103*, 1–4.

Kawai, S., Glatzel, T., Koch, S., Such, B., Baratoff, A., Meyer, E. (2010). Ultrasensitive detection of lateral atomic-scale interactions on graphite (0001) via bimodal dynamic force measurements. *Physical Review B - Condensed Matter and Materials Physics*, *81*, 1–7.

Keum, H., Carlson, A., Ning, H., Mihi, A., Eisenhaure, J. D., Braun, P.V, Rogers J.A., Kim, S. (2012). Silicon micro-masonry using elastomeric stamps for three-dimensional microfabrication. *Journal of Micromechanics and Microengineering*, *22*, 055018.

Keum, H., Yang, Z., Han, K., Handler, D.E., Nguyen, T.N., Schutt-Aine, J., Bahl G., Kim, S. (2016). Microassembly of Heterogeneous Materials using Transfer Printing and Thermal Processing. *Scientific Reports*, *6*, 29925.

Kocun, M., Labuda, A., Meinhold, W., Revenko, I., Proksch, R. (2017). Fast, High Resolution, and Wide Modulus Nanomechanical Mapping with Bimodal Tapping Mode. *ACS Nano, 11,* 10097-10105.

Labuda, A., Kocun, M., Meinhold, W., Walters, D., Proksch, R. (2016). Generalized Hertz model for bimodal nanomechanical mapping. *Beilstein Journal of Nanotechnology*, *7*, 970–982.

Lee S.I., Howell S.W., Raman A., Reifenberger R. (2003),. Nonlinear dynamic perspectives on dynamic force microscopy. *Ultramicroscopy, 97*, 185-198.

Li J.W., Cleveland J.P., Proksch R. (2009), Bimodal magnetic force microscopy: Separation of short and long range forces. *Appl. Phys. Lett*., *94*, 163118.

Lozano J.R., Garcia R. (2008). Theory of multifrequency atomic force microscopy. *Phys. Rev. Lett., 100*, 076102.

Lozano J.R., Garcia R. (2009). Theory of Phase spectroscopy in bimodal atomic force microscopy. *Phys. Rev. B, 79*, 014110.

Magonov S.N., Elings V., Whangbo M.H. (1996). Phase imaging and stiffness in tapping mode atomic force microscopy. *Surf. Sci*., *375*, L385-L391.

Mahaffy, R.E., Shih, C.K., MacKintosh, F.C., Kas, J. (2000). Scanning proble-based frequency-dependent microrheology of polymer gels and biological cells. *Physical Review Letters*, *85*, 880–883.

Mahaffy, R., Park, S., Gerde, E., Kas, J., and Shih, C. (2004). Quantitative Analysis of the Viscoelastic Properties of Thin Regions of Fibroblasts Using Atomic Force Microscopy. *Biophysical Journal*, *86*(March), 1777–1793.

Martin, Y., Williams, C.C., and Wickramasinghe, H.K. (1987). Atomic force microscope-force mapping and profiling on a sub 100-Å scale. *Journal of Applied Physics*, *61*, 4723–4729.

Martinez-Martin, D., Herruzo, E.T., Dietz, C., Gomez-Herrero, J., and Garcia, R. (2011). Noninvasive protein structural flexibility mapping by bimodal dynamic force microscopy. *Physical Review Letters*, *106*, 1–4.

Paulo, Á., and García, R. (2001). Tip-surface forces, amplitude, and energy dissipation in amplitude-modulation (tapping mode) force microscopy. *Physical Review B*, *64*, 1–4.

Potekin, R., Dharmasena, S., Keum H., Jiang X., Lee J., Kim S., Bergman, L. A., Vakakis, A. F., Cho, H. (2018). Multi-frequency ATomic Force Microscopy based on enhanced internal resonance of an inner-paddled cantilever. *Sensors and Actuators A: Physical*, *273*, 206-220.

Potekin, R., Dharmasena, S., McFarland, D. M., Bergman, L. A., Vakakis, A. F., Cho, H. (2017). Cantilever dynamics in higher-harmonic atomic force microscopy for enhanced material characterization. *International Journal of Solids and Structures*, *110–111*, 332–339.

Proksch, R., Kocun, M., Hurley, D., Viani, M., Labuda, A., Meinhold, W., Bemis, J. (2016). Practical loss tangent imaging with amplitude-modulated atomic force microscopy. *Journal of Applied Physics*, *119*, 134901.

Proksch, R., and Yablon, D.G. (2012). Loss tangent imaging: Theory and simulations of repulsive-mode tapping atomic force microscopy. *Applied Physics Letters*, *100*, 2014–2017.

Raman, A., Melcher, J., Tung, R. (2008). Cantilever dynamics in atomic force microscopy Dynamic atomic force microscopy , in essence , consists of a vibrating. *Nano Today*, *3*, 20–27.

Raman, A., Trigueros, S., Cartagena, A., Stevenson, A. P., Susilo, M., Nauman, E., Contera, S. A. (2011). Mapping nanomechanical properties of live cells using multi-harmonic atomic force microscopy. *Nat Nanotechnol*, *6*, 809–814.

Rodríguez, T. R., and García, R. (2004). Compositional mapping of surfaces in atomic force microscopy by excitation of the second normal mode of the microcantilever. *Applied Physics Letters*, *84*, 449–451.

Rother, J., Noding, H., Mey, I., and Janshoff, A. (2014). Atomic force microscopy-based microrheology reveals significant differences in the viscoelastic response between malign and benign cell lines. *Open Biology*, *4*, 140046–140046.

Sader, J.E., and Jarvis, S.P. (2004). Accurate formulas for interaction force and energy in frequency modulation force spectroscopy. *Applied Physics Letters*, *84*, 1801.

Sahin, O., Magonov, S., Su, C., Quate, C.F., and Solgaard, O. (2007). An atomic force microscope tip designed to measure time-varying nanomechanical forces. *Nature Nanotechnology*, *2*, 507–514.

Solares, S.D., An, S., and Long, C.J. (2014). Multi-frequency tapping-mode atomic force microscopy beyond three eigenmodes in ambient air. *Beilstein Journal of Nanotechnology*, *5*(1), 1637–1648.

Solares, S.D., Chawla, G. (2010a). Frequency response of higher cantilever eigenmodes in bimodal and trimodal tapping mode atomic force microscopy. *Measurement Science and Technology*, *21*, 125502.

Solares, S.D., Chawla, G. (2010b). Triple-frequency intermittent contact atomic force microscopy characterization: Simultaneous topographical, phase, and frequency shift contrast in ambient air. *Journal of Applied Physics*, *108*(5).

Santos, S., Barcons, V., Font, J., Verdaguer, A. (2014). Unlocking higher harmonics in atomic force microscopy with gentle interactions. *Beilstein Journal of Nanotechnology*, *5*, 268–277.

Stark, R.W. (2010). Bistability, higher harmonics, and chaos in AFM. *Materials Today*, *13*, 24–32.

Suresh, S., Spatz, J., Mills, J.P., Micoulet, A., Dao, M., Lim, C.T., Seufferlein, T. (2015). Connections between single-cell biomechanics and human disease states: gastrointestinal cancer and malaria. *Acta Biomaterialia*, *23*, S3–S15.

Tamayo, J., Garcia, R. (1997). Effects of elastic and inelastic interactions on phase contrast images in tapping-mode scanning force microscopy. *Applied Physics Letters*, *71*, 2394–2396.

Tamayo J., Garcia R. (1998), Relationship between phase shift and energy dissipation in tapping-mode scanning force microscopy. *Appl. Phys. Lett.*, *73*, 2926-2928.

Yablon, D.G., Proksch, R., Gannepalli, A., Tsou, A.H. (2012). Mapping Storage Modulus and Loss Modulus of Polyolefin/Polystyrene Blends With Atomic Force Microscopy. *Rubber Chemistry and Technology*, *85*, 559–564.

Yuya, P.A., Hurley, D.C., Turner, J.A. (2008). Contact-resonance atomic force microscopy for viscoelasticity. *Journal of Applied Physics*, *104*, 074916.

# Chapter 4

## Nonlinear dynamics of a micromechanical Duffing oscillator under harmonic base excitation

In this chapter I consider a clamped-clamped beam under harmonic base excitation having a concentrated mass at its center. The reduced-order model of the system is that of a Duffing oscillator, which is well known to result in hardening of the fundamental resonance curve. The primary role of the concentrated mass is to enhance the geometric nonlinearity of the system and thereby generate an ultra-wide resonance bandwidth. For a fixed forcing level of the beam, the range of frequencies that constitute the broadband resonance are determined by the linearized frequency (lower bound) and the jump-down frequency (upper bound). However, harmonic base excitation at the two clamped ends of the beam is used in this study and therefore the forcing level is not fixed, rather it is proportional to the square of the excitation frequency. Interestingly, I found that for sufficiently large base excitation amplitudes, there is no theoretically predicted jump-down frequency. The critical excitation level above which there is no theoretical jump-down event is significantly lowered by the presence of the concentrated mass. In fact, without the concentrated mass, it would not be practically feasible to achieve the *no drop phenomenon*, hence its critical role in the beam design (Potekin et al., 2018). Computational and experimental results confirm this theoretical prediction and a physical explanation of the phenomenon is outlined. Physically, of course, it is not possible to truly have no jump-down bifurcation point in the frequency response. In practice, this bifurcation point may occur due to the presence of nonlinear damping, the excitation of internal resonances, perturbations in the initial conditions and/or excitation amplitude caused by noise, the basin of attraction for the upper branch solution may become impractically small. A study of such practical limitations is also included in this chapter. As discussed in Chapter 5, by operating at an excitation amplitude above the critical threshold, the ultra-wide resonant bandwidth can be exploited in a mass sensing application.

### 4.1 Resonator design and reduced order model

In Fig. 4.1, a schematic of the system under consideration is depicted: a long thin clamped-clamped beam with a concentrated point mass at its center and harmonic base excitation at its clamped supports. Assuming that plane sections remain plane during the beam vibration, a linear stress-strain constitutive law, and planar motion, one can derive the equation of motion describing the transverse motion of the beam with nonlinearity due to midplane stretching,

$$\left[\rho A+m_c\delta(x-L)\right]w_{tt}+(\rho A\omega_1/Q)w_t+EIw_{xxxx}-(EA/4L)w_{xx}\int_0^{2L}w_x^2dx=0 \tag{4.1}$$

where $\rho$ is the mass density, $A$ is the cross-sectional area, $m_c$ is the mass of the concentrated point mass, $E$ is Young's modulus, $I$ is the area moment of inertia, $L$ is the half-length, $Q$ is the $Q$-factor, $\omega_1$ is the linearized eigenfrequency of the fundamental flexural mode, $\delta(x)$ is the Dirac delta function, $x$ is the spatial coordinate along the beam, $t$ is time and $w(x,t)$ is the transverse displacement. The boundary conditions are given by,

$$w(0,t)=w(2L,t)=a\sin(\omega t),\qquad w_x(0,t)=w_x(2L,t)=0 \tag{4.2}$$

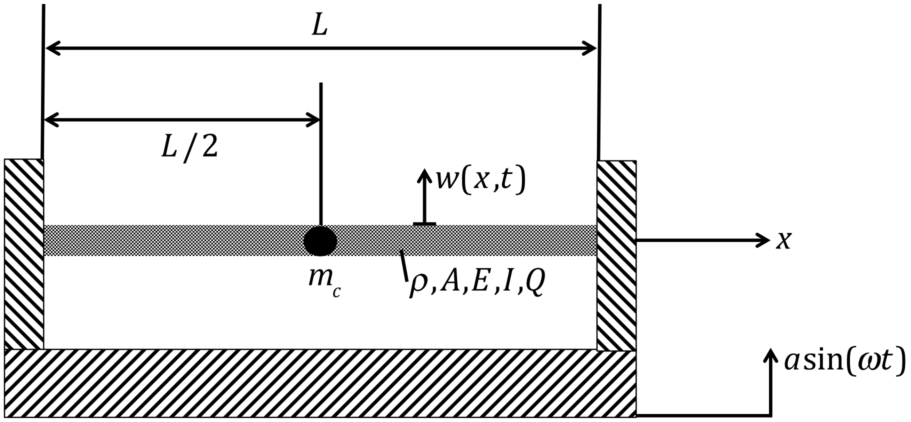

*Figure 4.1: Schematic of the system under consideration: A doubly clamped beam with a concentrated mass at its center under harmonic base excitation.*

By decomposing the displacement $w(x,t)$ into a "pseudo-static" component, $w_s(x,t)=-a\sin(\omega t)$, plus a "flexible" component, $w_{\mathrm{f}}(x,t)$, one can instead consider the following boundary value problem describing the relative transverse motion of the beam with respect to the clamped supports, given by

$$\begin{aligned}&\left[\rho A+m_c\delta(x-L)\right]w_{f,tt}+(\rho A\omega_1/Q)w_{f,t}+EIw_{f,xxxx}-(EA/4L)w_{f,xx}\int_0^{2L}\left(w_{f,x}\right)^2dx\\&\qquad=-\left[\rho A+m_c\delta(x-L)\right]a\omega^2\sin\omega t+(\rho A\omega_1\omega/Q)\cos\omega t\end{aligned}\tag{4.3a}$$

$$w_f(0,t)=w_f(2\mathrm{L},t)=0,\qquad w_{f,x}(0,t)=w_{f,x}(2\mathrm{L},t)=0\tag{4.3b}$$

Finally, by introducing the following normalizations,

$$\begin{gathered}\tilde{x}=\frac{x}{2L},\quad \tilde{w}_f=\frac{w_f}{2L},\quad \tilde{a}=\frac{a}{2L},\quad \tilde{\delta}(\tilde{x})=2L\delta(x),\quad \Theta^2=\frac{EI}{16\rho AL^4}\\ \mu=\frac{m_c}{2L\rho A},\quad \tau=\Theta t,\quad \Omega=\omega/\Theta,\quad \beta=\frac{2AL^2}{I}\end{gathered}\tag{4.4}$$

the equation of motion can be written in non-dimensional form,

$$\begin{aligned}&\left[1+\mu\tilde{\delta}(\tilde{x}-1/2)\right]\tilde{w}_{f,\tau\tau}+\frac{\Omega_1}{Q}\tilde{w}_{f,\tau}+\tilde{w}_{f,\tilde{x}\tilde{x}\tilde{x}\tilde{x}}-\beta\tilde{w}_{f,\tilde{x}\tilde{x}}\int_0^1\left(\tilde{w}_{f,\tilde{x}}\right)^2d\tilde{x}\\&\qquad=-\left[1+\mu\tilde{\delta}(\tilde{x}-1/2)\right]\tilde{a}\Omega^2\sin(\Omega\tau)+\frac{\tilde{a}\Omega\Omega_1}{Q}\cos(\Omega\tau)\end{aligned}\tag{4.5a}$$

$$w_f\left(0,\tau\right)=w_f\left(1,\tau\right)=0,\quad w_{f,\tilde{x}}\left(0,\tau\right)=w_{f,\tilde{x}}\left(1,\tau\right)=0\tag{4.5b}$$

If it is assumed that the mass-loaded beam vibrates in the fundamental flexural mode of the underlying linear system, the nondimensional displacement along the beam can be written as,

$$w_f\left(\tilde{x},\tau\right)=W_1\left(\tilde{x}\right)\phi_1\left(\tau\right)\tag{4.6}$$

where $W_1\left(\tilde{x}\right)$ is the fundamental linear mode shape and $\phi_1\left(\tau\right)$ is the corresponding modal amplitude. Specifically, $W_1\left(\tilde{x}\right)$ is the solution to the problem

$$W_1^{''''} = \left[ 1 + \mu \tilde{\delta}(\tilde{x} - 1/2) \right] \Omega_1^2 W_1 \tag{4.7a}$$

$$W_1(0) = W_1(1) = 0, \qquad W_1^{'}(0) = W_1^{'}(1) = 0 \tag{4.7b}$$

where prime denotes differentiation with respect to the normalized spatial variable. The solution can be written in terms of the Green's function of the system as,

$$W_1 = \mu \Omega_1^2 W_1(1/2) G(\tilde{x}; \Omega_1) \tag{4.8}$$

where the Green's function is given by,

$$G(\tilde{x}; \Omega_1) = \frac{1}{D(\Omega_1)} \begin{cases} G_1(\tilde{x}; \Omega_1), & 0 \le \tilde{x} \le 1/2 \\ G_2(\tilde{x}; \Omega_2), & 1/2 \le \tilde{x} \le 1 \end{cases} \tag{4.9}$$

where,

$$\begin{aligned} G_1(\tilde{x}; \Omega_1) = {} & \left\{ \varphi_3\left(\Omega_1/2\right) \varphi_2\left(\Omega_1\right) - \varphi_2\left(\Omega_1/2\right) \varphi_3\left(\Omega_1\right) \right\} \varphi_2\left(\Omega_1 \tilde{x}\right) \\ & + \left\{ \varphi_2\left(\Omega_1/2\right) \varphi_2\left(\Omega_1\right) - \varphi_3\left(\Omega_1/2\right) \varphi_1\left(\Omega_1\right) \right\} \varphi_3\left(\Omega_1 \tilde{x}\right) \end{aligned}$$

$$\begin{aligned} G_2(\tilde{x}; \Omega_1) = {} & \left\{ \varphi_3\left(\Omega_1/2\right) \varphi_2\left(\Omega_1\right) - \varphi_2\left(\Omega_1/2\right) \varphi_3\left(\Omega_1\right) \right\} \varphi_2\left[ \Omega_1\left(1 - \tilde{x}\right) \right] \\ & + \left\{ \varphi_2\left(\Omega_1/2\right) \varphi_2\left(\Omega_1\right) - \varphi_3\left(\Omega_1/2\right) \varphi_1\left(\Omega_1\right) \right\} \varphi_3\left[ \Omega_1\left(1 - \tilde{x}\right) \right] \end{aligned}$$

$$D\left(\Omega_1\right) = 4\Omega_1^3 \left( \cosh \Omega_1 \cos \Omega_1 - 1 \right), \quad \varphi_1\left(\tilde{x}\right) = \sinh \tilde{x} + \sin \tilde{x},$$

$$\varphi_2\left(\tilde{x}\right) = \cosh \tilde{x} - \cos \tilde{x}, \quad \varphi_3\left(\tilde{x}\right) = \sinh \tilde{x} - \sin \tilde{x},$$

Then, by projecting equation (4.5a) onto the fundamental mode shape and using the following mass-orthogonality and stiffness-orthogonality conditions,

$$\int_0^1 \left[1+\mu\tilde{\delta}(\tilde{x}-1/2)\right] W_1^2\, d\tilde{x} = 1, \quad \int_0^1 W_1'''' W_1\, d\tilde{x} = \Omega_1^2 \tag{4.10}$$

the following Duffing equation describing the fundamental modal amplitude is recovered,

$$\begin{aligned} &\ddot{\phi}_1 + \frac{\Omega_1}{Q}\left[1-\mu W_1^2\left(1/2\right)\right]\dot{\phi}_1 + \beta\left\{-\int_0^1 W_1''\left(\tilde{x}\right) W_1\left(\tilde{x}\right) d\tilde{x} \int_0^1 \left[W_1\left(\tilde{x}\right)\right]^2 d\tilde{x}\right\}\phi_1^3 \\ &\quad = -\tilde{a}\Omega^2\left[\int_0^1 W_1\left(\tilde{x}\right) d\tilde{x} + \mu W_1\left(1/2\right)\right]\sin(\omega\tau) + \tilde{a}\frac{\Omega\Omega_1}{Q}\left[\int_0^1 W_1\left(\tilde{x}\right) d\tilde{x}\right]\cos(\omega\tau) \end{aligned} \tag{4.11}$$

Finally, by introducing the notation $\tilde{z}(\tau) = \phi_1(\tau) W_1\left(1/2\right)$, the single-degree-of-freedom nonlinear reduced-order model is obtained,

$$\tilde{z}'' + \tilde{c}_e \tilde{z}' + \tilde{k}_e \tilde{z} + \tilde{k}_3 \tilde{z}^3 = \tilde{b}\Omega^2 \sin(\Omega\tau) + \tilde{d}\Omega_1\Omega\cos(\Omega\tau) \tag{4.12}$$

where,

$$\begin{aligned} &\tilde{c}_e = \frac{\Omega_1}{Q}\left[1-\mu W_1^2\left(1/2\right)\right], \quad \tilde{k}_e = \Omega_1^2, \quad \tilde{b} = -\ \left[\int_0^1 W_1\left(\tilde{x}\right) d\tilde{x} + \mu W_1\left(1/2\right)\right] \\ &\tilde{d} = \frac{\tilde{a}}{Q} W_1\left(1/2\right)\int_0^1 W_1\left(\tilde{x}\right) d\tilde{x}, \quad \tilde{k}_3 = \frac{\beta}{W_1^2\left(1/2\right)}\left\{-\int_0^1 W_1''\left(\tilde{x}\right) W_1\left(\tilde{x}\right) d\tilde{x}\int_0^1 \left[W_1\left(\tilde{x}\right)\right]^2 d\tilde{x}\right\} \end{aligned} \tag{4.13}$$

An interesting observation is that, due to the harmonic base excitation, there are two forcing terms on the right-hand-side of the reduced model (4.12) depending linearly and quadratically on the forcing frequency $\Omega$. This means that the overall amplitude of the combined forcing terms increases with increasing $\Omega$.

## 4.2 Theoretical prediction of a *no-drop phenomenon*

Beginning with the reduced order model of the beam stated in equations (4.12) and (4.13), the second term on the right-hand side of equation (4.12) is neglected since it is trivially small compared to the other forcing term present and recover the equation

$$\tilde{z}'' + \tilde{c}_e \tilde{z}' + \tilde{k}_e \tilde{z} + \tilde{k}_3 \tilde{z}^3 = \tilde{b}\Omega^2 \sin\left(\Omega\tau\right) \tag{4.14}$$

The forcing term proportional to $\tilde{d}$ in equation (4.12) is neglected because attention is restricted to systems with $Q$-factors on the order of 100 or higher ($\Rightarrow \tilde{d} << \tilde{b}$). I now take a one term expansion in the displacement at the center of the beam, $\tilde{z} = \tilde{A}\sin\left(\Omega\tau - \varphi\right)$, and balance the harmonics to obtain an approximate frequency-amplitude relation in the beam,

$$\frac{3}{4}\frac{\tilde{k}_3}{\Omega_1^2}\tilde{A}^3 = \left(\frac{\Omega^2}{\Omega_1^2} - 1\right)\tilde{A} + \frac{\tilde{b}\Omega^2}{\Omega_1^2}\sqrt{1 - \frac{\tilde{c}_e^2}{\tilde{b}^2\Omega^2}\tilde{A}^2} \tag{4.15}$$

The backbone curve of the frequency amplitude relation corresponds to the undamped, unforced system and hence is given by

$$\frac{3}{4}\frac{\tilde{k}_3}{\Omega_1^2}\tilde{A}^3 = \left(\frac{\Omega^2}{\Omega_1^2} - 1\right)\tilde{A} \tag{4.16}$$

At the intersection of the backbone curve and the frequency amplitude curve we have the point containing the drop frequency, $\Omega_\mathrm{d}$, and the drop amplitude, $\tilde{A}_\mathrm{d}$, and therefore the drop frequency is given by

$$\Omega_\mathrm{d} = \Omega_1 / \sqrt{1 - \frac{3\tilde{k}_3\tilde{b}^2}{4\tilde{c}_e^2}} \tag{4.17}$$

which gives real values only for $\tilde{b} \le \sqrt{\frac{4\tilde{c}_e^2}{3\tilde{k}_3}}$, indicating that there is no drop in the frequency amplitude curve for excitation amplitudes larger than a critical amplitude, $\tilde{a}_c$, given by

$$\tilde{a}_c = \frac{\sqrt{4\tilde{c}_e^2}}{\sqrt{3\tilde{k}_3}W_1(1/2)\left[\int_0^1 W_1(\tilde{x})d\tilde{x} + \mu W_1(1/2)\right]} \tag{4.18}$$

In order to verify this numerically, I construct computational frequency amplitude curves for the system by using parameters listed in Table 4.1. For the duration of this section, these system parameters will be used in all computational studies. According to equation (4.18), the critical excitation amplitude above which there is no drop frequency (for this set of parameters) is $a_c = 0.049\text{nm}$. The analytical and numerical results of forward frequency sweeps corresponding to $a = 0.03\text{nm}$, $a = 0.035\text{nm}$, $a = 0.045\text{nm}$ and $a = 0.05\text{nm}$ are compared in Fig. 4.2. We see that for $a < a_c$, there is strong correspondence between the theoretical and computational curves and that indeed there is a drop in the computational frequency amplitude curve as predicted. In contrast, for the case of $a > a_c$, there is no drop frequency within the large range of frequencies considered. This provides some numerical verification of the theoretically predicted no-drop phenomenon resulting from the harmonic balance analysis.

| | |
|---|---|
| Mass density of the beam | $\rho = 2{,}330\text{kg/m}^3$ |
| Young's modulus of the beam | $E = 169\text{GPa}$ |
| Half-length | $L = 25\mu\text{m}$ |
| Beam thickness | $t = 200\text{nm}$ |
| Beam width | $w = 20\mu\text{m}$ |
| Mass ratio of the concentrated mass to the mass of the rest of the beam | $\mu = 20$ |
| Q-factor | $Q = 100$ |

*Table 4.1. System parameters used in the computational study of the beam.*

In order to gain a physical understanding of this phenomenon, I consider the same system but with harmonic excitation applied directly to the center of the beam rather than the base. The reduced order equation of motion in this case is

$$\tilde{z}'' + \tilde{c}_e \tilde{z}' + \tilde{k}_e \tilde{z} + \tilde{k}_3 \tilde{z}^3 = q \sin\left(\Omega \tau\right) \tag{4.19}$$

where, here, $\tilde{z}$ is the *absolute* displacement at the center of the beam and $q$ is the (fixed) nondimensional force. Holding all system parameters fixed, the drop frequency is a function only of $q$, and for each value of $q$ there exists a drop frequency given by

$$\Omega_{\mathrm{d}}\left(q\right) = \sqrt{\frac{\tilde{k}_e}{2}\left(1 + \sqrt{1 + \frac{3\tilde{k}_3 q^2}{\Omega_1^4 \tilde{c}_e^2}}\right)}\,. \tag{4.20}$$

An increase in the forcing level results in an increase of the drop frequency as illustrated in Fig. 4.3. For base excitation, the forcing level is proportional to the square of the excitation frequency, $q = \tilde{b}\Omega^2$ and, hence, for a fixed base excitation I can compute the drop frequency as a function of the excitation frequency,

$$\Omega_{\mathrm{d}}\left(q\left(\Omega\right)\right) = \Omega_{\mathrm{d}}\left(\Omega\right) = \sqrt{\frac{\tilde{k}_e}{2}\left(1 + \sqrt{1 + \frac{3\tilde{k}_3 \tilde{b}^2 \Omega^4}{\omega_1^4 \tilde{c}_e^2}}\right)} \tag{4.21}$$

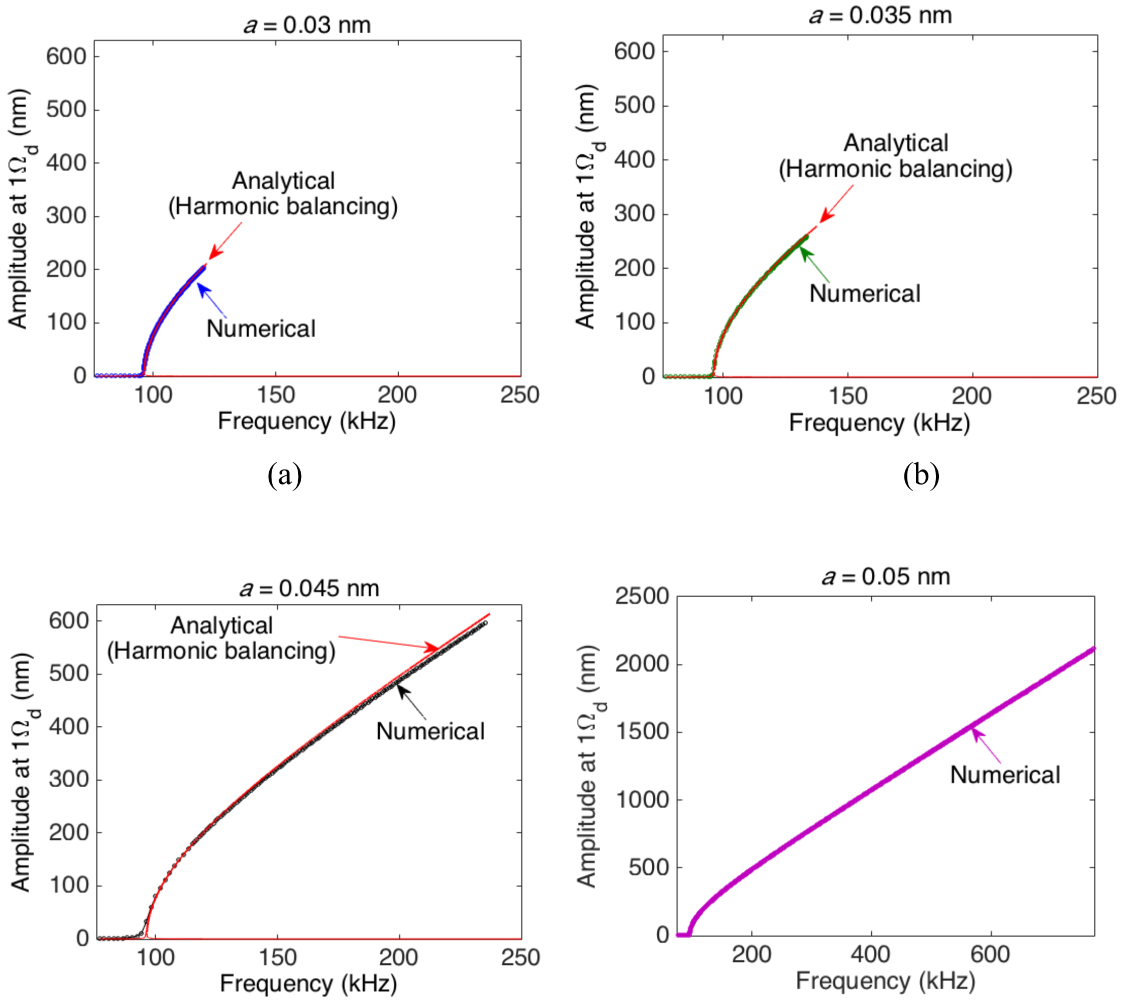

(a) (b)

(c) (d)

*Figure 4.2: Computational forward frequency sweeps and analytical frequency amplitude curves at excitation amplitudes of (a)* $a = 0.03\text{nm}$, *(b)* $a = 0.035\text{nm}$, *(c)* $a = 0.045\text{nm}$ *and (d)* $a = 0.05\text{nm}$.

In Fig. 4.4, the drop frequency as a function of the excitation frequency is plotted for several different base excitation amplitudes. In this plot, a drop occurs at $\Omega$ if $\Omega_\text{d}(\Omega) = \Omega$. Interestingly, we see that for $a < a_c = 0.049\text{nm}$ there indeed exists an $\Omega$ for which $\Omega_\text{d}(\Omega) = \Omega$; but for $a > a_c$, $\Omega_\text{d}(\Omega) > \Omega$ for all $\Omega$, and hence there is no drop frequency.

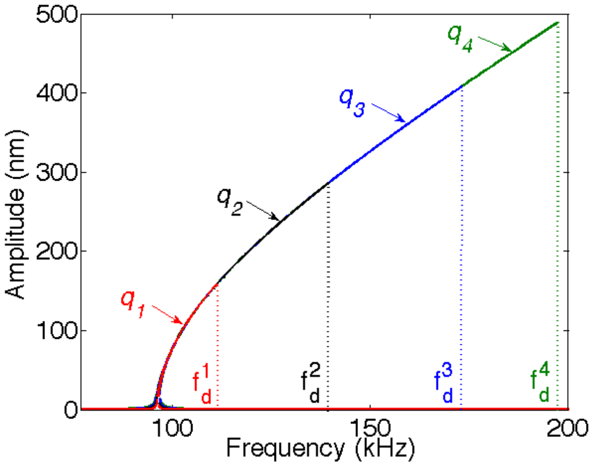

*Figure 4.3: Computational frequency amplitude curves for* $q_1 < q_2 < q_3 < q_4$. *The corresponding drop frequencies are denoted by* $\mathrm{f}_\mathrm{d}^i$, *where* $\mathrm{f}_\mathrm{d}(q) = \frac{\Theta}{2\pi}\Omega_\mathrm{d}$ *and* $\mathrm{f}_\mathrm{d}^i \equiv \mathrm{f}_\mathrm{d}(q_i)$.

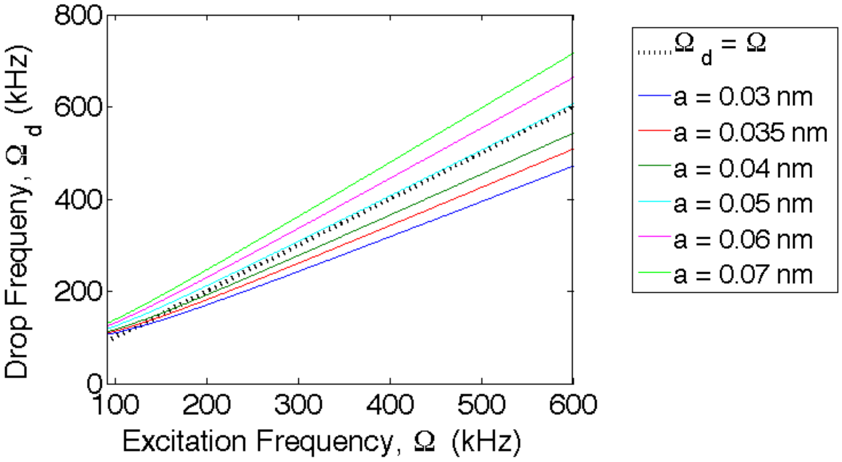

*Figure 4.4. Drop frequency associated with a fixed forcing level corresponding to* $q = \tilde{b}\Omega^2$ *versus excitation frequency for several different excitation amplitudes. For* $a < a_c = 0.049\text{nm}$, *the drop frequency occurs at* $\Omega_\mathrm{d}(\Omega) = \Omega$ *and for* $a > a_c$, *there is no drop frequency.*

### 4.3 Characterization of the nonlinearity in terms of system parameters

The next step in our analysis focuses on quantifying the nonlinearity in terms of system parameters. I restrict attention to the case when $a > a_c$ and introduce a parameter, $\lambda$, as a measure of the nonlinearity

$$\lambda = \frac{\bar{f} - f_1}{\mathrm{A}\left(\bar{f}\right)} = \frac{\hat{f}}{\mathrm{A}\left(\bar{f}\right)} \tag{4.22}$$

where $f_1$ is the linearized frequency, $\bar{f}$ is some frequency larger than $f_1$, $\hat{f} = \bar{f} - f_1$ is their difference and $A\left(\bar{f}\right)$ is the response amplitude at $\bar{f}$ as depicted in Fig. 4.5. For simplicity, $A\left(\bar{f}\right)$ is taken to be the response along the backbone curve and therefore, $\lambda$ can be written in terms of system parameters as

$$\lambda = \frac{\sqrt{6}}{32\pi}\sqrt{\frac{E}{\rho}}\frac{1}{L^2}F(\mu)\sqrt{\frac{\pi\hat{f}}{\pi\hat{f} + \frac{1}{8\sqrt{3}}\sqrt{\frac{E}{\rho}}\frac{t}{L^2}\Omega_1(\mu)}},$$

$$F(\mu) = \frac{1}{W_1(1/2)}\sqrt{-\int_0^1 W_1'' W_1 \; d\tilde{x} \int_0^1 \left(W_1'\right)^2 d\tilde{x}} \tag{4.23}$$

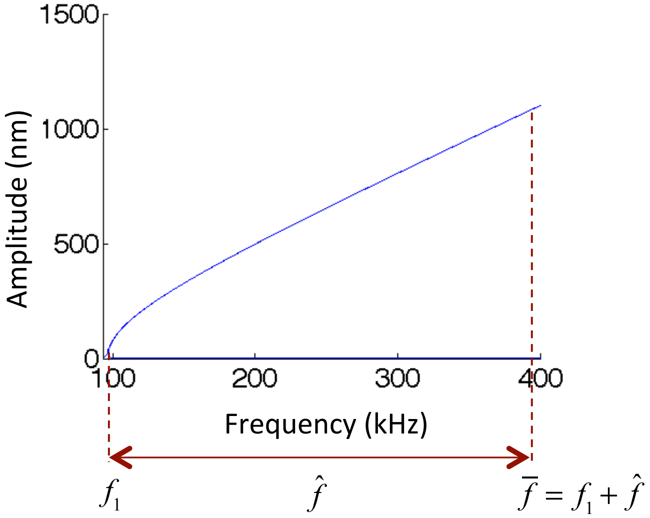

*Figure 4.5: Amplitude versus frequency curve for $a > a_c$. The quantity $\lambda$ is a measure of the bending of the frequency response curve.*

Notice that $\lambda$ does not depend on *w* (the beam width) but in practice, an increase in *w* may cause a decrease in $Q$. The dependence of $\lambda$ on $\hat{f}$ is of the form

$$\lambda \sim \sqrt{\frac{\hat{f} / a}{\hat{f} / a + 1}}, \quad a = \frac{1}{\pi 8\sqrt{3}}\sqrt{\frac{E}{\rho}}\frac{t}{L^2}\Omega_1(\mu)$$

so when $\hat{f} < a$, $\lambda$ increases with increasing $\hat{f}$ and when $\hat{f} >> a$, $\lambda$ is nearly independent of $\hat{f}$. This is due to the fact that slope of the backbone curve decreases rapidly (with respect to increasing frequency) in the immediate vicinity of the linear frequency, but nearly saturates for frequencies considerably larger than the linear frequency. The dependence of $\lambda$ on all other parameters is illustrated in Fig. 4.6. We see that a decrease in $\lambda$, $L$ and *t* (the beam thickness) and an increase in the ratio $E / \rho$ result in an increase of $\lambda$. The relationship between $\lambda$ and $\mu$ raises the question, what is the significance of the concentrated mass? As will be shown, the function of the concentrated mass is to lower the critical excitation amplitude to a level that is physically practical.

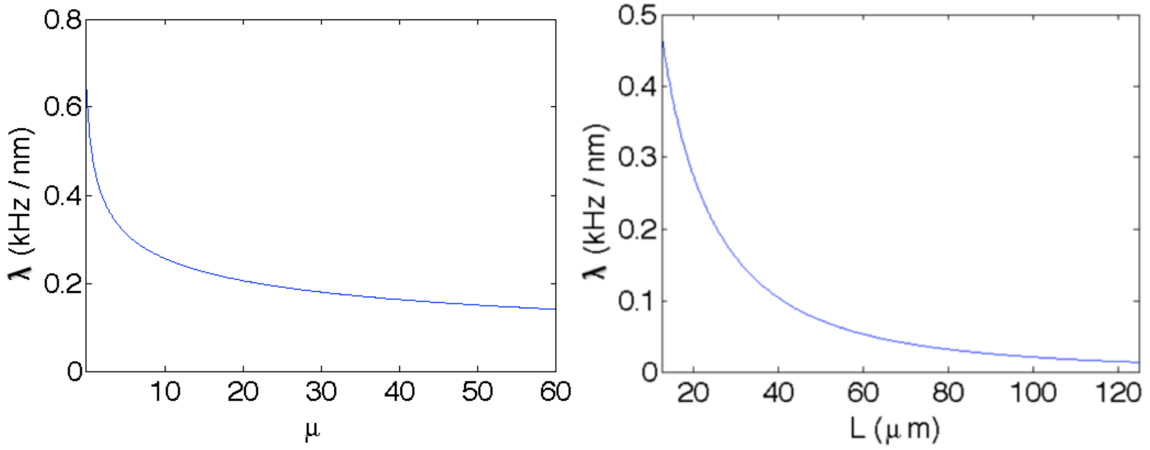

(a) (b)

*Figure 4.6: A measure of the nonlinearity, $\lambda$, versus the mass ratio of the concentrated mass to the mass of the rest of the beam, $\mu$, (a); the half-length of the beam, $L$, (b); the thickness of the beam, t, (c) and the ratio of the Young's modulus to the density of the beam, $E / \rho$, (d).*

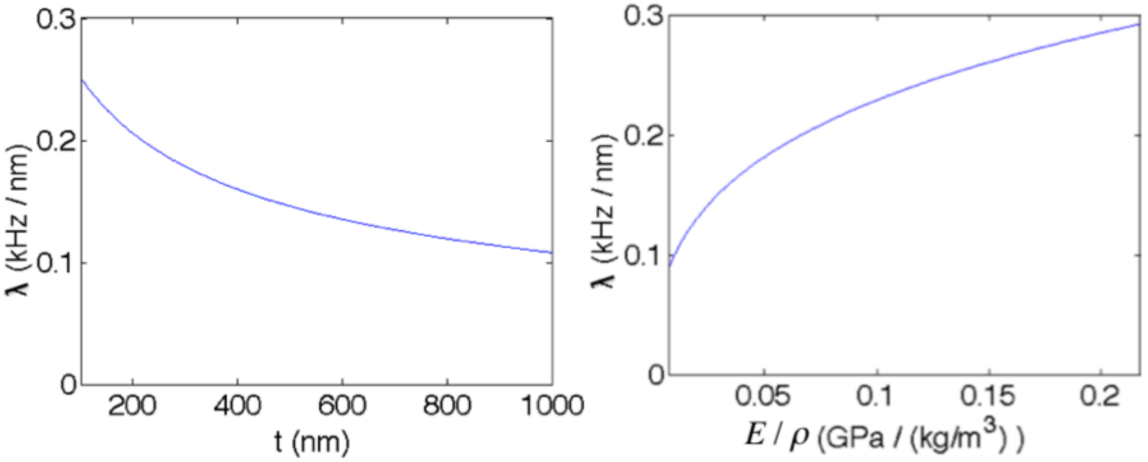

(c) (d)

*Figure 4.6 (cont.)*

### 4.4 The role of the concentrated mass

The critical excitation amplitude required to achieve the no drop phenomenon can also be written in terms of the system parameters,

$$a_c = \frac{2}{3\sqrt{2}}\frac{t}{Q}p(\mu), \quad p(\mu) = \frac{\Omega_1(\mu)\left[1 - W_1^2(1/2)\right]}{\left[\int_0^1 W_1 \; d\tilde{x} + \mu W_1(1/2)\right]\sqrt{-\int_0^1 W_1'' W_1 \; d\tilde{x} \int_0^1 \left(W_1'\right)^2 d\tilde{x}}} \tag{4.24}$$

For the thickness and *Q*-factor considered in this section, the critical amplitude as a function of the mass ratio is shown in Fig. 4.7. Clearly, the critical amplitude decreases dramatically as the mass ratio increases from 0 to around 10. For a mass ratio of 0 (no concentrated mass), the critical amplitude is nearly 3 nm, which is well above the commonly used excitation amplitudes on the order of 0.1 nm. This means that, without the concentrated mass, it would not be physically feasible to achieve the no drop phenomenon, hence its critical role in the beam design.

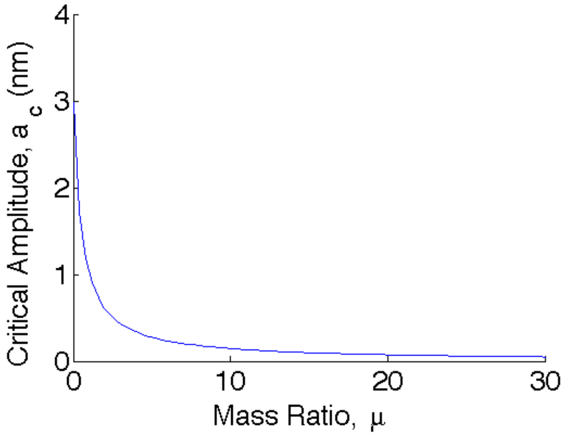

*Figure 4.7. Critical excitation amplitude above which there is no drop frequency versus the mass ratio of the concentrated mass to the mass of the rest of the beam.*

## 4.5 Practical limitations

### 4.5.1 Theoretical basins of attraction

One practical limitation to exploiting the *no drop phenomenon* may be the domain of attraction corresponding to the high-amplitude, upper solution branch as the drive frequency increases. Above the critical excitation amplitude, the upper solution branch may indeed exist for all drive frequencies (larger than the linearized frequency) but the set of initial conditions that give rise to this solution may be impractically small. In order to study this limitation, I use the method of averaging to study the domains of attraction at several different drive frequencies and excitation amplitudes. To this end, I assume a solution to (4.14) of the form

$$\tilde{z} = \tilde{A}(\tau)\sin\left[\Omega\tau - \varphi(\tau)\right], \quad \tilde{z}' = \tilde{A}(\tau)\Omega\cos\left[\Omega\tau - \varphi(\tau)\right] \tag{4.25}$$

which gives the following set of coupled ODEs governing the so-called slow flow of the dynamics

$$\tilde{A}' = \frac{\cos\theta}{\Omega}\left[\tilde{A}(\Omega^2 - \tilde{k}_{\mathrm{e}}) - \tilde{c}_{\mathrm{e}}\tilde{A}\Omega\cos\theta - \tilde{k}_3\tilde{A}^3\sin^3\theta + \tilde{b}\Omega^2\sin(\Omega\tau)\right] \tag{4.26a}$$

$$\varphi' = \frac{\sin\theta}{\tilde{A}\Omega}\left[\tilde{A}(\Omega^2 - \tilde{k}_{\mathrm{e}}) - \tilde{c}_{\mathrm{e}}\tilde{A}\Omega\cos\theta - \tilde{k}_3\tilde{A}^3\sin^3\theta + \tilde{b}\Omega^2\sin(\Omega\tau)\right] \tag{4.26b}$$

where $\theta = \Omega\tau - \varphi(\tau)$. By assuming sufficient time-scale separation between the "fast" dynamics corresponding to the harmonic motion at frequency $\Omega$, and the relatively "slow" dynamics corresponding to the modulation envelope characterized by (4.26), the right-hand-sides of 4.26a and 4.26b can be averaged. Specifically, it is assumed that $\tilde{A}$ and $\varphi$ remain constant over each "fast" oscillation cycle and that $\tilde{A}'$ and $\varphi'$ are equal to their *average* values over each "fast" oscillation cycle:

$$\tilde{A}'_{\mathrm{av}} = \frac{1}{2\pi}\int_0^{2\pi}\frac{\cos\theta}{\Omega}\left[\tilde{A}_{\mathrm{av}}(\Omega^2 - \tilde{k}_{\mathrm{e}}) - \tilde{c}_{\mathrm{e}}\tilde{A}_{\mathrm{av}}\Omega\cos\theta - \tilde{k}_3\tilde{A}^3_{\mathrm{av}}\sin^3\theta + \tilde{b}\Omega^2\sin(\theta + \varphi_{\mathrm{av}})\right]d\theta \tag{4.27a}$$

$$\varphi'_{\mathrm{av}} = \frac{1}{2\pi}\int_0^{2\pi}\frac{\sin\theta}{\tilde{A}_{\mathrm{av}}\Omega}\left[\tilde{A}_{\mathrm{av}}(\Omega^2 - \tilde{k}_{\mathrm{e}}) - \tilde{c}_{\mathrm{e}}\tilde{A}_{\mathrm{av}}\Omega\cos\theta - \tilde{k}_3\tilde{A}^3_{\mathrm{av}}\sin^3\theta + \tilde{b}\Omega^2\sin(\theta + \varphi_{\mathrm{av}})\right]d\theta \tag{4.27b}$$

The amplitude, $\tilde{A}_{\mathrm{av}}$, and phase, $\varphi_{\mathrm{av}}$, that result from this analysis are not exact; rather they are the approximate, averaged values. The averaging analysis is based on the fundamental assumption that $\tilde{A}$ and $\varphi$ are slowly varying (with respect to the fast dynamics) and, hence, the smaller $\tilde{A}'$ and $\varphi'$ are, the better the averaged values approximate the exact solution. In (4.26) we see that $\tilde{A}'$ and $\varphi'$ are proportional to $\Omega^2 - \tilde{k}_{\mathrm{e}}$, which means that, as the perturbation in the drive frequency from the linearized resonant frequency decreases, the accuracy of the averaging analysis improves.

Upon evaluating the integrals in (4.27), the following set of nonlinear, autonomous first order differential equations are recovered as

$$\tilde{A}'_{\mathrm{av}} + \frac{1}{2}\tilde{c}_{\mathrm{e}}\tilde{A}_{\mathrm{av}} - \frac{1}{2}\tilde{b}\Omega\sin(\varphi_{\mathrm{av}}) = 0 \tag{4.28a}$$

$$\Omega\tilde{A}_{\mathrm{av}}\varphi'_{\mathrm{av}} + \frac{1}{2}\left(\tilde{k}_{\mathrm{e}} - \Omega^2\right)\tilde{A}_{\mathrm{av}} + \frac{3}{8}\tilde{k}_3\tilde{A}^3_{\mathrm{av}} - \frac{1}{2}\tilde{b}\Omega^2\cos(\varphi_{\mathrm{av}}) = 0 \tag{4.28b}$$

The steady-state amplitude and phase correspond to the equilibrium point(s) of (4.28) for which $\tilde{A}'_{\mathrm{av}} = \varphi'_{\mathrm{av}} = 0$. Specifically, the equilibrium points satisfy

$$\tilde{c}_{\mathrm{e}}\tilde{A}_{\mathrm{eq}} = \tilde{b}\Omega\sin(\varphi_{\mathrm{eq}}) \tag{4.29a}$$

$$\left(\tilde{k}_{\mathrm{e}} - \Omega^2\right)\tilde{A}_{\mathrm{eq}} + \frac{3}{4}\tilde{k}_3\tilde{A}^3_{\mathrm{eq}} = \tilde{b}\Omega^2\cos(\varphi_{\mathrm{eq}}) \tag{4.29b}$$

The relations in (4.29) can be used to recover the frequency-amplitude and phase-amplitude relations at steady state

$$\left[\tilde{c}_{\mathrm{e}} + \left(\Omega^2 - \tilde{k}_{\mathrm{e}} - \frac{3}{4}\tilde{k}_3\tilde{A}^2_{\mathrm{ss}}\right)^2\right]\tilde{A}^2_{\mathrm{ss}} = \tilde{b}^2\Omega^4 \tag{4.30a}$$

$$\tan(\varphi_{\mathrm{ss}}) = \frac{-\Omega\tilde{c}_{\mathrm{e}}}{\Omega^2 - \tilde{k}_{\mathrm{e}} - \frac{3}{4}\tilde{k}_3\tilde{A}^2_{\mathrm{ss}}} \tag{4.30b}$$

The stability of the steady-state response can be determined by studying the stability of the equilibrium points of (4.28). To this end, I introduce small perturbations $\xi$ and $\psi$ from equilibrium in the amplitude and phase, respectively,

$$\tilde{A}_{\mathrm{av}} = \tilde{A}_{\mathrm{eq}} + \xi, \quad \varphi_{\mathrm{av}} = \varphi_{\mathrm{eq}} + \psi, \quad |\xi|,|\psi| \ll 1 \tag{4.31}$$

and substitute (4.31) into (4.28) to obtain the linearized first order differential equations, which govern the perturbations $\xi$ and $\psi$,

$$\begin{Bmatrix} \xi' \\ \psi' \end{Bmatrix} = \begin{bmatrix} -\dfrac{\tilde{c}_{\mathrm{e}}}{2} & \dfrac{\tilde{b}\Omega}{2}\cos(\varphi_{\mathrm{eq}}) \\ \dfrac{\Omega^2 - \tilde{k}_{\mathrm{e}}}{2\Omega A_{\mathrm{eq}}} - \dfrac{9\tilde{k}_3 A_{\mathrm{eq}}}{8\Omega} & -\dfrac{\tilde{b}\Omega}{2A_{\mathrm{eq}}}\sin(\varphi_{\mathrm{eq}}) \end{bmatrix} \begin{Bmatrix} \xi \\ \psi \end{Bmatrix} \tag{4.32}$$

This linear set of homogenous first order differential equations has solutions of the form

$$\xi = \Xi e^{\lambda t}, \quad \psi = \Psi e^{\lambda t} \tag{4.33}$$

Substituting (4.33) and (4.29) into (4.32), the expression satisfied by $\lambda$ is obtained as

$$\begin{vmatrix} -\dfrac{\tilde{c}_{\mathrm{e}}}{2} - \lambda & \dfrac{A_{\mathrm{eq}}}{2\Omega}\left(\Omega^2 - \tilde{k}_{\mathrm{e}} - \dfrac{9}{4}\tilde{k}_3 A_{\mathrm{eq}}^2\right) \\ \dfrac{1}{2\Omega A_{\mathrm{eq}}}\left(\Omega^2 - \tilde{k}_{\mathrm{e}} - \dfrac{9}{4}\tilde{k}_3 A_{\mathrm{eq}}^2\right) & -\dfrac{\tilde{c}_{\mathrm{e}}}{2} - \lambda \end{vmatrix} = 0$$

and expanding the determinant gives the equation

$$\lambda^2 + \tilde{c}_e \lambda + \frac{1}{4}\tilde{c}_e^2 + \frac{1}{4\Omega^2}\left(\Omega^2 - \tilde{k}_e - \frac{9}{4}\tilde{k}_3 A_{\mathrm{eq}}^2\right)\left(\Omega^2 - \tilde{k}_e - \frac{3}{4}\tilde{k}_3 A_{\mathrm{eq}}^2\right) = 0 \tag{4.34}$$

For stability, both eigenvalues must have non-positive real parts and hence, the steady-state response is unstable when

$$\Lambda = \frac{1}{4}\tilde{c}_{\mathrm{e}}^2 + \frac{1}{4\Omega^2}\left(\Omega^2 - \tilde{k}_{\mathrm{e}} - \frac{9}{4}\tilde{k}_3 A_{\mathrm{eq}}^2\right)\left(\Omega^2 - \tilde{k}_{\mathrm{e}} - \frac{3}{4}\tilde{k}_3 A_{\mathrm{eq}}^2\right) < 0 \tag{4.35}$$

The frequency-amplitude and frequency-phase relations at steady-state are given by (4.30), and the local stability of the steady-state solutions are determined by (4.33). In Fig. 4.8, the resonance curves are shown for an excitation amplitude of 0.3nm, which is below the critical level (Fig. 4.8a), and an excitation amplitude of 0.5nm, which is above the critical level (Fig. 4.8b). Again, the system parameters considered are stated in Table 4.1 for which the critical excitation amplitude is 0.495nm. The top row contains the steady-state amplitude versus drive frequency curves and the bottom row contains the steady-state phase (with respect to the excitation) versus drive frequency. For drive frequencies within the broadband resonance, there exist three equilibrium points of (4.28): two stable spirals and one unstable saddle. One of the stable equilibrium points is on the high-amplitude, upper solution branch and the other is on the low-amplitude, lower solution branch. For drive frequencies above the drop-down bifurcation point, there exists a single equilibrium point corresponding to a stable spiral. The blue curves correspond to the stable steady-state solutions (i.e., the stable equilibrium points of (4.28)) and the red curve corresponds to the unstable steady-state solutions (the unstable equilibrium points of (4.28)). Since the damping is relatively low (Q=100), the amplitude on the stable, upper solution branch is only slightly larger than the amplitude on the unstable solution branch for drive frequencies within the broadband and not in the immediate vicinity of the linearized frequency. As a result, the red amplitude curves in Fig. 4.8 nearly overlap with the high-amplitude blue curves. In contrast, we see a distinct difference in the steady-state phase versus frequency curves.

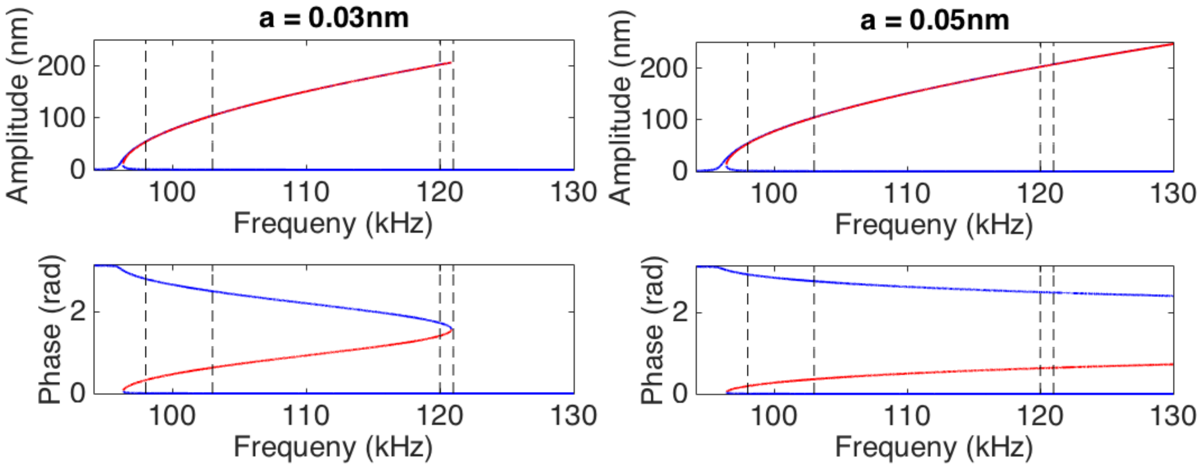

(a) (b)

*Fig. 4.8: Frequency-amplitude (top row) and phase-amplitude (bottom row) curves at steady state for (a) an excitation amplitude of 0.03nm and (b) an excitation amplitude of 0.05nm. The vertical dashed lines indicate the drive frequencies considered in the theoretical domains of attraction shown in Fig. 4.9 and 4.10. The stable solution branches correspond to the blue curves and the unstable branch corresponds to the red curve. Note that red curve partially covers the high-amplitude blue curve.*

When multiple solutions exist, the initial conditions determine which solution is physically realized. For a fixed excitation within the broadband, the domains of attraction for each solution and a global picture of the dynamics can be constructed by numerically computing the phase plane trajectories of (4.28). The phase plane trajectories at four different excitation frequencies are shown for $a = 0.5$nm in Fig. 4.9, and for $a = 0.3$nm in Fig.4.10. The four excitation frequencies considered are 98kHz, 103kHz, 120kHz and 121kHz, which are indicated by the vertical dashed lines in Fig. 4.8. The excitation amplitude 0.5nm is just above the critical excitation level and, hence, all four excitation frequencies are within the broadband resonance. In contrast, the excitation amplitude 0.3nm is below the critical amplitude, and the drop-down bifurcation frequency is 120.9kHz. This means that the excitation frequencies 98kHz, 103kHz and 120kHz are within the broadband where three solutions exist and the excitation frequency 121kHz is just outside the broadband where the single, low-amplitude solution exists.

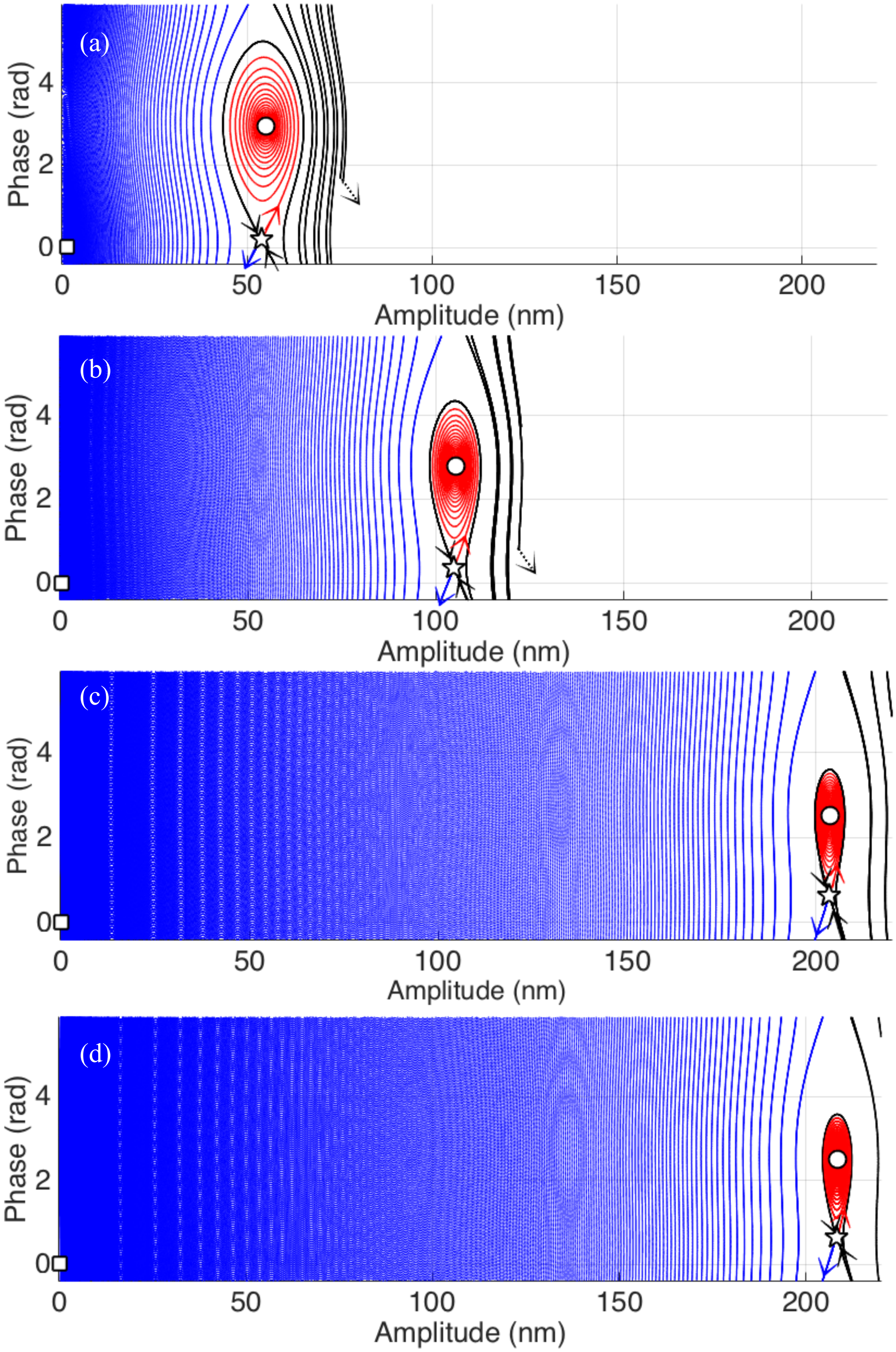

*Figure 4.9 : Theoretical domains of attraction  for a = 0.05nm at (a) 98kHz, (b) 103kHz, (c) 120kHz and (d) 121kHz.*

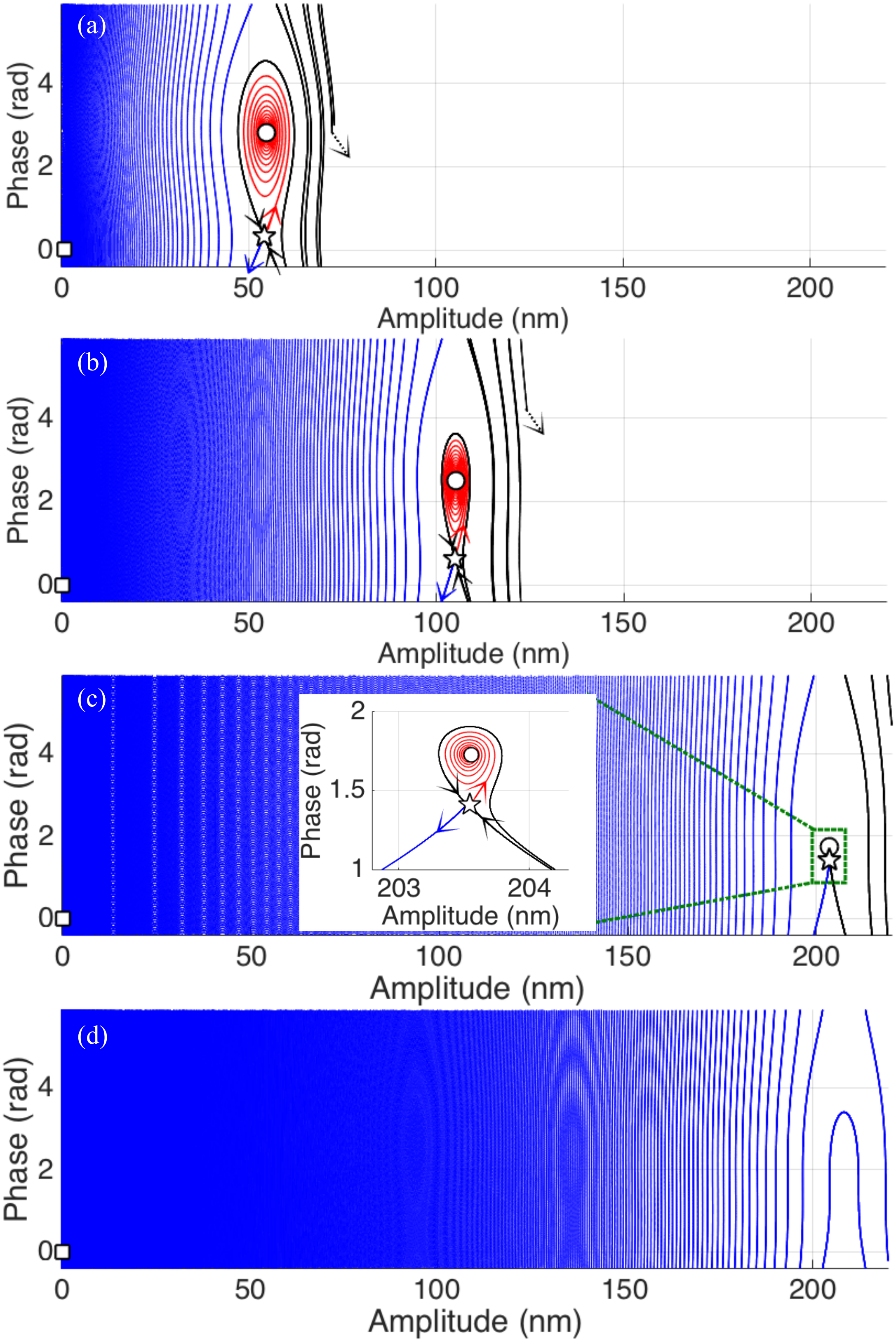

*Figure 4.10: Domains of attraction for a = 0.03nm at (a) 98kHz, (b) 103kHz, (c) 120kHz and (d) 121kHz.*

In Figs. 4.9 and 4.10, the low-amplitude stable spiral is indicated by a square marker, the high-amplitude stable spiral is indicated by a circle marker and the unstable saddle is indicated by a star marker. The domains of attraction for the two stable solutions are separated by the two separatrices, which are the black curves emanating from the saddle point. The saddle point is associated with two purely real eigenvalues: one positive and one negative. The separatrices correspond to the phase plane trajectories that lie along the eigenvector corresponding to the negative eigenvalue, in the vicinity of the saddle point. The arrows indicate the direction of the trajectories as time increases. Hence, any point along the separatricies will lead to the unstable saddle point as time passes. However, any perturbation from this path will give rise to one of the stable attractors, and for this reason, the saddle is not physically realizable. The red curves in Figs. 4.9 and 4.10 are the trajectories that emanate from the saddle and approach the high-amplitude response, whereas the blue curves are the trajectories that emanate from the saddle and approach the low-amplitude response. Close to the saddle point, the trajectories shown in red and blue lie along the eigenvector associated with the positive eigenvalue of the saddle. The separatrices partition the phase plane into two sections. The portion of the phase plane containing the red trajectory is the domain of attraction for the high-amplitude steady-state response, and the portion of the phase plane containing the blue trajectory is the domain of attraction for the low-amplitude response. The dashed arrows connected to the separatricies in Figs 4.8a, 4.8b, 4.9a, and 4.9b indicate that the trajectories indeed continue into the high amplitude portion of the phase plane, but are omitted in these figures since they are outside the area of interest.

Considering first the results corresponding $a = 0.5\text{nm}$ (Fig. 4.8), we see that the domains of attraction for the high-amplitude responses shrink as the excitation frequency increases. This underscores a practical limitation of achieving the no drop phenomenon since, for sufficiently small high-amplitude domains of attraction, small perturbations in the state variables will cause unwanted transitions to the low-amplitude response. In practice, the bandwidth of the broadband resonance may be restricted by the size of the domain of attraction corresponding to the high-amplitude response. This means that, the bandwidth of the broadband resonance will be finite, and that the size of the bandwidth may be dictated by the domains of attraction. By comparing Figs. 4.8a-4.8c with 4.9a-4.9c, respectively, we can see that as the excitation amplitude increases, the domain of attraction for the high-amplitude response increases. This trend indicates that the practical limitation owing to the domains of attraction may be overcome slightly by operating at an excitation amplitude even higher than 0.5nm, say 1nm. This will increase the effective bandwidth but, ultimately, the drop-down bifurcation will occur due to the impractically small size of the high-amplitude domain of attraction for a sufficiently large drive frequency.

In Figs. 4.9c and 4.9d, we see that the high-amplitude stable spiral and the unstable saddle coalesce as the drive frequency increases from 120kHz to 121kHz, and at 121kHz only the low-amplitude solution exists. As discussed in Section 4.2, this bifurcation occurs because, at 120.9kHz, the drop-down frequency associated with the forcing level $\tilde{b}\Omega^2$ is equal to the drive frequency. This type of bifurcation does not occur at $a = 0.5\text{nm}$ for any drive frequency, since it is above the critical amplitude.

### 4.5.2 The effect of noise on branch selection

Noise has an effect on nonlinear sensors for which there is no counterpart in linear mass sensors. For a nonlinear sensor, in addition to influencing the minimum detectable shift in observables, noise effects the branch selection within the bi-stable bandwidth by causing perturbations in the initial state of the resonator. In fact, stochastic variations in the response amplitude and phase effectively blur the separatrix between the basins of attraction for the two stable solutions (Asaleem and Younis, 2010; Kumar et al., 2012; Kozinsky et al., 2007). As the domain of attraction for the upper solution branch shrinks, the dynamics on the upper solution branch become increasingly susceptible to undesirable branch jumping in the presence of noise. For this reason, noise may ultimately trigger a drop down bifurcation as the drive frequency increases, and this effect will become more pronounced as the high-amplitude domain of attraction decreases in size.

### 4.6.3 Internal resonances

In general, internal resonance is possible in a nonlinear resonator whenever two or more modal frequencies are commensurable or nearly commensurable. That is, the necessary conditions for internal resonance occur when $\omega_q = m\omega_p + n\omega_r$, where $\omega_q$, $\omega_p$ and $\omega_r$ correspond to distinct frequencies associated with different vibration modes and $m$ and $n$ are integers. Depending on the type of nonlinearity present, these commensurable relationships may cause the corresponding modes to be nonlinearly coupled, and the nonlinear coupling between modes can cause energy exchanges between the modes involved in the internal resonance (Nayfeh and Mook, 1995; Vakakis et al., 2008).

If an internal resonance is excited in the proposed resonator design within the broadband of the fundamental flexural mode, the energy input to the fundamental flexural mode may be transferred to the other mode(s) participating in the internal resonance. This energy transfer can then trigger a drop down bifurcation in the response of the fundamental flexural mode. In recent studies, this very phenomenon was reported in an electrostatically actuated resonant microsensor (Antoinio et al., 2012; Chen et al., 2017). This system also exhibits geometric nonlinearity, but instead of base excitation, electrostatic actuation is imparted directly to the device. It was shown that the fundamental flexural mode of this device exhibits strong hardening behavior and, in some cases, the drop down bifurcation results from an internal resonance with the fundamental torsional mode. Further, Antonio et al. showed that, for sufficiently large excitation levels, the drop bifurcation is overcome by the large energy input, and for relatively low excitation levels, the drop frequency saturates due to the internal resonance.

### 4.5.4 Nonlinear damping

Finally, nonlinear damping may also serve as a practical limitation to the *no drop phenomenon*. Interestingly, I find that by including an additional nonlinear damping term in the reduced order model, there is in fact a theoretically predicted drop down bifurcation above the critical excitation amplitude. Yet still, theoretical analysis predicts a sudden increase in the drop frequency at the threshold amplitude, for sufficiently small nonlinear damping coefficients.

Specifically, the nonlinear damping considered is proportional to the product of the square of the displacement and the velocity. Details regarding the theoretical model and analysis are presented in Sections 4.6 and 4.7.

## 4.6 Experimental verification of the ultra-wide broadband resonance in heterogeneous microbeams

Here I experimentally show the existence of ultra-wide broadband resonances in nonprismatic, heterogeneous microbeam resonators. A scanning electron microscope (SEM) image of the system under consideration is shown in Fig. 4.4a. The system consists of a *Si* microcantilever that is connected by a polymer bridge to a fixed base. As discussed in a previous study by Asadi et al. (2017), by design, the *Si* cantilever has a significantly lower bending stiffness than the polymer attachment and, as a result, transverse loading induces a relatively larger bending deflection of the *Si* cantilever as compared to the polymer attachment. Similarly, the axial stiffness of the polymer bridge is designed to be considerably lower than that of the *Si* cantilever so that an axial force primarily stretches the polymer bridge and not the *Si* cantilever. The net effect is that harmonic excitation near a bending mode induces large flexural motion of the *Si* cantilever and relatively large axial stretching of the polymer attachment. In other words, under harmonic excitation, the *Si* cantilever behaves as a linear, damped harmonic oscillator, which is constrained in the transverse direction by a viscoelastic element (see Fig. 1b). Details regarding the fabrication of these devices are presented in Asadi et al., 2017.

I am particularly interested in the fundamental bending mode of the system and, hence, the parameters $k_1$, $c_1$ and $m$ correspond to the effective stiffness, damping coefficient and mass of the fundamental bending mode of the *Si* cantilever. The parameters $k_2$ and $c_2$ denote the effective stiffness and damping coefficient of the axial stretching of the polymer bridge. When this microcantilever-polymer system vibrates in its fundamental bending mode, the large vertical displacement of the free end of the *Si* cantilever causes large axial deflection of the polymer attachment and in turn, results in strong geometric nonlinearity. Assuming harmonic excitation applied to the base (i.e., to the fixed end of the *Si* cantilever and the fixed end of the polymer bridge) and including only leading order nonlinearity, the equation of motion governing transverse motion of the cantilever near the fundamental bending mode is given by (Anderson et al., 2012; Asadi et al., 2017; Cho et al., 2012; Jeong et al., 2013)

$$m\ddot{y}+c_1\dot{y}+k_1y+k_3y^3+c_3\dot{y}y^2=ma\omega^2\cos\omega t,\quad k_3=\frac{k_2}{2L_2^2},\quad c_3=\frac{c_2}{L_2^2} \tag{4.36}$$

where $L_2$ is the length of the polymer attachment and $y$ is the relative displacement of the free end of the *Si* cantilever with respect to the base. Equation (4.36) is in the form of the Duffing equation having cubic stiffness, with an additional nonlinear damping term, $c_3\dot{y}y^2$. The cubic stiffness and the nonlinear damping term originate from the axial stretching of the polymer attachment and are of geometric origin. Further, note that the excitation level is not fixed, but rather is proportional to the square of the drive frequency due to the presence of base excitation.

Aiming to experimentally verify the theoretical predictions outlined in Section 4.1, I experimentally investigate the dynamics of the device shown in Fig. 4.11 near its fundamental bending mode. It is important to note that the reduced order equation of motion for this system, stated in (4.36), is not exactly the same as the equation of motion considered in Section 4.1, which modeled a doubly clamped beam having a concentrated mass at the center. The difference is that equation (4.36) has one additional term corresponding to the nonlinear damping. Nevertheless, since the reduced order equation of motion for the microcantilever-polymer system is quite similar to that of a classic Duffing oscillator, it is reasonable to expect the microcantilever-polymer system to behave qualitatively similar to the doubly clamped beam in response to harmonic base excitation. Our goal is to see if the microcantilever-polymer system shows evidence of a threshold base excitation amplitude above which the resonant bandwidth expands substantially.

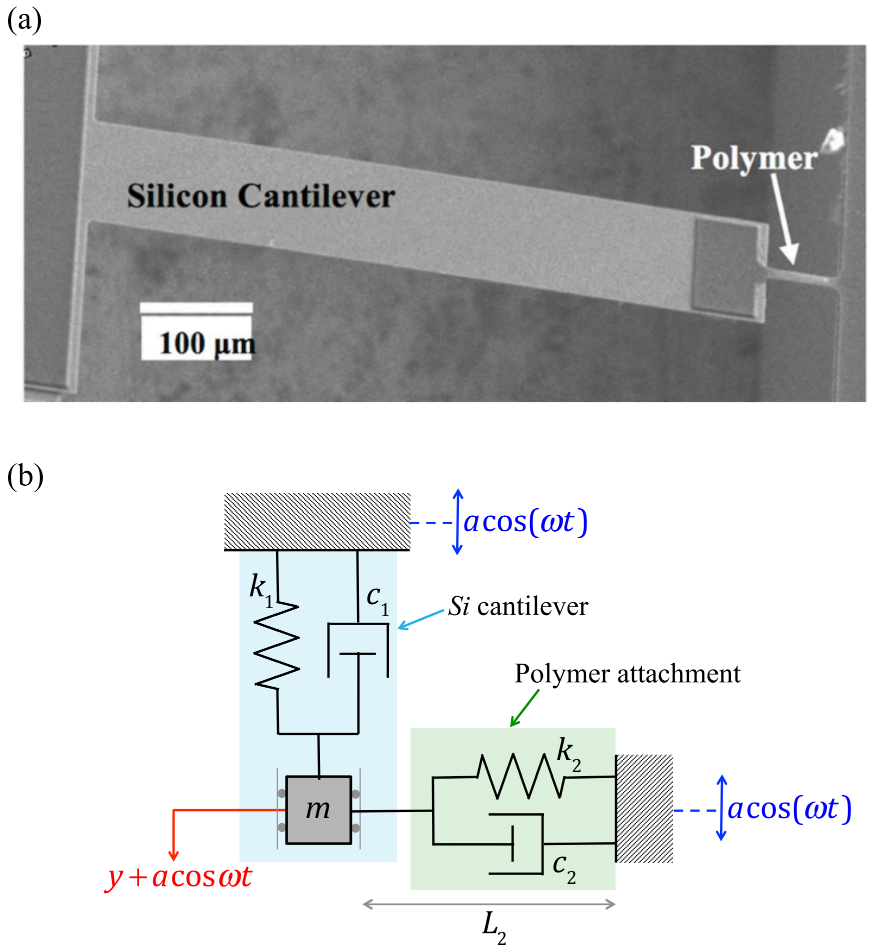

*Figure 4.11: (a) An SEM image of the system, which is presented in Fig. 1a of a journal publication by Asadi et al. (2017). The system consists of a silicon micro cantilever grounded to the base via a polymer attachment. The Si cantilever has dimensions 500* µm *x 100* µm *x 20* µm *and I consider two different devices having slightly different dimensions for the polymer attachment: 50* µm *x 30* µm *x 3* µm *and 40* µm *x 20* µm *x 3* µm*. (b) The lumped parameter model of the system. The flexural motion of the Si cantilever is modeled by a linear damped harmonic oscillator with effective stiffness* $k_1$*, effective mass m, and effective damping coefficient* $c_1$*, where the displacement of the effective mass corresponds to the displacement of the free end of the cantilever. The effective mass is constrained by a horizontal viscoelastic element with stiffness* $k_2$ *and damping coefficient* $c_2$*, which models the effect of the polymer attachment. The large flexural displacement of the cantilever induces axial stretching in the polymer attachment resulting in geometric nonlinearity in the cantilever's dynamics.*

To this end, experimental frequency response curves were obtained for two different microcantilever-polymer devices, at various excitation amplitudes. A piezoelectric shaker was used to provide the harmonic base excitation, and the shaker was carefully chosen so that the operational frequencies were well outside the resonance of the shaker. This allows us to assume that the shaker responds linearly to excitation. Due to the base excitation, a fixed voltage level corresponds to a fixed excitation amplitude, but not a fixed forcing level. The forcing level is proportional to the square of the drive frequency and the excitation amplitude. The shaker was excited with an AC voltage at peak-to-peak values ranging from 3V to 20V provided by a frequency generator. The dynamic response of the microbeam was measured by a laser Doppler vibrometer (LDV; Polytec OFV-534 sensor and OFV-5000 controller) and the laser was pointed at the free end of the *Si* cantilever in order to measure the maximum deflection of the structure. The measured signal was delivered to a remote computer via an oscilloscope (Tektronix DSOX4034A) where it was post-processed in LabView. The excitation frequency was incrementally swept forward and at each excitation frequency, an FFT of the steady-state motion was computed, and the response at the fundamental harmonic was recorded.

In Fig. 4.12 the dynamic response of two different devices are shown. The results shown in Fig. 4.12a correspond to “device 1”, which has a $50\,\mu\text{m}$ x $30\,\mu\text{m}$ x $3\,\mu\text{m}$ polymer attachment, and the results shown Fig. 4.12b correspond to “device 2”, which has a $40\,\mu\text{m}$ x $20\,\mu\text{m}$ x 3 $\mu\text{m}$ polymer attachment. Both devices have a *Si* cantilever with dimensions $500\,\mu\text{m}$ x $100\,\mu\text{m}$ x 20 $\mu\text{m}$. For each device, I began with a forward frequency sweep at 20V and incrementally decreased the excitation voltage until around 3V, at which point the structure behaved approximately linearly. For device 1 (see Fig. 4.12a), we see that, as the excitation voltage increases from 3V to 6V, the drop frequency steadily increases; from 6V to 7V, the drop frequency suddenly increases substantially; and from 7V to 20V, the drop frequency increases non-monotonically. For device 2 (see Fig. 4.12b), we see that as the excitation voltage increases from 3V to 7V, the drop frequency increases steadily; from 7V to 8V, the drop frequency suddenly increases substantially; and from 8V to 20V, the drop frequency steadily increases.

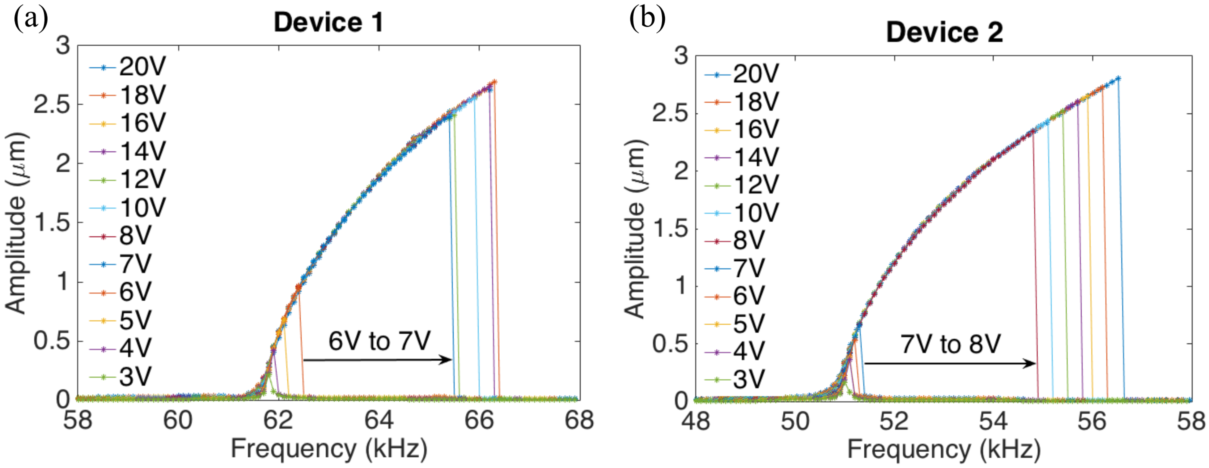

*Figure 4.12: Frequency response curves of two different micro beam structures consisting of a Si cantilevers constrained at its free end by a polymer attachment (shown in Fig. 4.11). Both devices have a 50* μm *x 30* μm *x 3* μm *Si cantilever and differ only in the dimensions of the polymer attachment: (a) device 1 has of 50* μm *x 30* μm *x 3* μm *polymer attachment and (b) device 2 has a 40* μm *x 20* μm *x 3* μm *polymer attachment. Note that in (a), the responses at 18V, 14V and 7V nearly cover the responses at 20V, 16V and 8V, respectively.*

I believe that the sudden jump in the drop frequency caused by a small increase in the excitation voltage, in both devices, is evidence of the critical excitation amplitude that was theoretically predicted for a Duffing oscillator under harmonic base excitation in Sections 4.1-4.4. Specifically, I believe the critical excitation amplitude for device 1 corresponds to a voltage of around 7V and the critical excitation amplitude for device 2 corresponds to voltage of around 8V.

### 4.7 Theoretical analysis of the Duffing equation with nonlinear damping

It appears that the microcantilever-polymer devices under base excitation exhibit ultra-wide broadband resonances above a threshold excitation amplitude. Below the critical amplitude, the bandwidth increases steadily as the excitation amplitude increases, and near the critical amplitude, the bandwidth increases abruptly given a small increase in the excitation amplitude. This is indeed the phenomenon described theoretically in Section 4.2; however, the reduced order equation of motion for the microcantilever-polymer device has an additional nonlinear damping term as compared to the classic Duffing equation considered in Section 4.2. Naturally, this raises the question, how does the nonlinear damping effect the dynamics of the Duffing oscillator, and does equation (4.36) also lead to the *no-drop phenomenon*?

As a first step, the following normalizations are introduced

$$\begin{aligned} &\tilde{y} = \frac{y}{L_1}, \quad \tau = \omega_0 t, \quad \omega_0 = \sqrt{\frac{k_1}{m}}, \quad \zeta_1 = \frac{c_1}{2m\omega_0} \\ &\zeta_2 = \frac{c_3 L_1^2}{m\omega_0}, \quad \Omega = \frac{\omega}{\omega_0}, \quad \alpha = \frac{k_3 L_1^2}{m\omega_0^2}, \quad \tilde{a} = \frac{a}{L_1} \end{aligned} \tag{4.37}$$

and (4.36) is written in non-dimensional form

$$\tilde{y}'' + 2\zeta_1 \tilde{y}' + \tilde{y} + \alpha \tilde{y}^3 + \zeta_2 \tilde{y}' \tilde{y}^2 = \tilde{a}\Omega^2 \cos\Omega\tau \tag{4.38}$$

where the linear damping coefficient is related to that the Q-factor according to

$$Q = \frac{1}{2\zeta_1} \tag{4.39}$$

In order to determine the system parameters of interest, the set of parameters that minimize the error between the theoretical and experimental results for devices 1 and 2 are found. Within the linear dynamic regime, for a fixed excitation frequency and amplitude, the steady-state amplitude of the system is given by,

$$A=\frac{a\left(\frac{f}{f_0}\right)^2}{\left\{\left[1-\left(\frac{f}{f_0}\right)^2\right]^2+\left(\frac{f}{Qf_0}\right)^2\right\}^{1/2}} \tag{4.40}$$

where $\omega=2\pi f$ and $\omega_0=2\pi f_0$. For the relatively large Q factors associated with microresonators, the peak of the linear resonant curve occurs at $f\approx f_0$ and, hence, the steady-state amplitude can be defined as

$$A=\frac{\frac{A_{\text{pk}}}{Q}\left(\frac{f}{f_0}\right)^2}{\left\{\left[1-\left(\frac{f}{f_0}\right)^2\right]^2+\left(\frac{f}{Qf_0}\right)^2\right\}^{1/2}} \tag{4.41}$$

where $A_{\text{pk}}$ is the peak steady state amplitude given by

$$A_{\text{pk}}=aQ\,. \tag{4.42}$$

Using the experimental resonance curves at sufficiently low excitation voltages (~0.1V) so that the dynamic response is linear, equation (4.41) can be used to simultaneously determine $f_0$ and $Q$. Once $Q$ is determined, the excitation amplitude can be identified using equation (4.42). Finally, by dividing the excitation amplitude by the corresponding excitation voltage, the sensitivity, $C$, of the actuation system can be computed. In other words, if a linear relationship between the excitation voltage, $V_{\text{ex}}$, and the base excitation amplitude is assumed, then $C$ is the conversion factor which can be computed using the relation

$$C = a / V_{\mathrm{ex}} \tag{4.43}$$

Following the steps outlined above, I computed a $Q$-factor of $Q = 2{,}915$ ($Q = 1515$) for device 1 (device 2), a linear resonant frequency of $f_0 = 61.8\mathrm{kHz}$ ($f_0 = 51\mathrm{kHz}$) for device 1 (device 2), and an average conversion factor of $C = 0.1\mathrm{nm/V}$. Next, the nonlinear stiffness coefficients, $\alpha$, are extracted for both devices based on the nonlinear dynamic responses at several different excitation voltages below the critical level. At each excitation level considered, the drop down bifurcation frequency and response amplitude (i.e. the peak amplitude, which occurs at the drop frequency) is extracted and used in a fitting with the backbone curve. The backbone curve of this system is given by

$$\tilde{A} = \left( \frac{4\left[ \left( f / f_0 \right)^2 - 1 \right]}{3\alpha} \right)^{1/2} \tag{4.44}$$

Note that since the backbone curve corresponds to zero damping and forcing, the backbone curve of the microcantilever-polymer system is the same as that of a classic Duffing oscillator. Equation (4.44) was derived using the method of harmonic balance, the details of which are provided in Section 4.2. Using this method, I found the nonlinear stiffness coefficient to be $\alpha = 6{,}838$ for device 1 and $\alpha = 9{,}174$ for device 2. In Fig. 4.13, the resulting comparisons of the theoretical backbone curve and the experimental resonance curves at excitation voltages below the critical level are shown.

At this point, a parametric study of the nonlinear damping coefficient, $\zeta_2$, is performed in order to assess how the nonlinear damping term affects the dynamics. Specifically, I want to investigate how the nonlinear damping term in (4.38) affects the ultra-wide broadband resonance of the underlying classical Duffing equation. When $\zeta_2 = 0$, the reduced order model of a classic Duffing oscillator under harmonic base excitation is recovered, which was theoretically analyzed in Sections 4.1 – 4.5. It was shown in Section 4.2 that there exists a critical excitation amplitude above which there is no theoretical drop down bifurcation in the primary resonance curve. Here I theoretically investigate whether or not there exists such a threshold excitation amplitude in the case $\zeta_2 > 0$ .

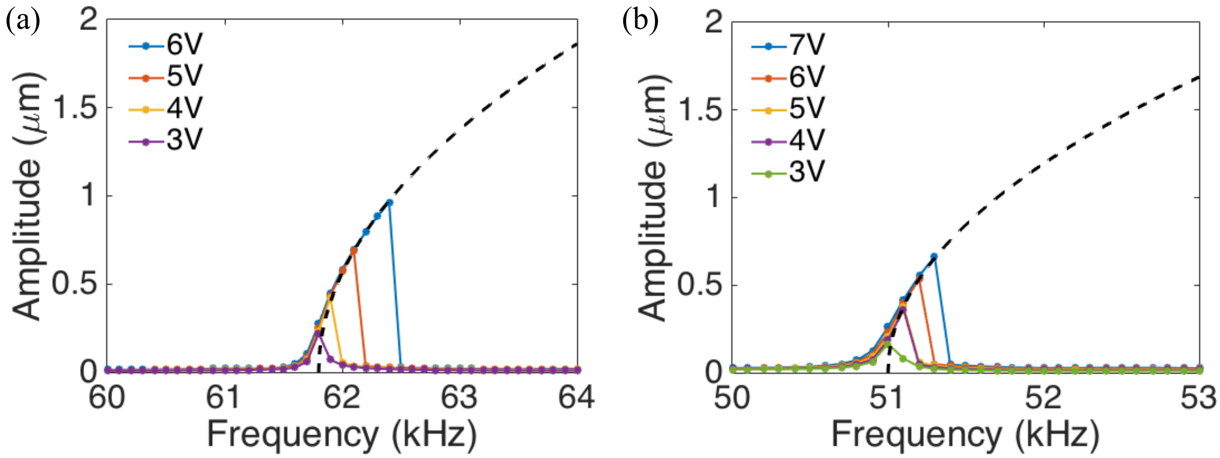

*Figure 4.13: Results of the fitting used to determine the nonlinear stiffness coefficients for (a) device 1 and (b) device 2. The black dashed line corresponds to the theoretical backbone curve for a nonlinear stiffness coefficient of (a) $\alpha = 6{,}838$ and (b) $\alpha = 9{,}174$, and the solid lines correspond to the experimental resonance curves at various excitation voltages below the critical excitation level.*

In Fig. 4.14, the theoretical drop frequency versus excitation amplitude is plotted for six different values of the nonlinear damping coefficient: $\zeta_2 = 0$ (black dashed line), $\zeta_2 = 5\times10^{-4}$ (solid blue line), $\zeta_2 = 5\times10^{-2}$ (solid orange line), $\zeta_2 = 5$ (solid yellow line), $\zeta_2 = 50$ (solid purple line) and $\zeta_2 = 500$ (solid green line). The curves shown in Fig. 4.14a correspond to the parameters previously extracted for device 1, namely, $f_0 = 61.8\text{kHz}$, $Q = 2{,}915$ and $\alpha = 6{,}838$, and the curves shown in Fig. 4.14b correspond to the parameters previously extracted for device 2, namely, $f_0 = 51\text{kHz}$, $Q = 1{,}515$ and $\alpha = 9{,}174$. These theoretical curves were constructed using the method of harmonic balance. Specifically, I assume a steady-state response of the form $\tilde{y} = \tilde{A}\cos(\Omega\tau - \varphi)$, substitute this expression into (4.38) and balance the first harmonic terms to obtain the frequency-amplitude relation at steady state:

$$\frac{3}{4}\alpha\tilde{A}^3=\left(\Omega^2-1\right)\tilde{A}+\sqrt{\tilde{a}^2\Omega^4-\left(2\zeta_1\Omega\tilde{A}+\frac{1}{2}\zeta_2\Omega\tilde{A}^3\right)^2} \tag{4.45}$$

The drop-down bifurcation point occurs at the intersection of the curve defined by (4.45) and the backbone curve defined by

$$\frac{3}{4}\alpha\tilde{A}^3=\left(\Omega^2-1\right)\tilde{A} \tag{4.46}$$

By combining (4.45) and (4.46), the third order polynomial defining the drop frequency, $\Omega_d$, is recovered

$$\frac{16\zeta_2^2}{27\alpha^3}\sigma^3+\frac{32\zeta_1\zeta_2}{9\alpha^2}\sigma^2+\left(\frac{16\zeta_1^2}{3\alpha}-\tilde{a}^2\right)\sigma-\tilde{a}^2=0, \quad \sigma=\Omega_d^2-1 \tag{4.47}$$

The relation in (4.47) was then numerically solved in order to generate the curves shown in Fig. 4.14. As expected, for the case of $\zeta_2=0$, there is no theoretical drop frequency above a critical excitation amplitude and in the immediate vicinity of the critical amplitude, the drop frequency increases dramatically. For $\zeta_2=5\times10^{-4}$, the drop frequency also increases drastically near the critical excitation amplitude, but at amplitudes higher than the critical level, there does exist a theoretical drop frequency in contrast to the case of $\zeta_2=0$. Further, the rate of increase in the drop frequency with respect to the excitation amplitude decreases considerably for excitation amplitudes above the critical level. As $\zeta_2$ increases, it appears that the bandwidth expansion near the critical excitation amplitude decreases until, in the limit of large nonlinear damping (e.g. $\zeta_2>\sim50$), there is no obvious critical excitation amplitude.

To further investigate the effect of $\zeta_2$ , I study the points where the slope in the drop frequency versus excitation frequency curves reach their maxima. I track the locus of points where $\frac{df_{\mathrm{d}}}{da}$ reaches a global maximum as $\zeta_2$ increases and summarize the results in Fig. 4.15. In particular, I plot the $\left(\frac{df_{\mathrm{d}}}{da}\right)_{\max}$ and $a_*$ versus $\zeta_2$ , where $\left(\frac{df_{\mathrm{d}}}{da}\right)_{\max}$ is the maximum slope and $a_*$ is the corresponding excitation amplitude. The results shown in Fig. 4.15a correspond to the fitted parameters for device 1 and the results shown in Fig 4.15b correspond to the fitted parameters for device 2. Nonlinear damping coefficients in the range $\zeta_2 = 5\times10^{-4}$ to $\zeta_2 = 100$ are considered, and the inset of each figure shows a zoomed in view for $\zeta_2$ in the range of $5\times10^{-4}$ to 3. Indeed we see that as $\zeta_2$ increases, the maximum slope decreases at an increasing rate. The excitation amplitude $a_*$ initially increases for small $\zeta_2$ and then decreases; for the fitted parameters corresponding to device 1 (device 2), $a_*$ increases until $\zeta_2 = 0.5$ ($\zeta_2 = 1.38$) and decreases thereafter.

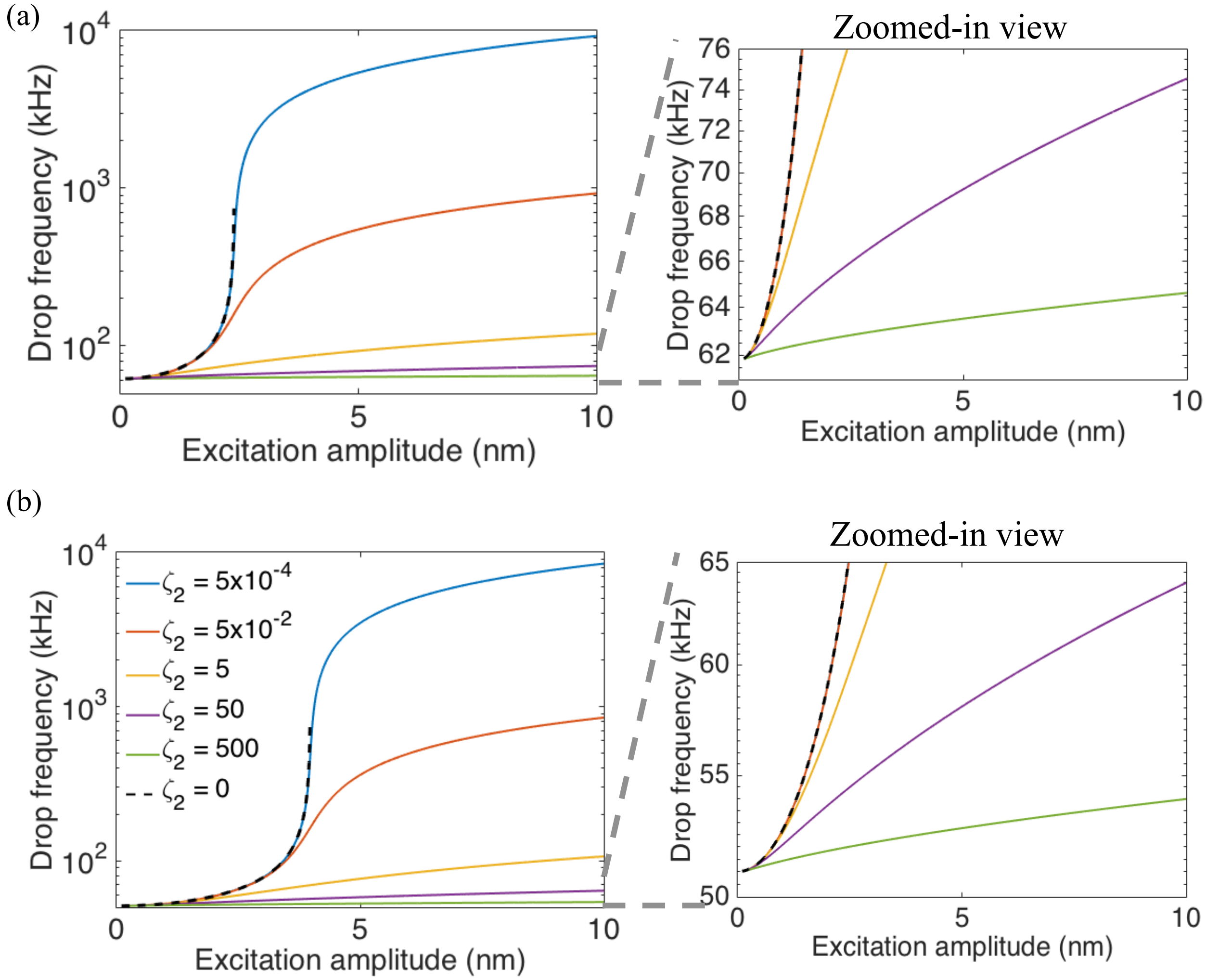

*Figure 4.14: Computational curves of the drop frequency versus the excitation amplitude at various levels of nonlinear damping for (a)* $f_0 = 61.8\text{kHz}$, $Q = 2{,}915$ and $\alpha = 6{,}838$ *(the fitted parameters corresponding to device 1) and (b)* $f_0 = 51\text{kHz}$, $Q = 1{,}515$ and $\alpha = 9{,}174$ *(the fitted parameters corresponding to device 2). The right column shows zoomed-in views for low drop frequencies.*

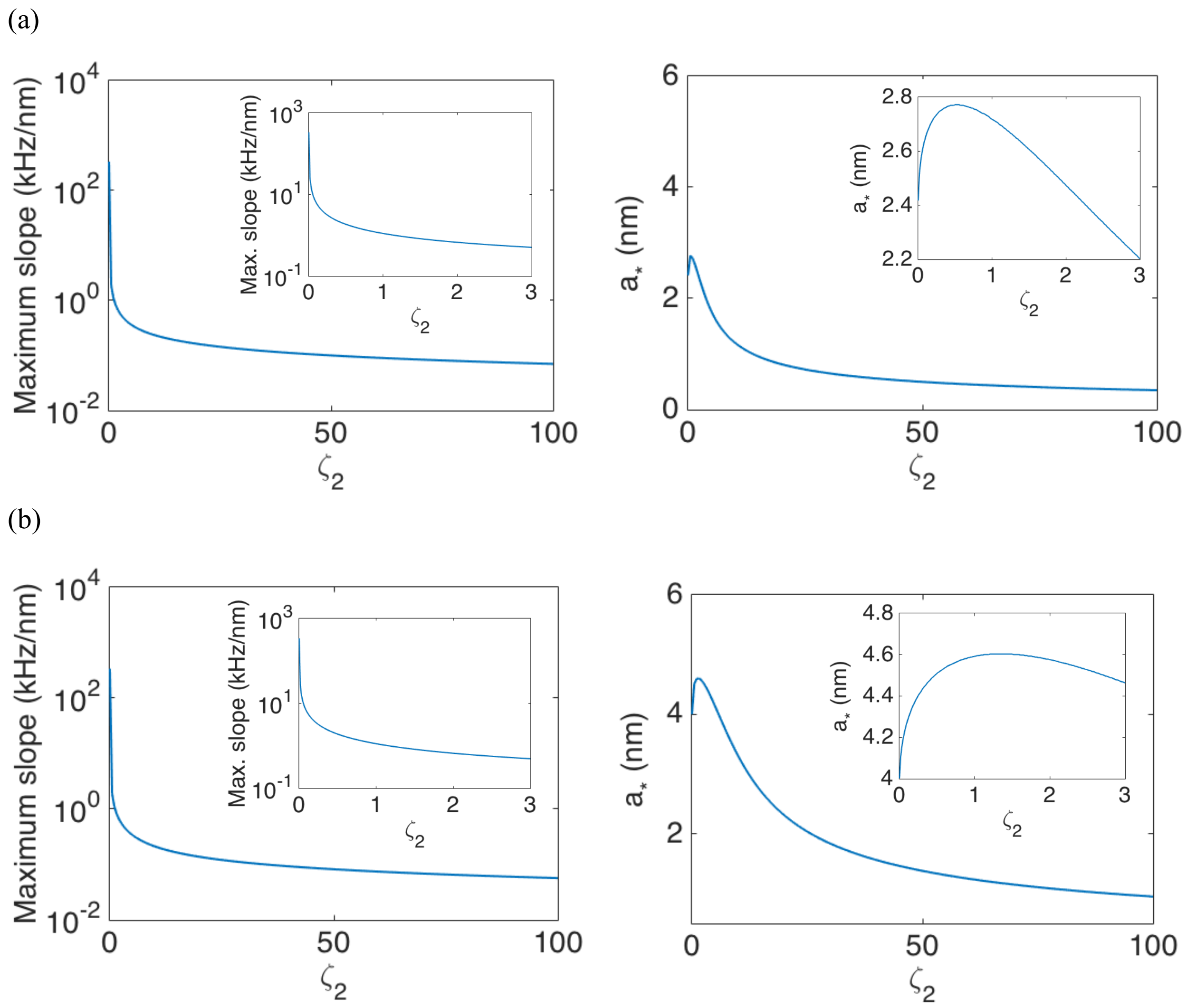

*Figure 4.15: Numerical analysis of the locust of points corresponding to global maxima of* $\frac{df_{\mathrm{d}}}{da}$*, where* $\frac{df_{\mathrm{d}}}{da}$ *is the slope of the drop frequency versus excitation amplitude curve for a fixed* $\zeta_2$*. In (a), the system parameters are* $f_0 = 61.8\mathrm{kHz}$, $Q = 2{,}915$ and $\alpha = 6{,}838$ *(the fitted parameters corresponding to device 1) and in (b), the system parameters are* $f_0 = 51\mathrm{kHz}$, $Q = 1{,}515$ and $\alpha = 9{,}174$ *(the fitted parameters corresponding to device 2. The left column shows the maximum slope,* $\left(\frac{df_{\mathrm{d}}}{da}\right)_{\max}$ *, versus* $\zeta_2$ *and the right column shows the corresponding excitation amplitude,* $a_*$*, versus* $\zeta_2$*. The inset of each plot shows a zoomed-in view for low* $\zeta_2$*.*

In summary, for relatively low values of the nonlinear damping coefficient, there exists a critical excitation amplitude above which the resonant bandwidth increases substantially. In contrast to the case of $\zeta_2 = 0$, there is indeed a theoretically predicted drop bifurcation above the critical excitation amplitude. Therefore, nonlinear damping may also be a practical limitation to the *no drop phenomenon* discussed in Section 4.2. As a final step, I plot the experimental drop frequency as a function of the excitation amplitude in Fig. 4.16, for both devices. The excitation amplitudes were computed from the excitation voltages using the average sensitivity among the two devices (see equation 4.43). If we compare the curves in Fig. 4.16a and 4.16b with the curves shown in Fig. 4.14a and 4.14b corresponding to $\zeta_2 = 5\times10^{-4}$, respectively, we see qualitative agreement but substantial quantitative discrepancies. The primary difference is that the theoretically predicted bandwidth expansion is substantially larger than that observed in the experiment. Also, the theoretically predicted critical amplitude is larger than the experimentally observed critical amplitude. Essentially, the theoretical model captures qualitatively the sudden bandwidth expansion observed in the experiment, but it does not predict the correct scaling. This may be due to a limitation of the theoretical model and perhaps additional sources of nonlinearity play a role in the dynamics of the microcantilever-polymer devices.

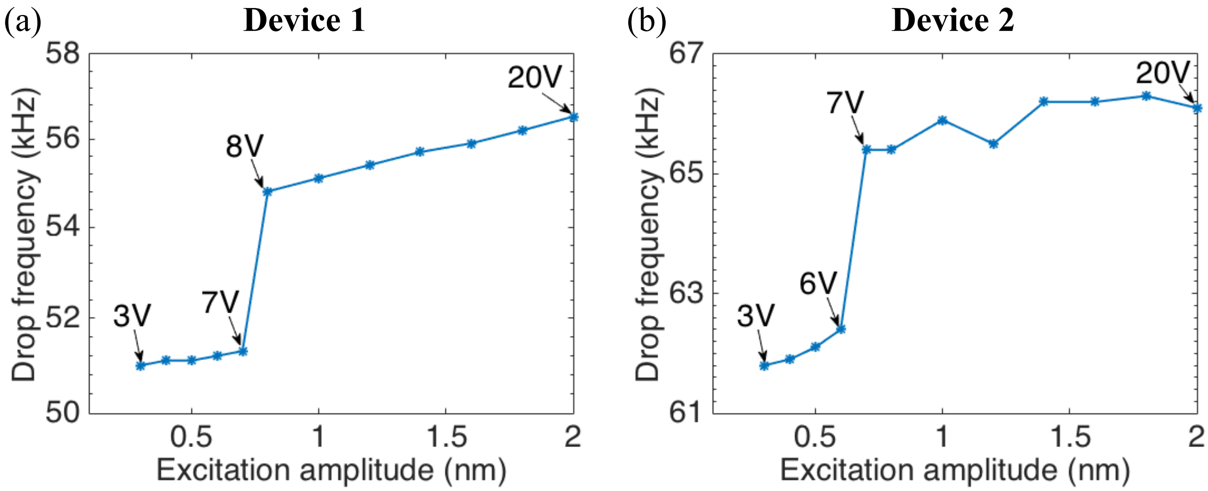

*Figure 4.16: Experimental plots of the drop frequency versus excitation amplitude for (a) device 1 and (b) device 2.*

## 4.8 Conclusions

In this Chapter, a new micromechanical resonant sensor design is introduced consisting of a doubly clamped beam having a concentrated mass at its center and under harmonic base excitation. The reduced order model of the fundamental flexural mode is constructed in the form of a discrete spring-mass system containing cubic stiffness due to geometric nonlinearity, in addition to linear stiffness. In other words, the fundamental bending mode is governed by the Duffing equation where the forcing level is not fixed, rather it is proportional to the square of the drive frequency due to the presence of base excitation. I found that there exists a critical excitation amplitude above which there is no theoretically predicted drop down bifurcation in the resonance curve. Further, the presence of the concentrated mass significantly lowers the critical excitation required for this theoretical *no drop phenomenon*. Practically, it is not possible to have no drop down bifurcation, and the inevitable drop down may result from the presence of nonlinear damping, the excitation of internal resonances, and/or shrinking of the high-amplitude domain of attraction combined with stochastic variations in the initial state due to noise. In practice, I believe that the critical excitation amplitude corresponds to an amplitude at which sudden bandwidth expansion occurs.

In order to experimentally investigate this phenomenon, I consider a microresonator system consisting of a *Si* microcantilever restricted at its free end by a polymer bridge. It had previously been shown that the fundamental bending mode of this device is characterized well by the Duffing equation with an additional nonlinear damping term (Asadi et al., 2017). Experimental resonance curves were obtained for two different microcantilever-polymer devices that were excited harmonically at the base via a piezoelectric actuator. For each device, various resonance curves were obtained at different excitation voltages, where a fixed excitation voltage corresponds to a fixed base excitation amplitude of the piezo shaker. In both structures, a sudden expansion in the bandwidth at a critical excitation voltage was observed. Further, theoretical analysis showed that the presence of weak nonlinear damping may also serve as a practical limitation to the *no drop phenomenon*. For relatively low values of the nonlinear damping coefficient, I theoretically predict a critical excitation amplitude at which a sudden increase in the bandwidth occurs, but for excitation amplitudes above the threshold level, there exists a theoretical drop down bifurcation in contrast to the case of zero nonlinear damping. The theoretical model qualitatively predicts the experimental results obtained from the microcantilever-polymer device but not quantitatively. The quantitative discrepancies may be due to shortcomings of the theoretical model.

## 4.9 References

Anderson D., Starosvetsky Y., Vakakis A., and Bergman L. (2012). *Nonlinear Dyn., 67,* 807-827.

Antonio, D., Zanette, D. H., and López, D. (2012). Frequency stabilization in nonlinear micromechanical oscillators. *Nature Communications*, *3*(May).

Asadi, K., Li, J., Peshin, S., Yeom, J., & Cho, H. (2017). Mechanism of geometric nonlinearity in a nonprismatic and heterogeneous microbeam resonator. *Physical Review B*, *96*(11).

Alsaleem F.M. and Younis M.I. (2010). Stabilization of electrostatic MEMS resonators using a delayed feedback controller. *Smart Mater. Struct.*, *19*, 035016,.

Chen, C., Zanette, D. H., Czaplewski, D. A., Shaw, S., and López, D. (2017). Direct observation of coherent energy transfer in nonlinear micromechanical oscillators. *Nature Communications*, *8*(May), 1–7.

Cho, H., Jeong, B., Yu, M.-F., Vakakis, A. F., McFarland, D. M., Bergman, L. A. (2012). Nonlinear Hardening and Softening Resonances in Micromechanical Cantilever-Nanotube Systems Originated from Nanoscale Geometric Nonlinearities, *Int. J. Solids Struct., 49*, 2059-2065.

Jeong, B., Cho, H., Yu, M.-F., Vakakis, A., McFarland, D. M., and Bergman, L.A. (2013) Modeling and measurement of geometrically nonlinear damping in a microcantilever nanotube system, *ACS Nano, 10*, 8547-8553.

Kumar, V., Yang, Y., Boley, J.W., Chiu, T.-C, Rhoads, J.F. (2012). Modeling , Analysis , and Experimental Validation of a Bifurcation-Based Microsensor. *J Microelectromech Syst.*, *21*(3), 549–558.

Nayfeh, A.H., Mook D. (1995). *Nonlinear Oscillations*, Wiley Interscience

Potekin, R., Kim, S., McFarland, D. M., Bergman, L. A., Cho, H., and Vakakis, A. F. (2018). A micromechanical mass sensing method based on amplitude tracking within an ultra-wide broadband resonance. *Nonlinear Dynamics*.

Vakakis, A.F., Gendelman, O., Bergman, L.A., McFarland, D.M., Kerschen, G., Lee, Y.S. (2008). *Passive Nonlinear Targeted Energy Transfer in Mechanical and Structural Systems: I and II*, Springer Verlag.

# Chapter 5

# A micromechanical mass-sensing method based on amplitude tracking within an ultra-wide broadband resonance

## 5.1 Background and motivation

Among linear resonant mass sensors (also known as “dynamic-mode mass sensors”) there are two different conventional methods typically used for detection. One requires a frequency generator to incrementally sweep the excitation frequency and record the steady-state response amplitude at each frequency, before and after the addition of a discrete mass (the object that is sensed). The resulting resonance curves typically reveal a downward shift in the linear resonant frequency from which the amount of added mass is deduced (Arlett et al., 2011; Johnson and Mutharasan, 2012; Mahmoud, 2016). This relatively simple, open-loop mass sensing method was among the earliest measurement techniques, commonly used in applications where ultra-high sensitivity is not required (Ilic et al., 2001; Ilic et al., 2005; Johnson and Mutharasan, 2012; Ma et al., 2012). Limitations of this technique include unaccounted-for contributions to the effective stiffness of the resonator; however, recent studies have investigated different ways to approximate the added stiffness (Grüter et al., 2010; Gupta et al., 2006; Ilic et al., 2012; Ma et al., 2012; Zhang, 2014).

The other common resonant mass sensing technique involves a closed-loop feedback procedure to ensure that as mass is added to the device, the system is always excited at resonance (Arlett et al., 2011; Johnson and Mutharasan, 2012). The advantage of this more complicated closed-loop method is that it eliminates the need for time-consuming frequency sweeps. Also, it allows for the use of ultra-high vacuum (UHV) conditions in which particularly high Q-factors arise, resulting in enhanced sensitivity (Ekinci et al., 2004; Kharrat et al., 2008; Garcia and Perez, 2002). The characteristic times associated with the decay of the transient terms are directly proportional to the Q-factor, and for most applications, the decay rate in UHV conditions is so slow that the open-loop approach becomes impractical (Garcia and Perez, 2002). For this reason, the closed-loop approach is usually used under UHV conditions to achieve extreme sensitivity, and it is the method required to realize state-of-the-art yoctogram resolution (Chaste et al., 2012; Chiu et al., 2008; Ekinci et al., 2004; Jensen et al., 2008; Yang et al., 2006; Yang et al., 2011). While closed-loop mass sensing offers the advantages of improved sensitivity and independence from frequency sweeps, it has the disadvantages of requiring sophisticated FM-PLL feedback control, and, typically, extremely small resonator designs and UHV operating conditions.

In the last couple of decades, researchers have studied the advantages of intentional nonlinearity in the design of microresonator mass sensors. A general feature of nano- and micro-scale resonators is that the relative magnitude of the resonance amplitude is quite large (compared to the device size) and, as a result, these devices often exhibit significant geometric nonlinearity. On the one hand, this limits the operational range for conventional mass sensing methods in which a linear dynamic regime is required. On the other hand, it underscores the potential of intentionally exploiting nonlinear phenomena to improve microresonant sensing technology (Askari et al., 2017; Bajaj et al., 2016; Bouchaala et al., 2016; Cho et al., 2010, Hiller et al., 2015; Jain et al., 2012; Kacem et al., 2010; Karabalin et al., 2008; Kumar et al., 2011; Kumar et al., 2012; Li et al., 2014; Rhoads et al., 2005; Rhoads et al., 2010; Turner et al., 1998; Younis and Alsaleem, 2009; Yu et al., 2002; Zhang et al., 2002; Zhang and Turner, 2005). One such research area is bifurcation-based mass sensing, which utilizes the large changes in amplitudes associated with bifurcations in the nonlinear frequency response of microresonators. Typically, the nonlinear microresonators considered display either a softening frequency response where the frequency response curve bends backward toward lower frequencies, or a hardening response where the frequency response curve bends forward toward higher frequencies. In either case, the bending of the frequency response results in bi-stability, hysteresis and bifurcation points in the frequency response. Bifurcation points associated with a sudden upward shift in the response amplitudes occur at *jump-up frequencies* and bifurcation points associated with a sudden downward shift in the response amplitude occur at a *jump-down frequencies*. The addition of mass on the microresonator shifts the entire frequency response towards lower frequencies and, hence, the dependence of the jump-up and jump-down frequencies on mass can be exploited in mass detection schemes.

Cho et al. (2010) theoretically and experimentally studied a harmonically driven, doubly-clamped carbon nanotube resonator and determined that the large resonance bandwidth and jump-down frequency are more sensitive to added mass and damping levels than the linearized natural frequency of a resonator. Zhang et al. (Zhang et al., 2002; Zhang and Turner, 2005) studied a single-crystal *Si* micro-oscillator where fringing-field electrostatic force was used to periodically change the effective stiffness of the resonator and thereby generate parametric harmonic excitation. Shifts in the jump-up frequency were used to detect mass, and the jump-up frequency was shown to be 1-2 times more sensitive to mass than the linearized frequency. Kumar et al. (Kumar et al., 2011; Kumar et al., 2012) studied a piezoelectrically-actuated microcantilever probe consisting of a *Si* cantilever with a piezoelectric layer that was initially designed for scanning probe microscopy. Due to the presence of geometric, material and inertial nonlinearity, both cubic and quadratic terms appear in the reduced order equation of motion for the microcantilever. Depending on the relative contribution of the different sources of nonlinearity, either a softening or stiffening behavior is observed in the frequency response. In either case, variations in both the jump-up and jump-down frequencies due to mass addition were studied analytically and experimentally. Bouchaala et al. (2016) studied an electrostatically actuated beam, which exhibited geometric (cubic) and electrostatic (quadratic) nonlinearity. The contribution of the electrostatic nonlinearity was controlled via the DC voltage, and for low DC voltages hardening was observed in the frequency response, whereas for large DC voltages, softening was observed in the frequency response. It was shown that in the case of softening, the jump-up event can be used as a switch to detect a threshold amount of added mass, and in the case of hardening changes in the response amplitude *prior* to the jump-down event can be used to quantify added mass in addition to the jump-down event signaling the addition of a critical amount of mass.

The incorporation of active feedback control in the aforementioned sensing techniques has also been explored. Hiller et al. (Hiller et al., 2015; Li et al., 2014) analytically and experimentally studied amplitude feedback control of a parametrically excited microbeam sensor during parametric resonance. As mass is added to the sensor, the excitation frequency varies in order to maintain a predetermined *set-point* response amplitude, and the resulting frequency shifts are used to quantify the amount of added mass. Interestingly, the operational frequencies and forcing levels considered lie within a parameter space that gives rise to a unique response amplitude (i.e., there is no hysteresis in the operational range considered).

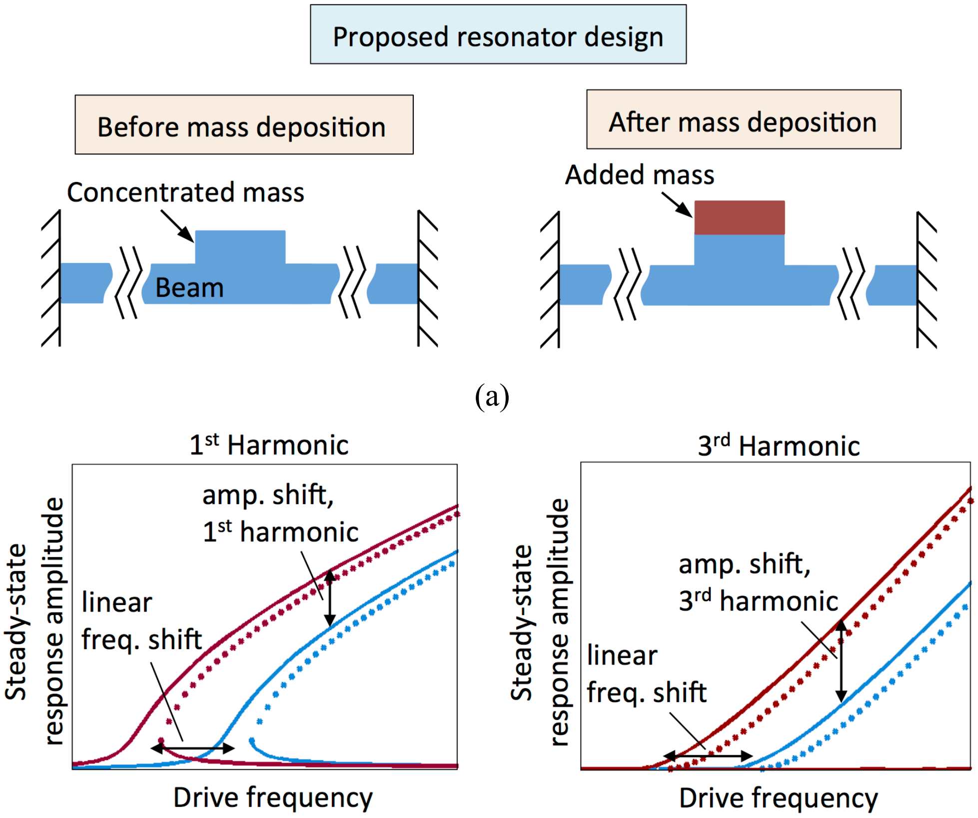

(a)

(b) (c)

*Figure 5.1: (a) Proposed nonlinear resonator design before (left) and after (right) mass deposition; (b) steady-state response amplitude at the* $1^{st}$ *harmonic versus excitation frequency, before (blue) and after (red) mass deposition and (c) steady-state response amplitude at the* $3^{rd}$ *harmonic versus excitation frequency, before (blue) and after (red) mass deposition. In (b) and (c), for drive frequencies lower than a critical value (corresponding to a bifurcation point), there exists a unique, stable response and for drive frequencies larger than this critical value, there co-exist two stable responses denoted by solid lines and one unstable response denoted by a dotted line.*

Bajaj et al. (2016) considered a microscale quartz tuning pitchfork and used feedback control to provide a source of cubic nonlinearity in the dynamics. Due to the feedback, the motion of the pitchfork was well described by the Duffing equation. By varying the gain of the cubic stiffness term from negative, zero to positive, the frequency response behavior varied from softening to linear to hardening, respectively. Analytical and experimental analysis of the bifurcation frequencies in this active Duffing oscillator demonstrated the viability of a tunable, commercially available bifurcation-based sensor.

In this Chapter, I consider the device introduced in Chapter 4 (Sections 4.1-4.4), namely, a clamped-clamped beam under harmonic base excitation having a concentrated mass at its center. As discussed in Chapter 4, the reduced-order model of the system is that of a Duffing oscillator, and for sufficiently large base excitation amplitudes there is theoretically no jump-down bifurcation point. Further, the critical excitation level above which there is no theoretical jump-down event is significantly lowered by the presence of the concentrated mass. By operating at an excitation amplitude above this critical threshold, the ultra-wide resonant bandwidth is exploited for a mass-sensing technique based on amplitude tracking. A secondary effect of the cubic nonlinearity is the strong amplification of the third harmonic and, hence, I track both the first and third harmonic amplitudes as mass is added to the microresonator.

For a fixed excitation frequency within the broadband resonance, as mass is added to the center of the beam, I computationally study the change in the steady-state response amplitudes of the first and third harmonics and find that they show strong sensitivity to mass. The novelty of the proposed mass sensor design is that its ultra-wide resonant bandwidth allows for a considerably larger range of operational frequencies and response amplitudes as compared to other micromechanical resonant mass sensors incorporating nonlinearity. Additionally, multi-harmonic measurements are considered (Dohn et al., 2010; Hanay et al., 2012; Olcum et al., 2015) and while both the first and third harmonic amplitudes prove to be more sensitive to mass than the linearized frequency, the third harmonic amplitude is found to be the most sensitive indicator. Furthermore, the design parameters are reasonable from a manufacturing point of view (beam width and thickness ~100 nm, beam length ~ 1 μm) and femtogram mass resolution is achieved. This study focuses on developing the analytical and computational framework for the proposed mass-sensing technique based on a new resonator design.

## 5.2 Harmonic balance analysis

A schematic of the resonator design is shown in Fig. 4.1. Assuming that plane sections remain plane during the beam vibration, a linear stress-strain constitutive law, and planar motion, and including geometric nonlinearity due to mid-plane stretching, the partial differential equation governing transverse motion in the beam is stated in (4.1). In Chapter 4, I show in detail how (4.1) can be reduced to an ordinary differential equation governing the fundamental bending mode, stated in (4.14). Specifically, (4.14) corresponds to the Duffing equation with harmonic excitation proportional to the square of the excitation frequency.

The reduced-model (4.14) is the starting point for the following dynamic analysis. In order to analytically approximate the backbones of the frequency-amplitude curves, I consider the underlying undamped, unforced system and perform harmonic balance using the two-term expansion,

$$\tilde{z}(\tau) = \tilde{A}_1(\tau)\sin\left(\Omega\tau + \varphi_1\right) + \tilde{A}_3(\tau)\sin\left(3\Omega\tau + \varphi_3\right) \tag{5.1}$$

or, equivalently,

$$\tilde{z}(\tau) = \tilde{A}_1(\tau)\sin\left(\theta\right) + \tilde{A}_3(\tau)\sin\left(3\theta + \psi\right) \tag{5.2}$$

where the two phases are defined as $\theta = \Omega\tau + \varphi_1$ and $\psi = \varphi_3 - 3\varphi_1$. The third harmonic is included in the two-term expansion since it is expected that the cubic stiffness nonlinearity of (4.14) contributes primarily to the amplification of the third harmonic in the response. Upon substitution of (5.2) into (4.14) while neglecting damping and forcing (i.e., setting $\tilde{c}_e = \tilde{b} = \tilde{d} = 0$ ), the coupled, nonlinear equations describing the amplitude-frequency relations for the *backbone curves* for the first and third harmonics are recovered,

$$\tilde{k}_3\tilde{A}_1^3 + 2\tilde{k}_3\tilde{A}_1\tilde{A}_3^2 \mp \tilde{k}_3\tilde{A}_1^2\tilde{A}_3 + \frac{4}{3}\left(\Omega_1^2 - \Omega^2\right)\tilde{A}_1 = 0 \tag{5.3a}$$

$$\mp\frac{1}{3}\tilde{k}_3\tilde{A}_1^3+\frac{4}{3}\left(\Omega_1^2-9\Omega^2\right)\tilde{A}_1+2\tilde{k}_3\tilde{A}_3\tilde{A}_1^2+\tilde{k}_3\tilde{A}_3^3=0 \tag{5.3b}$$

$$\psi=0,\pi \tag{5.3c}$$

Note that since the system has no damping, the phase lag between the two harmonics is either 0 or $\pi$ ; $\psi = 0$ holds when $\Omega < \Omega_1$ , whereas $\psi = \pi$ holds when $\Omega \geq \Omega_1$ . Further, the cubic nonlinearity has a hardening effect causing the backbone curves to bend toward higher frequencies so that their domains correspond to $\Omega \geq \Omega_1$ and, hence, it holds that $\psi = \pi$ along the backbone curves.

## 5.3 Primary resonances of the 1st and 3rd harmonics

In Fig. 5.2 I depict a comparison between computational frequency-amplitude resonance curves and the analytical backbone curves obtained by solving the system (5.3a) – (5.3c) for the first and third harmonics. I consider fundamental resonance of the reduced-order model (4.14); i.e., the forced steady-state responses with dominant harmonic component at the frequency $\Omega$ of the applied harmonic excitation. The computational resonance curves were obtained by numerically integrating the reduced-order model (4.14) for a specific frequency and amplitude of excitation and specific initial conditions, letting the dynamics reach a steady state and recording the steady-state response. The lumped-parameter model (4.14) was numerically integrated in Python for several hundreds of cycles into the steady state. Then, a fast Fourier transform (FFT) of the steady-state response was performed to compute the amplitudes of the 1st and 3rd harmonics at each value of the excitation frequency. In order to reduce edge effects in the FFT, the duration of the steady-state segment was set equal to an integer multiple of the drive period. While incrementally increasing or decreasing the drive frequency to simulate an upward or downward frequency sweep, respectively, the initial conditions of a new simulation were set equal to the final conditions of the preceding simulation. Finally, the total simulation time was chosen to be an integer multiple of the drive period to achieve consistency in the initial conditions of the base. The system parameters used to generate all computational and analytical results in this work are listed in Table 5.1.

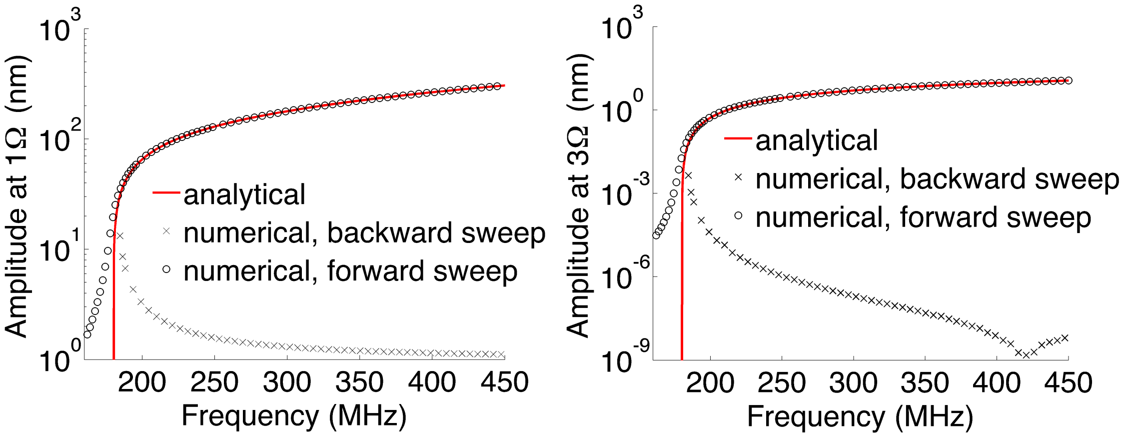

(a) (b)

*Figure 5.2: Comparison of numerical resonance curves (comprised of forward and backward sweeps) and the analytical backbone curves (resulting from harmonic balancing): (a) first and (b) third harmonic components of the steady-state response.*

Table 5.1. System parameters used in the computational study of the beam.

| | |
|---|---|
| **Mass density of the beam** | $\rho = 2,330\ \mathrm{kg/m^3}$ |
| **Young's modulus of the beam** | $E = 169\ \mathrm{GPa}$ |
| **Beam half-length** | $L = 0.6\ \mu\mathrm{m}$ |
| **Beam thickness** | $t = 100\ \mathrm{nm}$ |
| **Beam width`** | $w = 300\ \mathrm{nm}$ |
| **Ratio of concentrated mass to beam mass** | $\mu = 4$ |
| **Q-factor** | $Q = 100$ |
| **Base excitation amplitude** | $a = 0.5\ \mathrm{nm}$ |

Strong agreement between the computational frequency-amplitude curves and the analytical backbone curves is observed. The reason for this strong correlation is two-fold: the relatively low damping and forcing levels, and the accuracy of the harmonic balance model (5.1) and (5.2). Indeed, as the forcing and damping levels approach zero, the frequency-amplitude resonance curves become increasingly narrow and, in the limit of zero damping and forcing, by definition they coincide with the backbone curves. A Q-factor of 100 and a base excitation amplitude of 0.5 nm result in a damping coefficient and forcing levels small enough that, in (4.14), the harmonic forcing terms and the damping term are dominated by the other terms of the reduced-order model. Additionally, it is known *a posteriori* that most of the energy in the fundamental resonance response is localized in the first and third harmonics and, hence, the two-term approximation used in (5.1) is appropriate. In particular, I computed the energy partition in the system (i.e., the sum of the kinetic and potential energy of the system) among the first and third harmonics for each excitation frequency considered in Fig. 5.2 and found that the energy in the first harmonic decreased from 99.99% at the 182 MHz to 97.8% at 500 MHz whereas the energy in the third harmonic increased from ~0 at 182 MHz to 0.8% at 500 MHz. If we consider the total energy in both the first and third harmonics, we see that this amount decreases from 99.99% at 182 MHz to 98.6% at 500 MHz and, within this range of frequencies, is 99.2% on average. As a result, for the parameter values considered in Table 1, the harmonic balance analysis of the undamped, unforced system approximates well the response of the actual damped, forced system, at least for frequencies not in the immediate vicinity of the linearized natural frequency.

More importantly, considering the fundamental resonance branches in Fig. 5.2, we observe a large broadband resonance of the system encompassing a range of over 270 MHz or 2.5 times the linearized frequency; this broad bandwidth occurs even in the presence of viscous damping in the system. In fact, due to the base excitation and the presence of the concentrated mass at the center of the beam, there is no theoretical jump-down frequency for the excitation level considered (0.5 nm). A detailed analysis and physical explanation of this no-drop phenomenon is presented in the Chapter 4. It is shown here that, because the excitation level is not fixed, it is proportional to the square of the excitation frequency; for sufficiently large excitation amplitudes there should be theoretically no jump-down bifurcation point in the frequency response. The critical excitation amplitude required to achieve the no-drop phenomenon is found to be inversely related to the ratio of the concentrated mass to the beam mass. The role of the concentrated mass in the resonator design is to lower this critical excitation amplitude to a practical level. Specifically, for the system parameters considered in Table 1, the critical excitation amplitude in the absence of the concentrated mass is around 1.1 nm, whereas the critical excitation amplitude for a mass ratio of 4 is 0.1 nm. Hence, the concentrated mass lowers the critical excitation amplitude for the system by an order of magnitude and thereby enhances the feasibility of realizing the ultra-wide broadband.

As discussed in Section 4.5, it is not possible to truly have no jump-down bifurcation point in the frequency response. In practice, this bifurcation point may occur due to the excitation of higher resonances, perturbations in the initial conditions and/or excitation amplitude caused by noise, or the basin of attraction for the upper branch solution may become impractically small. Indeed, noise plays an important role in the dynamics of nonlinear systems near bifurcation points, and significant effort has been dedicated to this topic (Aldridge and Cleland, 2005; Alsaleem and Younis, 2010; Kozinsky et al., 2007; Unterreithmeier et al., 2008). An experimental investigation of the effect that noise has on the dynamics of the resonator near the jump-down bifurcation are critical to fully characterizing this system, but are beyond the scope of the present work. Based on the theoretical and numerical analysis shown in Section 4.2 and experimental the corresponding experimental verification presented in Section 4.6, it is clear that in practice, for excitation amplitudes larger than the critical excitation amplitude, the resonant bandwidth is significantly larger than for excitation amplitudes below the threshold.

The ultra-wide broadband resonance could be exploited in a mass sensing application based on amplitude tracking. To place this in context, recall the mass sensing scenario depicted in Fig. 5.1. When a foreign mass is attached to the beam, the nonlinear resonance curve (in blue) is shifted toward lower frequencies (in red). For mass sensing, a fixed driving frequency can be randomly chosen within the broad resonance bandwidth as an operating frequency, and the changes of the 1st and 3rd harmonic amplitudes provide the mass sensitivity. Owing to the broad resonance bandwidth, there is no need to adjust the operating frequency, either by sweeping the frequency around the resonance frequency (as in the open-loop method) or by modulating the frequency via a PLL (as in the closed-loop method) – as would be necessary for a linear resonator to follow the moving resonance peak. Further, the ultra-wide broadband allows for a significantly larger range of operational frequencies and amplitudes as compared to other mass sensing techniques relying on nonlinear resonances.

In Fig. 5.3 I analytically and computationally show how the first and third harmonics vary as mass is added to the center of the resonator at a fixed excitation frequency of 250 MHz. The selection of the frequency of 250 MHz was somewhat arbitrary and, in fact, any frequency within the broadband (i.e., higher than the linearized frequency) shown in Fig. 5.2 can be selected as the operational drive frequency. The computational results indicate that tracking the high-amplitude branch as mass is added is indeed feasible despite the perturbations in the concentrated mass. That is to say, the addition of mass in 25 fg increments does not trigger a transition to the lower solution branch. In practice, the excitation frequency would need to be swept up to the target operational frequency initially in order to attract the upper solution branch before mass is added. Once the upper solution branch is realized, the excitation frequency remains constant as mass is added and the upper solution branch is tracked. In other words, the mass sensing procedure would require an initial ramp up of the frequency but would not require frequency sweeping each time a discrete amount of mass is added. The excitation could be applied by a piezoelectric actuator.

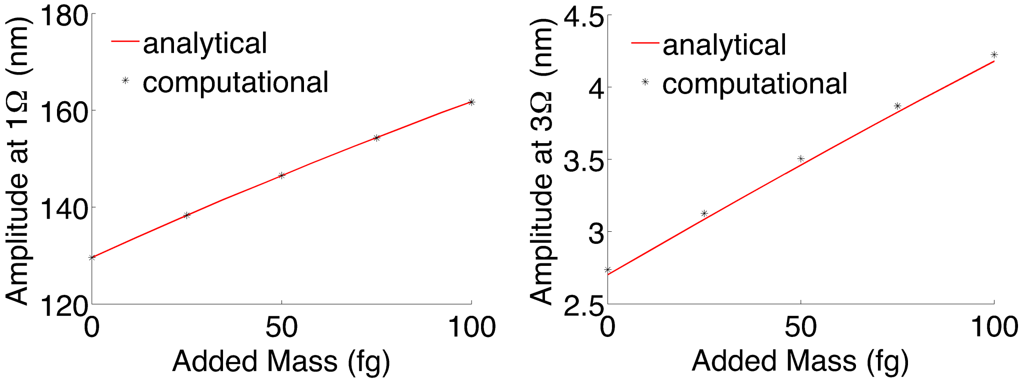

(a) (b)

*Figure 5.3: Comparison of numerical and analytical (resulting from harmonic balance) fundamental resonance amplitude curves versus added mass: (a) first and (b) third harmonics of the steady-state response at constant excitation frequency of 250 MHz.*

### 5.4 Sensitivity and mass resolution

As a way of estimating the efficacy of the proposed resonator design, I introduce the following *sensitivities*, of the linearized resonant frequency, $S_{\text{lin}}$, the amplitude of the first harmonic, $S_1$, and the amplitude of the third harmonic $S_3$,

$$S_{\text{lin}} = \omega_{10} / \omega_1, \quad S_1 = A_1 / A_{10}, \quad S_3 = A_3 / A_{30} \tag{5.4}$$

where $\omega_{10}\left(A_{10}\right)$ is the linearized resonant frequency (depending on the amplitude of the 1st harmonic, $A_{10}$) before any mass is added, and $\omega_1\left(A_1\right)$ is the linearized resonant frequency (depending on the amplitude of the 1st harmonic, $A_1$) after mass is added to the center of the beam, and $A_{30}$ and $A_3$ are the amplitudes of the third harmonic before and after mass is added. As discussed in the previous section, the proposed mass detection scheme relies on changes in the amplitudes at a fixed excitation frequency rather than changes in the linear resonant frequency. However, in the following exposition I include the sensitivity of the linearized frequency for comparison. Since the linearized resonant frequency decreases as mass is added while the amplitudes of the first and third harmonics increase as mass is added, the sensitivities are always greater than or equal to one.

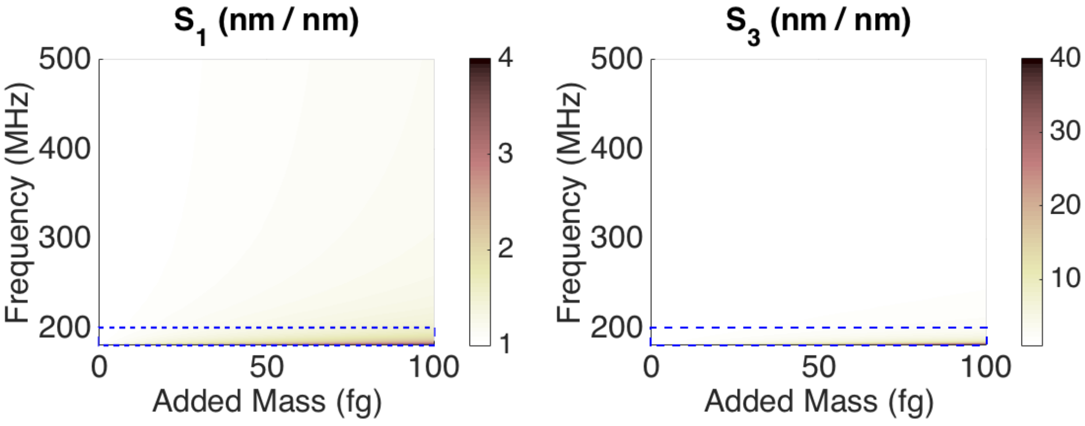

(a) (b)

*Figure 5.4: (a) Sensitivity of the first harmonic amplitude versus excitation frequency versus added mass for an operational frequency range of 182 MHz to 500 MHz, (b) sensitivity of the third harmonic amplitude versus excitation frequency versus added mass for an operational frequency range of 182 MHz to 500 MHz, (c) zoomed-in image of (a) for an operational frequency range of 182 MHz to 200 MHz, (d) zoomed-in image of (b) for an operational frequency range of 182 MHz to 200 MHz, (e) linearized frequency versus added mass and (f) sensitivity of the linearized frequency versus added mass. The operational ranges depicted in (c) and (d) are indicated by a dashed-blue rectangle in (a) and (b).*

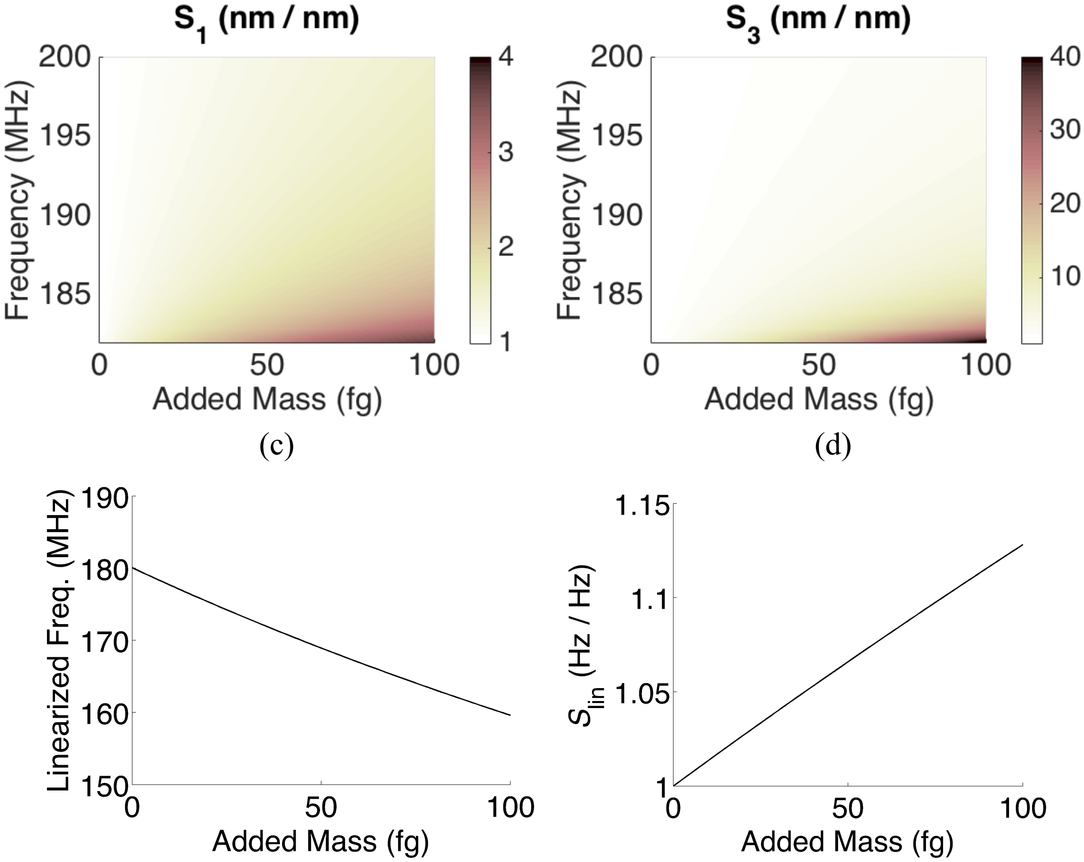

(c) (d)

(e) (f)

*Figure 5.4 (cont.)*

In Figs. 5.4a-b I plot the sensitivities of the first and third harmonic amplitudes versus excitation frequency and added mass for an operational frequency range of 182 MHz to 500 MHz. The sensitivities of both the first and third harmonic amplitudes increase significantly in the vicinity of the linearized frequency, and for this reason zoomed-in views of Figs. 5.4a-b are shown in Figs. 5.4c-5.4d for an operational frequency range of 182 MHz to 200 MHz. Due to the broadband resonance, the sensitivities of the steady-state response amplitudes depend on the excitation frequency as well as the added mass. This is due to the fact that the proposed mass sensor offers the advantage of a wide range of operational frequencies, so any excitation frequency that falls within the broad resonant bandwidth of the microresonator can be selected as the excitation frequency. In contrast, the sensitivity of the linearized frequency depends only on added mass (cf. Fig. 5.4d) since, for a given amount of added mass, there is a unique linearized resonant frequency (cf. Fig. 5.4c).

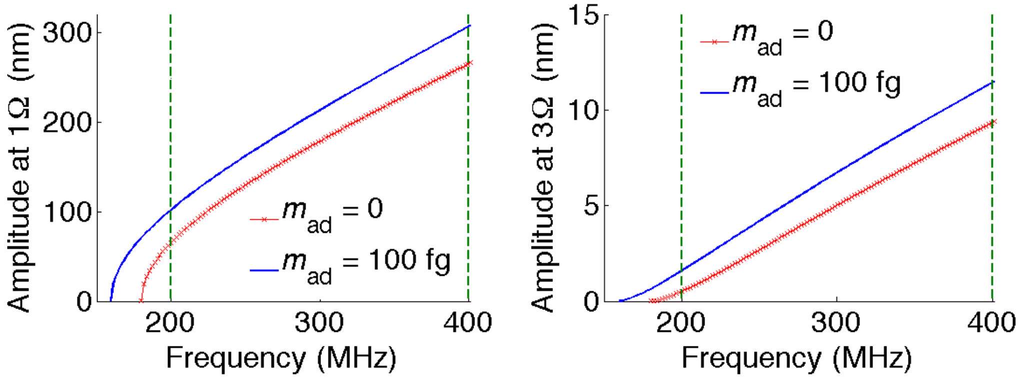

(a) (b)

*Figure 5.5. Analytical backbone curves of the first (a) and third (b) harmonics corresponding to zero damping and zero forcing and resulting from a two-term harmonic balance analysis.*

All three sensitivities are by construction equal to unity before any mass is added, and they all are directly proportional to the amount of mass added. The reason that the sensitivities increase as added mass increases is because the shift in the linearized frequency and the steady-state response amplitudes is greater for a larger amount of added mass than for a smaller amount of added mass. The peak sensitivity of the linearized frequency is $S_{\text{lin}} = 1.28$, the peak sensitivity of the first harmonic amplitude is $S_1 = 1.55$, and the peak sensitivity of the third harmonic amplitude is $S_3 = 2.95$. In fact, for a given amount of added mass, $S_1$ and $S_3$ are both greater than $S_{\text{lin}}$ at each excitation frequency considered and, in particular, $S_3$ is the largest.

Regarding the dependence of $S_1$ and $S_3$ on the excitation frequency, we clearly see that the sensitivities increase as the excitation frequency decreases. This trend can be understood by considering the analytical backbone curves shown in Fig. 5.5. Here I plot the backbone curves of the first and third harmonics before any mass is added, $m_{\text{ad}} = 0$, and after $m_{\text{ad}} = 100$ fg is added to the center. Note that the addition of mass causes the resonance curves to shift toward lower frequencies and, as a result, the steady-state amplitudes increase for a fixed frequency within the broadband. As a representative comparison, consider the cases corresponding to excitation frequencies of 200 MHz and 400 MHz, denoted by vertical dashed lines in Figures 5.5a and 5.5b.

The increases in the steady-state amplitudes are comparable at these two frequencies; yet the initial amplitudes (i.e., before mass is added – for $m_{\mathrm{ad}} = 0$) are significantly smaller at 200 MHz as compared to 400 MHz. Since the initial amplitudes are smaller at lower frequencies (although the increases in amplitudes with added mass are similar), the sensitivities $S_1$ and $S_3$ increase with decreasing frequency. This is especially true of the third harmonic for operational frequencies in the vicinity of the linearized resonant frequency; since the amplitude of the third harmonic is extremely small (~10 pm) at the linearized resonant frequency before mass is added, the ratio of the amplitude after mass is deposited to the initial amplitude is quite large for drive frequencies near the linear resonant frequency.

As a final step I define the *responsivities* of the linearized frequency, $R_{\mathrm{lin}}$, amplitude of the first harmonic, $R_1$, and amplitude of the third harmonic, $R_3$, as

$$R_{\mathrm{lin}} = \frac{d\omega_1}{dm_{\mathrm{ad}}}, \quad R_1 = \frac{dA_1}{dm_{\mathrm{ad}}}, \quad R_3 = \frac{dA_3}{dm_{\mathrm{ad}}} \tag{5.5}$$

Hence, the responsivities are the derivatives of the corresponding observable (measured) variables with respect to added mass.

As with the sensitivities, the responsivities of the nonlinear steady-state response amplitudes depend on the excitation frequency as well as the added mass, while the responsivity of the linearized frequency depends only on added mass. In Fig. 5.6a, I plot $R_{\mathrm{lin}}$ versus added mass; in Fig. 5.6b (5.6c) I show a contour plot of $R_1$ ($R_3$) as a function of added mass and excitation frequency; and in Fig. 5.6d (5.6e) I plot $R_1$ ($R_3$) versus added mass at five specific drive frequencies, namely, 182 MHz, 190 MHz, 200 MHz, 350 MHz and 500 MHz. Since the linearized frequency decreases with increasing added mass whereas the nonlinear steady-state amplitudes increase, the linear responsivity $R_{\mathrm{lin}}$ is always negative, while the nonlinear responsivities $R_1$ and $R_3$ are positive quantities.

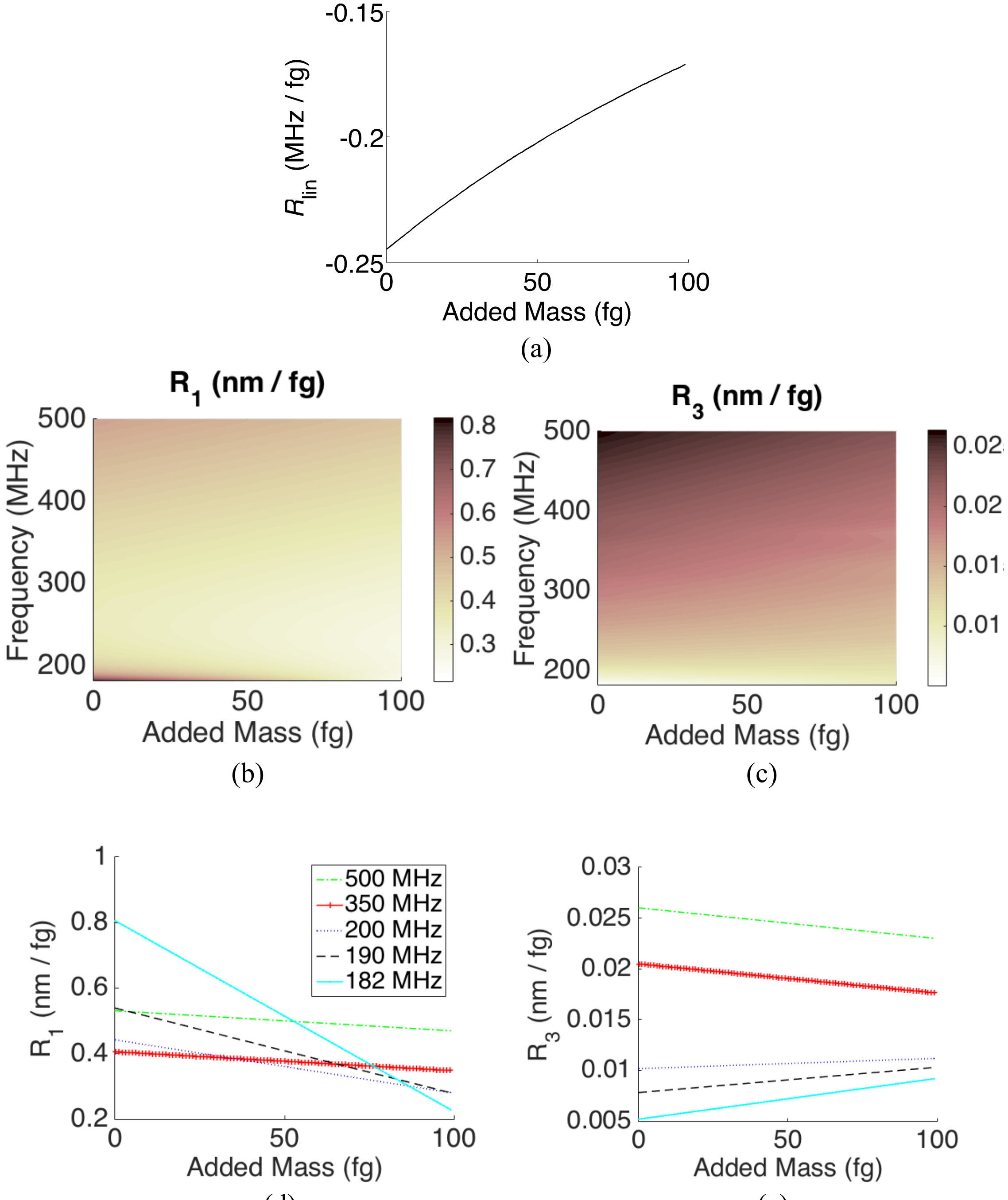

(a)

(b)

(c)

(d)

(e)

*Figure 5.6. (a) Responsivity versus added mass for the linearized frequency, responsivity versus added mass versus excitation frequency of the (b) first harmonic component, and (c) third harmonic component and responsivity versus added mass at five particular excitation frequencies of the (d) first harmonic component, and (e) third harmonic component. In (d) and (e), the responsivities of the amplitudes of the first and third harmonics are shown at 182 MHz (cyan), 190 MHz (black), 200 MHz (blue), 350 MHz (red) and 500 MHz (green).*

Interestingly, we see that $R_1$ is inversely related to the amount of added mass at all excitation frequencies whereas $R_3$ is inversely related to the amount of added mass for excitation frequencies above around 210 MHz and directly proportional to the amount of added mass for frequencies below 210 MHz. Regarding the dependence of the nonlinear responsivities on the operational frequency, $R_1$ decreases as the excitation frequency decreases for frequencies above 251 MHz. At 251 MHz, the trend of $R_1$ with respect to excitation frequency changes, and $R_1$ increases sharply as the drive frequency approaches the linearized frequency. In contrast, $R_3$ decreases with decreasing excitation frequency for the entire range of operational frequencies.

Another important mass sensing metric is the minimum detectable mass or mass resolution. For a conventional mass sensor designed to operate in the linear dynamic regime, the mass resolution, $\delta m_{\text{lin}}$, is given by

$$\delta m_{\text{lin}} = R_{\text{lin}}^{-1} \delta \omega_1 \tag{5.6}$$

where $\delta \omega_1$ is the minimum detectable shift in the linear resonant frequency. For the proposed nonlinear sensor that tracks shifts in the resonant amplitudes rather than frequency, the mass resolutions are given by

$$\delta m_1 = R_1^{-1} \delta A_1, \quad \delta m_3 = R_3^{-1} \delta A_3 \tag{5.7,5.8}$$

where $\delta m_1$ ($\delta m_3$) is the mass resolution that results from tracking shifts in the 1st harmonic (3rd harmonic) amplitude and $\delta A_1$ ($\delta A_3$) is the minimum detectable change in 1st harmonic (3rd harmonic) amplitude. The responsivities, $R_{\text{lin}}$, $R_1$ and $R_3$, are deterministic quantities determined by the sensor design, while the linear resonant frequency, $\omega_1$, and response amplitudes, $A_1$ and $A_3$, vary stochastically due to the presence of noise in the measurement system. As a result, the minimum detectable shifts in the linear frequency and response amplitudes, and the resulting mass resolutions, are largely influenced by noise (Kumar et al., 2012). The physical sources of noise are similar for linear and nonlinear sensors, but the primary role that noise plays can be quite different.

As the dissipation-fluctuation theorem states, any source of damping in the system can in turn serve as a source of noise due to thermal fluctuations (Heer, 1972). This includes the Nyquist-Johnson noise in the readout circuitry and the thermomechanical noise in the resonator itself. In the case of thermomechanical noise, the damping-mechanisms present in the resonator's dynamics induce random forcing along the beam such that the average force is zero, but the mean square amplitude of the resulting motion is nonzero (Albrecht et al., 1991; Butt and Jaschke, 1995; Cleland, 2005; Cleland and Roukes, 2002; Ekinci et al., 2004; Heer, 1972). Additionally, there exist so called parametric noise sources (Cleland and Roukes, 2002) that are associated with parametric changes in the resonator that do not necessarily result in thermal losses. Examples of parametric noise sources include adsorption and desorption of molecules in the surrounding medium, temperature fluctuations that induce thermal stresses, and defect motion within the resonator (Cleland and Roukes, 2002). Significant effort has been dedicated to quantifying the minimum detectable frequency shift, $\delta\omega_1$, and resulting mass resolution, $\delta m_{\text{lin}}$, for linear resonators due to the presence of such noise sources ( Albrecht et al., 1991; Butt and Jaschke, 1995; Cleland, 2005; Cleland and Roukes, 2002; Ekinci et al., 2004; Heer, 1972). Within the nonlinear dynamic regime, the signal-to-noise (SNR) is significantly larger due to the relatively large response amplitudes and, as a result, the dissipation-induced amplitude noise is less restrictive in practice. However, theoretical quantification of the minimum detectable amplitude shift is challenging due to the complex nonlinear behavior. As a crude estimate for the minimum detectable change in amplitude, the amplitude resolution can be taken to be an order of magnitude larger than the average dissipation-induced amplitude fluctuations (due to thermomechanical noise) near the primary resonance. For the linearized reduced order model of the doubly-clamped beam characterized by the effective stiffeness, $k = \frac{EI}{8L^3W_1^2\left(1/2\right)}$, and effective mass, $m = \frac{2\rho AL}{W_1^2\left(1/2\right)}$, the equipartition theorem says that the mean square displacement fluctuations of the center of the beam, $\left\langle z_{\text{th}}^2 \right\rangle$, satisfy $\frac{1}{2}k\left\langle z_{\text{th}}^2 \right\rangle = \frac{1}{2}m\omega_1^2\left\langle z_{\text{th}}^2 \right\rangle = \frac{1}{2}k_BT$ near the fundamental bending mode, where $k_B$ is the Boltzmann constant and $T$ is the temperature (Heer, 1972). Considering the system parameters stated in Table 1 and $T = 298\text{K}$, we have

$$\left\langle z_{\text{th}} \right\rangle \approx \sqrt{\frac{k_B T}{k}} \tag{5.9}$$

If the amplitude resolution is assumed to be an order of magnitude larger than $\left\langle z_{\text{th}} \right\rangle$, then the minimum detectable shift in amplitude is ~30 pm. Considering the maximum values of $R_1 = 0.75\text{nm/fg}$ and $R_3 = 0.026\text{nm/fg}$ shown in Figs. 5.6b and 5.6c (corresponding to 182 MHz and 500 MHz, respectively, with zero added mass) and using equations (21) and (22), I compute mass resolutions of 0.04 fg and 1.2 fg for the amplitudes of the first and third harmonics, respectively.

### 5.5 Conclusions

Following the work presented in Chapter 4 (Sections 4.1-4.4), in this Chapter I consider the doubly clamped beam having a concentrated mass at the center and under harmonic base excitation in a mass sensing scheme based on amplitude tracking. By operating at an excitation amplitude above the critical threshold, the bandwidth of the nonlinear resonance increases significantly. A two-term harmonic balance analysis was used to analytically predict the backbone curves (i.e., the frequency-amplitude relations of the underlying undamped, unforced system) of the first and third harmonics of the steady-state response of the beam. I also computationally generated frequency-amplitude curves of the damped, forced system and, interestingly, found that they coincide closely with the analytical backbones. The strong correspondence is due to the relatively low-damping and forcing levels of this system, and to the energy localization of the steady-state response in the first and third harmonics.

In order to exploit the large bandwidth for mass sensing, I studied shifts in the steady-state amplitudes of the first and third harmonics resulting from the addition of mass at the center of the beam. I found that tracking the high amplitude resonant response is indeed feasible and that the steady-state response amplitudes are quite sensitive to added mass. The advantage of the proposed resonator design as compared to other micromechanical mass sensors (both linear and nonlinear) is its ultra-wide range of operational frequencies and amplitudes with strong SNR. The design of the resonator is also simple in terms of fabrication with feature sizes larger than 100 nm. Finally, the first and third harmonic amplitudes demonstrated enhanced sensitivity to mass addition as compared to the linearized frequency, and their mass resolutions were found to be on the femtogram scale. In practice, the presence of electrical and parametric noise would likely increase the minimum detectable shift in amplitude and thereby increase the resulting mass resolutions for the 1st and 3rd harmonics. The primary focus of this study was to introduce the proposed resonator design and develop a theoretical framework for the mass sensing method based on amplitude tracking within ultra-wide resonant bandwidths.

## 5.6 References

Albrecht, T.R., Grütter, P., Horne, D., Rugar, D. (1991). Frequency modulation detection using high‐ Q cantilevers for enhanced force microscope sensitivity. *Journal of Applied Physics*, *69*(2), 668–673.

Aldridge, J.S., Cleland, A.N. (2005). Noise-enabled precision measurements of a duffing nanomechanical resonator. *Physical Review Letters*, *94*(15), 5–8.

Alsaleem, F.M., Younis, M.I. (2010). Stabilization of electrostatic MEMS resonators duffing nanomechanical resonator. *Physical Review Letters*, *94*(15): 5–8.

Antonio D., Zanette D.H., López D. (2012). Frequency stabilization in nonlinear micromechanical oscillators. *Nat. Commun.,. 3*, 806.

Arlett J.L, Myers E.B., RoukesM.L. (2011). Comparative advantages of mechanical biosensors. *Nature Nanotech*. 6: 203-215. Feedback. *Journal of Microelectromechanical Systems*, *25*(1), 2–10.

Askari H., Jamshidifar H., Fidan B. (2017). High resolution mass identification using nonlinear vibrations of a nanoplate. *Measurement: Journal of the International Measurement*, *101*, 166-174.

Bajaj, N., Sabater, A.B., Hickey, J.N., Chiu, G.T. C., Rhoads, J.F.J. (2016). Design and Implementation of a Tunable, Duffing-Like Electronic Resonator via Nonlinear Feedback. *Journal of Microelectromechanical systems*, *25*(1), 2-10.

Butt, H.-J., Jaschke, M. (1995). Calculation of thermal noise in atomic force microscopy. *Nanotechnology*, *6*: 1–7.

Bouchaala, A., Jaber, N., Yassine, O., Shekhah, O., Chernikova, V., Eddaoudi, M., Younis, M.I. (2016). Nonlinear-based MEMS sensors and active switches for gas detection. *Sensors*, *16*(6), 758.

Chaste J., Eichler A., Moser J., Ceballos G., Rurali R., Bachtold A. (2012) A nanomechanical mass sensor with yoctogram resolution. *Nature Nanotech*. *7*(5), 301-304.

Chiu H.-Y., Hung H., Postma H., Bockrath M. (2008). Atomic-scale mass sensing using carbon nanotube resonators. *Nano Lett.* 8(12): 4342-4346.

Cho H., Yu M.-F., Vakakis A., Bergman L., McFarland D.M. (2010). Tunable, broadband nonlinear nanomechanical resonator. *Nano Lett*., *10*(5), 1793-1798.

Cho H., Jeong B., Yu M.F., Vakakis A.F., McFarland D.M., Bergman L.A. (2012). Nonlinear hardening and softening resonances in micromechanical cantilever-nanotube systems originated from nanoscale geometric nonlinearities. *Int. J. Solids Str*., *49*, 2059-2065.

Cleland, A.N., Roukes, M.L. (2002). Noise processes in nanomechanical resonators. *Journal of Applied Physics*, *92*(5), 2758–2769.

Dai M.D., Eom K., Kim C.-W. (2009). Nanomechanical mass detection using nonlinear oscillations. *Appl. Phys. Lett., 95*, 203104.

Dohn, S., Schmid, S., Amiot, F., Boisen, A. (2010). Position and mass determination of multiple particles using cantilever based mass sensors. *Applied Physics Letters*, *97*, 044103.

Duo S., Jensen S. (2015). Optimization of nonlinear structural resonance using the incremental harmonic balancing method. *J. Sound Vib., 334*, 239-254.

Ekinci K.L., Yang Y.T., Roukes M.L. (2004). Ultimate limits to inertial mass sensing based upon nanoelectromechanical systems. *J. Appl. Phys., 95*(5), 2682-2689.

Garcia R., Perez R. (2002). Dynamic atomic force microscopy methods. *Surf. Sci., 47*, 197-301.

Grüter R.R., Khan Z., Paxman R., Ndieyira J.W., Dueck B., Bircher B.A., Yang J.L., Drechsler U., Despont M., McKendry R.A., Hoogenboom' B.W. (2010). Disentangling mechanical and mass effects on nanomechanical resonators. *Appl. Phys. Lett., 96*, 023113.

Gupta A.K., Nair P.R., Ladisch M.R., Broyles S., Alam M.A., Bashir R. (2006). Anamalous resonance in a nanomechanical biosensor. *PNAS, 103*(36), 13362-13367.

Hanay, M.S., Kelber, S., Naik, A.K, Chi D., Hentz, S., Bullard, E.C., Colinet, E., Duraffourg, L., Roukes, M.L. (2012). Single protein nanomechanical mass spectrometry in real time. *Nat Nanotechnol.*, *7*(9), 602–608.

Heer C.V., (1972). Statistical mechanics, kinetic theory and stochastic processes. Academic Press Inc, London, UK.

Hiller, T., Li, L.L., Holthoff, E.L., Bamieh, B., Turner, K.L. (2015). System Identification, Design, and Implementation of Amplitude Feedback Control on a Nonlinear Parametric MEM Resonator for Trace Nerve Agent Sensing. *Journal of Microelectromechanical Systems*, *24*(5), 1275–1284.

Ilic, B., Czaplewski, D., Zalautdinov, M., Craighead, H.G., Neuzil, P., Campagnolo, C., Batt, C. (2001). Single cell detection with micromechanical oscillators. *J. Vac. Sci. Tech. B.*, *19*, 2825–2828.

Ilic B., Yang Y., Aubin K., Reichenbach R., Krylov S., Craighead H.G. (2005). Enumeration of DNA Molecules Bound to a Nanomechanical Oscillator. *Nano Lett.*, *5*(5), 925-929.

Ilic B., Krylov S., Craighead H.G. (2010). Young's modulus and density measurements of thin atomic layer deposited films using resonant nanomechanics. *J. Appl. Phys.*, *108*, 044317.

Jain A., Nair P.R., Alam M.A. (2012). Flexure-FET biosensor to break the fundamental sensitivity limits of nanobiosensors using nonlinear electromechanical coupling. *PNAS, 109*(24), 9304-9308.

Jensen K., Kwanpyo K., Zettl A. (2008). An atomic-resolution nanomechanical mass sensor. *Nature Nanotechnology*, *3*, 533-537.

Johnson B.N., Mutharasan R. (2012). Biosensing using dynamic-mode cantilever sensors: A review. *Biosens. Bioelectr.*, *32*, 1-18.

Kacem, N., Arcamone, J., Perez-Murano, F., Hentz, S. (2010). Dynamic range enhancement of nonlinear nanomechanical resonant cantilevers for highly sensitive NEMS gas/mass sensor applications. *Journal of Micromechanics and Microengineering*, *20*(4), 45023.

Karabalin, R.B., Feng, X.L., Roukes, M.L. (2009). Parametric nanomechanical amplification at very high frequency. *Nanolett., 9*(9), 3116-3123.

Keum H., Yang Z., Han K., Handler D.E., Nguyen T.N., Schutt-Aine J., Bahl G., Kim S. (2016). Microassembly of heterogenous materials using transfer printing and thermal processing. *Nature Sc. Rep., 6*, 29925.

Kharrat C., Colinet E., Voda A. (2008). H∞ loop shaping control for PLL-based mechanical resonance tracking in NEMS resonant mass sensors. *Proceedings of IEEE Sensors, 2008* 1135-1138.

Kozinsky, I., Postma, H.W.C., Kogan, O., Husain, A., Roukes, M.L. (2007). Basins of attraction of a nonlinear nanomechanical resonator. *Physical Review Letters*, *99*(20), 8–11.

Kumar V., Boley J.W., Yang Y., Ekowaluyo H., Miller J.K., Chiu T.-C., Rhoads J.F. (2011). Bifurcation-based mass sensing using piezoelectrically-actuated microcantilevers. *Appl. Phys. Lett., 98*, 153510.

Kumar, V., Yang, Y., Boley, J.W., Chiu, T.-C, Rhoads, J.F. (2012). Modeling , Analysis , and Experimental Validation of a Bifurcation-Based Microsensor. *J Microelectromech Syst*., *21*(3), 549–558.

Li, L., Hiller, T., Bamieh, B., & Turner, K. (2014). Amplitude control of parametric resonances for mass sensing. *Proceedings of IEEE Sensors*, *2014* (December): 198–201.

Li L., Polunin P.M., Duo S., Shoshani O., Strachan B.S., Jensen J.S., Shaw S.W., Turner K.L (2017), Tailoring the nonlinear response of MEMS resonators using shape optimization. *Appl. Phys. Lett.* 110, 081902: 1-5.

Ma S., Huang H., Lu M., Veidt M. (2012). A simple resonant method that can simultaneously measure elastic modulus and density of thin films. *Surf. Coat. Tech*., *209*, 208-211.

Mahmoud M.A. (2016). Validity and accuracy of resonance shift prediction formulas for microcantilevers: A review and comparative study. *Critical Rev. Solid State Mat. Sc*., *41*(5), 386-429.

de Oteyza D.G., Gorman P., Chen Y.-C., Wickenburg S., Riss A., Mowbray D.J., Etkin G., Pedramrazi Z., Tsai H.-Z., Rubio A., Crommie M.F., Fischer F.R. (2013). Direct imaging of covalent bond structure in single-molecule chemical reactions. *Science, 340*, 1434-1437.

Olcum, S., Cermak, N., Wasserman, S. C., & Manalis, S. R. (2015). High-speed multiple- mode mass-sensing resolves dynamic nanoscale mass distributions. *Nature Communications*. 6: 7070.

Rhoads, J., Shaw, S., Turner, K., Baskaran, R. (2005). Tunable microelectromechanical filters that exploit parametric resonance. *J. Vib. Acoust., 127*, 423-430.

Rhoads, J.F., Shaw, S.W., Turner, K.L. (2010), Nonlinear Dynamics and Its Applications in Micro- and Nanoresonators. *J. Dyn. Sys., Meas., Control.*, *132*(3), 034001, 1-14.

Turner, K., Miller, S., Hartwell, P., MacDonald, N., Strogatz, S. (1998). Five parametric resonances in a microelectromechanical system. *Nature, 396*(6707), 149-152.

Unterreithmeier, Q. P., Faust, T., Kotthaus, J. P. (2010), Nonlinear switching dynamics in a nanomechanical resonator. *Physical Review B - Condensed Matter and Materials Physics*, *81*(24), 1–4.

Yang Y.T, Callegari C., Feng X.L., Ekinici K.L, and Roukes M.L. (2006). Zemptogram-Scale Nanomechanical Mass Sensing. *Nanolett.*, *6*, 4, 583-586.

Yang Y.T, Callegari C., Feng X.L., and Roukes M.L. (2011). Surface absorbate fluctuations and noise in nanoelectromechanical systems. *Nanolett.*, *11*, 1753-1759.

Younis M.I., Alsaleem F. (2009). Electrostatically-actuated structures based on nonlinear phenomena. *J. Comp. Nonl. Dyn.*, *4*, 021010.

Yu, M., Wagner, G., Ruoff, R., Dyer, M. (2002). Realization of parametric resonances in a nanowire mechanical system with nanomanipulation inside a scanning electron microscope. *Phys. Rev. B.*, *66*, 073406, 1-4.

Zhang, W., Baskaran, R., Turner, K.L. (2002). Effect of cubic nonlinearity on auto-parametrically amplified resonant MEMS mass sensor. *Sensors and Actuators, A: Physical*, *102*(1–2), 139–150.

Zhang W., Turner K.L. (2005). Application of parametric resonance amplification in a single-crystal silicon micro-oscillator based mass sensor. *Sensors and Actuators A,* 122, 23-30.

Zhang Y. (2014) Detecting the stiffness of biochemical absorbates. *Sensors and Actuators B, 202*, 286-293.

# Chapter 6: Concluding remarks and suggestions for future work

## 6.1 Summary

In this dissertation, nonlinear microresonator designs have been considered for application in AFM and mass sensing. Through computational and experimental analysis, the proposed resonator designs have been shown to offer unique advantages over existing sensor designs. The thesis began with an overview of basic operating principles and limitations of linear and nonlinear micromechanical resonators. This included a discussion of reduced order modeling, relevant linear and nonlinear analytical analyses, motivations for intentional nonlinearity and common sources of nonlinearity.

In Chapter 3, I studied the performance of a new probe design to be used in multi-frequency tapping mode AFM. The cantilever is composed of a base microcantilever with an inner paddle made of a *Si* nanomembrane. The reduced order model of the inner-paddled cantilever was constructed in the form of two linearly coupled damped harmonic oscillators having a lower, in-phase vibration mode and a higher, out-of-phase vibration mode. By design, the out-of-phase vibration frequency is an integer multiple of the in-phase vibration frequency providing the necessary conditions for internal resonance. The nonlinear vibro-impacts between the tip and sample during tapping mode AFM trigger the internal resonance leading to strong, passive amplification of a higher harmonic. Through computational and experimental studies, the reduced order model of the inner-paddled cantilever was verified, and it was shown that a 1:2 internal resonance is optimal. Further, it was shown that the internal resonance-based design leads to enhanced compositional sensitivity as compared to commercial cantilevers. In some instances, the material characterization was based on branch selection among coexisting solution branches. In other cases, the internal resonance-based design introduced sensitivity to Young's modulus in the phase that would otherwise not be there for a purely elastic sample. At the end of the chapter, an outline for material property inversion analysis is presented which can be used to convert the inner-paddle's observables to quantitative compositional measurements.

In Chapter 4, a micromechanical resonator consisting of a doubly clamped beam having a concentrated mass at the center was studied. The reduced order model of this system was shown to be in the form of the Duffing equation, which is well known to exhibit nonlinear bending of the primary resonance curve. The nonlinear bending results in a broadband resonance where the lower bound of the resonant bandwidth is linear frequency and the upper bound is the jump-down bifurcation frequency. It was shown that under harmonic base excitation, there is no theoretically predicted jump-down bifurcation above a critical excitation amplitude. It was further shown that the presence of the concentrated mass lowers the critical excitation amplitude required to achieve this *no drop phenomenon.* In practice, the drop bifurcation may inevitably be triggered by the presence of noise, excitation of internal resonances, shrinking domain of attraction for the upper solution branch and/or the presence of nonlinear damping.

A related system was studied experimentally in order to investigate the prediction of sudden bandwidth expansion at a critical excitation amplitude. The system consists of a *Si* microcantilever that is constrained at its free end by a polymer bridge. The reduced order model of this system is also that of a Duffing oscillator but with an additional nonlinear damping term. Two different microcantilever-polymer devices showed evidence of sudden bandwidth expansion at a threshold excitation level, providing some validation of the theoretical predictions. Further, theoretical analysis showed that the presence of nonlinear damping is also a practical limitation to the *no drop phenomenon* and may indeed be responsible for the jump bifurcations observed in the microcantilever-polymer devices at large excitation levels.

In Chapter 5, the microresonator design consisting of a doubly-clamped beam with a concentrated mass at the center was considered in a mass sensing application. By operating at an excitation amplitude above the critical level, the ultra-wide bandwidth can be exploited in a mass detection method based on amplitude tracking. I computationally studied variations in the first and third harmonic amplitudes as mass was added to the device, at a fixed base excitation frequency within the broadband. Both the first and third harmonic amplitudes proved to be more sensitive to added mass than the linear resonant frequency and, in particular, the third harmonic amplitude was the most sensitive indicator. In comparison to other linear and nonlinear micromechanical sensors, this device provides a wide range of operational frequencies and amplitudes while maintaining simplicity in the microfabrication and actuation methods.

## 6.2 Suggestions for future work

In this section, suggestions for future research topics based on the present work are provided.

### Quantitative compositional mapping with the inner-paddled cantilever

Using the material property inversion analysis included in the end of Chapter 3, the observables of this cantilever system can be transformed into quantitative material property measurements. One of the primary limitations to quantitative compositional mapping in multi-harmonic AFM is the SNR of the higher harmonic signals (Cartagena et al., 2013; Raman et al., 2011; Stark et al., 2010). Special techniques need to be used to amplify the higher harmonics or 0th harmonic that may not be available to most AFM users. For example, Cartagena et al. (2013) used a magnetically excited AFM cantilever that is pre-compressed onto a sample submerged in liquid in order to achieve a strong 0th harmonic signal. In other approaches to quantitative compositional mapping using tapping mode AFM, such as the commercially available AM-FM Viscoelastic Mapping Mode offered by Asylum Research, multiple feedback control loops are required, one of which utilizes relatively sophisticated frequency modulation feedback control scheme (Kocun et al., 2017; Hurley et al., 2015). This type of technique is not well suited for a novice AFM user and further, the required tools may not be widely available. Quantitative compositional mapping with the proposed inner-paddled cantilever would offer a considerably simpler alternative to the methods currently available. The main drawback is that the inner-paddled cantilever is not commercially available; however, methods for batch microfabrication of this device are currently being investigated.

### Further experimental verification of ultra-wide broadband resonances

Following the work presented in Chapter 4, a more systematic validation of the theoretical predictions outlined in Section 4.1 may be possible with the use of electrostatic actuation. If the resonator is excited electrostatically, the excitation force acts directly on the resonator rather than at the base (Younis and Asaleem, 2009; Younis, 2011). In this case, the forcing level of the harmonic excitation is independent of the excitation frequency, and the theoretical *no drop phenomenon* should be impossible. Practically, this means that the resonance curves of the microcantilever-polymer devices should show no evidence of sudden bandwidth expansion. If indeed it can be shown that, under electrostatic actuation, the devices do not exhibit sudden bandwidth expansion, this would further underscore the conclusions drawn from the resonance curves shown in Fig. 4.12; specifically, that the sudden bandwidth expansion observed in the microcantielver-polymer devises under harmonic base excitation is due to the existence of a critical excitation amplitude as predicted in Sections 4.1 and 4.7. Additionally, this procedure can be repeated for other Duffing-like microresonant systems in order to test the robustness of this phenomenon.

### Eliminating cross-talk in AFM-IR using the inner-paddled cantilever

AFM-IR is a technique that combines atomic force microscopy and infrared (IR) spectroscopy to achieve chemical analysis of samples with high spatial resolution. In AFM-IR, a small region of a sample is locally irradiated with a monochromatic IR light source, and if the frequency of the IR laser coincides with a frequency associated with the molecular vibrations of the irradiated region, the light will be absorbed. The light absorption results in photothermal expansion of the irradiated region, which is detected by an AFM probe interrogating the region. The thermal expansion of the region provides an impulsive excitation to the AFM cantilever and thereby excites the vibration modes of the cantilever. A fast Fourier transform (FFT) of the cantilever's response measures the amplitudes and frequencies of the cantilever's vibration modes at a specific IR wavelength. The wavelength of the IR laser is incrementally swept while the magnitude of the highest peak in the FFT is recorded. Typically, the fundamental bending mode provides the highest peak in the FFT and is therefore the ideal candidate for monitoring IR absorption. The amplitude of a specific vibration mode as a function of IR wavelength provides the absorption spectrum for the irradiated region, and this absorption spectrum is a unique chemical "fingerprint" that can be used to identify the local material (Dazzi et al., 2010; Dazzi et al., 2012). One limitation to this technique is crosstalk between the IR absorption and the contact condition between the tip and sample (e.g., the sample's local Young's modulus). Variations in the contact stiffness between a commercial AFM tip and the sample cause variations in the vibration frequencies of the cantilever. The shifts in the vibration frequencies resulting from changes in the contact stiffness influence the AFM-IR measurements and, therefore, cause undesirable crosstalk. In a recently submitted paper (Dharmasena et al., *submitted*) it was shown that, under certain conditions, the in-phase vibration frequency of the inner-paddled cantilever is independent of the tip-sample contact stiffness. On the other hand, the out-of-phase vibration frequency shows strong sensitivity to the tip-sample contact stiffness. The stability of the in-phase frequency with respect to the contact stiffness can potentially be exploited in order to eliminate crosstalk in AFM-IR measurements and thereby enhance the accuracy of the chemical analysis. Secondly, it is possible that by simultaneously tracking shifts in the out-of-phase frequency, the local contact stiffness can be measured as well.

### Bifurcation based photothermal spectroscopy using nonlinear microresonators

AFM-IR offers state-of-the-art spatial resolution for IR spectroscopy and the ultimate spatial resolution of AFM-IR is on the order of 10nm. However, as the feature size decreases, the magnitude of the thermal expansion associated with IR absorption decreases as well making it difficult to measure absorption spectra in features smaller than ~10nm (Felts et al., 2013). To overcome this limitation with regard to feature size, it may be possible to utilize ultra-sensitive bifurcation frequencies. Specifically, the nanoparticulate sample of interest may be attached directly to a doubly clamped microbeam (Larsen et al., 2013) where the IR laser is irradiated upon the sample. By specifically designing the beam to enhance geometric nonlinearity, strong hardening in the primary resonance curve can be achieved. If the microbeam is excited harmonically at an operating point just below the jump-down bifurcation frequency on the upper solution branch, the resonator will be extremely sensitive to small perturbations in the state variables. This operating point can be realized by sweeping the drive frequency forward to a frequency just under the jump-down frequency. When the IR laser is tuned to a wavelength corresponding to absorption by the nanoparticle, the thermal expansion will provide an impulsive excitation directly to the resonating microbeam. Since the domain of attraction for the upper solution branch is so small in this operating regime, extremely small impulsive forces should cause the dynamics to transition from the upper branch to the lower branch. This will be indicated by a sudden decrease in the response amplitude. The jump bifurcation can be used as a switch, detecting a threshold amount of thermal expansion in the sample (Bouchaala et al., 2016). As the IR frequency is swept, the jump-down bifurcation should happen at frequencies corresponding to the molecular vibration frequencies of the sample. In the end, this technique could be used to identify the molecular vibration frequencies for extremely small nanoparticles. That is, the frequencies of the peaks in the absorption spectra would be identified, but not the relative amplitudes. In light of the discussion presented in Section 4.6, noise may cause artificial peaks in the measured absorption spectra but repeating the spectroscopy process several times might filter out the noise-induced peaks. Also, UHV and low temperature operating conditions may help eliminate undesirable branch jumping due to noise.

## 6.3 References

Bouchaala, A., Jaber, N., Yassine, O., Shekhah, O., Chernikova, V., Eddaoudi, M., Younis, M.I. (2016). Nonlinear-based MEMS sensors and active switches for gas detection. *Sensors*, *16*(6), 758.

Cartagena, A., Hernando-Pérez, M., Carrascosa, J.L., de Pablo, P.J., and Raman, A. (2013). Mapping in vitro local material properties of intact and disrupted virions at high resolution using multi-harmonic atomic force microscopy. *Nanoscale*, *5*, 4729–36.

Dazzi, A., Glotin, F., and Carminati, R. (2010). Theory of infrared nanospectroscopy by photothermal induced resonance. *Journal of Applied Physics*, *107*(12).

Dazzi, A., Prater, C. B., Hu, Q., Chase, D. B., Rabolt, J. F., and Marcott, C. (2012). AFM-IR: Combining atomic force microscopy and infrared spectroscopy for nanoscale chemical characterization. *Applied Spectroscopy*, *66*(12), 1365–1384.

Dharmasena, S.M., Ynag Z., Kim S., Bergman L.A., Vakakis A.F., Cho H. (2018). Ultimate decoupling between surface topography and material functionality in atomic force microscopy using an inner-paddled cantilever. *ACS Nano*, *12*(6), 5559-5569.

Felts, J. R., Cho, H., Yu, M. F., Bergman, L. A., Vakakis, A. F., and King, W. P. (2013). Atomic force microscope infrared spectroscopy on 15 nm scale polymer nanostructures. *Review of Scientific Instruments*, *84*(2).

Garcia R. (2010). *Amplitude Modulation Atomic Force Microscopy*. Wiley-VCH Verlag GmbH & Co. KGaA, Weinheim, Germany.

Hurley, D., Kocun, M., Revenko, I., Ohler, B., and Proksch, R. (2015). Fast, quantitative AFM nanomechanical measurements using AM-FM Viscoelastic Mapping Mode. *Microscopy and Analysis*, SPM Supplement, March/April, 9-13.

Kocun, M., Labuda, A., Meinhold, W., Revenko, I., Proksch, R. (2017). Fast, High Resolution, and Wide Modulus Nanomechanical Mapping with Bimodal Tapping Mode. *ACS Nano, 11,* 10097-10105.

Larsen, T., Schmid, S., Villanueva, L. G., and Boisen, A. (2013). Photothermal analysis of individual nanoparticulate samples using micromechanical resonators. *ACS Nano*, *7*(7), 6188–6193.

Raman, A., Trigueros, S., Cartagena, A., Stevenson, A. P., Susilo, M., Nauman, E., Contera, S. A. (2011). Mapping nanomechanical properties of live cells using multi-harmonic atomic force microscopy. *Nat Nanotechnol*, *6*, 809–814.

Stark W.R. (2010). Bistability, higher harmonics and chaos in AFM. *Materials Today, 13,* 24-32.

Younis, M. I., (2011). *MEMS Linear and Nonlinear Static and Dynamics (Microsystems)*, Springer, Berlin.

Younis M.I., Alsaleem F. (2009). Electrostatically-actuated structures based on nonlinear phenomena. *J. Comp. Nonl. Dyn.*, *4*, 021010.